TECHNISCHE UNIVERSITÄT MÜNCHEN

FAKULTÄT FÜR CHEMIE

LEHRSTUHL FÜR ANORGANISCHE UND METALLORGANISCHE CHEMIE

Encapsulation of Atom-Precise Clusters in Metal-Organic Frameworks for Electrocatalytic Applications

KATHRIN KRATZL

Vollständiger Abdruck der von der Fakultät für Chemie der Technischen Universität München zur Erlangung des akademischen Grades eines

Doktors der Naturwissenschaften (Dr. rer. nat.)

genehmigten Dissertation.

Vorsitzender:	Prof. Dr. Dr. h.c. Bernard Rieger
Prüfer der Dissertation:	1. Prof. Dr. Roland A. Fischer
	2. Prof. Dr. Ulrich K. Heiz

Die Dissertation wurde am 19.02.2020 bei der Technischen Universität München eingereicht und durch die Fakultät für Chemie am 30.03.2020 angenommen.

ENCAPSULATION OF ATOM-PRECISE CLUSTERS IN METAL-ORGANIC FRAMEWORKS FOR ELECTROCATALYTIC APPLICATIONS

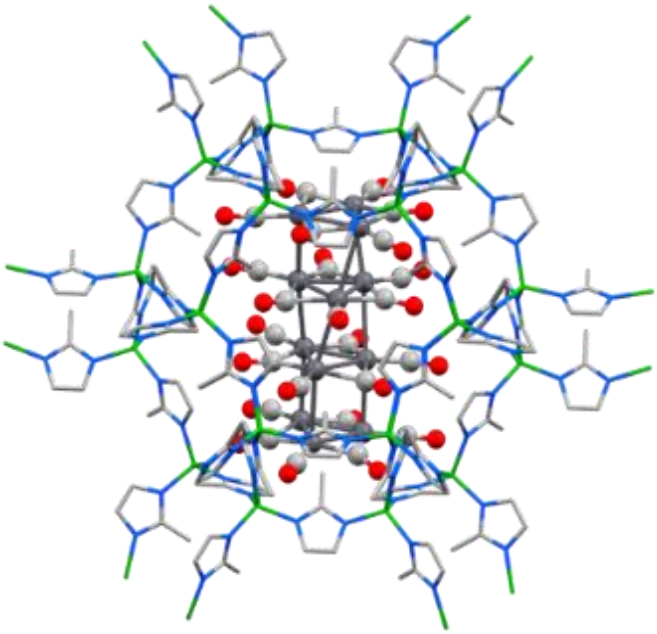

Dissertation

Kathrin Kratzl

Die vorliegende Arbeit wurde im Zeitraum von Januar 2017 bis Februar 2020 im Fachgebiet Anorganische und Metallorganische Chemie der Technischen Universität München angefertigt.

DANKSAGUNG

Zu Beginn möchte ich mich bei Prof. Roland A. Fischer bedanken, der mich als erste „TUMlerin“ an seinem Lehrstuhl aufgenommen hat. Über meine gesamte Promotion haben Sie mir immer größtes Vertrauen entgegengebracht und mich völlig frei arbeiten lassen, obwohl ich mit nur wenig anorganischem Hintergrund bei Ihnen angefangen habe. Ihr ansteckender Enthusiasmus an der Wissenschaft, die Möglichkeiten zu internationalen Kooperationen und zu Konferenzbesuchen, sowie die gemeinsamen Events außerhalb von Labor und Büro werden mir die letzten drei Jahre in guter Erinnerung bleiben lassen.

Mein Dank gilt außerdem unserem gesamten Mittelbau, mit Augenzwinkern die „Hateful Eight“ genannt, die unseren Lehrstuhl reibungslos am Laufen halten und die wissenschaftliche Seite der Organisation fest im Griff haben. Ohne Martin Schellerer und Dana Weiß, unsere Felsen in der Brandung im Sekretariat, wären wir alle schon längst im Chaos versunken. Vielen Dank für eure allzeit Erreichbarkeit und Geduld in jeder Situation. Außerdem möchte ich mich bedanken bei allen anderen Technikern und den Mädels aus der Elementaranalyse für Unterstützung bei Messungen und organisatorischen Angelegenheiten.

Des Weiteren ein großes Dankeschön an meine Kooperationspartner im In- und Ausland, ganz besonders an Batyr Garlyyev, Tim Kratky und Ondřej Tomanec, für diverse Messungen, deren Ergebnisse ihren Weg in diese Arbeit gefunden haben. A huge thank you to all of you for helping me with measurements of all kind!

Vielen Dank auch an meine fleißigen Bacheloranden, Forschungspraktikanten und Masteranden: Michaela Würbser, Lisa Schlor, Marina Wittig, Raphael Bühler, Eva Krois, Lorenzo Facco und Kathrin Kollmannsberger. Bei Letzterer möchte ich mich noch einmal besonders bedanken, weil du schon ein Forschungspraktikum bei mir ertragen hast und trotzdem zur Masterarbeit wiedergekommen bist. Dich zu betreuen war immer mehr Vergnügen als Arbeit und ich könnte mir keine bessere Nachfolgerin vorstellen. Ich wünsche dir ganz viel Glück und Erfolg bei deiner Promotion!

Ich bedanke mich ganz herzlich beim ganzen AMC-Lehrstuhl für die tolle Zeit mit euch, angefangen mit Jana und Hung, die mir in den ersten Monaten jede noch so dumme Frage geduldig beantwortet haben, und der Rest der OM-Gruppe mit Julius, Patti, Maxi und meinen Reihenkollegen Max, der fast drei Jahre lang meinen Putzfimmel ertragen musste. Danke auch an meine Lehrstuhlbandkollegen Pia, David, Phipps und Alex für kreative Nachmittage und Begeisterung, auch wenn ich noch so falsch gesungen habe. Vielen Dank an euch alle hier nicht namentlich genannten für ein offenes Ohr, wenn ich unbedingt jemandem meine Laborprobleme erzählen musste oder jemandem zeigen, wie schön farbig mein Cluster ist. Ihr

habt alle dafür gesorgt, dass der Spaß vor lauter Wissenschaft nicht zu kurz kommt. Danke dafür!

Der legendären Damn-Gruppe ein riesiges Dankeschön für die tollen acht Jahre Chemiestudium mit euch. Von der „Lerngruppe“ in der Bib über Sommerurlaube und Mittwochabende im P11, ihr habt das Studium zur schönsten Zeit meines Lebens gemacht und ich hoffe, dass wir den Kontakt auch nach der Promotion halten, auch wenn wir alle #business sind.

Liebe Mama, lieber Papa, liebe Dona, ihr seid die beste Familie der Welt und habt mich während meiner ganzen Studienzeit immer unterstützt und mir den Rücken freigehalten. Ihr seid immer für mich da, und auch wenn ihr euch sicher manchmal fragt, was ich die letzten drei Jahre da eigentlich getrieben habe, wart ihr euch immer sicher, dass ich das schon schaffe.

Wie immer kommt das Beste zum Schluss: Vielen Dank an Michael Weger – partner in crime, life and chemistry. Erste Hilfe im OCA, Bachelorarbeit im selben Chaotenlabor, das beste Echinger-See-Team in Prüfungsphasen – du hast mich durch mein gesamtes Studium und die letzten Jahre auch darüber hinaus begleitet und unterstützt. Viele Probleme und Ärgernisse schauen schon viel weniger schlimm aus, nachdem ich mich bei dir darüber aufgeregt habe. Danke für deinen Humor, deine Geduld und deine bedingungslose Liebe.

„Results! Why, man, I have gotten a lot of results.
I know several thousand things that won't work."

Thomas A. Edison

TABLE OF CONTENTS

KURZZUSAMMENFASSUNG

In dieser Arbeit wurde eine neue Methode zur Synthese von ligandfreien („nackten“), atompräzisen Metallnanoclustern entwickelt, die auf der Verkapselung in metallorganische Gerüste (metal-organic frameworks, MOFs) basiert. Hierbei wurde zunächst der molekulare, ligandstabilisierte *Chini*-Cluster $[Pt_9(CO)_{18}](NBu_4)_2$ in das zeolitische Imidazolatgerüst ZIF-8 eingebracht und anschließend die CO-Liganden bei 200 °C thermisch abgespalten. Das resultierende, überraschend stabile Kompositmaterial Pt_n@ZIF-8 mit einer Clustergröße n nahe 12 Atomen zeigte keine Clusteragglomeration unabhängig von der experimentell erreichbaren Pt-Beladung im Bereich von 1-20 Gew.-%. Pt_n@ZIF-8 wurde erfolgreich für Alkenhydrierungen sowie in der elektrokatalytischen Sauerstoffreduktion (oxygen reduction reaction, ORR) eingesetzt. Im sauren Elektrolyten $HClO_4$ löst sich das stabilisierende ZIF-8 langsam auf und die kontrollierte Clusterfreisetzung führt zur Bildung von kleinen, präzisen Pt-Nanopartikeln (1,14±0,35 nm) auf der Glaskohlenstoffelektrode. Die beobachteten ORR-Massenaktivitäten (0,87±0,14 A/mgPt) stimmen mit der theoretischen Vorhersage (0,99 A/mgPt) überein und weisen die höchste bisher gemessene Massenaktivität von reinen Pt-Katalysatoren in der ORR in einem vergleichbaren Größenbereich auf. Die spezifische Aktivität und Massenaktivität sind doppelt so hoch wie die des kommerziellen Pt/C-Katalysators nach *Tanaka*.

Diese vielversprechenden Ergebnisse führten zu einer Erweiterung des allgemeinen, MOF-basierten Konzepts (Verkapselung, Ligandenentfernung, MOF-Aufschluss) mit dem Ziel, weitere Nanopartikel mit ähnlicher Präzision zugänglich zu machen und potentiell hochaktive Katalysatoren zu identifizieren. Die Kombination von größeren Pt-Carbonylclustern mit ZIF-8 oder anderen ZIFs bedarf aber wegen der bisher noch unvollständigen Verkapselung und niedrigen Clusterbeladungen weiterer Optimierung der experimentellen Parameter. Erste Ergebnisse hinsichtlich einer verbesserten Stabilisierung konnten allerdings mit $[Pt_9(CO)_{18}](NBu_4)_2$@ZIF-90 erzielt werden.

Die Übertragung auf andere Metallcluster gelang anhand des phosphinstabilisierten Goldclusters $[Au_8(TPPMS)_8](NO_3)_2$ (TPPMS = Triphenylphosphan-3-sulfonsäure). Dieser wurde erfolgreich in ZIF-8 verkapselt und die Beladung im Bereich von 1-8 Gew.-% variiert. Die Phosphanliganden in $[Au_8(TPPMS)_8](NO_3)_2$@ZIF-8 konnten durch thermische Behandlung unter Sauerstoffatmosphäre oxidativ abgespalten werden und Temperstudien zeigten keine Clusteragglomeration bis 250 °C.

ABSTRACT

To tackle the synthesis of ligand-free (naked), atom-precise metal nanoclusters, a metal-organic framework (MOF) template method was developed in this work. The proof-of-principle system is based on encapsulating the CO-ligated, molecular *Chini* cluster $[Pt_9(CO)_{18}](NBu_4)_2$ in the zeolitic imidazolate framework ZIF-8. Thermally induced decarbonylation at 200 °C yields the surprisingly stable composite material Pt_n@ZIF-8 with a cluster atomicity n close to 12, irrespective of the experimentally implemented Pt loading ranging from 1-20 wt%. The composite material was successfully applied in catalytic alkene hydrogenations and as a catalyst precursor for the electrocatalytic oxygen reduction reaction (ORR). In the acidic electrolyte $HClO_4$ the ZIF-8 matrix slowly dissolves and controlled cluster release yields defined aggregation to small Pt nanoparticles (1.14±0.35 nm) on the glassy carbon electrode. The observed ORR mass activities (0.87±0.14 A/mg_{Pt}) are close to the theoretical prediction (0.99 A/mg_{Pt}) and constitute the so far highest mass activity among pure Pt catalysts for the ORR within a similar size range. The specific and mass activities are twice as high as for the *Tanaka* commercial Pt/C catalysis.

These promising results led to an expansion of the general concept (encapsulation, ligand removal, MOF digestion) with the goal of accessing further nanoparticle sizes with similar precision that could potentially harbor high catalytic activities. The combination of larger Pt carbonyl clusters with ZIF-8 or other ZIFs involved incomplete encapsulation and unsatisfying cluster loadings and demands further optimization of the experimental parameters, although first promising results in terms of enhanced stabilization could be obtained with $[Pt_9(CO)_{18}](NBu_4)_2$@ZIF-90.

The transfer to other metal clusters succeeded with the phosphine-stabilized gold cluster $[Au_8(TPPMS)_8](NO_3)_2$ (TPPMS = triphenyl-phosphine-3-sulfonic acid) that could be successfully encapsulated in ZIF-8 with a Au loading of 1-8 wt%. The phosphine ligands in the $[Au_8(TPPMS)_8](NO_3)_2$@ZIF-8 material were detached by an oxidative ligand stripping procedure and tempering studies revealed no cluster agglomeration up to 250 °C.

LIST OF ABBREVIATIONS

BDC	1,4-benzenedicarboxylic acid
BET	Brunauer-Emmett-Teller
bIm	benzimidazole
CN	coordination number (with $\overline{CN}$ as the general coordination number)
COD	cyclooctadiene
Cp	cyclopentadienyl
Cp*	1,2,3,4,5-pentamethylcyclopentadienyl
CUS	coordinatively unsaturated site
CVD	chemical vapor deposition
dcIm	4,5-dichloroimidazole
DFT	density functional theory
dppp	1,3-bis(diphenylphosphino)propane
EDX	energy-dispersive X-ray spectroscopy
ESI-MS	electrospray ionization with mass spectrometry
EXAFS	extended X-ray absorption fine structure
FT	*Fourier*-transform
HAADF-STEM	high-angle annular dark-field scanning transmission electron microscopy
HER	hydrogen evolution reaction
HKUST	Hong Kong University of Science and Technology
HOMO	highest occupied molecular orbital
HPLC	high performance liquid chromatography
HR-TEM	high-resolution transmission electron microscopy
Im	imidazole
ImCOH	2-imidazolecarboxaldehyde
IR	infrared
L	ligand
LEIST	ligand exchange-induced size/structure transformation
LUMO	lowest unoccupied molecular orbital
M	metal atom
MAS-NMR	magic-angle spinning nuclear magnetic resonance

2-mIm	2-methyl imidazole
MOF	metal-organic framework
m/z	mass-to-charge ratio
NC	nanocluster
nIm	2-nitroimidazole
NMR	nuclear magnetic resonance
NP	nanoparticle
ORR	oxygen reduction reaction
PAGE	polyacrylamide gel electrophoresis
PEMFC	proton-exchange membrane fuel cell
ppm	parts per million
PVP	polyvinylpyrrolidone
PXRD	powder X-ray diffraction
RDE	rotating disk electrode
SBU	secondary building unit
TGA-MS	thermogravimetric analysis with mass spectrometry
THF	tetrahydrofurane
TPPMS	triphenylphosphine-3-sulfonic acid sodium salt
TOF	turnover frequency
TON	turnover number
UiO	Universitetet i Oslo
XANES	X-ray absorption near edge structure
XPS	X-ray photoelectron spectroscopy
ZIF	zeolitic imidazolate framework

1 MOTIVATION

It has been general knowledge that a metal atom carries distinctly different properties than the respective bulk metal. Still, only in the last few decades the question could be answered what happens in between, when bulk metal is cut down to smaller and smaller pieces, approaching the atomic state. A partial explanation was provided with the discovery of nanoparticles (NPs), where in the range of a few hundred atoms highly interesting properties emerge that differ from those of the bulk state.[1–3] When going even smaller from nanoparticles, reaching a range below 50 atoms, we enter the regime of sub-nanometer metal clusters. They, in turn, bridge the gap between nanoparticles and atoms and can be viewed as “superatoms”.[4] Their properties are highly dependent on their atomicity to the extent that one atom in difference can change the cluster characteristics profoundly. Some fascinating cluster features, including electronic properties and catalytic activity, could be studied on nanogram scales or by theoretical methods.[5] Recently, the question arose how the unique properties of clusters can be exploited experimentally, especially in the field of catalysis where such clusters would be extremely atom-efficient due to their high ratio of potentially active surface atoms. To meet this challenge, cluster synthesis has to be scalable to feasible amounts without losing control over the exact size and structure of the metal species as “every atom counts” on the subnanometer regime. Synthetic problems lie in the tendency to agglomerate due to high surface energies and thus in the control of narrow size distributions. Therefore, either stabilization by ligands in solution or deposition on supports is necessary. In the latter case, especially porous materials are suitable hosts for metal species and can prevent deactivation and side reactions.

Metal-organic frameworks (MOFs) have been considered as promising porous materials not only for gas separation or gas storage, but also for incorporating and stabilizing metal species. The high porosity and tunability of the frameworks assembled from metal-containing nodes and organic linkers has been exploited in a plethora of studies to form nanoparticles from monometallic precursors and subsequently use the hybrid metal@MOF materials for catalysis.[6,7] The framework pores have been reported to give a certain degree of control over particle sizes, but reports with actual atomically precise metal clusters are scarce, although materials with rather defined and ultrasmall metal species could be obtained in some rare cases.[8,9] Most studies either produce large nanoparticle size distributions in the MOF or encapsulate ligand-stabilized nanoparticles with difficulties in removing these stabilizing species that block the access of substrates to catalyst surface sites. Examples for ligand-free, atomically precise clusters stabilized in MOFs can be counted on the fingers of one hand, with most notable work by *Emilio Pardo* with outstanding catalytic activities for linear Pd_4 and Pt_2 clusters dispersed in highly sophisticated and specifically designed MOFs.[10,11]

Designated objective of this thesis was the exploration of a more generally applicable and scalable pathway towards atomically precise and ligand-free clusters. The idea for this concept emerged from the combination of our group's two fields of expertise, namely ligand-stabilized organometallic clusters on the one hand, and MOFs on the other. We first planned on the solution synthesis of literature-known, ligand-stabilized clusters with a defined number of metal atoms in their core. Subsequently, a MOF should be assembled around these clusters, with the MOF's pores being large enough to host the cluster but with small pore openings that prevent its mobility and restrict agglomeration. If the cluster is unable to move out of the pore due to the small diameter of the pore window, the stabilizing ligands can be removed *via* chemical, thermal or photolytic cleavage without agglomeration or leaching of the resulting naked metal clusters. Thus, with the retained size of the initial cluster core, atomically precise clusters in the MOF pores should be obtained (Scheme 1).[12]

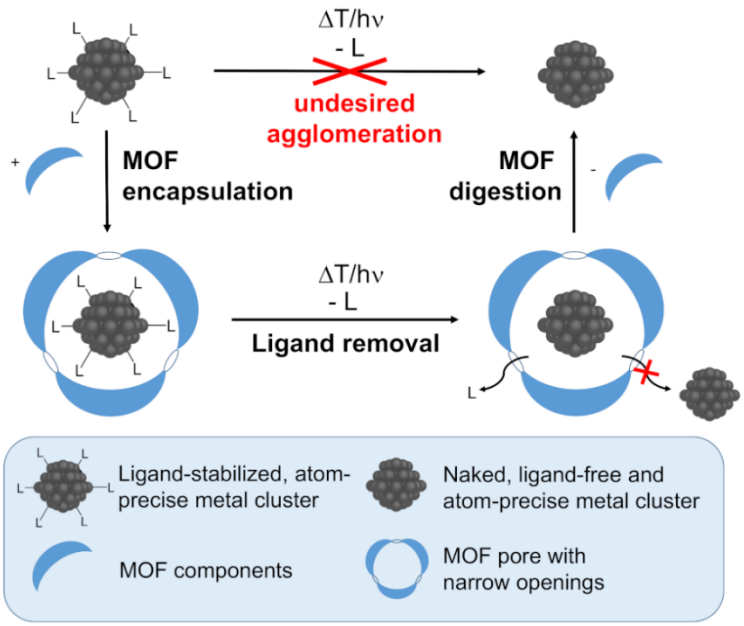

Scheme 1: General concept for the synthesis of ligand-free, atom-precise metal clusters and ultrasmall metal NPs, based on the encapsulation of ligated metal clusters into size-matching pores of MOFs chosen as removable protective matrix. Reprinted with permission from K. Kratzl, T. Kratky, S. Günther, O. Tomanec, R. Zbořil, J. Michalička, J. M. Macak, M. Cokoja, R. A. Fischer, J. Am. Chem. Soc. 2019, 141, 13962. Copyright 2019 American Chemical Society.[12]

As an ideal MOF for this study, the family of zeolitic imidazolate frameworks (ZIFs) was identified due to their ready crystallization under mild conditions, their cage-type pores with narrow pore windows and their high thermal stability.[13] As model cluster systems we chose so-called *Chini* clusters, platinum carbonyl clusters of the general formula $[Pt_3(CO)_6]_n^{2-}$ (n = 2-8).[14] Their encapsulation had already been demonstrated for zeolites, where mixtures of clusters were formed inside of the porous network and the carbonyl ligands could be easily removed at moderately elevated temperatures.[15] After successful synthesis and characterization of these Pt_n@MOF materials, they were to be evaluated in catalytic

processes, starting with proof-of-principle reactions like simple hydrogenations. Because ZIF-8 can be easily digested under acidic conditions, the controlled release of the Pt clusters onto a stabilizing support to form precise NPs should be explored, with a use for electrocatalytic reactions such as the oxygen reduction, related to applications in fuel cell systems. In a further step, the implemented method could be transferred to other cluster/MOF combinations upon variation of the cluster size, the MOF composition or the cluster metal.

2 INTRODUCTION

2.1 Metal Nanoclusters – Size Matters

With bulk metals as well as metal atoms well understood, at the beginning of the 20th century scientists first theorized about a class of materials “in between”, that bridge the gap between known small metal particles and single metal atom species.[16] Today, we know the intermediate species between molecules and bulk metal are nanoparticles (NPs) and nanoclusters (NCs), the latter being initially defined by *Cotton* in 1966 as “*a finite group of metal atoms which are held together entirely, mainly, or at least to a significant extent, by bonds directly between the metal atoms”*.[17] Nanoparticles are mainly understood as species between 1 and 100 nm with a more or less broad size distribution, while most clusters exhibit a diameter below 2 nm and are atom-precise.[18] To differentiate between nanoparticles and nanoclusters, their optical properties are crucial, with nanoparticles exhibiting surface plasmon resonance, while nanoclusters show a discrete electronic structure and molecule-like properties.[19] Extended interest in nanomaterials first arose in the 1980s, when researchers were looking for the onset of bulk metal phenomena like electrical conductivity, interaction with light and magnetic properties. It was found that upon decrease of the particle diameter, metallic properties fade to highly size-dependent and unique features (Figure 1).[20]

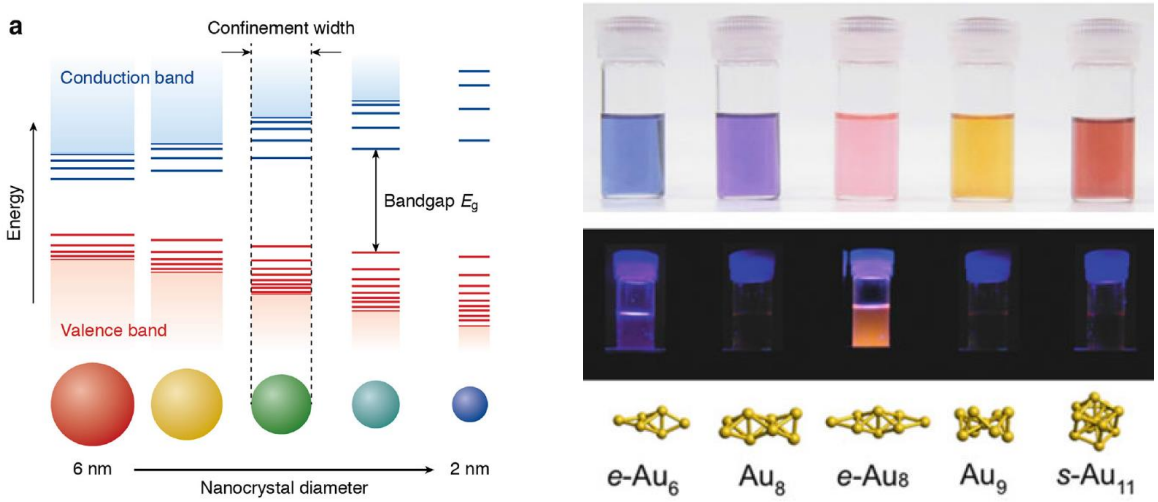

Figure 1: *Left:* Quantum confinement effect illustrated for semiconductor nanocrystals. With decreasing size, the HOMO-LUMO bandgap increases and discrete energy levels emerge from the valence and conduction bands.[21] *Right:* For nanoclusters below 50 atoms, properties like electronic transitions and resulting colors as well as photoluminescence are unique to every cluster core structure. This is exemplarily demonstrated for the colors and fluorescent properties of solubilized, phosphine-stabilized gold clusters. Reprinted by permission from Springer Nature Customer Service Centre GmbH: Springer Nature, Structure and Bonding, Phosphine-Coordinated Pure-Gold Clusters: Diverse Geometrical Structures and Unique Optical Properties/Responses, K. Konishi, Copyright 2014.[22]

For clusters, these properties can be attributed to several unique features that are in part still not completely understood. Next to their high surface-to-bulk ratios, quantum confinement effects can play a role, where discrete energy levels emerge from the conduction band due to the confined movement of electrons in nanoscale materials (Figure 1, left).[21] The jellium model simplifies the theoretical observation of metal clusters by replacing the charge distribution of the ionic metal cores by a constant, positive background charge. A delocalized cloud of valence electrons stemming from individual atoms then interacts with the spherical *Coulomb* potential of this uniform background. Based on the jellium model, one-electron energy eigenvalues of the cluster's molecular "superatomic" orbitals can be calculated, resulting in a new set of orbitals that is defined by the entire metal atom group ($1S^2$, $1P^6$, $1D^{10}$, $2S^2$, $1F^{14}$, $2P^6$… in contrast to $1s^2$, $2s^2$, $2p^6$, $3s^2$, $3p^6$, $4s^2$, $3d^{10}$… for individual atoms). Following this superatom concept, enhanced stability is predicted for clusters with a number of valence electrons that corresponds to fully filled energy levels, i.e. superatomic noble gases (n_e = 2, 8, 18, 20, 34, 40, 58, …) (Figure 2). [4,23] Indeed, many reported clusters fulfill this condition, exemplarily the gold clusters $[Au_{11}(PR_3)_8]Cl_3$ with $n_e = 8$ and $[Au_{102}(SR)_{44}]$ with $n_e = 58$. With this superatomic approach of electron counting, the chemical behavior of clusters has successfully been predicted especially for naked gas-phase clusters, based on their desire to enter electronic closed shell configurations. Such "shell closing" is also observed for cluster geometries where the respective species are denoted as "magic number" clusters, although the term "magic number" is in part also used in connection with electronically closed shells. Here, a central atom is surrounded by twelve metal atoms in the first coordination sphere, typically yielding a polyhedron with icosahedral symmetry (I_h).[23,24] The number of atoms in the n^{th} shell is described by the formula $10n^2+2$ and the resulting cluster core atomicities of m = 13, 55, 147, 309… (with n = 1, 2, 3,…) depict the *Mackay* numbers for clusters with high stability (Figure 2).[25]

A prime experimentally confirmed example for the superior stability of "magic number" clusters is Al_{13}^-, that was observed in greater abundance than other cluster sizes in gas phase experiments under oxygen etching conditions. Interestingly, Al_{13}^- exhibits not only geometric, but also electronic shell closing, which further justifies its superior stability. With three valence electrons each and one overall negative charge, the total electron number amounts to 40, which represents electronic shell closing according to the superatom concept. Thus, Al_{13}^- is more stable against oxidation than other open-shell clusters.[26]

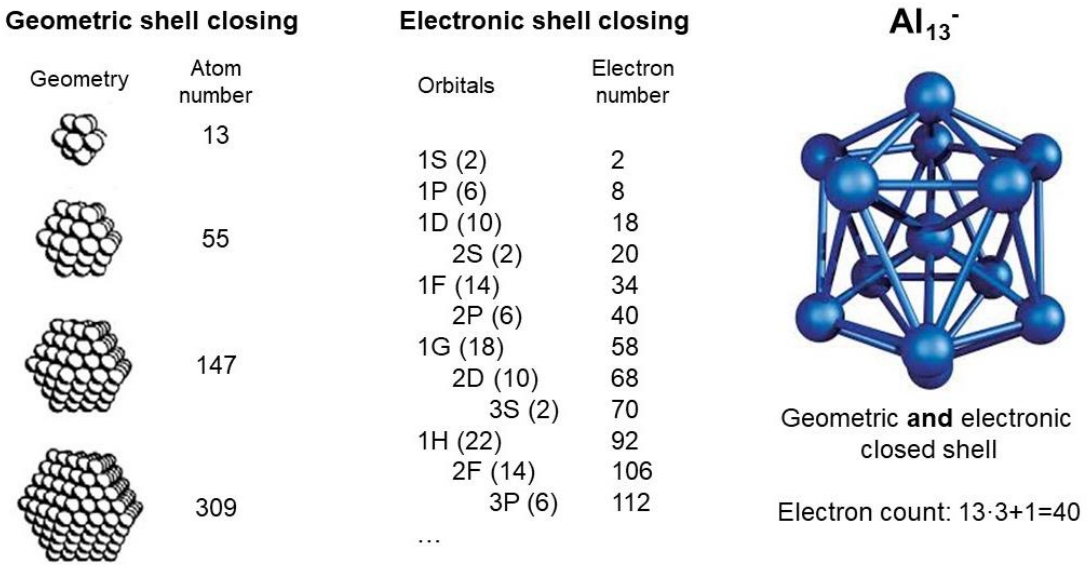

Figure 2: Shell closing phenomena in naked metal clusters. *Left:* Enhanced stability is observed for "magic number" clusters with highly symmetric geometries that occur for clusters with n = 13, 55, 147, 309 and so on.[27] *Middle:* The listed electron numbers correspond to filled molecular orbitals and the clusters fulfilling this condition often exhibit pronounced stability. *Right:* With a perfect icosahedral geometry and 40 valence electrons, Al_{13}^- is an example for both geometric and electronic shell closing.[26]

Most relevant catalysts comprise metals as the active species and under an economic viewpoint, the cost reduction of industrially applied catalysts is crucial. Because rare and therefore expensive precious metals like platinum, palladium or rhodium are indispensable for certain processes, generating catalysts with higher activity or smaller size is of great importance for the efficient usage of limited resources. Reducing metal particle size to less than 50 atoms and generating clusters effectively addresses this problem and at the same time opens new ways to increase the catalytic activity.[28,29] Due to unique surface geometries and defects arising from the high ratio of surface atoms, a cluster's performance as a catalyst is highly size-dependent and the addition or removal of only one atom can drastically increase a reaction's turnover. With the ability to synthesize atomically precise, naked metal clusters comes the chance to exploit highly active structural features that are not present in the bulk and tune their reactivity on an atomic scale.[5] An additional benefit lies in the simplification of a catalytic system when instead of a metal surface with a diversity of steps, edges and kinks, well-defined cluster species are studied. With clusters comprising only few atoms and stabilized on a support, adsorption and activation of substrates becomes easier to study, especially on a density functional theory (DFT) level.[30] Meanwhile, *Tao et al.* proved that the thus gained insights are absolutely relevant to understand processes on extended metal lattices: They found that upon CO adsorption on a stepped Pt surface, the stress of CO repulsion upon high coverage is relieved by breaking up into nanoclusters. Interestingly, the process is completely reversible upon CO desorption.[31]

First studies utilized mass spectrometric techniques to study few-atom clusters in the gas phase,[32,33] while later investigations paved the way towards the understanding of

heterogeneous catalysts by depositing the generated cluster species on supports.[34] Beside the enhanced stability, the deposition also allows for a better understanding of support effects beneficially influencing some catalytic processes.[35] A great variety of cluster and support combinations has been used for small molecule activation, e.g. oxygen or hydrogen activation,[32,36] oxidations,[37] as well as C-H or C-C bond cleavage.[38] With the prerequisite of atomic precision, cluster generation on supports is difficult and often limited to extremely small scales.[5] A more scalable alternative is the bottom-up generation of ligand-stabilized clusters in solution, in combination with techniques for ligand removal.[15,39]

Synthetic methods to access naked clusters with atomic precision can be divided into top-down and bottom-up approaches. While the former relies on breaking down bulk metals or metal particles, in the latter clusters are generated from mononuclear metal species.[40] Top-down syntheses use sputtering or vaporization techniques and the emerging distribution of cluster ions is subsequently mass-selected by quadrupole or time of flight analysers. Laser ablation as an exemplary vaporization method relies on focussing a high-energy laser beam on a metal plate, with ensuing size selection of one specific cluster size by a quadrupole mass spectrometer and soft-landing on the respective substrate (Figure 3).[5,41] Although almost any cluster size of a broad scope of metals is accessible by this approach, the disadvantages lie in the sophisticated and expensive setups, in low cluster amounts and the difficulty to generate sufficient metal loadings for feasible catalysis.

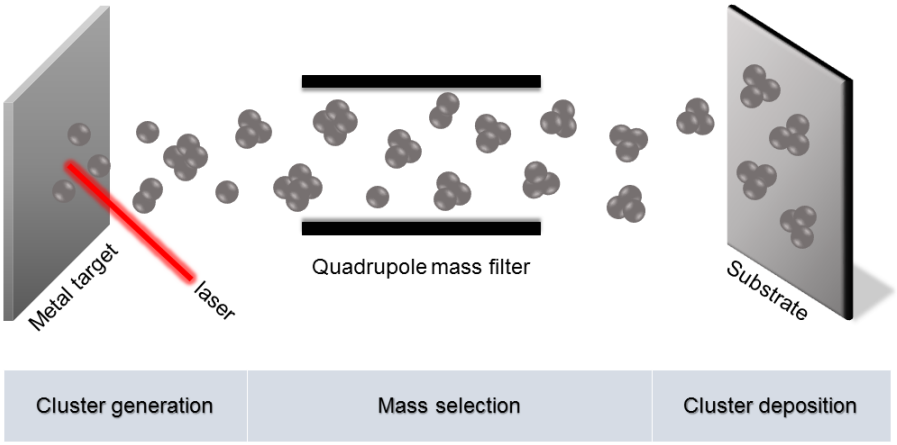

Figure 3: Simplified representation of the laser ablation technique for generation of atom-precise clusters. A mix of various cluster sizes is generated by laser sputtering, and subsequent size selection from the cluster beam in a quadrupole field yields the desired cluster size. After deceleration, the clusters are deposited on a stabilizing substrate and analyzed.

Most common bottom-up approaches rely on simple metal complexes in solution that are converted more or less selectively to clusters of higher atomicity by reduction.[29] Due to their high surface energy that comes with the large portion of exposed surface atoms, naked clusters are extremely prone to agglomeration and unstable in solution. Therefore,

coordinating ligand shells are necessary to prevent coalescence processes and retain the small cluster dimensions. Well-established ligands are polymers like polyvinylpyrrolidone (PVP),[42] that is mostly used for larger NPs, thiols that are popular in gold chemistry,[43][43] as well as discrete ligands such as phosphines,[22] carbonyls[44] or hydrocarbon ligands like Cp or Cp*.[45] With this approach, atom-precise clusters are easily accessible by wet-chemical methods and interactions between metal core and ligands enable characterization methods that are not applicable for supported clusters. Thus, especially nuclear magnetic resonance (NMR) spectroscopy and single crystal XRD measurements allow for precise identification of cluster species. The drawbacks of the reduction of metal salt-like precusors consist in the partly unselective reactions and the limited accessibility of clusters since not for every cluster core size a selective procedure is known, and syntheses as well as application in catalysis without decomposition are not trivial.[46]

A very elegant and selective method based on precursor reduction was developed by the group of *Imaoka* who used dendrimers to access a series of naked platinum clusters (Scheme 2).[47-49] By introducing a defined number of pyridine or imine coordination sites in the dendrimer, a precisely defined stoichiometry of Pt precursors could be introduced into each dendrimer cage. Upon reduction, a naked cluster with precise atomicity was formed, sterically protected against agglomeration by the surrounding dendrimer and analysable by mass spectrometry. Unfortunately, in addition to the rather intricate dendrimer syntheses, these clusters were only stable on a limited timescale because the protection in the dendrimer proved to be insufficient.

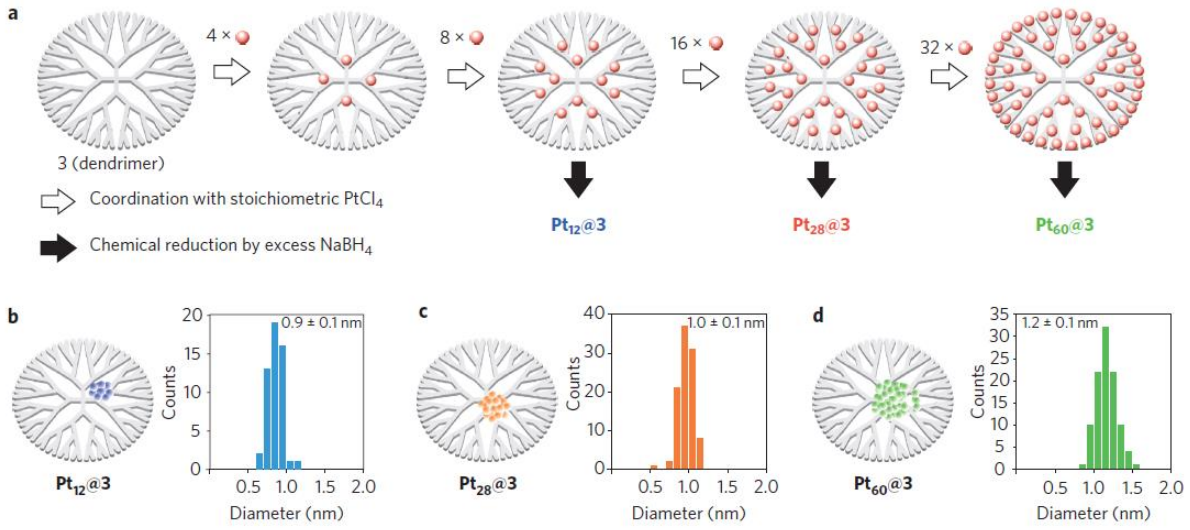

Scheme 2: Dendrimer-based approach towards atom-precise Pt clusters developed by *Imaoka et al*. A dendrimer with a defined number of coordination sites is loaded with a Pt precursor and upon reduction, naked and atom-precise clusters are obtained that are stabilized in the dendrimer shell. Reprinted by permission from Springer Nature Customer Service Centre GmbH: Springer Nature, Nature Communications, Size-specific catalytic activity of platinum clusters enhances oxygen reduction reactions, K. Yamamoto, T. Imaoka, W.-J. Chun, O. Enoki, H. Katoh, M. Takenaga, A. Sonoi, Copyright 2009.[49]

2.1.1 Platinum Clusters

The vast catalytic potential of platinum has led to significant improvements in our everyday lives, whether in catalytic converters for efficient exhaust gas purification,[50] as catalyst for fuel cells,[51] or in the industrial synthesis of nitric acid that is essential for fertilizer production.[52] To render existing Pt catalysts even more efficient, a detailed understanding of surface reaction mechanisms is of crucial importance. Therefore, Pt clusters are generating interest, not only as model systems,[33] but as new and maybe even more active catalytic species themselves.

Chini Clusters $[Pt_3(CO)_6]_n^{2-}$ (*n* = 2-8)

In 1966, one of the lab students of *Prof. Paolo Chini*, *Giuliano Longoni*, was on the hunt for platinum phosphine carbonyl clusters. In the course, he reduced $Pt(CO)_2Cl_2$ with lithium in tetrahydrofurane (THF) and observed intensely coloured solutions ranging from green to red.[53] Although the columnar structure of the now so-called *Chini* clusters was already proposed then, their elucidation proved difficult with the analytical techniques available. Years later, the series of platinum carbonyl clusters with the general formula $[Pt_3(CO)_6]_n^{2-}$ (*n* = 2-8) was reported,[14,54] back then still with some gaps that could be filled by contributions of *Chini's* successors *Zammit*, *Ceriotti* and *Zacchini,* amongst others (Figure 4).[55,56–58]

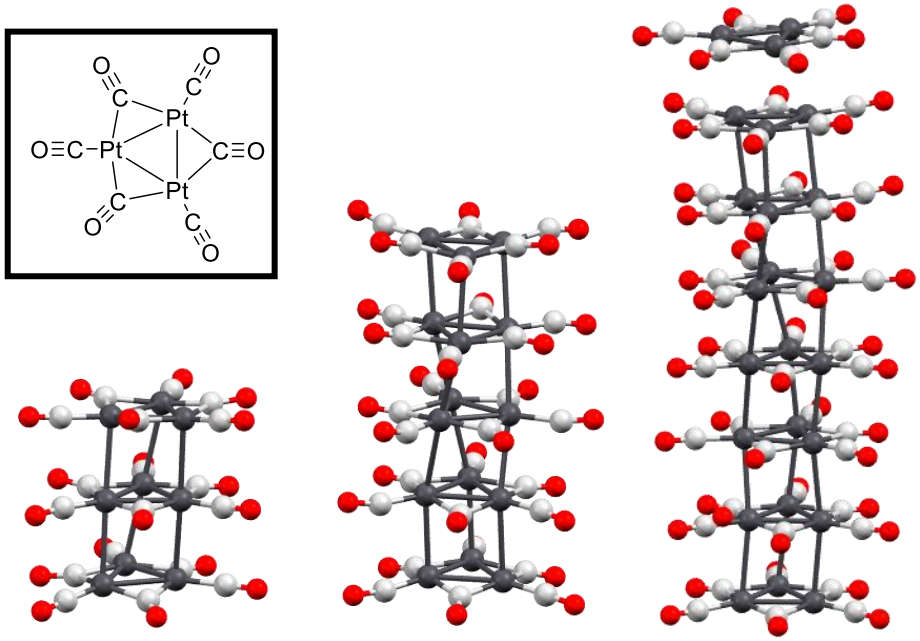

Figure 4: Crystal structures of *Chini* clusters $[Pt_3(CO)_6]_n^{2-}$ for n = 3, 5 and 8.[54] In the top left corner, the structure of the planar sub-unit $Pt_3(CO)_6$ is depicted. In the crystal structure of $[Pt_{24}(CO)_{48}]^{2-}$ (*right*), seven subunits crystallize with one $Pt_3(CO)_6$ in between, forming rod-like structures in the solid state. This indicates the ability of *Chini* clusters to exchange whole $Pt_3(CO)_6$ subunits upon oxidation or reduction.[56]

The clusters consist of triangular platinum units with Pt-Pt distances of 2.66 Å that contain three bridging and three terminally coordinated carbonyl ligands. Several Pt triangles then form stacks with interlayer distances of ca. 3 Å, resulting in helicoidally distorted trigonal prisms. The twist of around 13° for two adjacent triangular layers stems from a balance between the steric repulsion of the carbonyl ligands and the electronically favoured regular prismatic structure. The tendency to form stacks and the limit of n = 10 for discrete molecular compounds is not finally resolved. A possible explanation is based on Extended *Hückel* Molecular Calculations (EHMO) that state an in-phase combination of the Pt p_z orbitals as the metal contribution for the clusters' highest occupied molecular orbital (HOMO).[59] This orbital is populated by only one electron pair that is solely responsible for the intertriangular Pt-Pt interactions and becomes increasingly insufficient to keep the Pt layers together with increasing n. Consequently, above n > 10, higher nuclearity clusters assemble into Pt wires. Analogous structures are observed in the solid state for clusters with n ≥ 5. The valence electrons of the *Chini* clusters are formally determined as 44 e^- for one triangle (carrying the twofold negative charge, 30 e^- from the three Pt atoms and 12 e^- from the six CO ligands), in addition to 42 e^- for every further triangular $Pt_3(CO)_6$ unit. The cluster valence electrons therefore follow *Wade*'s rule for triangulated polyhedral clusters (42n+2).[14] It has been found that the $Pt_3(CO)_6$ units rotate on the ^{195}Pt NMR time scale, likely due to the detaching and reattaching of triangular Pt units surrounded by a solvent cage.[60] This process is confirmed by crystal structures, where single Pt triangles are "frozen" between wired clusters, giving a hint towards the growth mechanisms in solution. Thus, under oxidizing conditions, $[Pt_9(CO)_{18}]^{2-}$ quickly transforms to the next bigger cluster $[Pt_{12}(CO)_{24}]^{2-}$ and subsequently $[Pt_{15}(CO)_{30}]^{2-}$, continuing until polymeric structures emerge (Figure 4).

Generally, the chemical behaviour of the *Chini* clusters depends strongly on their nuclearity. With lower n, the sensitivity towards oxidizing and electrophilic substrates increases as well as their reactivity towards acids. Hence, while exhibiting a relatively high stability towards water, the smaller the Pt clusters, the easier they are oxidized under atmospheric conditions:

$$(n+1)[Pt_3(CO)_6]_n{}^{2-} + \frac{1}{2}O_2 + H_2O \;\rightarrow\; n[Pt_3(CO)_6]_{n+1}{}^{2-} + 2OH^-$$

Under elevated temperatures, the *Chini* clusters have been shown to lose carbonyl ligands at 70 °C and to completely decompose to metallic Pt between 150 °C and 200 °C. Nonetheless, the clusters show sufficient stability for some catalytic conversions e.g. in hydroformylations. Under a pressure of 100 bar H_2 and CO at 120 °C, 1-pentene could be converted by $[Pt_{12}(CO)_{24}]^{2-}$ into a mixture of the corresponding aldehyde and *iso*aldehyde, although the catalyst could not be retrieved purely but only as a mixture of different cluster sizes.[14]

The easy cluster interconversions also constitute the major challenge in their synthesis. Due to their almost identical solubility, the separation of clusters with consecutive *n* by fractioned crystallization is next to impossible. To avoid cluster mixtures, reaction conditions must be carefully tuned, and a variety of possible synthetic strategies has been investigated over the years. Due to the hardly accessible starting material $Pt(CO)_2Cl_2$ of the original synthesis, the group of *Chini* soon switched to $Na_2PtCl_6 \cdot H_2O$. By addition of specific amounts of bases like sodium acetate or hydroxide, the basicity of the solution during reductive carbonylation could be adjusted to selectively yield only one *Chini* cluster.[14] A disadvantage of this synthetic pathway consists in the excess of toxic carbon monoxide that is bubbled through the reaction solutions over extended periods of time. Other methods take advantage of the defined basicity of supports like magnesia[61] or silica[62] to achieve selective cluster formations. The latter uses different Pt precursors, loadings and bases that are first adsorbed on fumed silica to be then exposed to a defined and low amount of CO. As in solution, an increase in basicity leads to a decrease in cluster size.[62]

Thanks to their intense colours in solution, *Chini* clusters can be easily identified in UV/Vis spectra where impurities of smaller or larger clusters occur as shoulders in the respective most intense bands. DFT calculations attribute the coloration mainly to metal-to-ligand-charge-transfer ($dz^{2*} \rightarrow \pi^*$) and ligand-to-ligand-charge-transfer ($\pi \rightarrow \pi^*$) processes.[63] In addition, CO band positions in IR spectra make the clusters clearly distinguishable due to the correlation between ν_{CO} and the ratio of Pt atoms and cluster charge.[54] With the twofold negative charge of all *Chini* clusters, a decrease in negative charge per Pt atom with higher *n* leads to less electron density per atom in the cluster. The resulting decrease in backbonding renders Pt-CO bonds stronger, therefore shifting both ν_{CO} for terminal and bridging CO ligands to higher wavelengths.

Higher Nuclearity Platinum Carbonyl Clusters

Platinum carbonyl clusters start to deviate from the classical *Chini* formula $[Pt_3(CO)_6]_n^{2-}$ when the ratio of CO ligands to Pt surface atoms is decreased below 2. Instead of triangular Pt units, spherical clusters start to form whose core structures often resemble chunks of the *fcc* lattice of the bulk metal (Figure 5, left).[53] With even less carbonyl ligands, the metal cores rather represent interpenetrated pentagonal prismatic and antiprismatic structures as e.g. in $[Pt_{19}(CO)_{22}]^{4-}$.[58] This rearrangement can be justified by the decrease of electron density that is made available by the carbonyl ligand shell. The CO ligands stabilize the clusters by terminal, edge-bridging or face-bridging coordination as is nicely seen in one of the few neutral Pt carbonyl species $[Pt_{31}(CO)_{36}]$.[53] Its carbonyl groups are evenly distributed as twelve terminal, twelve edge- and twelve face-bridging ligands. It is noteworthy that even with 31 Pt

atoms, only one atom is interstitial, while the rest lies on the surface of the cluster, resulting in a ratio of surface atoms of 97%. Synthetically, larger Pt carbonyl clusters are accessible by heating smaller clusters upon loss of CO ligands and cluster rearrangement. The so far largest, molecular Pt carbonyl cluster is $[Pt_{40}(CO)_{40}]^{6-}$ with an – among known Pt clusters and NPs unique – *bcc* core structure, 24 terminal and 16 edge-bridging CO ligands.[64] Such higher nuclearity Pt carbonyl clusters are stable in various oxidation states and have been extensively investigated by cyclovoltammetry. The very regularly structured $[Pt_{40}(CO)_{40}]^{n}$ can even tolerate electronic deviations $n = -4$ to $n = -11$ which is an attractive property for nanocapacitors.

Next to purely carbonyl surrounded Pt clusters, several phosphine substituted derivatives are known, but still way less stable compounds were found than for palladium (Figure 5, right).[65] Additionally, a vast variety of bimetallic Pt carbonyl species have been synthesized, that go beyond the scope of this work.[53]

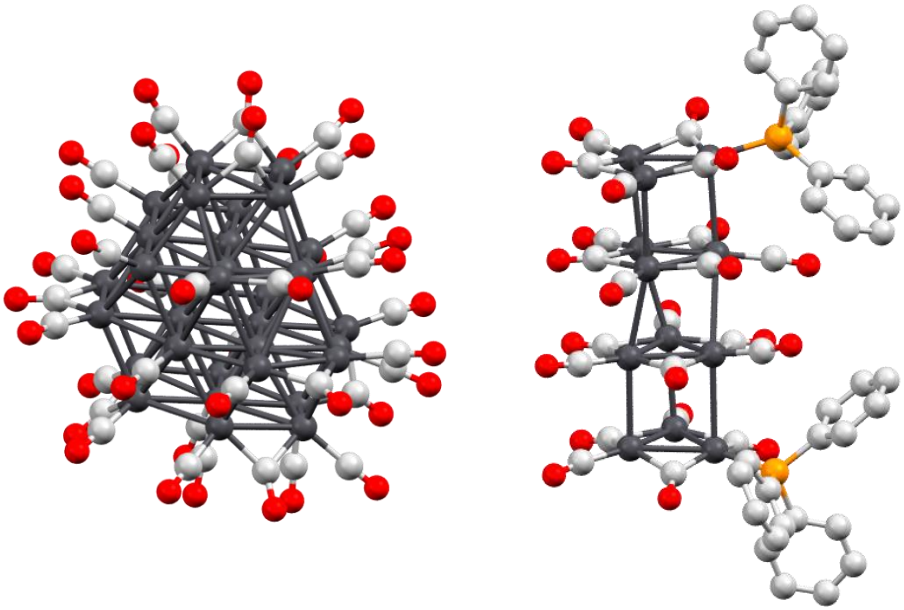

Figure 5: Exemplary crystal structures for a large platinum carbonyl cluster, namely $[Pt_{38}(CO)_{44}]^{2-}$,[44] and for a phosphine stabilized cluster, $[Pt_{12}(CO)_{22}(PPh_3)_2]^{2-}$.[65]

Naked Platinum Clusters for Electrocatalysis

Naked Pt clusters have become a topic of great interest for catalytic studies in the last decades and a vast scope of works exists that deal with their exploitation for certain reactions as well as their size-dependent activity.[51] They have a more accessible surface for substrates to be catalytically converted on, but are at the same time hard to synthesize because of their high surface energy that renders them prone to agglomeration. Platinum has also been identified as the most feasible catalytic material for proton exchange membrane fuel cells (PEMFCs), a technology that is handled as one of the most promising solutions for future mobility.[66] Although first fuel cell electric cars are on the market, a key factor limiting their widespread implementation is the expensive Pt electrocatalyst.[67] While the catalytic converter of a typical

diesel passenger vehicle uses 3–7 g of Pt, a comparable fuel-cell vehicle needs 30–60 g of the expensive precious metal.[68] Therefore, reducing Pt loadings and increasing the activity per mass is a highly sought field of research. First studies indeed indicate that Pt clusters significantly increase the activity per mass in comparison to Pt NPs.[69] In PEMFCs, two reactions take place, namely the hydrogen oxidation/evolution reaction (HER) on the anode, and the oxygen reduction reaction (ORR) on the cathode, while the electrons produced in the former take a detour through an external circuit generating electricity (Figure 6).

$$H_2 \rightarrow 2H^+ + 2e^-$$

$$\frac{1}{2}O_2 + 2H^+ + 2e^- \rightarrow H_2O$$

In commercial PEMFCs, both electrodes consist of carbon coated with finely dispersed Pt NPs where the loadings differ significantly on the anode and the cathode side (<0.05 mg_{Pt}/cm^2 vs. 0.4 mg_{Pt}/cm^2).[51] While the HER proceeds quite readily, the sluggish reaction kinetics (five orders of magnitude slower!) of the ORR require high platinum loadings.[70] This problem has been tackled on the one hand with the development of non-precious metal catalysts, on the other hand, the active mass of Pt catalyst species are boosted by alloying or applying core-shell structures.[71,72]

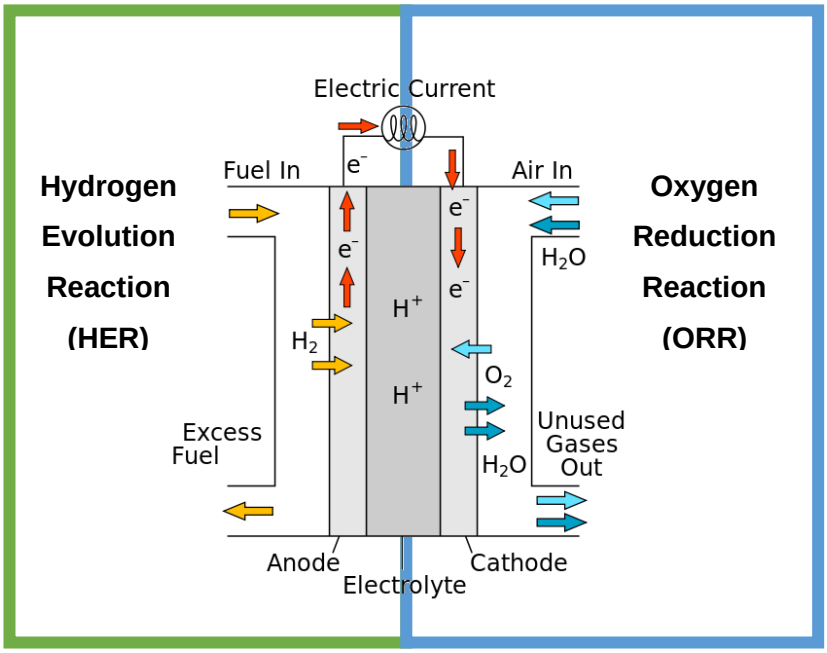

Figure 6: Proton exchange membrane fuel cell with the hydrogen evolution reaction (HER) at the anode (*left*) and the oxygen reduction reaction (ORR) at the cathode (*right*) of the cell. In the former, H_2 is oxidized to protons and electrons, in the latter they react with oxygen to form water. Electricity is generated by conducting the electrons through an external circuit.

Mechanism of the Oxygen Reduction Reaction

Two mechanisms are proposed for electrocatalytic reductions, with the more common mechanism for the ORR being a four-electron process:

$$O_2 + 4H^+ + 4e^- \rightarrow 2H_2O$$

The alternative two-electron process involves hydrogen peroxide and is generally not favoured in the case of the ORR:

$$O_2 + 2H^+ + 2e^- \rightarrow 2H_2O_2$$

$$H_2O_2 + 2H^+ + 2e^- \rightarrow 2H_2O$$

The simplest mechanism to explain the intermediate steps of the oxygen reduction reaction at the cathode is the dissociative mechanism. In this case, oxygen dissociates before adsorbing at an open surface site, here denoted with *. The favored process thus involves the adsorption of oxygen on a surface site, the scission of the O_2 bond and the formation of adsorbed hydroxyl species *via* proton and electron transfers, until finally water dissociates from the surface.[73]

$$\frac{1}{2}O_2 + * \rightarrow O^*$$

$$O^* + H^+ + e^- \rightarrow HO^*$$

$$HO^* + H^+ + e^- \rightarrow H_2O + *$$

Alternative mechanisms have also been proposed with some involving peroxo species such as OOH* and HOOH*, although all alternatives are also four-electron processes. An important tool to confirm the four-electron mechanism of an electrocatalytic reaction is the *Levich* analysis, for which several voltammograms are recorded at different rotation speeds of the disk electrode.[74] When plotting the reciprocal current of each experiment vs. the reciprocal square root of the rotation rate, the resulting *Koutecky-Levich* plot can give information about the kinetics and mechanism of the reaction. While normally, the linear plot intercepts the vertical axis at zero, this is not the case for the oxygen reduction that is limited by sluggish kinetics rather than by mass transport. From the intercept and the slope of the plot one can determine the rate constant and the number of electrons transferred, respectively.

A further phenomenon observed in the ORR is a high overpotential, that is defined as the potential difference between the theoretical, thermodynamic reduction potential that is needed for a reaction to proceed, and the experimentally observed reaction potential. While its exact origin was a critical point of discussion for a long time, *Norskov et al.* could link this phenomenon to extremely stable adsorbed oxygen and hydroxide species on Pt(111) surfaces *via* DFT calculations.[75] While at high potentials, these species become so stable that the

proceeding of the ORR is hindered, at lower potentials, the stability of the adsorbed intermediates decreases. Thus, the adsorbed oxygen and hydroxide species can be activated, with the necessary energy resulting in the observed overpotential.

The oxygen binding energies are also used as the decisive parameters for the theoretical prediction of mass activities on Pt surfaces as is elaborated in the next paragraph.

Prediction of Mass Activities Using Generalized Coordination Numbers

Keeping in mind the economic aspect of minimizing Pt loadings, computational methods could help to identify potential catalyst species with high activities to make a targeted synthesis feasible. When calculating small Pt species, DFT methods quickly run into the problem that nanoparticles and –clusters increase in complexity with every atom added because of the many possible geometries and resulting minima on the potential energy surface.[76] The arising calculation effort becomes less and less practicable with larger NPs. In contrast, NCs as highly defined species present ideal models to study ORR mechanisms.

The group of *Bandarenka* introduced the concept of generalized coordination numbers ($\overline{CN}$) which bases the prediction of ORR mass activity on an arithmetic calculation method, thus making DFT calculations unnecessary and significantly cutting computation times and efforts.[77] They rely on the *Sabatier* principle for optimal catalyst design. The theory states that an ideal catalyst neither exhibits too weak interactions with a reaction intermediate, therefore failing to react on its surface, nor binds the intermediate species too strongly and prevents dissociation. Analysis results are visualized in so-called volcano plots where the oxygen binding energy is plotted versus a specific parameter, e.g. the catalytic activity or in the case of the ORR the electrode potential (Figure 7, left). The potential-determining step on the left (low coordination – strong binding) and right (high coordination – weak binding) sides of the volcano are indicated.

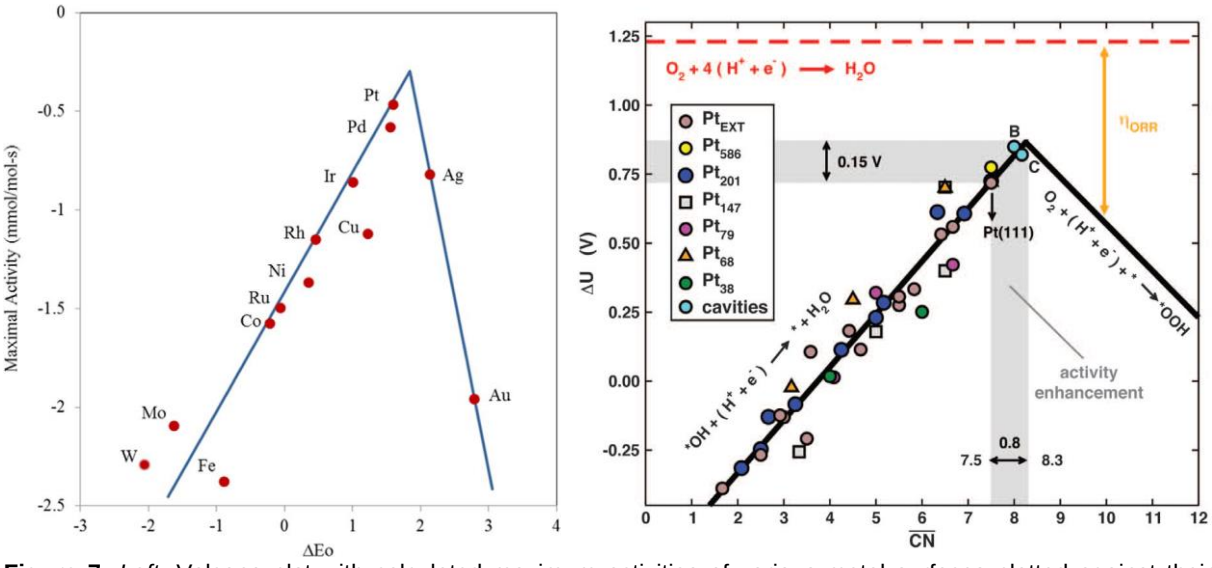

Figure 7: *Left:* Volcano plot with calculated maximum activities of various metal surfaces plotted against their oxygen binding energies. The pointed shape of the resulting trend is indicated and Pt and Pd are identified as the most active candidates. Reprinted from Renewable and Sustainable Energy Reviews, 69, J. Stacy, Y. N. Regma, B. Leonard, M. Fan, The recent progress and future of oxygen reduction reaction catalysis: A review, 401-414, Copyright 2017, with permission from Elsevier.[78] *Right:* Coordination-activity plot for surface sites on various Pt clusters where their potential is described by the generalized coordination number $\overline{CN}$. Optimal catalysts have $\overline{CN}$ ≈ 8.3 and *OH adsorption energies ~0.15 eV weaker than Pt(111) (area in gray). From F. Calle-Vallejo, J. Tymoczko, V. Colic, Q. H. Vu, M. D. Pohl, K. Morgenstern, D. Loffreda, P. Sautet, W. Schuhmann, A. S. Bandarenka, Science 2015, 350, 185. Reprinted with permission from AAAS.[75,77]

For a theoretical investigation of the intermediates' binding energies, elaborate studies have been conducted to gain a better understanding of the reaction steps at the electrode.[75] DFT calculations have determined that the binding strength of an optimal catalyst site towards a hydroxyl species (OH*) in the predominant dissociative mechanism should ideally be 0.1 eV lower than that of Pt(111).[79] Even more specific is the approach to look at the geometry of a potentially active surface site as it has been introduced by *Calle-Vallejo et al.* in 2015.[77] Their prediction model is based on the direct correlation of the calculated intermediates' binding energies with the coordination environment of Pt surface atoms, because the binding energies are determined by the electron density at a specific surface site. In turn, this electron density is dependent on the coordination environment of a surface atom. Thus, by "coordination-activity plots", surface sites with exceptional activities can be identified and finally maximized (Figure **7**, right). This simple coordination number (CN) model is valid for small species on extended surfaces,[80] while an extension to the second nearest neighbors becomes necessary in the case of NPs because of finite size effects. To estimate this "generalized" coordination number ($\overline{CN}$) for a surface site i, the formula

$$\overline{CN}(i) = \sum_{j=1}^{n_i} \frac{cn(j)}{cn_{max}}$$

is used. When plotting $\overline{CN}$ of various Pt surface sites versus the electrode potential, the resulting volcano plot demonstrates that the most active sites of Pt(111) with $\overline{CN} = 7.5$ are already near the optimum, emphasizing the superior activity of platinum compared to other metals.[77] These are only exceeded by surface sites with $7.5 \leq \overline{CN} \leq 8.3$. Therefore, the ratio of such highly active sites to the total number of surface sites can be directly linked to the activity of a pure Pt NP. The concept can even be used to predict ORR activities in absolute units of A/mg_{Pt}.[81]

Size-dependent Activity and Atom-precise Platinum Clusters for ORR

Previously it has been shown that the ORR activity of pure Pt catalysts is highly dependent on the particle size. This is easily explained by the pronounced size dependence of electronic parameters like band gaps and orbital energies as well as geometries with specific types of binding sites. Thus, *Shao et al.* showed a peak in mass activity for 2.2 nm sized Pt NPs with size distributions between 0.2 and 0.3 nm.[69] They rationalized their finding with a high ratio of Pt(111) facets exposed on the cuboctahedral particles of this size that show optimal binding energies for oxygen species. *Perez-Alonso et al.* directly correlated the amount of these faceted sites with the measured activity of size-selected clusters and could substantiate *Shao's* findings by identifying a peak in mass activity around 3 nm, although their particles also exhibited significant size distributions.[82] Many papers suggest that the ORR activity continuously decreases with decreasing particle size, to the extent that clusters below 2 nm in diameter only show negligible activity. Theory reasons that this is caused by the increase of undercoordinated surface sites that bind oxygen too strongly. Calculations by *Liu et al.* confirmed the known trend that for Pt/C, the highest mass activities are achieved for narrow size distributions of the smallest Pt NPs around 2 nm.[83]

Recent investigations demonstrated that not primarily the size is the decisive factor, but the shape of the particle and thus the exposure of extraordinarily active surface sites.[84] Since especially for Pt clusters, the size directly correlates with surface structures, the two factors of exact size and "shape", meaning surface structure, are directly connected.[85] This fact can also explain findings that show atom-precise clusters in the subnanometer range exhibiting high mass activities for ORR – although many publications predict no or only minor activity for such small clusters (Figure 8).[48] Additionally, the unique electronic structure has been proposed to play a key role in the exceptional activities of subnanometer clusters. However, due to the challenging synthesis, only few synthetic methods with application in electrocatalysis have been reported so far.[49]

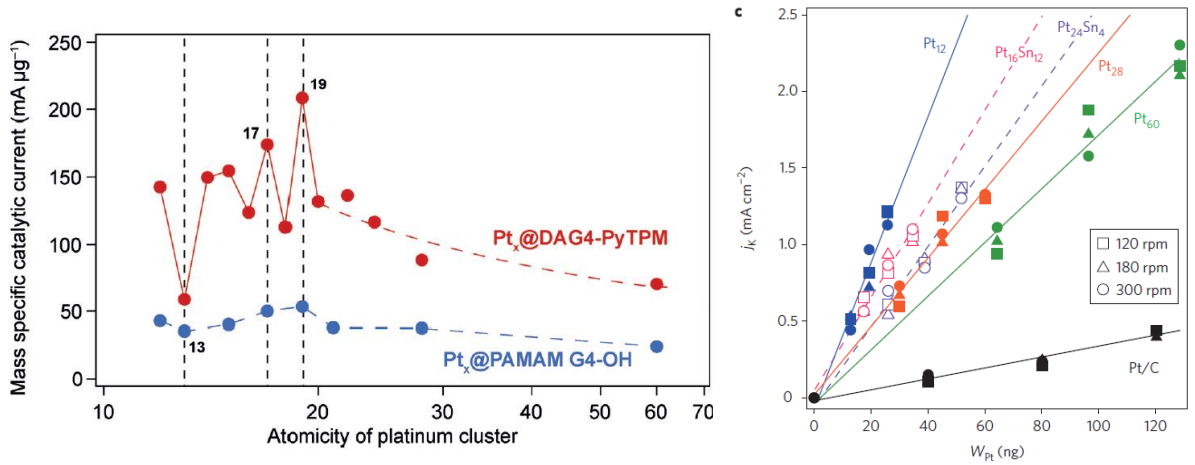

Figure 8: ORR activities of atom-precise, ultrasmall Pt clusters. *Left:* Variations of the Pt cluster mass activity *vs.* the cluster atomicity for two different stabilizing dendrimers, demonstrating the high size-sensitivity. Reprinted with permission of T. Imaoka, H. Kitazawa, W.-J. Chun, K. Yamamoto, Angew. Chem. Int. Ed. 2015, 54, 9810. Copyright 2015 Wiley-VCH Verlag GmbH & Co. KGaA, Weinheim.[48] *Right:* Kinetic current density (j_K) *vs.* the weight of Pt for different mono- and heterometallic Pt clusters, all outperforming a commercially available Pt/C catalyst. Reprinted by permission from Springer Nature Customer Service Centre GmbH: Springer Nature, Nature Communications, Size-specific catalytic activity of platinum clusters enhances oxygen reduction reactions, K. Yamamoto, T. Imaoka, W.-J. Chun, O. Enoki, H. Katoh, M. Takenaga, A. Sonoi, Copyright 2009.[49]

Among others, the groups of *Ueli Heiz* and *Scott L. Anderson* have made significant contributions in the field of catalytic properties of atom-precise clusters produced by laser ablation. They investigated activities of supported clusters *in situ* for a broad variety of reactions with one main focus on electrocatalytic applications of Pt clusters.[41,86] In a detailed study by *von Weber et al.*, a series of such size-selected Pt_n clusters ($n \leq 14$) generated by laser ablation were investigated towards their activity in the ORR and a distinctive size-dependency was established.[87] Almost all clusters outperformed Pt NPs due to their high fraction of active surface atoms. The results confirmed previous studies that claim the Pt 4d band energy being responsible for the catalytic properties of a cluster in the ORR.[88]

The previously presented, dendrimer-stabilized clusters by the group of *Imaoka* were also investigated for their ORR activity (Scheme 2).[47–49] They compared the activity of a Pt_{12} and a Pt_{13} cluster in the ORR and came to the conclusion that the former cluster is more than twice as active as the “magic number” cluster Pt_{13} despite differing in only one atom in nuclearity.[47] Previously, Pt_{12} also showed a higher activity than Pt_{28} and Pt_{60}, thus rebutting existing studies that state a lower activity for smaller Pt particles due to their too high Pt–O bonding energy. The outstanding activity of Pt_{12} is attributed by DFT studies to highly active surface sites that are unique to the structure of this specific cluster. When expanding this study to a broader scope of clusters Pt_n ($n = 12–20$), Pt_{17} and Pt_{19} exhibited even higher activities and computational modelling suggested especially active edge sites to be responsible for this effect.[48]

In summary, many studies report a decreasing activity of Pt particles for the ORR when their diameter falls below 2 nm. This is attributed to the Pt 4d band shifting to energies close to the *Fermi* level E_F and the resulting increased oxygen adsorption energy that is detrimental to the ORR activity. First hints that the surface structure has a major effect for the catalytic activity were given for shape-selective Pt NPs, but *Imaoka*, *Heiz* and others only made breakthroughs in this area when accessing atom-precise Pt clusters in the range close to 1 nm (20–30 atoms). They could show that only one atom difference in cluster size lead to huge increases in activity due to unique and highly active surface structures. Therefore, the goal is to select such atom-precise clusters in a size regime around 1 nm and exploit their catalytic activity. Nevertheless, their challenging synthesis hampers this goal and a scalable way to atom-precise, sub-nanometer species is highly sought after.

2.1.2 Gold Clusters

The rise of gold NP chemistry is based on the first discovery by *Faraday* in 1857, who described a “beautiful ruby fluid” that he obtained from the reduction of gold chloride with phosphorus in the presence of CS_2.[2] This compound, denoted as “potable gold”, was investigated by *Mie* in 1908 who concluded that the intense color stems from the absorption and scattering of light by the contained plasmonic gold NPs.[3] With intense research being devoted to such NPs, the first molecular gold cluster compound was reported in 1981 by the group of *Schmid*, who was able to synthesize $Au_{55}(PPh_3)_{12}Cl_6$,[89] although its exact structure is under debate until today.[90] In the early 90s began the success story of thiol-stabilized gold clusters that were initially synthesized in a two-phase system. Although gold clusters are of less interest for biomedical applications than NPs due to their high cytotoxicity, their unique optical and electronic properties made them a worthy subject of study for the last decades.[91] For clusters below 20 atoms, next to thiol-containing clusters, a great variety of phosphine-stabilized Au compounds with the general formula $[Au_n(PR_3)_mX_s]^{z+}$ (n>z) is known, where X stands for additional sub-ligands like halides or thiolates.[22] In this work, the focus lies on these clusters due to their selective synthesis and the absence of staple motifs like in thiolate-capped clusters (S-Au-S) that hinder ligand removal without changes to the core nuclearity.[92] In addition, PR_3 ligands enable the unambiguous identification of compounds *via* ^{31}P-NMR spectroscopy.

Synthetic Methods and Characterization

The synthesis of gold NPs still relies on the bottom-up principle established by *Faraday*, namely the reduction of molecular gold precursors in the presence of surface-active agents. The latter act as stabilizing ligands that prevent agglomeration by steric or electronic repulsion. For clusters, where only one specific core nuclearity with a specific number of ligands should be selected, this method often produces mixtures of several compounds. These can be separated with gel electrophoresis methods (PAGE)[93] or high performance liquid chromatography (HPLC).[94] In this context, electrospray ionization coupled with mass spectrometry (ESI-MS) provides an important tool to identify which species are present in the mixture and if the separation was successful.[93] To directly target atom-precise clusters, two approaches have been established: Size focussing[95] and the so-called ligand exchange-induced size/structure transformation (LEIST) methodology.[96] Combining these techniques lead to a plethora of ligand-stabilized, precise Au clusters with atomicities up to several hundreds of atoms, such as $Au_{279}(SR)_{84}$ with the so far largest reported crystal structure.[97]

For the size focussing technique, one of the first examples was the thiol-stabilized $Au_{25}(SR)_{18}$ cluster.[98] By careful selection of solvent, temperature, reducing agent and reactant ratio, a kinetically controlled cluster formation gives rise to several small species with a narrow size distribution. Prolonged aging leads to a thermodynamic selection where only one cluster

species is formed preferentially, and smaller and larger ones are slowly transformed to the desired compound. With the same method, also other cluster like $Au_{38}(SR)_{24}$, $Au_{144}(SR)_{60}$ and many others could be obtained without further purification.[99,100] Nevertheless, not all possible cluster sizes are accessible by size focussing when energy is necessary to overcome the barrier between two stable structures. In the LEIST approach, this problem can be tackled by adding a large excess of new ligand to an already formed, precise cluster. Such transformation reactions can selectively lead to new core nuclearities with fascinating properties (Scheme 3).

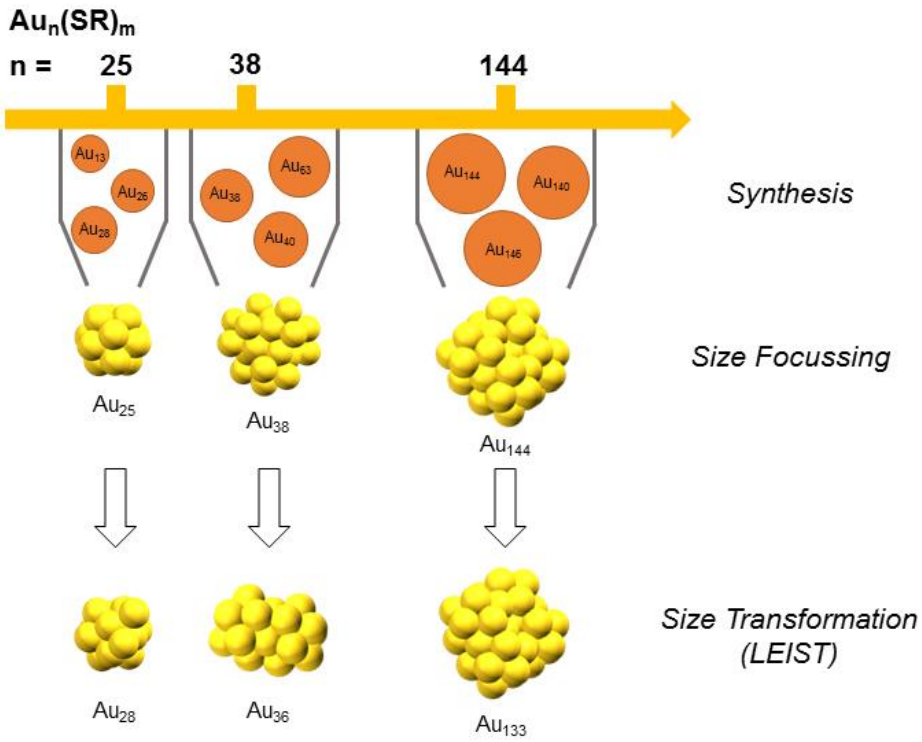

Scheme 3: Synthetic approaches towards atom-precise, thiol-stabilized Au clusters. While some clusters can be obtained by thermodynamic size focussing, other structures are accessed by size transformation (LEIST), e.g. *via* addition of an excess of ligand.

Both principles have been transferred to gold phosphine clusters in the late 1960s by the pioneering works of *Malatesta*.[101] These are structurally less diverse, but also simpler than thiolate clusters due to their core-shell structure whereas thiolate clusters often contain several layers of ligands around the cluster core that hamper a precise structure determination. Several gold phosphine compounds can be obtained directly from mononuclear gold precursors, mostly linear gold phosphines, by hydride reduction. Especially $Au_9(PAr_3)_8$ and Au_{11} compounds are well accessible and it has been found that strongly coordinating anions (Cl^-, I^-, SCN^-,…) favour the formation of a Au_{11} core, whereas with nitrate as a weakly coordinating ion, Au_9 clusters are formed preferentially.[22] Starting from these cluster sizes, further atom-precise compounds can be obtained when following the LEIST principle. For cluster growth, further mononuclear gold precursor is added, and cluster etching is achieved with the addition

of an excess of ligand. In the latter case, the use of chelating phosphine ligands is another parameter to achieve selective core transformations.

The best way to identify the exact structure of a cluster is single crystal XRD, but many gold clusters are extremely challenging to crystallize. In NMR spectroscopy, especially with ^{31}P-NMR spectra, most Au phosphine clusters are clearly distinguishable with few characteristic signals. Transformations in the cluster core or the ligand shell result in a change of the electronic structure and thus also in a shift of the ^{31}P signals so that the integrity of a cluster can be easily determined.[22] UV/Vis spectroscopy exhibits a similar sensitivity for the electronic structure and is especially suited for revealing the cluster core structure. Using distinctive bands, unknown structures can be compared to reported spectra to draw conclusions about the core structure of a compound.[102] Another effective tool for cluster characterization is the use of mass spectrometry techniques (e.g. ESI-MS), but fragmentation or reactions during the ionization process often hamper the detection of the signal stemming from the intact cluster. With the ligand shell disintegrating and a variety of possible cluster charges, the evaluation of obtained spectra is often tedious.[103]

Cluster Properties

Gold NPs are well known for their plasmon resonances important for medical applications, but with a diameter below 2 nm these properties disappear and are replaced by discrete electronic transitions causing a vibrant colour spectrum of the solubilized clusters.[104] Such molecule-like properties are consistent with the description of subnanometer clusters as “superatoms” (see chapter 2.1).[105] Theoretical investigations support the hypothesis of a discrete electronic structure that is caused by quantum size effects and is highly characteristic for each core size and structure.[100] Therefore, absorption spectra can be used to learn about the electronic structure of the metal core and the ligand shell. Although in most cases similar core structures lead to similar UV/Vis spectra, it has been reported that ligands influence the electronic structure of the whole compound.[102] This is especially the case for diphosphine ligands including chlorides where ligand-mediated transitions come into play.[22]

The core structure of gold clusters is mainly based on centered polyhedra, but interesting and unique structures have been reported for smaller clusters, e.g. non-centered polyhedral and core+*exo* structures (Scheme 4). In the latter, a central polyhedron exhibits additional atoms attached to the base structure together with anionic sub-ligands like halides. The core+*exo* structure of the $[Au_8(dppp)_4Cl_2]^{2+}$ cluster (dppp = 1,3-bis(diphenylphosphino)propane) is also a representative example for a gold cluster showing photoluminescent properties, in the case of Au_8 an intense pink.[106] Although photoluminescence of atom-precise gold clusters is not well studied yet, mostly core+*exo* type clusters are known to show this effect.

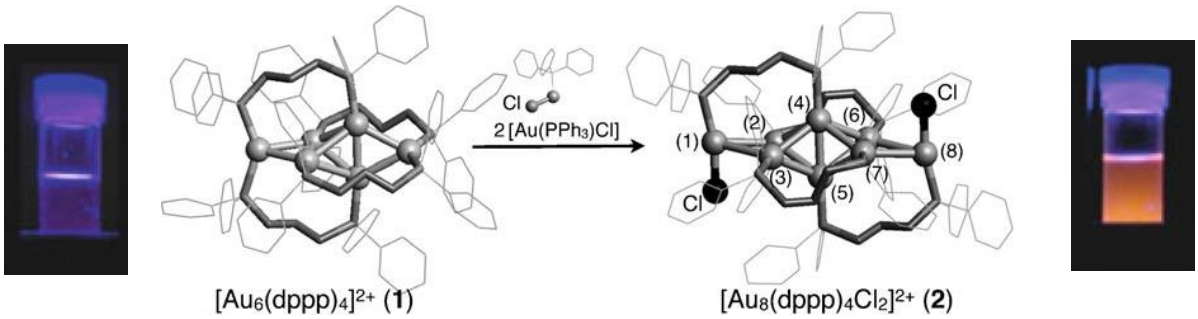

Scheme 4: X-ray crystal structures of two core+*exo* type clusters, namely $[Au_6(dppp)_4]^{2+}$ and $[Au_8(dppp)_4Cl_2]^{2+}$, that is obtained from the former cluster *via* the addition of $Au(PPh_3)Cl$. Both clusters show fluorescent properties. Reprinted and adapted with permission of Y. Kamei, Y. Shichibu, K. Konishi, *Angew. Chem. Int. Ed.* **2011**, *50*, 7442. Copyright 2011 Wiley-VCH Verlag GmbH & Co. KGaA, Weinheim.[22,106]

Catalytic Applications of Gold Clusters

The great variety of reports about precise gold compounds in literature opens up new pathways to investigate size/structure-activity relationships of small metal clusters. Well-studied gold clusters can act as model catalysts to understand catalytic processes on an atomic level. Next to countless theoretical studies, ligand-stabilized as well as naked gold clusters have been applied in homogeneous, heterogeneous and electrocatalysis. Fundamental studies research clusters in the gas phase to minimize all external influences on the cluster core reactivity, such as interactions with ligands, supports or solvents. Thus, naked gold cluster cations with less than ten atoms have been found to cleave the highly stable C-H bond of methane already at room temperature. Such reactivities towards small molecules like methane, O_2 or H_2 reveal the potential of gold clusters in the synthesis of base chemicals like methanol[107] and hydrocarbons.[108] Naked gold clusters generated by vaporization and size selection techniques are stabilized on supports and have shown highly size-dependent catalytic activity, e.g. in CO oxidation. However, some studies report a lower size limit for catalytic activity of these ligand-free clusters, in the case of the mentioned CO oxidation a core nuclearity of eight.[109]

Wet-chemically synthesized clusters often show catalytic activity despite their ligand stabilization and the blocking of some potentially active surface sites. Exemplarily, the thiol-stabilized cluster Au_{25} is a popular subject of study due to its comparably facile synthesis. The compound has been applied in homogeneous processes like the reduction of 4-nitrophenol or the selective hydrogenation of ketones and aldehydes.[110] In addition, ligand-stabilized gold NCs have been frequently used as precursors for catalytically active gold species. Said Au_{25} cluster was stabilized on porous carbon by the group of *Tsukuda* and subsequently calcined with minimal agglomeration to yield naked clusters with high activity in the selective epoxidation of styrene.[111] The catalytic activity increased significantly upon removal of the stabilizing thiol

ligands, albeit with the drawback of decreasing selectivity. In a similar approach, *Anderson et al.* deposited phosphine-stabilized Au_8, Au_9 and Au_{101} clusters on titania and applied the materials in benzyl alcohol oxidation after different treatments. The active species were determined to be agglomerated Au NPs with a diameter around 2 nm that formed in the course of ligand cleavage.[112]

Au NCs and NPs in the nanometer range also showed promising activities in several electrocatalytic conversions. *Liu et al.* demonstrated the high activity of naked Au NCs supported on nitrided carbon for the electrocatalytic methanol oxidation.[113] With their sophisticated synthesis procedure, ultrasmall clusters with a narrow size distribution of 1.6±0.3 nm could be obtained that outperformed similar catalysts with larger sizes or bearing ligands. Next to naked, supported gold NCs, also clusters stabilized by organic surfactants showed electrochemical activity, e.g. in the ORR. *Chen et al.* showed that the ligand-stabilized Au NCs (Au_{11}, Au_{25} and Au_{55}) exhibit higher activity in the ORR than single-crystalline Au particles and similar performance to commercial Pt catalysts, although no investigations towards the integrity of the clusters after catalysis are reported.[114] Also in the HER, the thiol-stabilized Au_{25} cluster showed significant electrocatalytic activity, whereas the Pt-doped cluster with a $PtAu_{24}$ core could even outperform platinum benchmark catalysts.[115]

In summary, gold clusters differ distinctly from platinum carbonyl clusters in their electronic and chemical properties. Precisely because of these differences, Au clusters open new possibilities for the investigation of size effects and the enhancement of catalytic activity. Especially phosphine-stabilized Au clusters are highly interesting due to their comparably facile synthesis, the broad variety of literature-known compounds and their defined core structures.

2.2 Metal-Organic Frameworks – Endless Possibilities

Since the 1990s, metal-organic frameworks (MOFs) developed as a subclass of coordination polymers and experienced an explosion of scientific interest with the discovery of MOF-5 in 1999.[116] Assembled from zirconium oxo clusters OZn_4 as metal-containing "nodes" connected by 1,4-benzenedicarboxylate (BDC) linkers as "struts", MOF-5 was the first material that showed permanent porosity even when removing solvent molecules from its pores (Figure 9). Researchers were surprised by the extreme fraction of empty volume of 80% that exceeded most of the known porous materials at the time. Although only stable under exclusion of moisture, MOF-5 inspired a flood of new MOF structures based on the principle of connecting metal-organic building blocks, soon denoted as secondary building units (SBUs), by coordinating organic linkers, mostly di- or tricarboxylic acids.[117] By slow, solvothermal synthesis, defects in the network are rearranged and large crystals can be grown over several days. Additionally, mechanochemical synthesis methods have been intensely investigated in the last years.[118] The great advantages of MOFs lie in their versatile structure: Not only the metal-containing SBU but also the organic linker leaves vast possibilities for variation by attaching different functional groups, introducing chiral centers or extending the linkers in a so-called reticular synthesis approach, which results in an extension of the framework and in higher pore volumes. In comparison to zeolites, the MOFs' high tunability comes with the disadvantage of lower thermal and chemical stability due to the weaker coordinating bonds between metal and linker. While zeolites tolerate up to 1000 °C, most MOFs decompose way below 500 °C.[119]

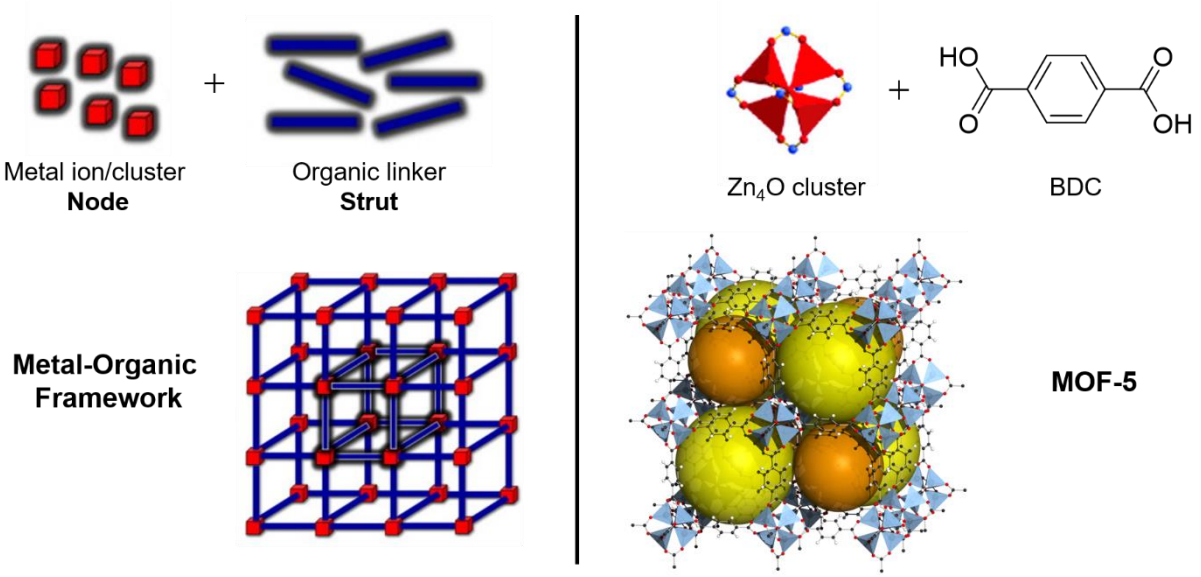

Figure 9: *Left:* General structure of a metal-organic framework (MOF) composed of metal-containing nodes and organic struts. *Right:* Structure of MOF-5 with Zn_4O as nodes and BDC as organic linker.[120]

2.2.1 MOFs for Gas Storage and Separation

The fascinating properties of MOFs have been exploited for a variety of applications, especially in gas storage and separation where their high porosity and internal surface area is favorable. Thus, MOFs have been identified as one of the most promising candidates for hydrogen storage and capacities as high as 49 g/L volumetric uptake and 8.5 wt% excess hydrogen uptake at 100 bar and 77 K have been reported, even exceeding the targets given by the department of energy for 2020 for low temperature H_2 storage.[121] Because hydrogen only interacts by weak dispersion forces (physisorption) with a potential storage material, the way to higher storage capacities is either the increase of internal surface area and pore volume or the maximization of *Van-der-Waals* forces and additional bonding interactions like dipole-induced dipole attractions.[122] In MOFs the latter can be achieved for instance by introducing positive or negative partial charges in the framework. One promising approach consists in the maximization of coordinatively unsaturated sites (CUS), where a coordination site at the metal node is not occupied by a linker molecule but other species can interact at the coordination site.[123] CUS are generated by removing adsorbed solvent molecules during an activation procedure subsequent to the synthesis to generate vacant sites at the node. The vast possibilities for MOF design also allow for an optimization of the H_2 uptake by tuning the pore size that has been found to have a pronounced effect on the stacking of hydrogen molecules and thus the storage capability.[124]

The tunability of MOFs is also beneficial for gas separation processes as the affinity for a certain compound can be finely tuned and adjusted to the respective separation problem.[125] This thermodynamic equilibrium effect has been applied for example in the separation of acetylene from CO_2 that is highly challenging due to the similar size and adsorption properties of the two molecules.[126] For the separation of gas molecules with a large enough size difference, the pores of a MOF can contribute a molecular sieving effect. In this case, only one substrate of a mixture can penetrate the empty volume while the diameter of a second substrate is too large to easily fit through the pore openings. This effect has been shown in the selective adsorption of H_2 over N_2 and of CO_2 over CH_4 at low temperatures.[127]

Although additional fascinating properties like flexibility,[128] luminescence[129] or magnetism[130] have been reported aplenty, their discussion would go beyond the scope of this introduction and is not relevant for this thesis.

2.2.2 MOFs as Catalysts

Due to their outstanding porosity, the first proposed application for MOFs was indeed catalysis because the also highly porous family of zeolites are among the commercially most important compounds in this field. Although the organic component in MOFs makes them less resistant to high temperatures compared to the purely inorganic zeolites, their chemical variability may open a niche in high-value-added reactions, i.e. in the production of fine chemicals. Still, many targeted functions in a MOF ultimately aim towards catalytic applications, where again the high tunability comes into play for a possible fine optimization of activity.[119]

MOFs exhibit various unique features that make them interesting for catalysis. Their porous structure can impart shape or size selectivity to a catalytic reaction, where only certain substrates are able to access active centers in the free volume while large substrates are not converted. The highly defined catalytic environment that is represented by a MOF pore has led to fascinating and unique reactivities where the pore space acts as a nanoreactor.[131] Additionally, catalytic species can be stabilized and controlled by confinement in the framework. Nevertheless, when positioning reactive centers in a porous MOF matrix, diffusion limitations come into play and in part severely hamper the kinetics of a catalytic reaction. Downscaling MOF particles to the nanosize regime or fabrication of MOF thin films and membranes are strategies to overcome such problems.[132]

Catalytic activity in MOFs can be either attributed to the metal nodes or originates from the organic linkers. In the former case, open metal sites can act as *Lewis* acid catalysts, with the iconic HKUST-1 as the most famous example.[133] Its copper paddlewheel units exhibit coordinated solvent molecules in the two axial positions that can be removed thermally. The thus generated CUSs can be found in many MOFs and readily convert a broad scope of substrates in *Lewis* acid catalyzed reactions: Cyanosilylations,[133] *Diels-Alder* reactions[134] as well as the cycloaddition of CO_2 with epoxides,[135] to name only a few. The introduction of defects in the network, where "*the regular periodic arrangement of atoms or ions of the crystalline parent framework* [is broken] *because of missing or dislocated atoms or ions*" can increase the catalytic activity.[136] Upon increase of defective sites, a larger portion of partially undercoordinated metal nodes is exposed, with the result of increased *Lewis* acidity and thus higher catalytic activity.

Not only the metal containing node, but also the organic strut can be the source of catalytic activity. As the most straightforward way, homogeneous catalysts are heterogenized by incorporating them as the organic linker themselves. Given their utility as homogeneous catalysts and their function as active center in many enzymes, metalloporphyrins have been identified as suitable candidate compounds for this approach. Despite the challenging MOF

synthesis – considering the large pores prone to collapse and the coordination sites that are easily blocked during MOF formation – various structures have been reported and applied for oxidations, hydrolyses[137] as well as acyl transfer[138] and Hetero-*Diels-Alder* reactions.[139] The unique structure of MOFs also opens new pathways in enantioselective catalysis. Some MOFs show homochirality even though completely achiral starting compounds are used due to self-resolution during the crystallization process, although mostly racemic mixtures are obtained.[140] By incorporating enantiopure ligands directly into the MOF, better control over the resulting structure is obtained and only one enantiomer can be targeted. Despite the challenges of designing suitably large pores for the often sterically demanding substrates, high yields and enantiomeric excesses were achieved in asymmetric olefin epoxidations,[141] ring openings[142] or hydrogenations.[143]

Another approach towards catalytically active MOFs is to comprise an active species inside the framework pores. Due to the mentioned challenges of porphyrin-based MOFs, metallated and non-metallated porphyrins have been encapsulated into the sufficiently large pores of a MOF and then used for peroxide-assisted oxidations. As another early example, *Keggin*-type polyoxometallate clusters could be contained in the empty volume of MIL-101 and facilitated oxidations reactions with only modest turnover frequencies.[144] Next to these very specific examples, the highest interest by far lies in the encapsulation of metal NPs and NCs due to their known outstanding catalytic activities and their need for stabilization. This class of "metal@MOF" compounds will be discussed in detail in chapter 2.3.

2.2.3 Zeolitic Imidazolate Frameworks

As already mentioned, aluminosilicate zeolites are superior to MOFs in processes that require more drastic reaction conditions due to greater thermal and chemical stability. Since the beginning of MOF chemistry, it has been sought to combine the advantages of MOF tunability with the strong network of zeolites by strengthening the coordination bond between metal and linker. This was in part accomplished in the early 2000s by the group of *Omar Yaghi* that developed a subclass of MOFs, the so-called zeolitic imidazolate frameworks (ZIFs).[145] Assembled from imidazolate linkers and tetrahedrally coordinated transition metals, mostly Zn and Co, ZIFs showed high stability in boiling water, organic solvents and even in refluxing alkaline solutions. With their often zeolite-like topologies, some ZIFs can tolerate up to 500 °C without losing their crystallinity. This enhanced stability is attributed to the similar bridging angles (145°) of the Si-O-Si unit in zeolites and the M-Im-M fragment in a ZIF.[13] The exact topology has been found to be dependent on the solvent composition as well as on linker-linker interactions, thus on the functional groups on the imidazole. Despite of the short time that ZIFs

have been researched, already over 100 structures have been reported so far.[146] Even mixed-linker experiments often lead to single-phase compounds, further broadening the scope with more complex structures. The pore sizes range from a few Å with pore openings even under 1 Å to huge supercages, e.g. in the case of ZIF-95 or ZIF-100, that dwarfs common zeolite cages with its inner pore diameter of 35.6 Å and an outer diameter of 67.2 Å (Figure 10).[147]

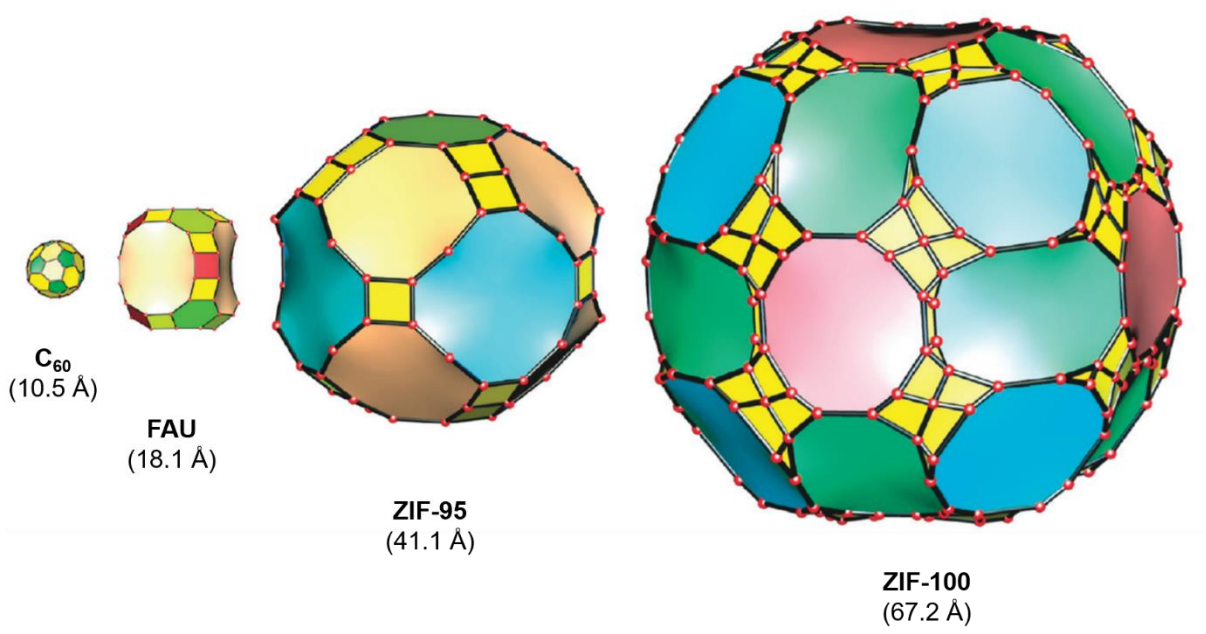

Figure 10: Comparison of C_{60} and the faujasite (FAU) supercage with the cages in ZIF-95 and ZIF-100, shown as natural tiling (Zn atoms as red spheres). Reprinted with permission from A. Phan, C. J. Doonan, F. J. Uribe-Romo, C. B. Knobler, M. O'Keeffe, O. M. Yaghi, Acc. Chem. Res. 2010, 43, 58. Copyright 2010 American Chemical Society.[13]

An additional advantage of ZIFs are the very mild synthesis conditions that allow the formation of highly crystalline frameworks even at room temperature and ambient pressure. Generally, either a high excess of the linker itself or an additional base is applied for imidazole deprotonation and the method is applicable way more generally for the whole ZIF family than is usual for MOFs or zeolites. While under solvothermal conditions crystal formation can take up to several days, many reports state immediate ZIF precipitation at room temperature.[148,149]

Next to their outstanding thermal stability, ZIFs are mainly known for their CO_2 storage and separation properties.[13] They outperform other MOFs particularly in selectivity over other gases, e.g. CO, and the CO_2 storage capacity of the best-performing ZIF, ZIF-69, even exceeds the one of the commercially used BPL carbon.[146] Nonetheless, ZIFs have only few applications in catalysis, among which mainly base-catalyzed reactions are feasible due to the basic imidazolate linkers, since the metal sites are fully coordinated and inaccessible for substrates. Thus, ZIF-8 was successfully used as a heterogeneous catalyst for the *Knoevenagel* reaction of benzaldehyde with malonitrile at low temperatures.[150] To enhance

the catalytic performance of ZIFs, a variety of active compounds have been included in ZIF matrices with the special advantage that the mild synthesis conditions of ZIFs even allow for the encapsulation of sensitive compounds such as enzymes.[151,152] The successful synthesis of such inclusion compounds also demonstrates the high affinity of ZIFs to crystallize around compounds larger than their pores, forming defects in the process. Additionally, ZIFs have been frequently combined with metal NPs and NCs to metal@MOF compounds, that are elaborated in detail in the following chapter.

2.3 Metal@MOF – The Best of Both Worlds

With metal species as the crucial component in the majority of all reported catalytic systems, an efficient exploitation of the catalyst mass is desired especially for rare and expensive metals. With downscaling to metal NPs and nanoclusters, the economic feasibility of a catalytic process can be increased dramatically when a higher fraction of metal atoms is located at the potentially active surface (see chapter 2.1). The prerequisite of cluster surface accessibility clashes with the requirement of nanocluster stabilization to prevent agglomeration. MOFs have been applied as a versatile scaffold to achieve such stabilization while not or only minimally interacting with the cluster surface.[153]

Before encapsulating metal species in a MOF, several factors should be considered. Ideally, the pore diameter of the MOF should be sufficiently large to host the particle without having to form defects in its periodic structure at the expense of the crystallinity. On the other hand, the size of the pore opening is crucial to restrict the mobility of the encapsulated compound. If the pore is too large, agglomeration and leaching of the NPs cannot be prevented efficiently, but with a too narrow pore window, substrates cannot enter the pore to be converted by the catalytically active species. Additionally, the NP cannot simply enter the pore due to its diameter larger than the pore opening and the compound either has to be assembled inside of the MOF or the MOF is constructed around the metal species. These different encapsulation methods are elucidated in the following with a focus on gold and platinum NPs in MOFs as they are subject of this work. Additionally, only pure metal NPs are mentioned, omitting encapsulated metal oxides, sulfides and others.

2.3.1 Encapsulation Methods

One extensively investigated approach to comprise NPs and NCs inside a MOF is the so-called “ship-in-bottle” approach, where a precursor is first infiltrated into the MOF.[7] This can be either achieved by soaking the MOF in a precursor solution in liquid or incipient wetness impregnation,[154] by microwave-assisted methods,[155] solid grinding[156][156] or by choosing a volatile precursor and bringing it into the framework over the gas phase *via* chemical vapour deposition (CVD).[157] Subsequently, heat, reducing agents like $NaBH_4$, or radiation is applied to convert the monometallic precursors to NPs (Scheme 5, top). While this approach is synthetically quite simple and naked NPs are obtained, a major drawback lies in the broad NP distributions that often result from the uncontrolled reduction process. During NP formation, the remaining precursor molecules and already formed, small clusters are still freely mobile in the framework and their coalescence with large NPs leads to a broad size range with particles often even exceeding the pore diameters.

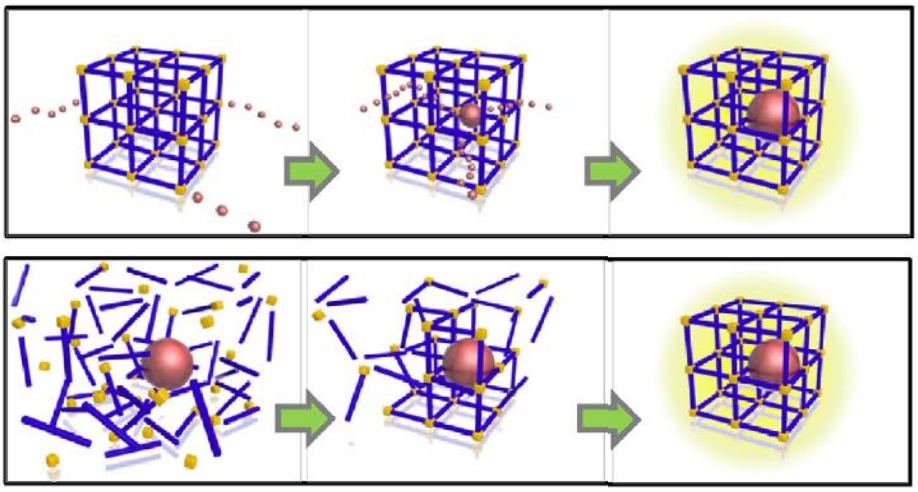

Scheme 5: Representation of the two most common encapsulation techniques, namely the "ship-in-bottle" (*top*) and the "bottle-around-ship" (*bottom*) method. In the former, a monometallic precursor is infiltrated into the porous MOF and subsequently reduced to form metal NPs. In the latter, the MOF is assembled around a preformed, ligand-stabilized metal species. Reprinted from Coordination Chemistry Reviews, 307, P. Falcaro, R. Ricco, A. Yazdi, I. Imaz, S. Furukawa, D. Maspoch, R. Ameloot, J. D. Evans, C. J. Doonan, Application of metal and metal oxide nanoparticles@MOFs, 237-254, Copyright 2016, with permission from Elsevier.[7]

In contrast, the "bottle-around-ship" or "templated synthesis" approach relies on preformed metal species, e.g. colloidal NPs that are stabilized by polymers like PVP, surfactants or other surface active agents (thiols, phosphines…).[42] Under the right reaction conditions, the MOF assembles around the metal species, comprising it within its pores without any changes in size or structure (e.g. agglomeration) (Scheme 5, bottom). The prerequisite for this encapsulation method is sufficient stability of the metal species under the reaction conditions which is challenging in the case of solvothermal synthesis. The "bottle-around-ship" approach enables the encapsulation of compounds with diameters greater than the pore size as some MOFs readily form defects around encapsulated species while retaining their crystallinity in the overall network. In contrast to the "ship-in-bottle" method, the properties of the encapsulated species are easily controllable by choosing the appropriate, preformed species. Thus, NPs with precisely defined properties and size distribution can be selected and brought into the MOF. However, while in the "ship-in-bottle" approach, naked metal NPs are formed, in the "bottle-around-ship" synthesis, the ligands that stabilize the NPs in solution are brought into the MOF and can only be removed post-encapsulation. Especially in the case of polymers, this ligand removal turns out to be complicated. Potentially active surface sites remain blocked and the access to naked metal clusters inside a MOF may be impossible.

A third, elegant way of metal@MOF synthesis is a method that was termed "pseudomorphic replication" by *Susumu Kitagawa*.[158] Here, the to-be-encapsulated particle is prepared with a shell that acts as feedstock material for the inorganic nodes of the MOF and rapidly reacts with organic linkers. The product is a crystalline MOF with the original NP core left inside of the

pores.[159] This highly specific approach requires precisely appropriate reaction conditions and has not been widely implemented.

In a last encapsulation approach, the simple infiltration of the preformed NP/NC into the MOF is possible, with the prerequisite of large enough pore openings.[160] In case of adequate interaction with the pore walls ensuring immobilization of the NPs, leaching and agglomeration can be avoided, although a preferential deposition of NPs on the outer surface of the MOF is probable.

2.3.2 NP@MOF: Control and Catalysis

A variety of metals has been brought into MOFs, including Pd, Pt, Au, Ru, Cu, and many more.[9,157,161,162] Early examples using MOF-5 and others encountered problems with large size distributions and partial destruction of the framework by particle agglomeration in the reduction process. By introducing functional groups dangling into the pores that interact with precursors and formed NPs, enhanced control over particle sizes could be achieved. Hence, *Roland A. Fischer* and his group reported the “ship-in-bottle” synthesis of Au NPs in ZIF-90, where the aldehyde groups of the imidazole linkers were highly beneficial for a narrow size distribution (Figure 11).[9] The gold NPs were fabricated by gas phase loading with Au(CO)Cl and subsequent thermal hydrogenation in ZIF-8 and ZIF-90. When ZIF-8 with only methyl groups was applied, a broad size distribution with particles from 1-5 nm was observed. With ZIF-90, in contrast, Au NPs exhibited a size of 1.2±0.2 nm which matches the pore diameter of the MOF and only few large aggregates were found in TEM studies. This effect is attributed to a stabilization by the aldehyde linkers that results in significantly smaller particles. In the gold-catalysed oxidation of benzyl alcohol to methyl benzoate, however, this material performed poorly due to the accompanying oxidation of the ZIF’s aldehyde groups and resulting pore blocking.

A similar result was obtained with Pt NPs in amino-functionalized UiO-66, where K_2PtCl_4 was introduced into the MOF *via* liquid impregnation.[8] The amino group was beneficial to the platinum loading and elemental analysis proved most of the Pt precursor to remain in the MOF, whereas Pt was largely removed from unfunctionalized UiO-66 upon washing. After hydrogen reduction, UiO-66-NH_2 contained ultrasmall and narrowly distributed Pt NPs with only 1.2±0.2 nm in size. Larger agglomerates were completely absent, showing that UiO-66-NH_2 can indeed confine particle growth within its pores. The material showed excellent selectivity in the hydrogenation of cinnamaldehyde with preferred hydrogenation of the C=O bond over the C=C double bond. Conversions and selectivity of over 90% were obtained without catalyst degradation.

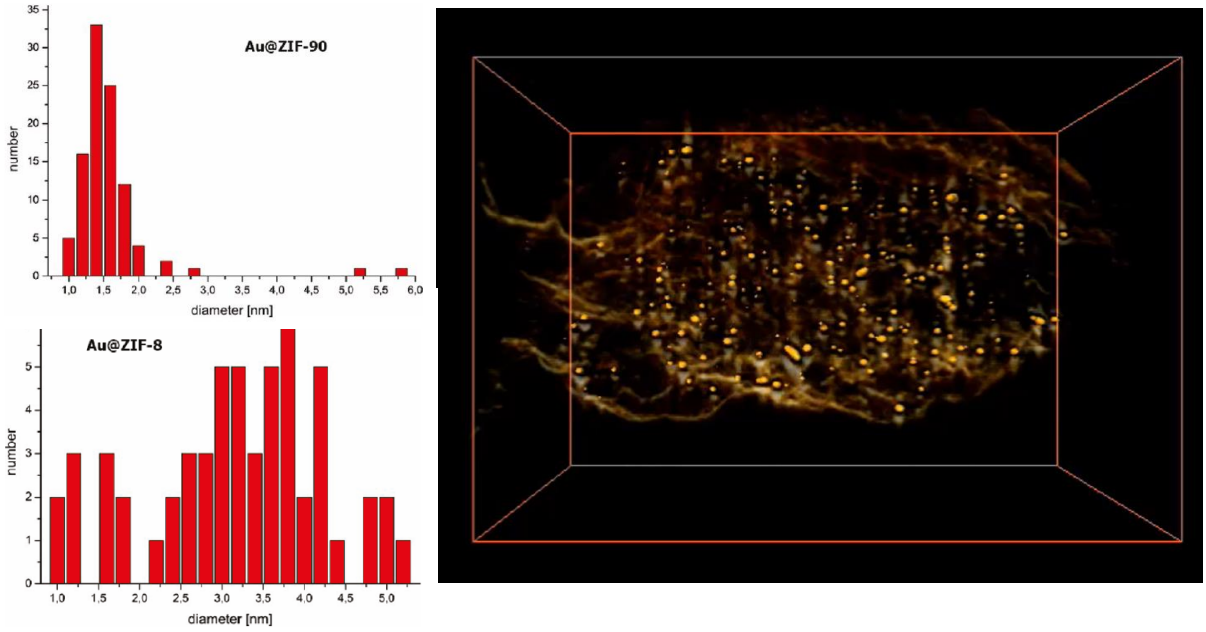

Figure 11: Size distributions of Au@ZIF-90 (*top left*) in comparison to Au@ZIF-8 (*bottom left*). In contrast to ZIF-8, a narrow size distribution with uniform Au NPs is obtained in ZIF-90 as observed in HR-TEM tomography (*right*). Reprinted and adapted with permission from D. Esken, S. Turner, O. I. Lebedev, G. van Tendeloo, R. A. Fischer, Chem. Mater. 2010, 22, 6393. Copyright 2010 American Chemical Society.[9]

The versatility of the “bottle-around-ship” method in contrast was first demonstrated by the groups of *Hupp* and *Huo* that used ZIF-8 to encapsulate a broad scope of various metal NPs with different sizes and shapes.[42] Encapsulation was achieved by simple mixing of the ZIF-8 precursor solutions with a suspension of the NPs and the metal@MOF compounds precipitated during the reaction time of 24 h. Without difficulties, PVP stabilized Au, Pt, CdTe, CdSe and Fe_3O_4 NPs, Ag nanocubes, polystyrene spheres, as well as β-FeOOH and $NaYF_4$ nanorods could be confined inside the ZIF-8 pores. Even the spatial distribution of the NPs in the ZIF-8 matrix could be influenced easily *via* the moment of NP addition during ZIF formation (Figure 12). This study impressively illustrates the versatility of ZIF-8 as an encapsulation scaffold and has inspired numerous further works. When the preformed NP species can be synthesized with precisely determined diameters and narrow size distributions, these properties are maintained also after the encapsulation and the thus gained control over the encapsulated species represents a clear advantage over “ship-in-bottle” methods. Still, the stabilizing ligands, in the case of *Hupp* and *Huo* mostly PVP, are hardly removable once inside the framework and can hamper catalytic activity.

Despite the many tools at hand for the encapsulation of nanosized species inside MOFs, reports with high atomic precision of the encapsulated species are scarce and almost all known studies refer to narrow size distributions with NPs exceeding the typical cavity size. However, for the investigation of the unique properties of one specific cluster size, such hybrid materials are highly sought after.

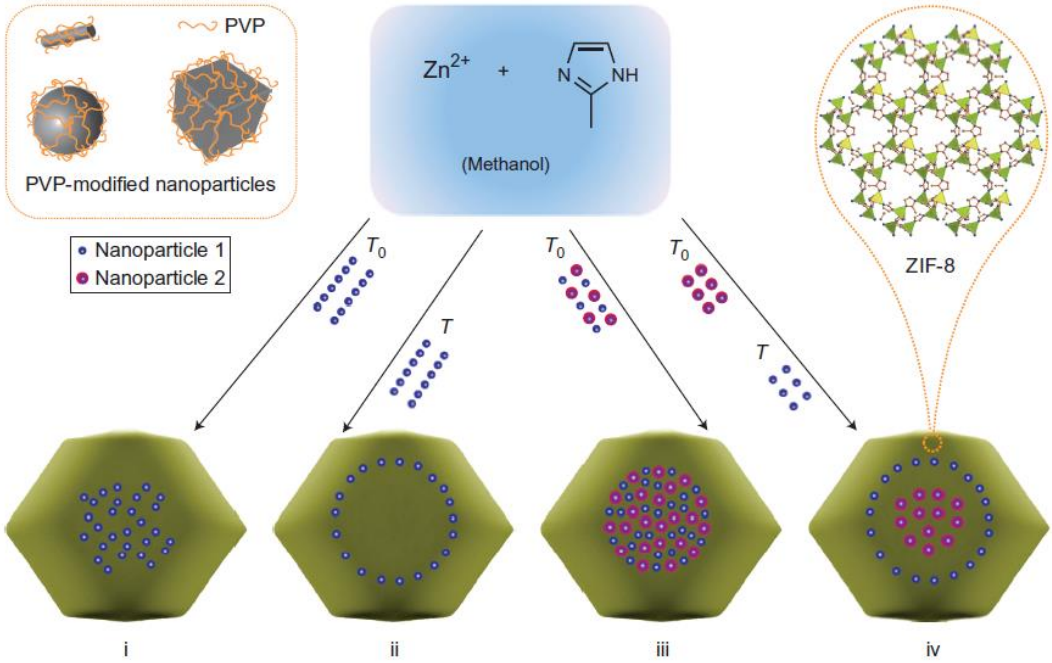

Figure 12: "Bottle-around-ship" encapsulation of different PVP-stabilized NPs in ZIF-8 with various spatial distributions. By either adding NPs at the start (T_0) or after a certain time of the ZIF-8 crystallization process (T), NPs could be selectively contained either in the core of ZIF-8 crystals or formed a core-shell-like structure, respectively. Reprinted by permission from Springer Nature Customer Service Centre GmbH: Springer Nature, Nature Chemistry, Imparting functionality to a metal–organic framework material by controlled nanoparticle encapsulation, G. Lu, S. Li, Z. Guo, O. K. Farha, B. G. Hauser, X. Qi, Y. Wang, X. Wang, S. Han, X. Liu *et al*., Copyright 2012.[42]

2.3.3 Atom-precise Clusters in MOFs

The encapsulation of atom-precise clusters below 50 atoms inside a MOF has so far not been studied intensely and only few reports could demonstrate such metal@MOF materials. In this chapter, we exclude the topic of single-atom species hosted in MOFs and focus on clusters from 2-50 atoms. ZIF-8 especially has been exploited as a scaffold for the encapsulation of gold species which still carry their ligands after being brought into the MOF. Thus, *Luo et al.* could assemble ZIF-8 around $Au_{25}(SG)_{18}$ clusters (SG = glutathione) with a "bottle-around-ship" approach with metal loadings as high as 3.8 wt% Au.[163] The $Au_{25}(SG)_{18}$@ZIF-8 material was characterized with nitrogen sorption, thermal gravimetric analysis (TGA), X-ray photoelectron spectroscopy (XPS) and DR-UV/Vis spectroscopy and was compared to an analogous compound synthesized by infiltration of empty ZIF-8 with the solubilized Au_{25} cluster. In the latter the clusters were mainly situated on the outer surface of the ZIF crystals which is why they were denoted as $Au_{25}(SG)_{18}$/ZIF-8. The distribution of the clusters in the framework can be imaged in high-resolution transmission electron microscopy (HR-TEM) and high-angle annular dark-field scanning transmission electron microscopy (HAADF-STEM) studies including elemental mapping with energy dispersive X-ray spectroscopy (EDX). This

way, the homogeneous distribution of Au_{25} in ZIF-8 could be demonstrated for $Au_{25}(SG)_{18}$@ZIF-8, while $Au_{25}(SG)_{18}$/ZIF-8 shows a bright ring around the MOF crystals, indicating the preferential deposition on the outer surface since the 15 Å sized cluster cannot enter the narrow pore window (3.4 Å). The materials were studied for the catalytic reduction of 4-nitrophenol where $Au_{25}(SG)_{18}$/ZIF-8 exhibited a significantly higher activity than $Au_{25}(SG)_{18}$@ZIF-8 due to the easier accessibility of the clusters on the crystal surface in contrast to the inside of the pores, where severe diffusion limitations hamper the conversion to 4-aminophenol. The reaction was monitored in UV/Vis spectroscopy and while for the former catalyst 95% conversion were reached after only 12 min, the encapsulated cluster showed the same conversion only after 15 h. Importantly, the free $Au_{25}(SG)_{18}$ catalyzed the same reaction to full conversion in 10 min without decomposition which questions the benefit of supporting the cluster on or in ZIF-8. In other words, ZIF-8 just acts as an inert support to immobilize the catalytically active cluster species.

In a study by *Liu et al.*, a “ship-in-bottle” approach was chosen to synthesize $Au_{11}(PPh_3)_8$ clusters inside of ZIF-8 by infiltration with $HAuCl_4$ as a precursor and subsequent reduction by $NaBH_4$ in the presence of PPh_3.[164] The authors state that they could re-dissolve ZIF-8 in CH_2Cl_2 and confirm the contained cluster with ESI-MS, UV/Vis spectroscopy, TGA and BET (Brunauer-Emmett-Teller) nitrogen adsorption measurements. Unfortunately, they could not convincingly demonstrate the location of the Au_{11} clusters in the pores of the ZIF, but HR-TEM images rather show a cluster formation on the external crystal surface. Since almost all analyses were conducted after removal of ZIF-8, a formation of the cluster in solution and subsequent deposition on the preformed MOF is likely. *Liu et al.* also claim to remove the ligands by calcination at high temperatures, but fail to provide any prove thereof and just show the small extent of cluster agglomeration by HR-TEM images. In catalytic oxidation of benzyl alcohol, all catalysts performed poorly.

Ji et al. recognized the potential of metal carbonyl clusters as precursors for atom-precise clusters and brought $Ru_3(CO)_{12}$ into ZIF-8 by using a “bottle-around-ship” method.[162] The presence of the cluster in ZIF-8 was confirmed in IR spectra where the distinctive carbonyl bands are clearly visible, although an adsorption only on the outer crystal surface was not explicitly disproven. $Ru_3(CO)_{12}$@ZIF-8 was subsequently calcined to give Ru_3 clusters embedded in nitrogen doped porous carbon (CN). The homogeneous distribution and atomic precision of the clusters were confirmed by HR-TEM, HAADF-STEM with elemental mapping, extended X-ray absorption fine structure (EXAFS) and X-ray absorption near edge structure (XANES) measurements. In the catalytic conversion of 2-aminobenzyl alcohol, the activity of Ru_3@CN exceeded those of so-called single-atom and nanoparticular Ru@CN catalysts with a high turnover frequency (TOF) of 4320 h^{-1}. Despite the fast conversion, no overoxidation

products were observed, confirming a high chemoselectivity. This study demonstrates that also by calcination of metal@MOF compounds, catalysts with high activity can be obtained when the high precision of cluster size is retained.

Lastly, the very elegant work of *Emilio Pardo's* group in terms of atom-precise metal-chain synthesis in MOF pores warrants attention. The authors could obtain a Ni-MOF, namely $Ni_2^{II}\{Ni_4^{II}[Cu_2^{II}(Me_3mpba)_2]_3\}\cdot 54H_2O$, by a first metal exchange with Ni for Mg and subsequently loading the framework with $[Pd(NH_3)_4]^{3+}$.[10] The coordinated Ni^{II} ions were thus replaced by Pd^{II} to give $[Pd^{II}(NH_3)_4][Pd_2^{II}(\mu\text{-}O)(NH_3)_6(NH_4)_2]_{0.5}\{Ni_4^{II}[Cu_2^{II}(Me_3mpba)_2]_3\}\cdot 52H_2O$ and after reduction by $NaBH_4$, quasi-linear Pd_4 cluster were obtained that lined the pore walls in $[Pd_4]_{0.5}@Na_3\{Ni_4^{II}[Cu_2^{II}(Me_3mpba)_2]_3\}\cdot 56H_2O$. All reaction steps could be visualized by beautiful single-crystal to single-crystal X-ray diffraction measurements (Scheme 6) and the compounds were thoroughly characterized by a variety of analytical methods, including DFT calculations. The latter predicted an electronic arrangement of $Pd^+Pd^0Pd^0Pd^+$ in the Pd_4 clusters that could be corroborated by *Fourier*-transform infrared (FT-IR) spectroscopy coupled with CO adsorption. The Pd_4@MOF showed surprisingly high activity for inter- and intramolecular carbene transfer reactions. More specifically, the *Buchner* reaction to cycloheptatriene products was catalyzed with high yields (>90% after 6 h with 5 and 1 mol% catalyst for inter- and intramolecular reactions, respectively) and turnover numbers (TON) up to 100,000 which exceeds the activity of the state-of-the-art rhodium catalyst by several orders of magnitude.

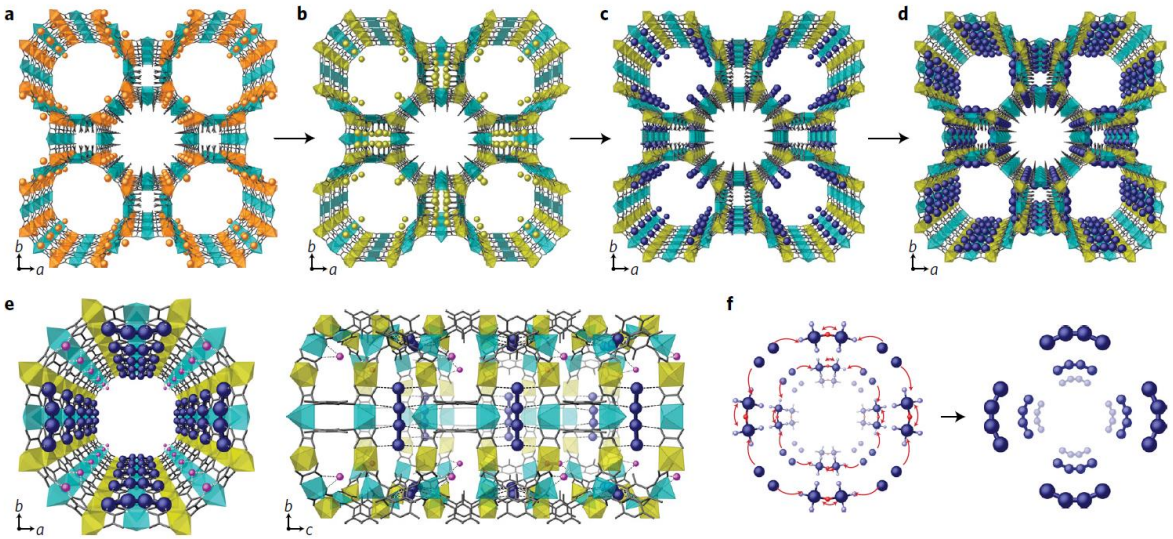

Scheme 6: X-ray crystal structures of the synthetic procedure towards $[Pd_4]_{0.5}@Na_3\{Ni_4^{II}[Cu_2^{II}(Me_3mpba)_2]_3\}\cdot 56H_2O$. The three-step post-synthetic process comprises a transmetallation (**a-b**), followed by an exchange of the Ni^{II} cations with $[Pd^{II}(NH_3)_4]^{2+}$ (**c**) and the final reduction (**d**). The resulting, near-linear Pd_4 clusters on the pore walls are depicted from different perspectives in **e** and **f**. Palladium, copper, magnesium and nickel atoms are represented by dark blue, cyan, orange and yellow polyhedra, respectively, whereas organic ligands are depicted as sticks. Reprinted by permission from Springer Nature Customer Service Centre GmbH: Springer Nature, Nature Materials, The MOF-driven synthesis of supported palladium clusters with catalytic activity for carbene-mediated chemistry, F. R. Fortea-Pérez, M. Mon, J. Ferrando-Soria, M. Boronat, A. Leyva-Pérez, A. Corma, J. M. Herrera, D. Osadchii, J. Gascon, D. Armentano *et al*., Copyright 2017.[10]

Additionally, reactions could be run in flow without additional activation or purification steps of the catalyst and the material was recyclable several times without activity loss. Thus, the material is one of the so far still rare examples where a MOF material surpasses all other catalyst in terms of activity and stability, stressing the vast catalytic potential that lies in ultrasmall, high-precision clusters.

This approach was transferred to a different MOF, $\{Ca^{II}Cu_6^{II}[(S,S)\text{-methox}]_3(OH)_2(H_2O)\}\cdot 16H_2O$, where amino acid derived linkers provided thioalkyl chains dangling into the pores.[11] By infiltration of the pores with K_2PtCl_4, Pt^{2+} ions coordinated to the sulphur groups and reduction produced Pt_2 clusters stabilized on the pore walls similar to the Pd_4@MOF compound. The material $(Pt_2^0)_{0.5}(Pt^{II}Cl_2)@\{Ca^{II}Cu_6^{II}[(S,S)\text{-methox}]_3(OH)_2(H_2O)\}\cdot 15H_2O$ was subjected to thorough characterization, again including a monitoring of the synthetic process by crystal structures. The catalytic performance of Pd_4@MOF could not be matched although the Pt_2@MOF material was active for ammonium cyanide formation from NH_3 and CO, for CO_2 methanation and for ethylene hydrogenation. With the focus on the first reaction, despite a high initial TOF of 1260 h^{-1} under mild conditions, the catalyst is quickly deactivated by formation of platinum cyanide species as evidenced by IR spectroscopy, among others.

3 RESULTS AND DISCUSSION

3.1 Encapsulation of Naked Platinum Clusters in Zeolitic Imidazolate Frameworks

3.1.1 Synthesis and Characterization of $Pt_{12\pm x}$@ZIF-8[1]

Synthesis of *Chini* Clusters

The *Chini* clusters chosen as exemplary systems for the encapsulation in MOFs were first synthesized according to the literature-known procedure by *Longoni et al.* (Figure 13).[54] Starting with $[Pt_{12}(CO)_{24}]^{2-}$, the challenges of solution synthesis quickly became apparent when Na_2PtCl_6 as a precursor was reacted with carbon monoxide in the presence of sodium hydroxide in methanol. The toxic carbon monoxide was bubbled through the Pt precursor solution over several hours through a syringe that was frequently blocked by the precipitating salt. Although the presented synthesis was selective for $[Pt_{12}(CO)_{24}]^{2-}$ and $[Pt_{15}(CO)_{30}]^{2-}$, literature reports the presence of cluster mixtures in many cases. To make the reaction easier to handle and safer by reducing the necessary volume of CO, a procedure of *Dragonetti et al.* was applied, where the *Chini* cluster is synthesized on a silica surface.[62] As reported, only fumed silica by *Evonik* lead to the desired clusters, while other silica batches did not yield the respective products. Nevertheless, also with the appropriate fumed silica system, only $[Pt_9(CO)_{18}]^{2-}$ could be obtained reliably, while the synthesis of $[Pt_{15}(CO)_{30}]^{2-}$ was highly irreproducible and $[Pt_{12}(CO)_{24}]^{2-}$ could not be obtained at all despite several trials.

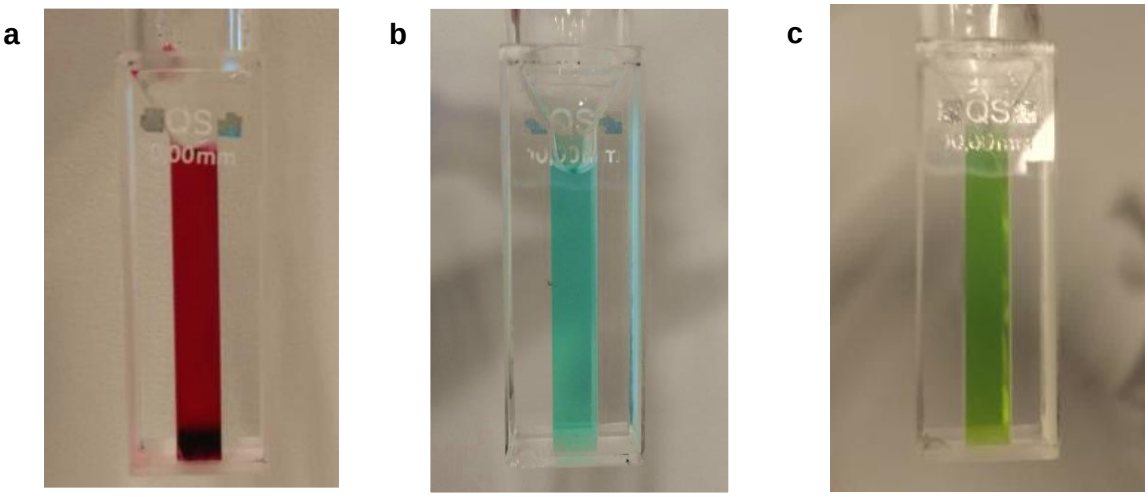

Figure 13: Photographs of (a) red $[Pt_9(CO)_{18}](NBu_4)_2$, (b) blue $[Pt_{12}(CO)_{24}](NBu_4)_2$ and (c) green $[Pt_{15}(CO)_{30}](NBu_4)_2$ in methanol solution.

[1] This chapter is largely based on the publication of K. Kratzl, T. Kratky, S. Günther, O. Tomanec, R. Zbořil, J. Michalička, J. M. Macak, M. Cokoja, R. A. Fischer, *J. Am. Chem. Soc.* **2019**, *141*, 13962.[12]

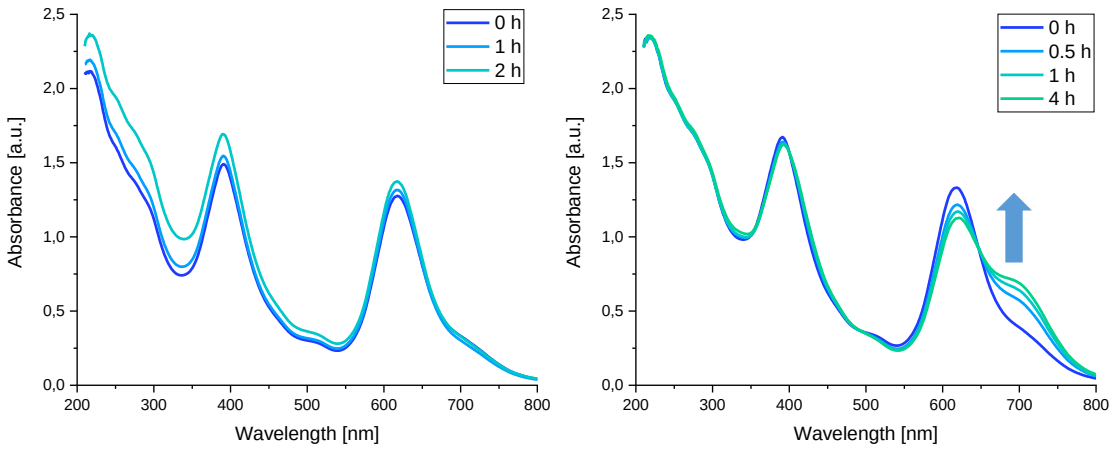

Figure 14: Time-resolved UV/Vis spectra of $[Pt_{12}(CO)_{24}]^{2-}$ after addition of H_2O (*left*) and O_2 (*right*), showing its stability in water as well as the sensitivity towards oxidation.

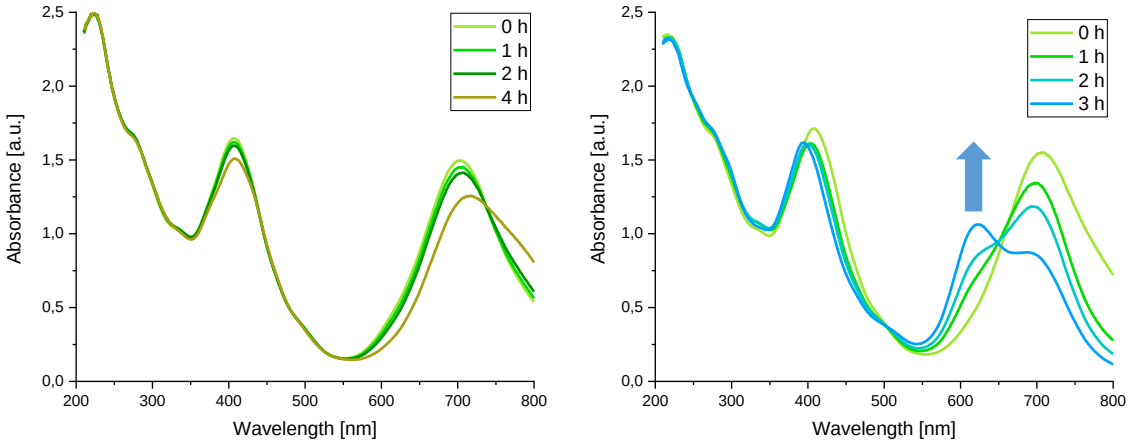

Figure 15: Time-resolved UV/Vis spectra of $[Pt_{15}(CO)_{30}]^{2-}$ after addition of O_2 (*left*) and H_2O (*right*) showing the reduction to $[Pt_{12}(CO)_{24}]^{2-}$ in the presence of water.

IR spectroscopy revealed two intense CO bands for bridging and terminal carbonyl ligands, in the case of $[Pt_9(CO)_{18}](NBu_4)_2$ in the solid state at 1790 cm^{-1} and 1992 cm^{-1}, respectively (Supplementary Figure 1, see experimental part). The two larger clusters' sensitivity towards oxygen and water was investigated with *in situ* UV/Vis experiments, where a defined, small amount of O_2/H_2O was added to a *Schlenk* UV/Vis cuvette and the cluster decomposition was monitored over several hours. $[Pt_{12}(CO)_{24}]^{2-}$ showed good stability towards water but was quickly transformed in the presence of oxygen to the larger $[Pt_{15}(CO)_{30}]^{2-}$ cluster, indicated by the formation of a shoulder in the main UV/Vis band at 620 nm (Figure 14). In contrast, $[Pt_{15}(CO)_{30}]^{2-}$ itself exhibited a different redox behavior, being oxidized only very slowly under atmospheric conditions. In contrast, the addition of water resulted in a reduction with the $[Pt_{12}(CO)_{24}]^{2-}$ band emerging from the main band of $[Pt_{15}(CO)_{30}]^{2-}$ at 706 nm (Figure 15). All transformations also were observable with the naked eye due to an intense color change from $[Pt_9(CO)_{18}]^{2-}$ to $[Pt_{15}(CO)_{30}]^{2-}$ from red over blue to green (Figure 13). For $[Pt_9(CO)_{18}]^{2-}$ with the

main UV/Vis band at 562 nm, the aqueous work-up proved its stability towards water, while a pronounced sensitivity to oxygen resulted in the transformation to $[Pt_{12}(CO)_{24}]^{2-}$ and larger clusters. The latter was observed with the naked eye without extensive UV/Vis studies because of the fast oxidation process that was difficult to follow.

One of the most reliable identification methods for metal clusters is ESI-MS spectroscopy that was also tried with the *Chini* clusters. Despite significant efforts to exclude oxygen and moisture from the measurement to prevent cluster decomposition, in the few obtained spectra, fragmentation was observed that made the identification of single cluster species or mixtures impossible. Carbonyl ligands were easily lost during ionization as shown exemplarily for a measurement with $[Pt_9(CO)_{18}]^{2-}$ (Supplementary Figure 2, see experimental part). Twofold negatively charged fragments can easily be distinguished because the signals of gradual CO loss differ in only 14 m/z instead of 28 m/z for the fragments with one negative charge.

^{195}Pt-NMR measurements of the *Chini* clusters were not successful as no signals could be observed. The tedious nature of NMR spectroscopy of these Pt carbonyl clusters has been reported in literature where triangular Pt units readily exchange and even traces of other cluster nuclearities can cause the complete collapse of sharp NMR signals at temperatures as low as –50 °C.[60] In consequence, ESI-MS and ^{195}Pt-NMR were discarded as reliable methods for cluster identification, and mainly IR and UV/Vis spectroscopy were used throughout this work to determine the integrity of the cluster species.

Encapsulation of $[Pt_9(CO)_{18}]^{2-}$

Due to the stability towards water and the reliable synthesis, we settled for the cluster $[Pt_9(CO)_{18}]^{2-}$, precipitated and isolated as the tetrabutylammonium salt $[Pt_9(CO)_{18}](NBu_4)_2$, to perform encapsulation experiments. Before the actual encapsulation, the synthesis of ZIF-8 from $Zn(NO_3)_2{\cdot}6H_2O$ and 2-methylimidazole (2-mIm) as precursors was performed under *Schlenk* conditions to ensure a compatibility with the oxygen sensitive cluster. The material showed high crystallinity and porosity in PXRD and BET measurements, and comparison with literature-reported diffractograms confirmed the formation of ZIF-8. However, the encapsulation step turned out to be nontrivial because of the cluster's high sensitivity not only to oxygen, but also to the high excess of basic 2-mIm that is needed for self-deprotonation and the precipitation of ZIF-8. This resulted in an oxidation and eventual decomposition of $[Pt_9(CO)_{18}](NBu_4)_2$ while the crystallization process of ZIF-8 was not yet completed. Thus, in all room temperature experiments, either mainly $[Pt_{12}(CO)_{24}](NBu_4)_2$ was encapsulated due to pronounced oxidation or even complete decomposition to large platinum clusters without distinctive UV/Vis signals was observed. When switching to other zinc precursors in the hope of faster crystallization, either no reliable MOF precipitation occurred as observed with $ZnAc_2$, or low solubility in MeOH as in the case of $ZnSO_4$ prevented the synthesis of feasible amounts

of material. According to literature, less reactive zinc precursors were disregarded.[165] Another approach to accelerate the crystallization is to increase the temperature moderately without compromising the integrity of the sensitive platinum cluster. With again $Zn(NO_3)_2 \cdot 6H_2O$ as the precursor, at 50 °C a successful encapsulation of $[Pt_9(CO)_{18}](NBu_4)_2$ in ZIF-8 could be achieved where no or only small $[Pt_{12}(CO)_{24}]^{2-}$ shoulders are observable in DR-UV/Vis spectra of the resulting material $[Pt_9(CO)_{18}](NBu_4)_2$@ZIF-8. The loading of platinum cluster inside the MOF was easily tunable by the amount of cluster applied during the synthesis.

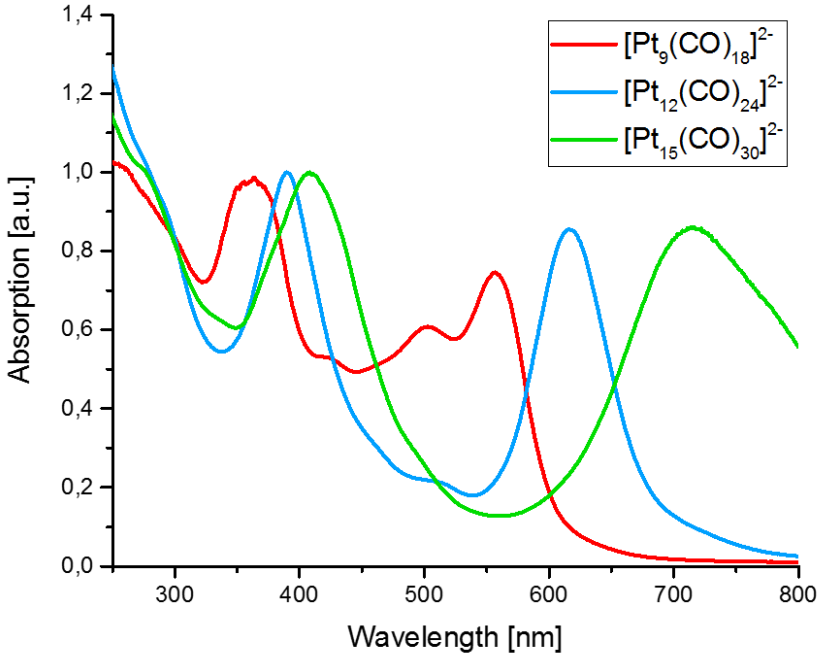

Figure 16: UV/Vis spectra of the *Chini* clusters $[Pt_9(CO)_{18}]^{2-}$, $[Pt_{12}(CO)_{24}]^{2-}$, and $[Pt_{15}(CO)_{30}]^{2-}$ in solution with the characteristic bands at 562 nm, 620 nm and 706 nm, respectively.

The red material $[Pt_9(CO)_{18}](NBu_4)_2$@ZIF-8 is stable under argon, but interestingly, after exposure to air, the color changes to a bright blue that matches the color of the free $[Pt_{12}(CO)_{24}]^{2-}$ cluster. This transition was monitored in DR-UV/Vis spectroscopy, where the characteristic band for $[Pt_9(CO)_{18}]^{2-}$ disappeared over time and was replaced by the one of $[Pt_{12}(CO)_{24}]^{2-}$, indicating the selective and quantitative formation of the next larger cluster (Figure 17). While the latter would continuously oxidize and decompose in solution, encapsulated in ZIF-8 further oxidation is prevented and the resulting $[Pt_{12}(CO)_{24}](NBu_4)_2$@ZIF-8 can be handled and stored under air indefinitely without degradation. Even when stirring for 24 h in boiling H_2O or in 1M NaOH solution, the majority of clusters inside the material was still intact as shown by the unchanged cluster bands in DR-UV/Vis spectra (Supplementary Figure 3 and Supplementary Figure 4, see experimental part). PXRD proved the high crystallinity of the framework when compared with pristine ZIF-8 (Figure 18) and in nitrogen adsorption, a high internal surface area of up to 1698 m^2/g was found, with the BET surface decreasing linearly with the cluster loading (Figure 19).

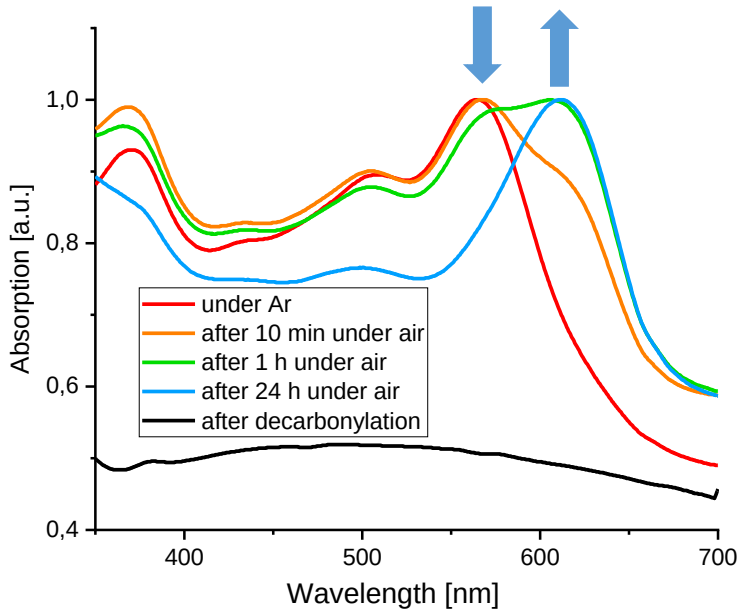

Figure 17: UV/Vis spectra showing the gradual transformation of $[Pt_9(CO)_{18}](NBu_4)_2$@ZIF-8 to $[Pt_{12}(CO)_{24}](NBu_4)_2$@ZIF-8 as observed in DR-UV/Vis spectroscopy. Reprinted with permission from K. Kratzl, T. Kratky, S. Günther, O. Tomanec, R. Zbořil, J. Michalička, J. M. Macak, M. Cokoja, R. A. Fischer, J. Am. Chem. Soc. 2019, 141, 13962. Copyright 2019 American Chemical Society.[12]

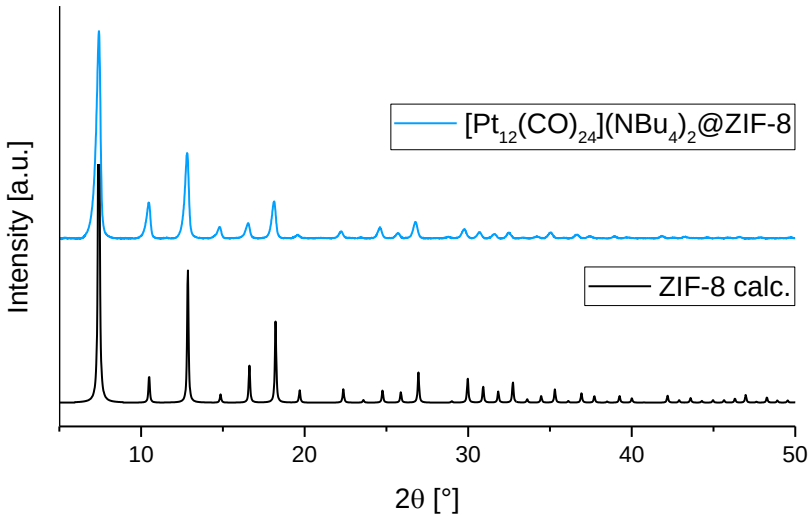

Figure 18: PXRD pattern of $[Pt_{12}(CO)_{24}](NBu_4)_2$@ZIF-8 compared to the calculated pattern of ZIF-8, demonstrating the crystallinity of the encapsulating framework.

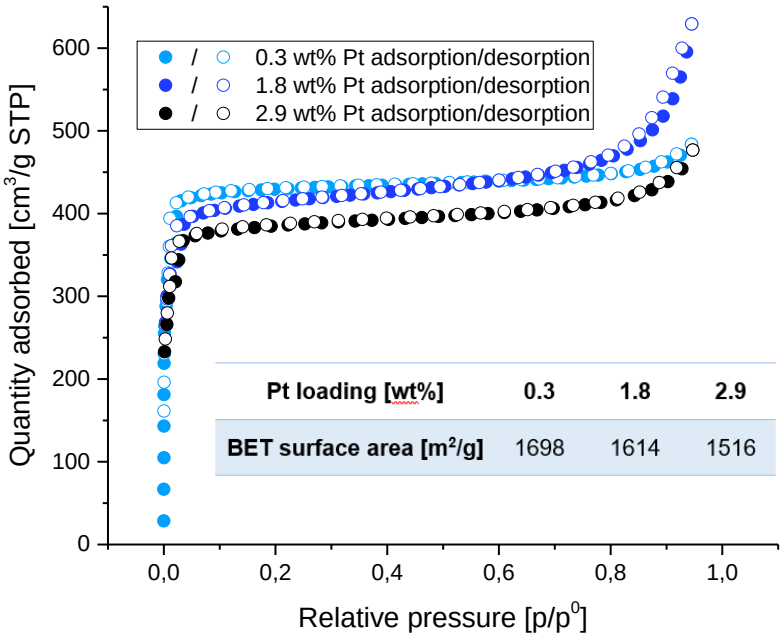

Figure 19: Nitrogen adsorption isotherms for $[Pt_{12}(CO)_{24}](NBu_4)_2$@ZIF-8 with various platinum loadings. All samples exhibit high porosity and the BET surface areas decrease linearly with the Pt loading (see inset).

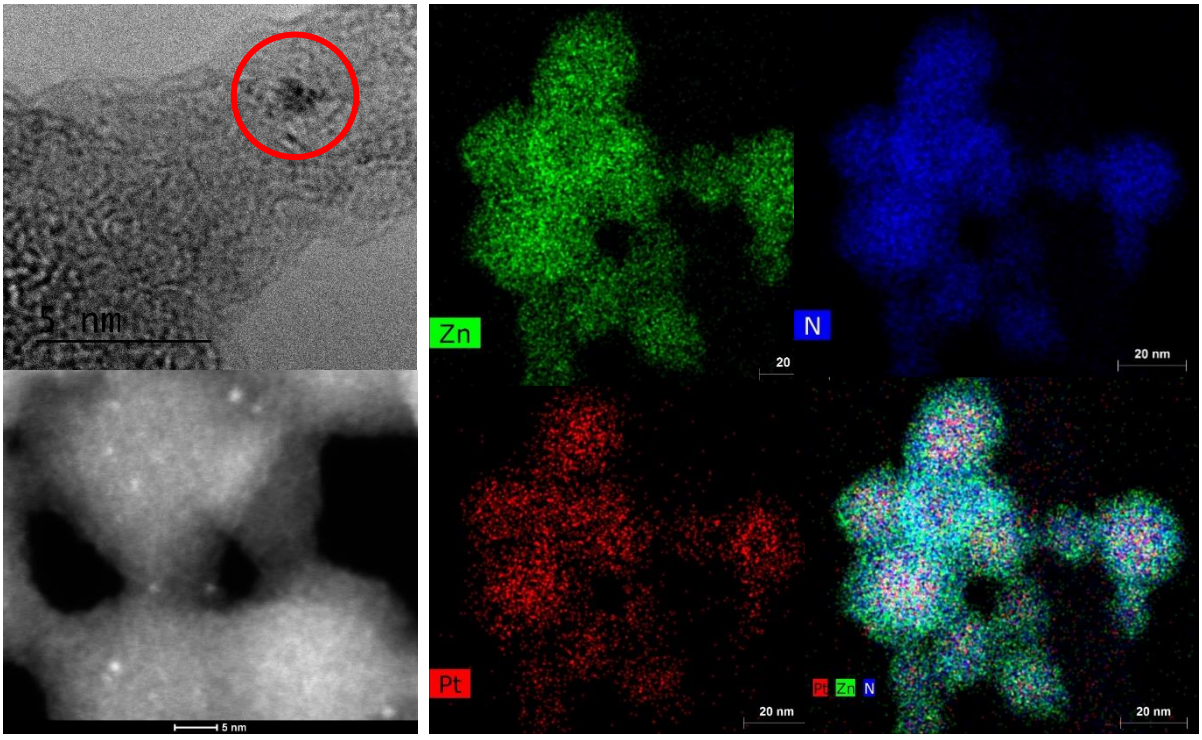

Figure 20: Microscopic imaging analysis of $[Pt_{12}(CO)_{24}](NBu_4)_2$@ZIF-8. *Top left:* HR-TEM image of a single platinum cluster in ZIF-8 with a diameter of around 1 nm. *Bottom left:* HAADF-STEM image of $[Pt_{12}(CO)_{24}](NBu_4)_2$@ZIF-8 where platinum clusters are visible as bright dots. *Right:* HAADF-STEM image of $[Pt_{12}(CO)_{24}](NBu_4)_2$@ZIF-8 with elemental mapping of Zn (green), N (blue) and Pt (red) and overlay picture, showing a homogeneous distribution of platinum throughout the ZIF crystals.

In IR spectra, the bands for bridging and terminal carbonyl ligands are clearly distinguishable at 1868 cm^{-1} and 2051 cm^{-1}, respectively (Figure 21). Microscopic imaging of the clusters in ZIF-8 was challenging due to the destruction of the framework under the high-intensity electron beam that resulted in cluster movement, agglomeration and thus a limited resolution. Nonetheless, HR-TEM and HAADF-STEM images showed no agglomerated species throughout all ZIF-8 crystals and a platinum cluster size of around 1 nm (Figure 20). A more exact determination, even including size distribution histograms, was not conducted due to the aforementioned sensitivity to beam damage. Elemental mappings confirm a homogeneous distribution of Pt and thus the cluster throughout the ZIF.

Decarbonylation of $[Pt_{12}(CO)_{24}](NBu_4)_2$@ZIF-8 to $Pt_{12\pm x}$@ZIF-8

As previously shown for *Chini* cluster mixtures in zeolites and porous silica, the carbonyl ligands can easily be removed from the platinum cluster core at elevated temperatures.[166] An *in situ* IR experiment demonstrated that the CO loss is initiated at 140 °C and completed after 15 min at 200 °C as visible from the disappearance of the bands for both bridging and terminal CO (Figure 21).

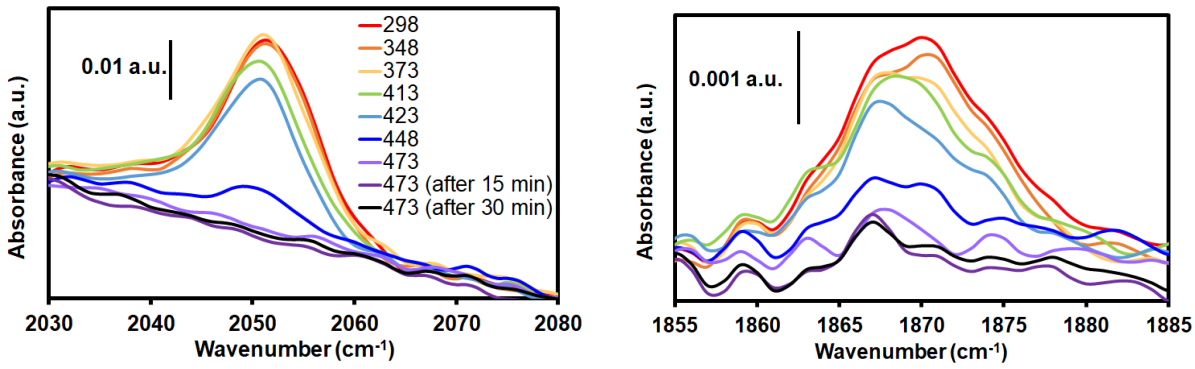

Figure 21: *In-situ* IR measurements of the decarbonylation of $[Pt_{12}(CO)_{24}](NBu_4)_2$@ZIF-8 showing the decrease of the two CO bands at 2051 cm^{-1} and 1868 cm^{-1} upon increasing temperature.

Under this aspect, the decarbonylation of $[Pt_{12}(CO)_{24}](NBu_4)_2$@ZIF-8 is conducted in a sand bath at 200 °C under *Schlenk* vacuum for three hours to ensure complete ligand removal (Figure 22). A comparison of IR spectra of the starting material and the product showed the absence of both CO bands. In *in-situ* IR spectra, a recarbonylation of the clusters was tried with a pressure of 600 mbar (10% CO/He), but the original signals did not reappear even after 15 h. Because a rearrangement of the platinum cluster core to a more stable geometry is expected after ligand removal, the recovery of the original layered structure is not expected. Still, it is surprising that surface adsorbed CO could not even be observed at cryo temperatures (85 K). This fact is attributed to the difficult sample preparation and the resulting low band intensities that make a detection of adsorbed CO impossible. With the naked eye, the decarbonylation process can be followed as a transformation from a blue to a grey powder. Accordingly, the characteristic UV/Vis bands for $[Pt_{12}(CO)_{24}](NBu_4)_2$ disappear and no further

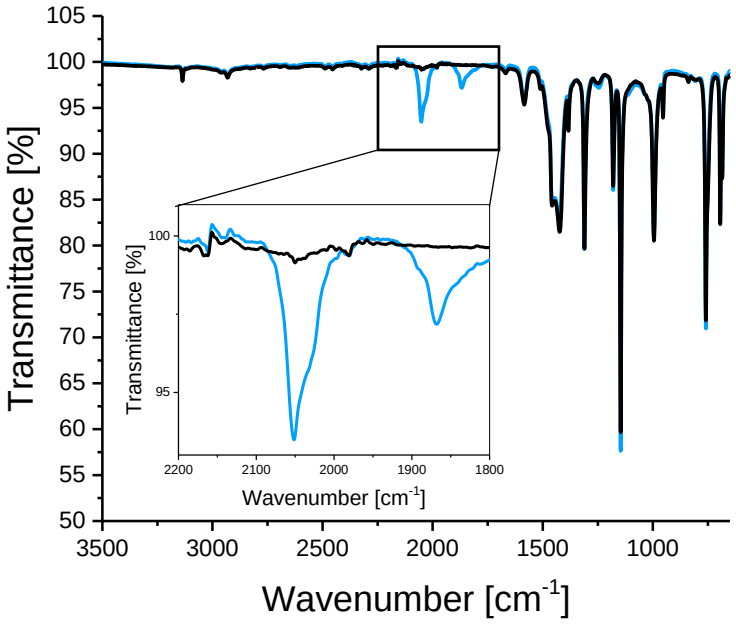

Figure 22: IR spectra of $[Pt_{12}(CO)_{24}](NBu_4)_2$@ZIF-8 before (blue) and after (black) decarbonylation, respectively. CO bands are shown enlarged in the inset, demonstrating complete decarbonylation at the chosen conditions. Reprinted with permission from K. Kratzl, T. Kratky, S. Günther, O. Tomanec, R. Zbořil, J. Michalička, J. M. Macak, M. Cokoja, R. A. Fischer, J. Am. Chem. Soc. 2019, 141, 13962. Copyright 2019 American Chemical Society.[12]

bands are observed due to the absence of the respective electronic transitions after the ligand removal and the collapse of the layered, triangular core structure (Figure 16).

The crystallinity of ZIF-8 is retained after the decarbonylation process as seen in PXRD patterns, and nitrogen sorption showed a remaining high internal surface area of 1643 m^2/g for a loading of 2.9 wt% Pt (determined photometrically, see experimental section) (Figure 23). XPS spectra were difficult to obtain due to the pronounced beam damage that the sample suffered in *in situ* experiments. $[Pt_9(CO)_{18}](NBu_4)_2$@ZIF-8 and $[Pt_{12}(CO)_{24}](NBu_4)_2$@ZIF-8 could not be measured as immediate decarbonylation occurred even with lowest X-ray flux. Therefore, $[Pt_9(CO)_{18}](NBu_4)_2$@ZIF-8 was oxidized in 200 mbar O_2 at room temperature overnight and subsequently decarbonylated in vacuum at 200 °C for three hours in a preparation chamber attached to the XPS analysis chamber. One pair of spin-orbit split peaks is used to deconvolute the rather weak and broad Pt 4f photoelectron signal (Figure 20). The binding energy of 71.1 eV (Pt $4f_{7/2}$) is close to that reported for decarbonylated PtNCs. Zn 2p and N 1s signals coincide with ZIF-8 spectra reported in literature.[167]

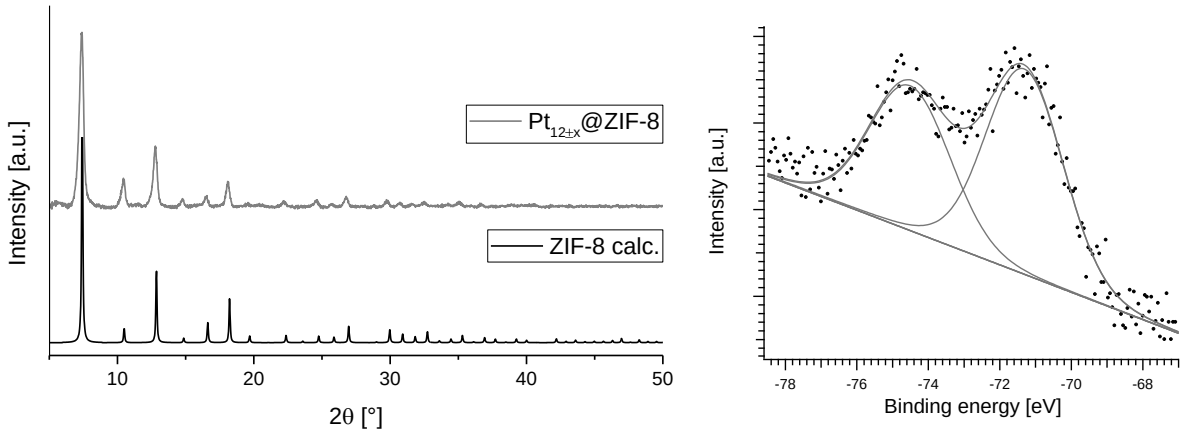

Figure 23: PXRD and XPS measurements of $Pt_{12\pm x}$@ZIF-8. *Left:* PXRD of $Pt_{12\pm x}$@ZIF-8 compared to the calculated ZIF-8 pattern, proving the integrity of the framework after decarbonylation. *Right:* Pt4f region of the XPS spectrum of $Pt_{12\pm x}$@ZIF-8.

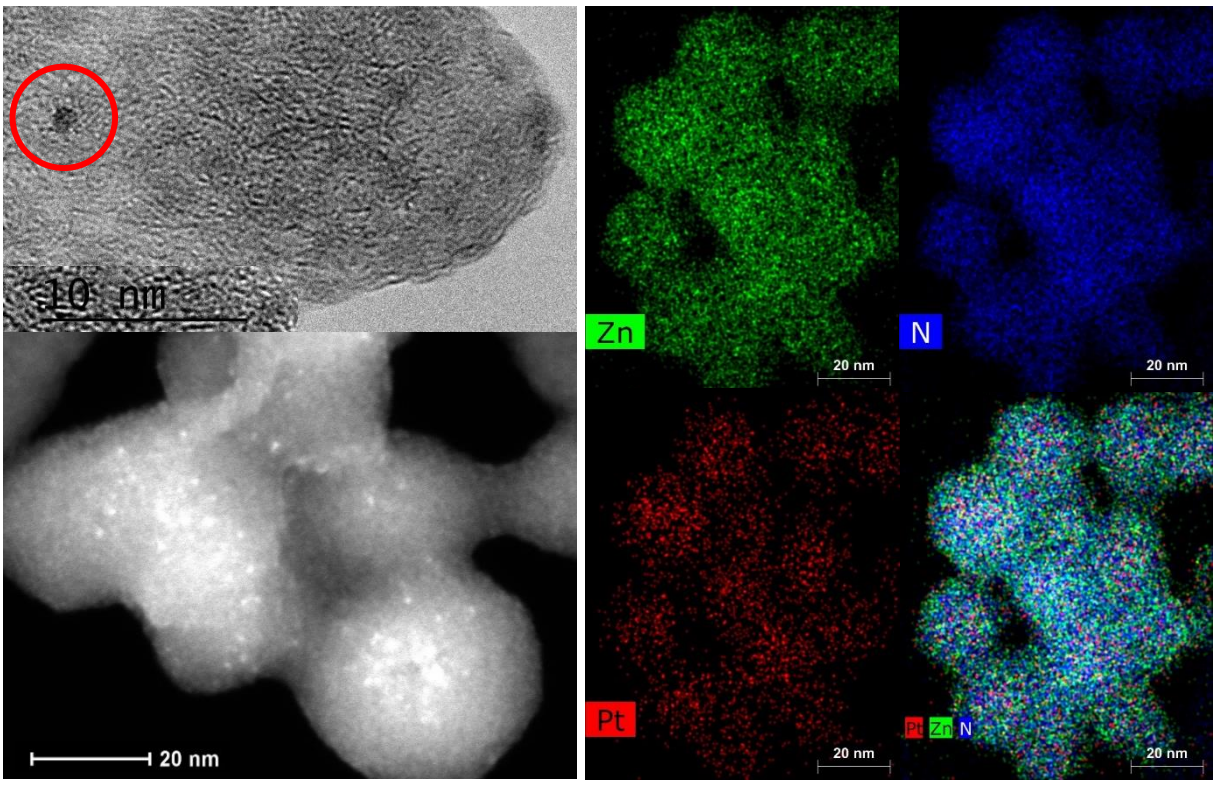

Figure 24: Microscopic images of $Pt_{12\pm x}$@ZIF-8. *Top left:* HR-TEM image of a single Pt nanocluster in ZIF-8 with identical diameter compared to the clusters in $[Pt_{12}(CO)_{24}](NBu_4)_2$@ZIF-8. *Bottom left:* HAADF-STEM image of $Pt_{12\pm x}$@ZIF-8, showing no agglomerates throughout the ZIF-8 crystals. *Right:* HAADF-STEM with elemental mapping of Zn (green), N (blue) and Pt (red) and overlay picture, demonstrating a homogeneous distribution of Pt in ZIF-8.

Microscopic studies of the material $Pt_{12\pm x}$@ZIF-8 demonstrated a successful stabilization even of the ligand-free platinum clusters by ZIF-8 because no agglomerated species were found neither in HR-TEM nor in HAADF-STEM images (Figure 24). The Pt clusters retained their size

of around 1 nm and elemental mapping once more confirmed a homogeneous distribution of Pt clusters in ZIF-8. Unfortunately, atomic resolution which is crucial to obtain a suitable accuracy for conclusive determination of cluster diameters is extremely difficult to achieve due to the instability of ZIF-8 under the electron beam that destroyed the framework upon longer exposure.[168] Therefore, no exact diameters or size distributions could be stated, although when comparing HR-TEM images of the material before and after decarbonylation, no changes in cluster size distribution are observable. A significant degree of sintering can thus be excluded based on HR-TEM and HAADF-STEM pictures, justifying the description of the material as $Pt_{12\pm x}$@ZIF-8, with a small uncertainty x in the range of a few atoms.

Additional investigations towards the exact cluster atomicity with extended X-ray fine structure spectroscopy (EXAFS) failed, that could potentially give the cluster atomicity by determining the average coordination number of Pt. No conclusive data that hinted towards the presence of small Pt clusters could be obtained neither for $[Pt_{12}(CO)_{24}](NBu_4)_2$@ZIF-8 nor for the decarbonylated $Pt_{12\pm x}$@ZIF-8 sample. As the integrity of the Pt carbonyl clusters in the former material could be unambiguously shown in DR-UV/Vis, it is assumed that the samples suffer significant beam damage during the experiment.

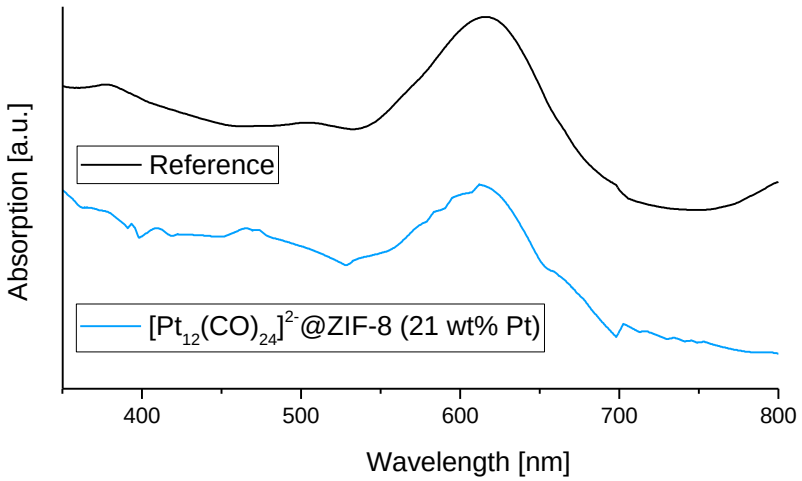

Figure 25: Solid state UV/Vis spectrum of $Pt_{12\pm x}$@ZIF-8 with a maximum platinum loading of 21 wt% compared to $[Pt_{12}(CO)_{24}](NBu_4)_2$@ZIF-8 with lower loading. The band at 612 nm demonstrates the integrity of the clusters, although the black color of the material causes an irregular curve shape.

To probe the stability against sintering even upon close proximity of the clusters, an excess of *Chini* cluster is applied during the encapsulation. Elemental analysis showed a Pt content of 21 wt%, with the clusters' integrity being demonstrated by DR-UV/Vis spectroscopy (Figure 25). The bands in the latter spectrum are irregularly shaped due to the dark, almost black, color of the material. PXRD patterns and BET measurements showed a decreased, but still intact crystallinity, with an internal surface area of 670 m^2/g (Figure 26). The fraction of

occupied pores was calculated by comparing the molar amount of cluster with the number of pores and resulted in a pore filling of 44% for the maximum loading case (calculation see experimental part). This high pore filling ratio explains the decreased crystallinity and surface area, as pore blocking and defect formation occur during MOF crystallization. Additionally, in BET measurements the fraction of non-porous mass increases with a higher cluster loading.

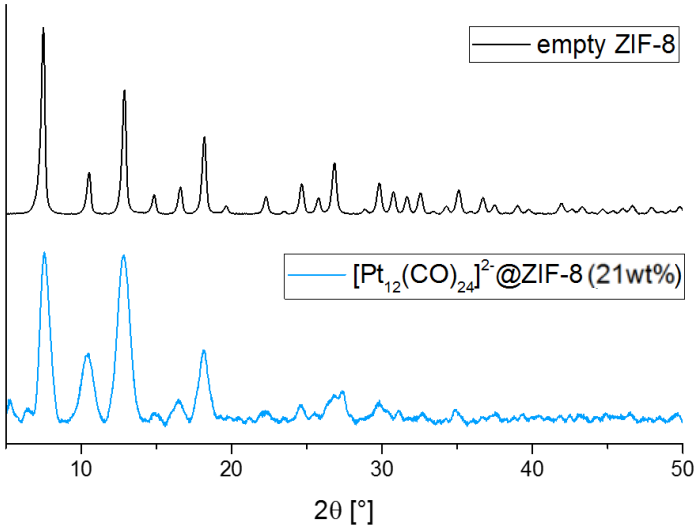

Figure 26: PXRD pattern of $Pt_{12\pm x}$@ZIF-8 with maximum loading of 21 wt% compared to pristine ZIF-8, showing the remaining, if decreased, crystallinity of ZIF-8.

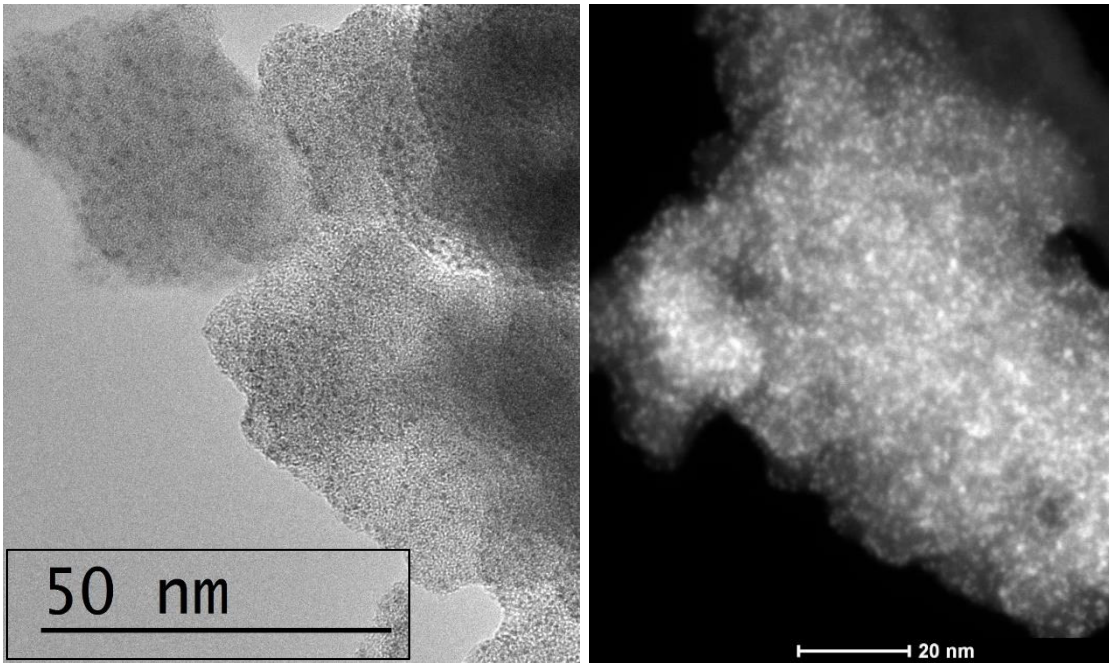

Figure 27: HR-TEM (*left*) and HAADF-STEM (*right*) images of $Pt_{12\pm x}$@ZIF-8 with a maximum platinum loading of 21 wt%. In both images, no agglomerates can be observed despite the close spatial proximity of the clusters, proving an excellent stabilization of the clusters in the MOF pores.

Microscopic experiments further support the integrity of the clusters as no agglomerated species can be found neither in HR-TEM nor in HAADF-STEM images. Although the clusters

are very tightly packed in the framework, the excellent stabilization in the pores of ZIF-8 prevents sintering of any kind (Figure 27). With the intention of using the cluster@MOF material in later catalytic applications, upscaling experiments were conducted to probe the feasibility of the synthesis for large scale applications. The experimental scale was increased eightfold to finally yield 1.80 g of material with a platinum loading of 1 wt%. The integrity of the initial $[Pt_9(CO)_{18}](NBu_4)_2$ cluster in ZIF-8 was even improved because no $[Pt_9(CO)_{18}]^{2-}$/$[Pt_{12}(CO)_{24}]^{2-}$ mixtures were observed as reported for various experiments on the smaller scale. The limiting factor to further increase the scale of the experiment is not the encapsulation procedure, but the cluster synthesis that is time consuming and requires exclusion of oxygen as well as large volumes of solvent.

One question left unanswered is the fate of the alkylammonium cation in the encapsulation and decarbonylation process. Due to the low amount of cluster and the even lower amount of ammonium cations present in the framework, their detection proved challenging. TGA-MS studies were conducted to detect possible decomposition products during the decarbonylation process. In a first experiment, NBu_4Cl was gradually heated to learn about the most intense mass traces during the decomposition that could also be detected way less intensely for $[Pt_{12}(CO)_{24}](NBu_4)_2$@ZIF-8. When comparing NBu_4^+, NBu_3, NBu_2^+ and Bu^+ cations as possible fragments, a TGA-MS measurement showed that the Bu^+ signal is by far the most intense mass and develops at 170 °C with the highest intensity reached at 210 °C (Supplementary Figure 5, see experimental part). NBu_2^+ can be detected in the same range, while the signals for NBu_4^+ and NBu_3 are barely discernible. In consequence, the decomposition of the NBu_4^+ cation in $[Pt_{12}(CO)_{24}](NBu_4)_2$@ZIF-8 is traced by monitoring the Bu^+ signal in TGA-MS (m/z = 57). With normally loaded materials (<10 wt% Pt), no mass signal was detected, but the $Pt_{12\pm x}$@ZIF-8 with maximum loading delivered evaluable results. Around 230 °C and 370 °C, the mass of butyl cations is detected (Figure 28). The first signal is attributed to the decomposition of NBu_4^+ to NBu_3 and a butyl species following a *Hofmann* elimination. This decomposition of tetrabutylammonium salts in ZIF-8 has been previously reported by *Sadakiyo et al.* who infiltrated ZIF-8 with NBu_4OH and observed cleavage of 1-butene, water and CO_2 in TGA-MS.[169] It is unclear if the remaining NBu_3 is removed under *Schlenk* vacuum ($1 \cdot 10^{-3}$ mbar), therefore the experiment was repeated with PBu_4^+ as the counter cation of the *Chini* cluster. While nitrogen is present in large amounts from the imidazole linkers and can therefore not be detected by elemental analysis, with PBu_4^+ the cation is the only source of phosphorous and can selectively be identified. Although ^{31}P-MAS-NMR could not detect any signals due to the low phosphorus concentration, in $[Pt_{12}(CO)_{24}](PBu_4)_2$@ZIF-8 a small content of phosphorous is found by elemental analysis (0.04 wt%), while after decarbonylation of the material, all phosphorous species are completely absent (0.00 wt%). Thus, it is concluded that the decomposition products after butyl cleavage are removed from the framework.

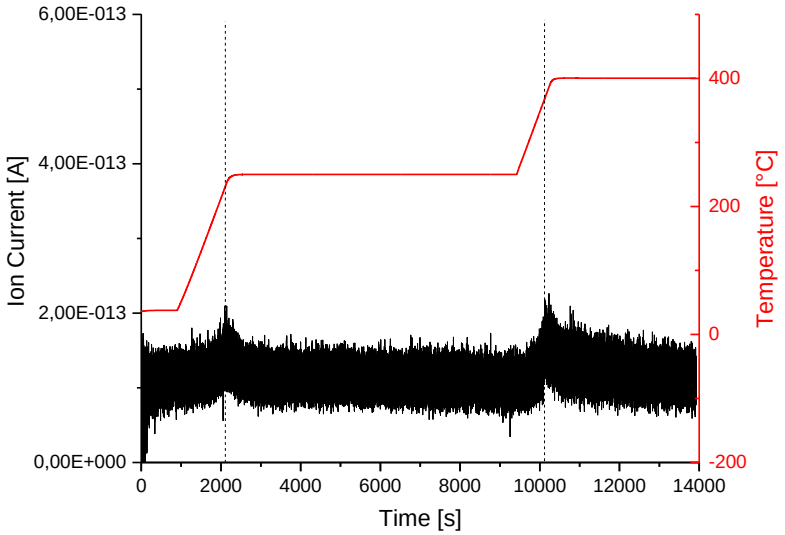

Figure 28: TGA-MS of $Pt_{12\pm x}$@ZIF-8. In the mass spectrum, butyl fragments (m/z = 57) are detected around 230 °C and 370 °C.

$Pt_{12\pm x}$@ZIF-8 as olefin hydrogenation catalyst

Platinum is known for its ability to enhance hydrogen storage performance due to spillover effects. Because of the high porosity of MOFs, they have successfully been applied in a variety of gas storage applications. The combination of platinum and the highly porous and stable ZIF-8 could therefore constitute a promising combination for enhanced performance in hydrogen uptake. $Pt_{12\pm x}$@ZIF-8 showed an excess hydrogen uptake of 0.90 wt% H_2 for a platinum loading of 1 wt%, compared to 0.88 wt% H_2 uptake for pristine ZIF-8 (Supplementary Figure 6, see experimental part). This small improvement of 2.7% could certainly be further increased with a higher platinum loading, but the obtained values are far from high-performance MOF materials with uptakes as high as 8.5 wt%.[121]

Methanol adsorption measurements are an interesting way to estimate the hydrophilicity and reactivity of a porous system before any catalytic experiments. According to *Henry's* law, the amount of adsorbed methanol molecules is proportional to its partial pressure at a given temperature and the interaction between adsorbent and adsorbate is described by *Henry's* constant k_H. When comparing $Pt_{12\pm x}$@ZIF-8 with empty ZIF-8, the maximum methanol uptake as well as the isotherm shape are similar, indicating that the pore is accessible despite the presence of Pt clusters and no change in adsorption mechanism occurs. Thus, the pores are likely unblocked by the incorporation of Pt which is not surprising considering the low platinum loading. The absence of a hysteresis hints to a reversible adsorption and no platinum leaching is evident from the measurement. The most crucial difference between the two compounds is the initial high adsorption (shown in the enlarged region in Supplementary Figure 7, see

experimental part) of $Pt_{12±x}$@ZIF-8 that indicates a stronger interaction between adsorbate and adsorbent and thus an increased reactivity. Calculations of *Henry's* constant for both materials yields a value three orders of magnitude higher for $Pt_{12±x}$@ZIF-8 than for ZIF-8 alone ($1 \cdot 10^{-6}$ mol/Pa vs. $3 \cdot 10^{-3}$ mol/Pa).

With methanol adsorption giving first indications to the accessibility of the clusters in ZIF-8, in a next step $Pt_{12±x}$@ZIF-8 is applied in catalytic hydrogenation experiments. 1-Hexene was chosen as a test substrate due to its small hydrodynamic radius that should enable a penetration into the pores of ZIF-8, and the easy handling in liquid phase. In a *Young* NMR tube, 1 mol% of the catalyst $Pt_{12±x}$@ZIF-8 (1 wt% Pt) was combined with the substrate in toluene-d_8 and pressurized with 1.5 bar hydrogen. The conversion of 1-hexene to hexane was monitored in regular time intervals *via* ^{1}H-NMR spectroscopy (Figure 29). With $Pt_{12±x}$@ZIF-8, a fast and complete conversion in under three hours was observed which results in a high turnover frequency of around 2000 h^{-1}. Despite diffusion limitations of the surrounding MOF, the clusters thus show a high activity in the hydrogenation, albeit homogeneous or supported Pt complex catalysts without diffusion limitations easily reach TOFs of at least one order of magnitude higher.[170] In contrast to the high activity in toluene as the solvent, in chloroform rapid deactivation was observed that is attributed to chlorine poisoning of the Pt catalyst. For comparison, the same reaction was conducted with $[Pt_{12}(CO)_{24}](NBu_4)_2$@ZIF-8, but after the same reaction time, only 24% of 1-hexene are converted (Figure 29). This observation confirms that the removal of the carbonyl ligands from the encapsulated clusters increases the accessibility or abundance of active Pt sites and thus boosts the catalytic activity. The few accessible sites in $[Pt_{12}(CO)_{24}](NBu_4)_2$@ZIF-8 are rapidly saturated by solvent and product molecules, and the reaction approaches the steady state after a short reaction time. Even after catalysis, the distinctive band of the catalyst is intact in DR-UV/Vis spectrum, showing the preservation of most clusters in $[Pt_{12}(CO)_{24}](NBu_4)_2$@ZIF-8. The mentioned saturation of active sites is also evident from the need for activation after one catalytic cycle for $Pt_{12±x}$@ZIF-8 to reach full conversion at the same rate. If an activation under elevated temperatures and vacuum is included after every cycle, the catalyst $Pt_{12±x}$@ZIF-8 could be recycled ten times without any apparent loss in activity.

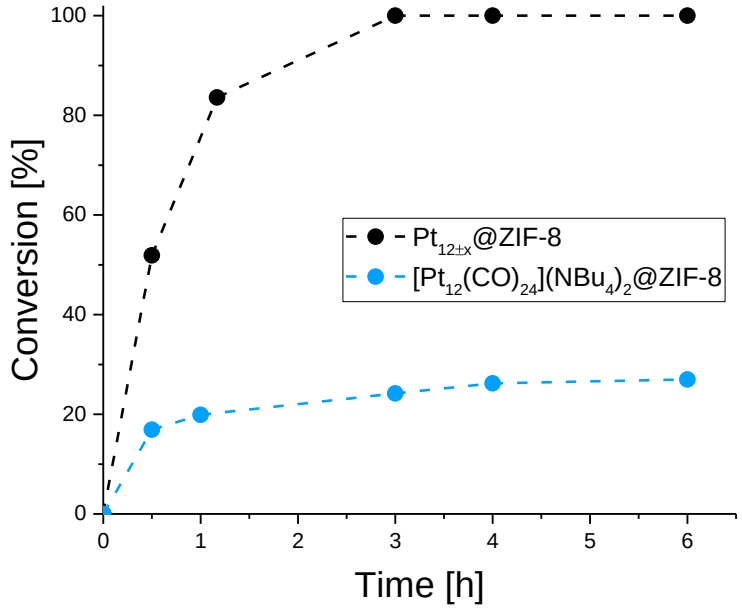

Figure 29: Catalytic hydrogenation of 1-hexene with $[Pt_{12}(CO)_{24}](NBu_4)_2$@ZIF-8 (blue) and $Pt_{12\pm x}$@ZIF-8 (black) as catalysts, demonstrating the increased catalytic activity upon ligand removal from the Pt clusters.

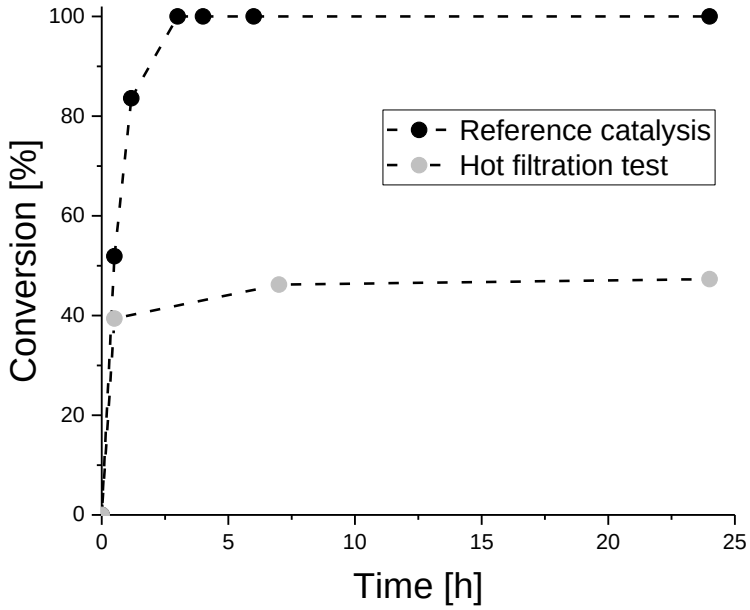

Figure 30: Hot filtration test of $Pt_{12\pm x}$@ZIF-8 compared to full conversion catalysis. The catalyst is separated after 30 min by syringe filtration and centrifugation at a conversion of 39.4%. Upon pressurization with hydrogen, only minimal further conversion is observed.

To exclude leaching of platinum species from the framework, a hot filtration test is conducted where the solid catalyst is separated from the reaction solution at a conversion of 39.4% *via* syringe filtration (PTFE, 0.2 mm) and centrifugation (Figure 30). Only minimally increased conversion of 47.3% after 24 h was observed upon re-adding hydrogen pressure, which could stem from incomplete catalyst removal due to the small ZIF-8 crystallites that are neither retained by the syringe filter nor completely separated by centrifugation, or a small amount of

leached Pt species from surface-near NCs. Either way, it could be shown that the crucial catalytic species are indeed encapsulated platinum clusters in $Pt_{12\pm x}$@ZIF-8 and no solubilized platinum compounds. To additionally evaluate the size exclusion effect that the MOF can contribute to the catalysis, cyclooctene was also applied under the same hydrogenation conditions as 1-hexene with $Pt_{12\pm x}$@ZIF-8 as the catalyst. In contrast to the very fast and complete conversion of the latter, cyclooctene showed only 23% conversion after a prolonged reaction time of 24 h, demonstrating that exclusively substrates which are small enough to penetrate the MOF pores can be converted efficiently. The remaining activity can be explained with the previously conducted hot filtration experiment that hinted towards a small amount of leached platinum species or surface-near platinum clusters that can be reached by the bulkier substrate.

The catalyst $Pt_{12\pm x}$@ZIF-8 is characterized after the catalysis *via* PXRD, XPS and microscopic measurements. PXRD patterns showed an undiminished crystallinity (Figure 31) and XPS confirmed the unchanged nature of the Pt 4f signals (Figure 32). In HR-TEM and HAADF-STEM images, no change in cluster size or morphology was observable and all platinum species retained their size of around 1 nm without agglomeration (Figure 33). With hydrogenation experiments it could thus be confirmed that the Pt clusters in ZIF-8 are still accessible for catalytic conversions, show high activity and the catalyst is easily recyclable.

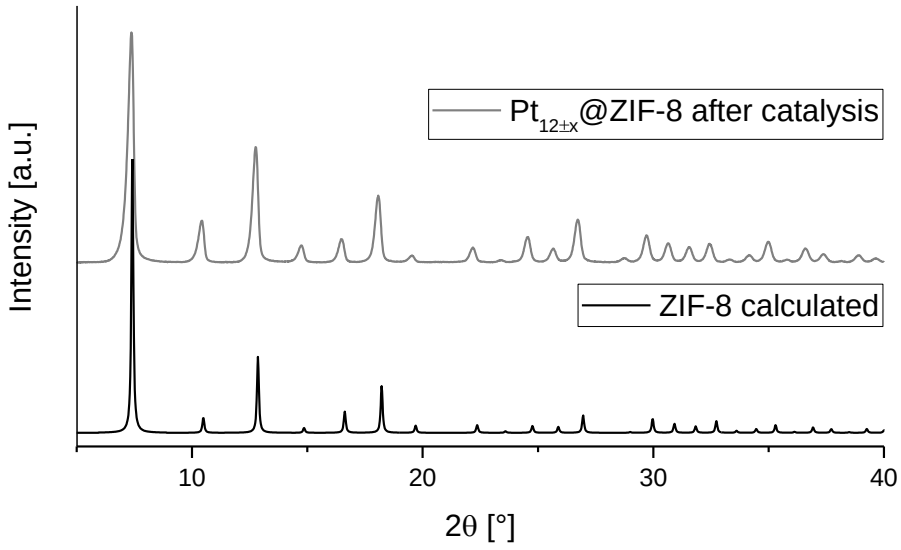

Figure 31: PXRD pattern of $Pt_{12\pm x}$@ZIF-8 after application in hydrogenation catalysis compared to calculated diffractogram of ZIF-8, showing the high crystallinity.

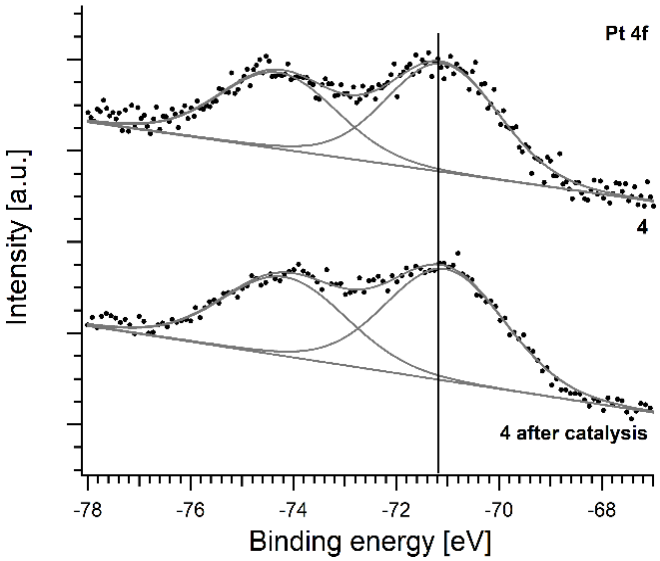

Figure 32: XPS spectra of $Pt_{12\pm x}$@ZIF-8 after application in hydrogenation catalysis. The spectra show no changes before and after catalysis in the Pt 4f signals.

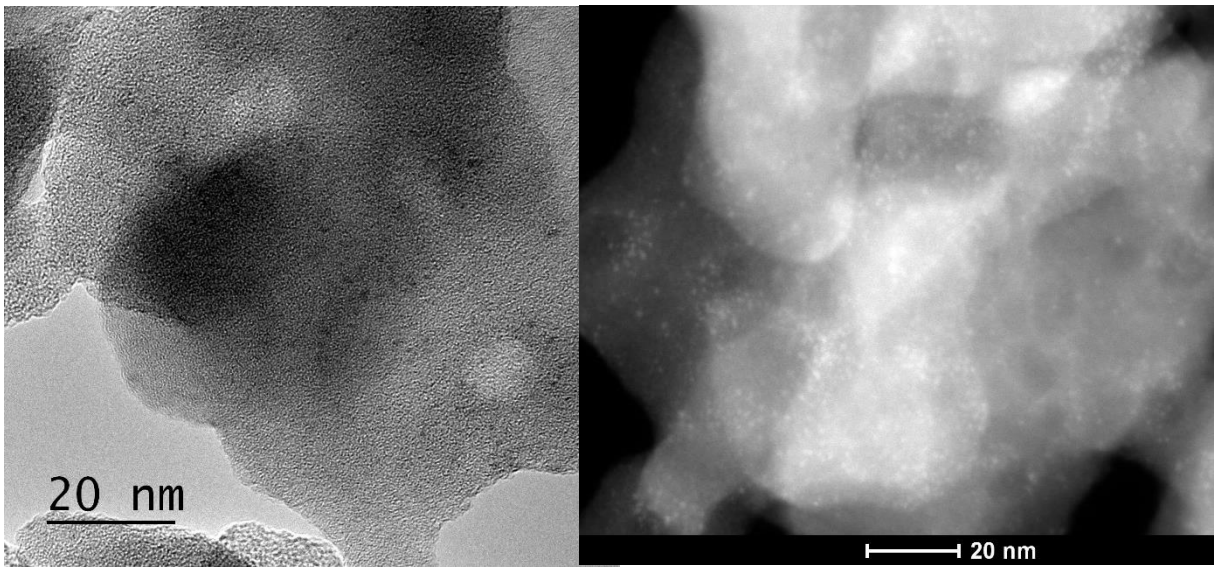

Figure 33: HR-TEM (*left*) and HAADF-STEM (*right*) images of $Pt_{12\pm x}$@ZIF-8 after application in hydrogenation catalysis. Both images show only nanometer-sized platinum clusters and no agglomerates.

3.1.2 $Pt_{12\pm x}$@ZIF-8 for the Oxygen Reduction Reaction[2]

As explained in chapter 2.1.1, the group around *Alessio Gagliardi* developed a method to predict the mass activity of platinum NPs in absolute units of A/mg_{Pt}.[81] When investigating activities of platinum NPs in a range between 1-3 nm in diameter, species with exceptional activity were predicted for diameters of 1.1 nm, 2.07 nm and 2.87 nm. For these diameters, a maximum number of sites with enhanced activity due to a generalized coordination number of $7.5 \leq \overline{CN} \leq 8.3$ was found. The calculations by *Marlon Rück* included a size distribution of 0.1 nm, that diminished the expected mass activities from 2.3 A/mg_{Pt} to 1.25 A/mg_{Pt}, underlining the crucial importance of narrow size distributions to achieve high activities in the ORR.[171] In the calculations, it also became evident that small changes in size can rearrange the surfaces of the NPs considerably (Figure 35). One of the optimal NPs with a diameter of 2.87 nm exhibits highly active sites at step bottoms beside small (111) islands (enclosed by dashed lines in Figure 35) that are stacked on top of (111) surfaces. When changing the NP diameter slightly to 3 nm, less active sites are evident that are located at step bottoms between (111) and (100) surfaces as well as in the center of (111) surfaces.

It is important to mention that the sites fulfilling the criterion of $7.5 \leq \overline{CN} \leq 8.3$ significantly vary amongst each other concerning their predicted activity. Although all are expected to be more active than the Pt(111) surface, sites with $\overline{CN}$ = 8.1 surpass the activity of Pt(111) by more than eight times, while other coordination numbers in the given range only minimally increase the activity of pure Pt. Therefore, the ratio between active sites and the total number of sites can only act as a rough estimate for the predicted activity. When comparing two NPs with diameters of 1.1 nm and 2.07 nm, the former should exhibit three times higher activity than the latter according to the fraction of active sites. In fact, the computationally associated activities for both particles are almost equal. Contrarily, the ratio of active sites of 2.5 nm and 2.87 nm NPs only differs in 5%, but the latter NP has 50% higher predicted mass activity. This highlights that the NP mass activities are controlled by the interplay between a high fraction of active surface sites with $7.5 \leq \overline{CN} \leq 8.3$ and among those, few sites with superior activity. The pronounced structure sensitivity of the Pt NPs increases with smaller diameters around 1 nm, where already small deviations from the predicted optimal size at 1.1 nm can lead to NPs without suitable surface sites as exemplified for the NP with 1.5 nm diameter in Figure 34. In this context, it is important to note that the presented method underestimates the activity for

[2] This chapter is largely based on the publication by B. Garlyyev, K. Kratzl, M. Rück, J. Michalička, J. Fichtner, J. M. Macak, T. Kratky, S. Günther, M. Cokoja, A. S. Bandarenka, A. Gagliardi, R. A. Fischer, *Angew. Chem. Int. Ed.* **2019**, *58*, 9596. All computational screenings were performed and evaluated by Marlon Rück at the chair of Simulation of Nanosystems for Energy Conversion (Prof. Gagliardi), TUM. All electrochemical measurements (cyclovoltammetry, determination of electrochemical activity and stability, …) were carried out and evaluated by Dr. Batyr Garlyyev at the chair of Physics of Energy Conversion and Storage (Prof. Bandarenka), TUM.

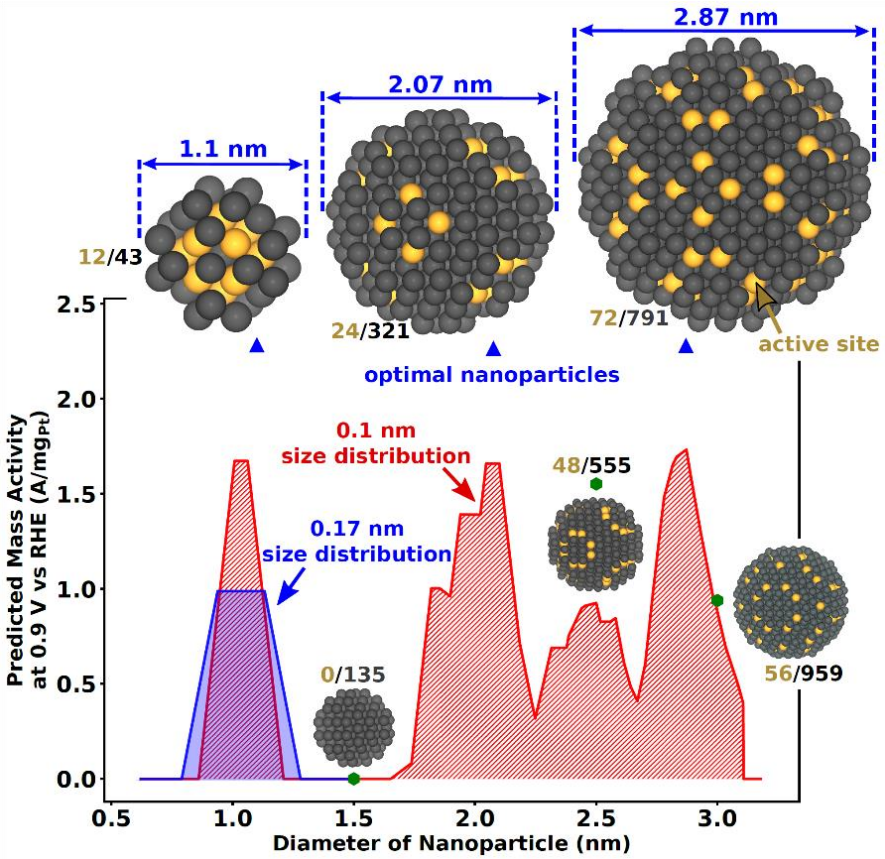

Figure 34: Predicted mass activities plotted versus NP diameters. Optimal NPs (blue triangles) are identified at diameters of 1.1 nm, 2.07 nm, and 2.87 nm. Three less active NPs (green hexagons) are exemplified at 1.5 nm, 2.5 nm, and 3 nm. The red and blue curves show predicted mass activities for NPs with 0.1 nm and 0.17 nm size distribution, respectively. The ratio between active sites with 7.5 ≤ $\overline{CN}$ ≤ 8.3 (highlighted in yellow) and the total number of sites is given for all illustrated NPs. Reprinted with permission of B. Garlyyev, K. Kratzl, M. Rück, J. Michalička, J. Fichtner, J. M. Macak, T. Kratky, S. Günther, M. Cokoja, A. S. Bandarenka, A. Gagliardi, R. A. Fischer, Angew. Chem. Int. Ed. 2019, 58, 9596. Copyright 2019 Wiley-VCH Verlag GmbH & Co. KGaA, Weinheim.[171]

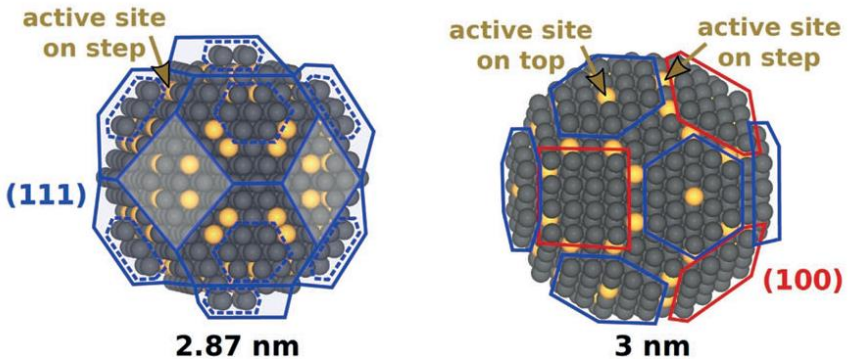

Figure 35: Low-index surfaces (111) (blue) and (100) (red) depicted on the 2.87 and 3 nm NP. On the 2.87 nm, dashed enclosed (111) surfaces are stacked on top of solid enclosed (111) surfaces. Reprinted with permission of B. Garlyyev, K. Kratzl, M. Rück, J. Michalička, J. Fichtner, J. M. Macak, T. Kratky, S. Günther, M. Cokoja, A. S. Bandarenka, A. Gagliardi, R. A. Fischer, Angew. Chem. Int. Ed. 2019, 58, 9596. Copyright 2019 Wiley-VCH Verlag GmbH & Co. KGaA, Weinheim.[171]

NPs without sites with $7.5 \leq \overline{CN} \leq 8.3$. The experimental mass activity of particles like the 1.5 nm one is expected to be low, but not zero as predicted here.

In collaboration with *Dr. Batyr Garlyyev* from the chair of *Prof. Bandarenka*, $Pt_{12\pm x}$@ZIF-8 was tested for its activity in the electrocatalytic ORR. On the lab scale, testing the activities for ORR in a whole-cell setup with a membrane would require high amounts of material and special equipment. A more practical approach was developed with the rotating disk electrode (RDE) where a porous catalyst film is applied on a carbon disk and immersed in the electrolyte (Figure 36). Catalyst powders are dispersed in water or water-alcohol mixtures and then spin-coated or drop-casted directly on the electrode surface. Nafion®, a perfluorinated polymer, is frequently added as a binder to increase the adhesive strength of the catalyst on the electrode. During the measurement, the electrode is rotated at a defined speed to increase the oxygen mass transfer and to eliminate diffusion limitation effects to the catalyst on the surface. Mass activities are determined using the *Koutecky-Levich* equation:[172]

$$\frac{1}{j} = \frac{1}{j_k} + \frac{1}{j_{l,c}} = \frac{1}{j_k} + \frac{1}{0.62nFAC_0^* D_0^{2/3} \nu^{-1/6} \varpi^{1/2}}$$

The current density, kinetic current density and the diffusion-limited current density are denoted as j, j_k and $j_{l,c}$, respectively, where the latter is determined by the number n of electrons transferred, the Faraday constant F, the electrode's surface area A, the concentration of oxygen in solution (C_0^*) and its diffusion coefficient D_0, the kinetic viscosity ν of the solution as well as the rotation speed ϖ of the electrode. Additionally, the measurement outcome depends on the quality of the ink and the catalyst film and even on the drying conditions.[51] For a detailed description of the electrode preparation, see the experimental part.

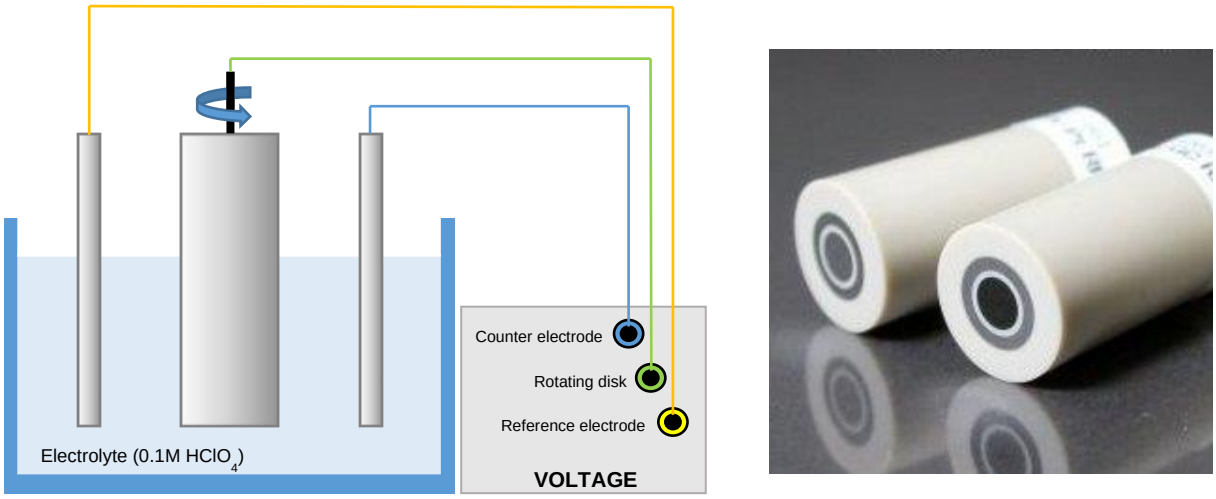

Figure 36: Laboratory setup for the ORR (*left*) with a rotating disk electrode (RDE) (*right*). The latter is immersed in an electrolyte and the voltage is measured upon rotation together with those of a counter and a reference electrode.

On those accounts, $Pt_{12\pm x}$@ZIF-8 was dispersed in methanol and subsequently drop-casted on the glassy carbon of an RDE. When conducting cyclic voltammetry in a basic electrolyte, no activity was observed due to the non-conductive nature of the ZIF that made it impossible for charges to reach the catalytically active platinum centers encapsulated in the non-conductive matrix. In contrast, in an acidic electrolyte (0.1M $HClO_4$) high specific and mass activities were found after an induction period of around 90 cycles (1 h, 50 mV/s, 1600 rpm). The resulting specific activity at 0.9 V vs. RHE amounted to 1.49 A/mg_{Pt} and the respective mass activity to 0.87±0.14 A/mg_{Pt}, which exceeds the values of the commercially used Pt/C catalyst (specific activity of 0.61 mA/cm^2, mass activity of 0.42 A/mg_{Pt}) by more than two times. This was highly surprising, as we initially expected pronounced agglomeration to large NPs when the ZIF matrix is dissolved in acidic media due to the protonation of the imidazolate linkers.[171]

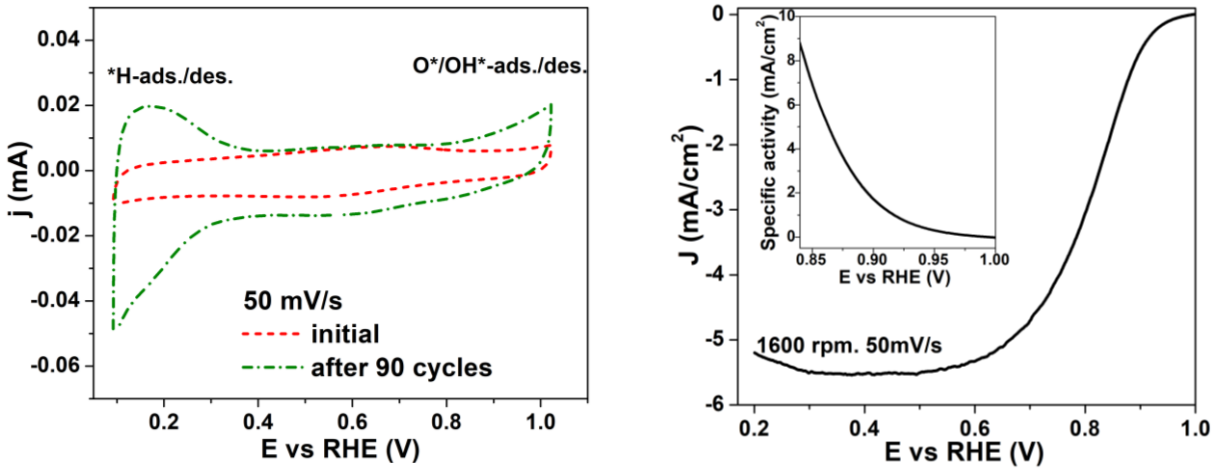

Figure 37: Electrochemical measurements with $Pt_{12\pm x}$@ZIF-8 on a RDE. *Left:* Cyclic voltammogram of the fabricated electrode at the beginning and after 90 cycles in Ar-saturated 0.1M $HClO_4$. Initially, the characteristic features of Pt are not observed because the Pt NPs are encapsulated in non-conductive ZIF-8. ZIF-8 is completely digested after around 90 cycles, and typical H*/O*-adsorption/desorption peaks on the Pt surface are observed. *Right:* Anodic polarization curve (iR-corrected) of the Pt NPs in O_2-saturated 0.1M $HClO_4$. The inset shows the specific activity of Pt NPs plotted against the potential. Reprinted with permission of B. Garlyyev, K. Kratzl, M. Rück, J. Michalička, J. Fichtner, J. M. Macak, T. Kratky, S. Günther, M. Cokoja, A. S. Bandarenka, A. Gagliardi, R. A. Fischer, Angew. Chem. Int. Ed. 2019, 58, 9596. Copyright 2019 Wiley-VCH Verlag GmbH & Co. KGaA, Weinheim.[171]

Because of the extremely small amount of platinum on the electrode surface, analytical characterization of the actual catalytic species is complicated. It was possible to measure XPS spectra directly on the electrode surface thanks to a specially designed sample holder. Therefore, a glassy carbon electrode was coated with the $Pt_{12\pm x}$@ZIF-8 compound and potential cycles between 0.1 to 1 V in 0.1M $HClO_4$ were conducted to achieve dissolution of ZIF-8 and release of the Pt clusters onto the electrode. In the resulting XPS spectrum, no Zn signals could be detected which confirms a complete digestion of ZIF-8 and all synergetic effects of Zn on the catalysis can thus be excluded. Deconvolution of the Pt 4f signal into two

pairs of doublets reveals the presence of metallic Pt (at 70.9 eV and 74.2 eV) as well as PtO and $Pt(OH)_2$ (at 72.5 eV and 75.5 eV). Integration of the peak areas results in 67% Pt(0) and 33% Pt(II) (Figure 33).

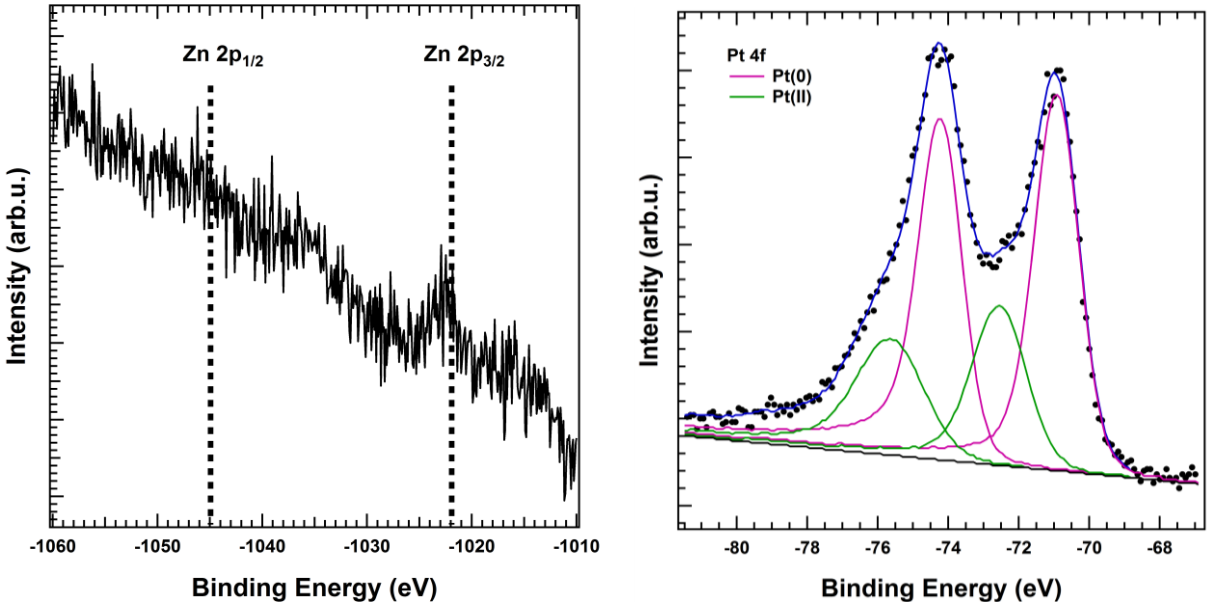

Figure 38: XPS spectrum of the Zn 2p and the Pt 4f region of the $Pt_{12\pm x}$@ZIF-8-coated RDE after 90 cycles between 0.1 and 1 V, showing the absence of Zn species on the electrode surface and the presence of metallic Pt as well as PtO and $Pt(OH)_2$.

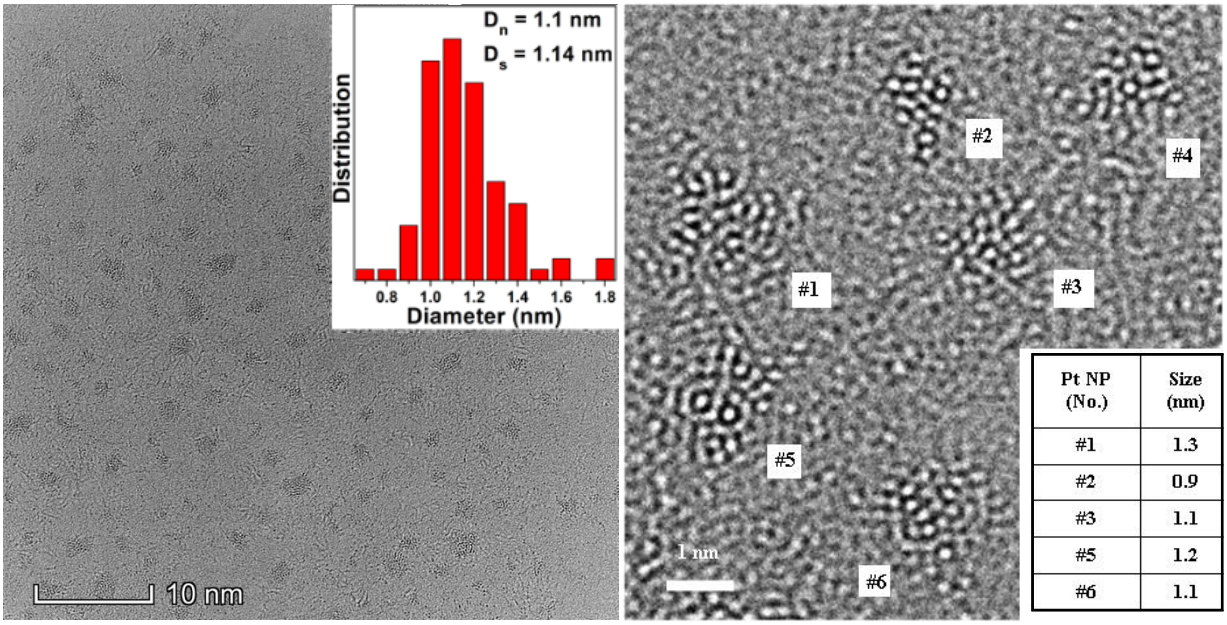

Figure 39: HR-TEM images of $Pt_{12\pm x}$@ZIF-8 on a copper carbon grid after immersion in 0.1M $HClO_4$ to release the clusters from the MOF. *Left:* Overview image, including a size distribution histogram in the inset, showing the size distribution of 1.1±0.1 nm. *Right:* Detailed HR-TEM image of six single Pt NPs with the corresponding diameters. Reprinted with permission of B. Garlyyev, K. Kratzl, M. Rück, J. Michalička, J. Fichtner, J. M. Macak, T. Kratky, S. Günther, M. Cokoja, A. S. Bandarenka, A. Gagliardi, R. A. Fischer, Angew. Chem. Int. Ed. 2019, 58, 9596. Copyright 2019 Wiley-VCH Verlag GmbH & Co. KGaA, Weinheim.[171]

To gain insight into the shape and size of active platinum species on the electrode, a direct imaging of the electrode surface is not possible, as the sample has to be brought onto a TEM grid. Therefore, the $Pt_{12\pm x}$@ZIF-8 ink in methanol was coated onto a holey carbon copper grid that is assumed to have a similar stabilizing effect on the naked platinum compounds as the glassy carbon electrode. Analogously to the electrode, the grid is immersed in 0.1M $HClO_4$ to dissolve the ZIF and the resulting grid is used for HR-TEM imaging (Figure 39). Only a small degree of agglomeration was found, indicating that the platinum clusters are gradually released upon ZIF digestion to form small and high precision NPs with a diameter of 1.1±0.17 nm. For the respective size distribution histogram, the dimensions of over 100 NPs were determined. As the size distribution is very narrow, but still lies above the value incorporated in the theoretical investigations, the calculated activity for platinum NPs with a size of 1.1±0.17 nm is corrected to 0.99 A/mg_{Pt}. This result matches well with the experimentally observed value of 0.87±0.14 A/mg_{Pt} within the limits of uncertainty. Because the calculations are based on perfectly spherical particles, but the experimentally synthesized particles deviate from that shape, calculations are repeated with ellipsoidal NPs (Figure 40). As a result, the previously determined activities were confirmed, and it was concluded that a slight deviation towards ellipsoidal shapes does not change the predicted activity to a significant degree.

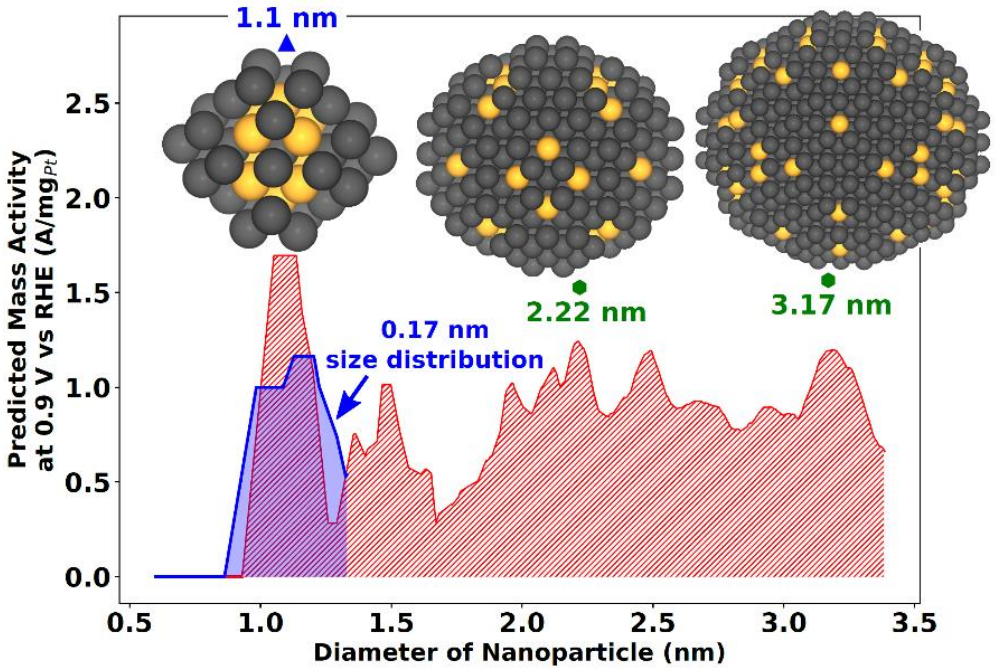

Figure 40: Predicted mass activities plotted versus nanoparticle diameters for ellipsoid NPs, including 0.1 nm (red) and 0.17 nm (blue) size distributions. The ideal NP diameter 1.1 nm is marked with a blue triangle, other ellipsoidal NPs with moderate activities are marked by green hexagons. Reprinted with permission of B. Garlyyev, K. Kratzl, M. Rück, J. Michalička, J. Fichtner, J. M. Macak, T. Kratky, S. Günther, M. Cokoja, A. S. Bandarenka, A. Gagliardi, R. A. Fischer, Angew. Chem. Int. Ed. 2019, 58, 9596. Copyright 2019 Wiley-VCH Verlag GmbH & Co. KGaA, Weinheim.[171]

The presented platinum catalyst is also able to compete with the commercial catalyst in terms of stability. In a durability test of 1500 cycles, only a minimal loss in activity is observed that is comparable to the one of the commercial Pt/C (Supplementary Figure 8, see experimental part). To confirm the $4e^-$ mechanism of the ORR known from the commercial Pt/C catalyst on our ~1 nm sized Pt NPs, the *Levich* plot of both the commercial and the $Pt_{12\pm x}$@ZIF-8-derived sample were plotted (Supplementary Figure 8, see experimental part). As expected, the linear plot does not intercept the y axis at zero, confirming the known sluggish reaction kinetics of the ORR. The number of electrons transferred during the reaction is evident from the slope of the *Levich* plot. Both the commercial and the MOF-derived Pt catalysts show similar *Levich* plot slopes that confirm an analogous mechanism of the ORR for both systems.

In summary, we could derive a highly active electrocatalyst from $Pt_{12\pm x}$@ZIF-8 by depositing the material directly on a glassy carbon electrode where small and narrowly distributed Pt NPs could be obtained by acidic digestion of ZIF-8. The specific and mass activity of this catalyst outperformed the commercial Pt/C catalyst by more than two times and also the catalyst stability was comparably high. The results from the computational screening and the experimental activities coincided with respect to the error interval. The reported activity is the so far highest among pure Pt-based electrocatalysts for the ORR of similar sizes.[171]

3.1.3 Transfer to other Pt_x@ZIF-X Systems

With the established synthetic procedure for $Pt_{12\pm x}$@ZIF-8, we aimed at expanding this general approach to similar metal@MOF systems with the goal to gain a better understanding of the properties of naked clusters and the template effect of the stabilizing ZIF matrix. Before transferring the procedure to completely new systems with other metals, metal alloys or different MOFs, we planned to stay close to the established system. Therefore, the variation of the Pt carbonyl cluster to compounds with different atomicity was planned, as well as the variation of the ZIF by exchanging the methyl group of ZIF-8 with other functional groups.

Variation of ZIF[3]

Varying only the functional group at the imidazole linker of the ZIF initially seemed trivial. However, for most ZIFs, apart from ZIF-8, no synthetic procedures under mild conditions are known to literature. Because solvothermal conditions would compromise the integrity of the *Chini* cluster, syntheses at room temperature and atmospheric pressure needed to be established before further inclusion compounds could be envisaged. An overview of the scope of imidazole linkers tried in the following is given in Figure 41, together with the denomination

[3] This chapter is based on the master thesis of Lorenzo Facco, who was a guest from the University of Padua in the ERASMUS program and stayed at our labs for a duration of six months.

of the respectively obtained ZIF. Next to ZIF-8, a room-temperature synthesis in a suitable solvent is known only for ZIF-90, where pyridine is added to the linker solution as an additional base to boost the deprotonation of the imidazole.[173] Without the base, no crystalline precipitate forms, while with the nitrogen base, ZIF-90 is obtained with high crystallinity and yields of 30%. An adapted approach with triethylamine is targeted for the synthesis of ZIFs with unfunctionalized imidazole, 2-imidazolecarboxyaldehyde, 2-nitroimidazole, 4,5-dichloro-imidazole and benzimidazole. The ZIF screening was monitored with a *PANalytical* Benchtop PXRD that gave patterns of lower quality than the more sophisticated *Empyrean* diffractometer but was sufficient to evaluate the crystallinity of the various ZIFs. All structures were synthesized under air and under inert conditions to ensure the crystallinity of the respective ZIF in the absence of moisture.

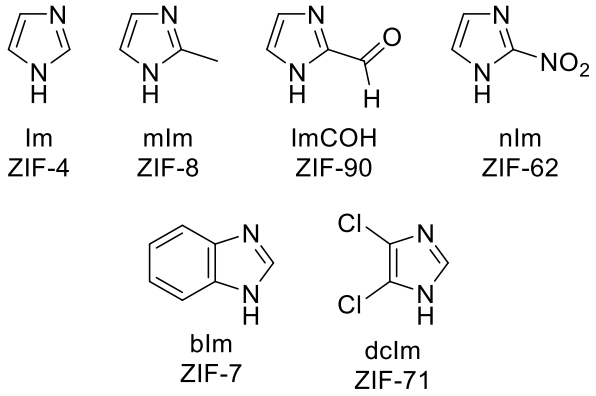

Figure 41: Overview of imidazole linkers with abbreviations and the respective ZIFs.

For the $Zn(Im)_2$ framework, the assignment of the crystalline PXRD pattern to a literature structure was tedious due to the plethora of structures known for the combination of Im and Zn/Co. Nonetheless, the obtained diffractogram was consistent with a $Zn(Im)_2$ structure reported by *Tian et al.* (Supplementary Figure 9, see experimental part). It is noteworthy that no reflections are visible in the range from 5° to 14° and the structure is denoted as ZIF-4 in this work, because the actual structure was not separately named and ZIF-4 is the most common $Zn(Im)_2$ compound. Despite its crystalline structure, the $Zn(Im)_2$ material showed no porosity in nitrogen adsorption experiments. With the chloride-functionalized linker dcIm, the few observed reflections can be assigned to ZIF-71, but a large fraction of the product is amorphous as deduced from the low signal intensity and the - compared to ZIF-8 - low BET surface area of 763 m^2/g (Supplementary Figure 10, see experimental part). Thus, both ZIF-4 and ZIF-71 are discarded as a stabilizing matrix for Pt clusters. With the bIm linker, a pattern with sharp reflections was obtained in a ZIF synthesis under air that matched the one of ZIF-7 reported by *Park et al.* (Supplementary Figure 11, see experimental part).[145] Unfortunately, these results could not be transferred to inert conditions, where only amorphous product was

obtained. Further optimization to preserve the crystallinity also in the synthesis under argon would be necessary and nitrogen adsorption was not carried out with the amorphous material.

Sharp reflections were observed when applying nIm in a base-assisted ZIF synthesis, but no literature-known patterns for Zn-based MOFs matched to the measured one. Only the framework $Co(nIm)_2$, denoted as ZIF-65, coincides with the observed diffractogram, although some peak intensities deviate from the calculated pattern (Figure 42). Therefore, it is assumed that the Zn analogue of ZIF-65 with a sodalite (SOD) topology was synthesized that is very common in ZIF structures. Despite the high crystallinity observed in PXRD, BET measurements revealed a surface area of only 333 m^2/g that falls short of the extremely high porosity of most other ZIFs (Supplementary Figure 12, see experimental part). As a second successful ZIF synthesis, the synthesis of ZIF-90 with ImCOH as a linker could be established with high crystallinity under atmospheric as well as under inert conditions (Figure 42). Nitrogen adsorption revealed a surface area of 949 m^2/g that lies slightly below the literature value of 1250 m^2/g that was reported for a solvothermally synthesized ZIF (Supplementary Figure 12, see experimental part). With a small library of room-temperature ZIF syntheses in hand, the encapsulation experiments were conducted only with ZIF-65 and ZIF-90 due to their high crystallinity and interesting nitro and aldehyde functionalities.

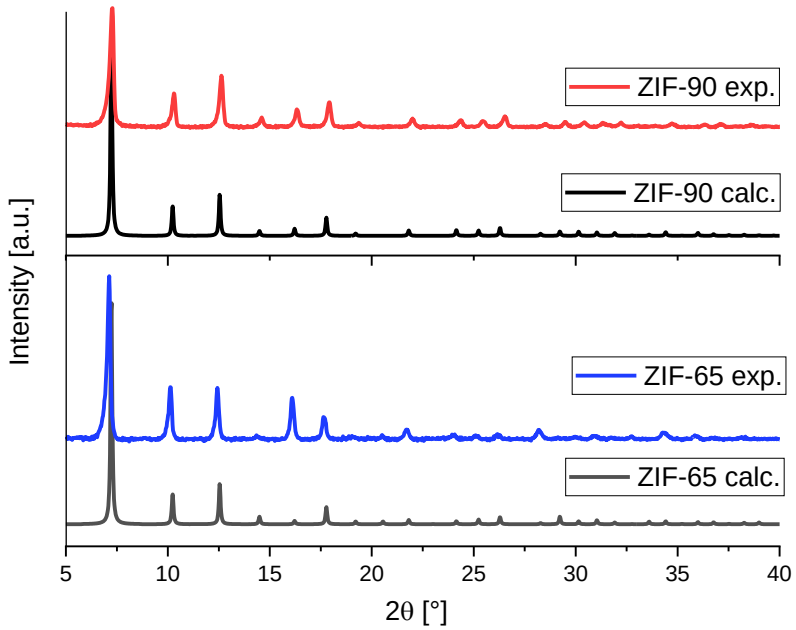

Figure 42: Experimental PXRD patterns of ZIF-90 and ZIF-65 compared to calculated patterns, showing the crystallinity of both frameworks.

The first encapsulation experiment with $[Pt_9(CO)_{18}](NBu_4)_2$ in ZIF-65 did not yield the desired scaffolding product. Instead, the deeply red supernatant after MOF centrifugation indicated an unsuccessful encapsulation. Accordingly, DR-UV/Vis spectra did not show the characteristic band of the Pt_9 cluster or any oxidation products. The absence of carbonyl bands in IR spectroscopy excluded the presence of larger Pt carbonyl cluster species. Possible reasons

could be the smaller pore diameter of only 10.4 Å or insufficient interactions between the clusters and the framework during precipitation that could also stem from the low observed surface area.

In contrast, the encapsulation of $[Pt_9(CO)_{18}](NBu_4)_2$ in ZIF-90 resulted in a pale red precipitate, while after centrifugation, the supernatant again exhibited a dark red color. This indicated that the majority of the cluster stayed in solution and was not integrated in ZIF-8. Indeed, after washing and drying of the solid, in DR-UV/Vis spectroscopy only an extremely weak band was observed, that nonetheless corresponded to the intact Pt_9 cluster (Figure 43). Elemental analysis revealed a Pt content of only 0.4 wt% in the inclusion compound that cannot be attributed to a change in pore diameter because ZIF-90 and ZIF-8 exhibit nearly identical pore dimensions (11.2 Å vs. 11.6 Å).[13] Alternatively, it was suspected if the extremely fast precipitation of ZIF-90 in the presence of NEt_3 did not leave enough time for the framework to assemble around the clusters because the solid crashed out of solution instantly. Therefore, a slow addition either of the solution with base and linker was tried, or the base was added together with the cluster solution to a mixture of the zinc precursor and 2-mIm in methanol. Both approaches to achieve a gradual formation of ZIF-90 led either to cluster decomposition or did not improve the Pt content in the final product. A second idea to explain the incomplete encapsulation was the steric demand of the amine that could block the MOF pores and therefore inhibit the incorporation of the cluster. Because ZIF-90 also formed with high crystallinity when using sodium hydroxide as a base instead of NEt_3, pore blocking should be prevented with this small base. Nonetheless, no higher amount of the *Chini* cluster was found in ZIF-90 also when using NaOH as a base. To finally confirm that the external base is not responsible for the inhibited incorporation of Pt_9, the procedure with NEt_3 is transferred back to the established ZIF-8 system. Although the crystallinity of ZIF-8 is decreased with NEt_3 present in the synthesis, a complete encapsulation of the cluster was immediately evident after centrifugation, because of the colorless supernatant and the dark red-purple precipitate. This only leaves the altered electronic and geometric properties of the ZIF-90 pore as the reason for the poor encapsulation, although the effect is not understood to date.

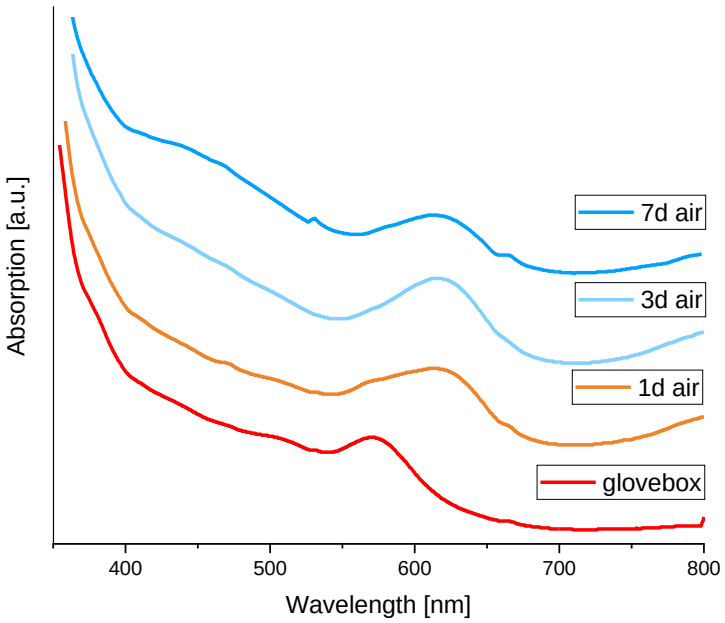

Figure 43: DR-UV/Vis spectra of $[Pt_9(CO)_{18}](NBu_4)_2$@ZIF-90 under inert conditions and after exposure to air for various lengths of time, showing the slow oxidation to $[Pt_{12}(CO)_{24}](NBu_4)_2$@ZIF-90.

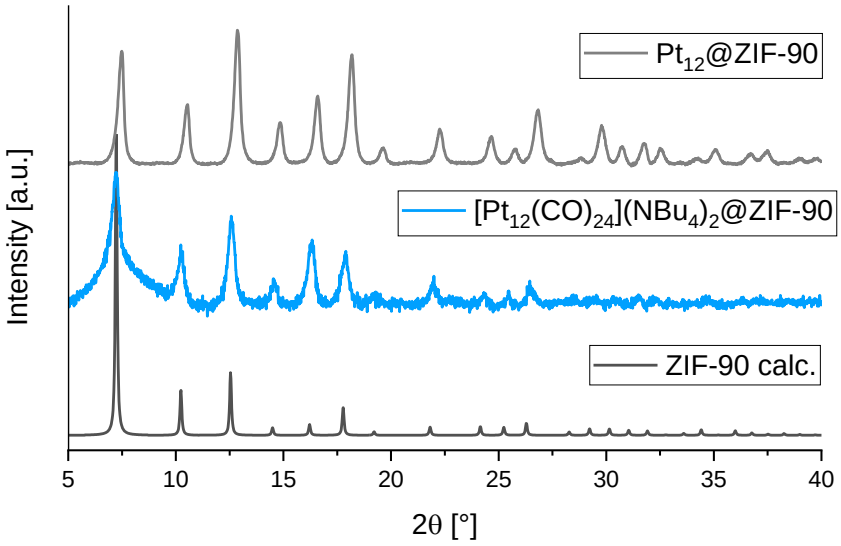

Figure 44: PXRD of $[Pt_{12}(CO)_{24}](NBu_4)_2$@ZIF-90 before and after decarbonylation compared to calculated pattern of ZIF-90, showing the intact crystallinity of the framework.

Despite the pending problem of low loadings of $[Pt_9(CO)_{18}](NBu_4)_2$@ZIF-90, we observed an enhanced stabilization of the cluster compared to the inclusion compound in ZIF-8 (Figure 43). While the latter showed complete oxidation to $[Pt_{12}(CO)_{24}](NBu_4)_2$@ZIF-8 in the course of only ten minutes, the analogous compound $[Pt_{12}(CO)_{24}](NBu_4)_2$@ZIF-90 was only formed after several days under atmospheric conditions as observed in DR-UV/Vis spectroscopy. This enhanced stability is attributed to the better interaction of the clusters with the aldehyde functionalities dangling into the pores of ZIF-90. This interaction likely decreases the mobility

of triangular Pt subunits and hampers the transformation to the larger *Chini* cluster under oxidizing conditions.

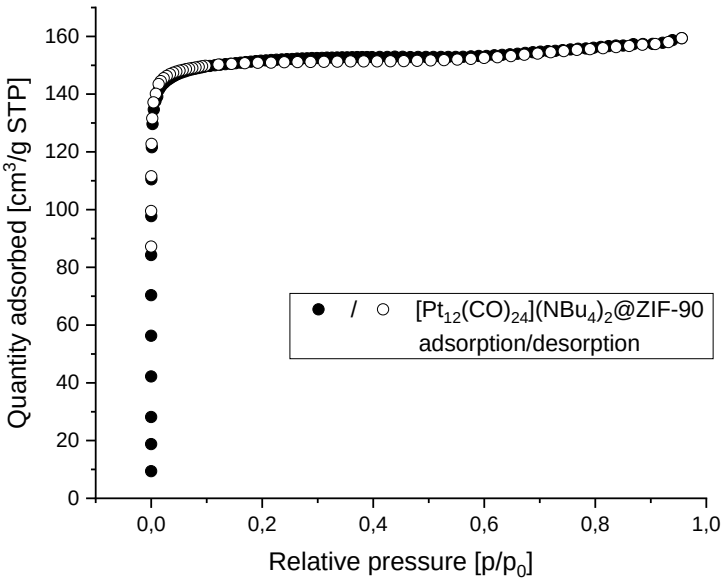

Figure 45: BET isotherm of $[Pt_{12}(CO)_{24}](NBu_4)_2$@ZIF-90 demonstrating the intact porosity of the framework with an internal surface area of 619 m^2/g.

ZIF-90 has been previously reported by our group to have a directing effect towards metal nanospecies, in this case the control of size distribution in a “ship-in-bottle” approach for Au@ZIF-90 materials.[9] $[Pt_{12}(CO)_{24}](NBu_4)_2$@ZIF-90 was further analyzed with PXRD and nitrogen adsorption and showed a high crystallinity and internal surface area of 619 m^2/g (Figure 44, Figure 45). Due to the low cluster loading and the resulting low intensity, no CO bands could be detected in IR spectroscopy. Nonetheless, a thermal decarbonylation was conducted to remove the stabilizing ligands analogously to the ZIF-8 material. The PXRD pattern confirmed the integrity of the framework (Figure 44), while BET measurements need to be repeated with larger sample amounts. HR-TEM and HAADF-STEM with elemental mapping confirmed the absence of any agglomerates and the homogeneous distribution of the clusters with a diameter around 1 nm throughout the framework (Figure 46). As expected, due to the rapid synthesis under harsh basic conditions, the ZIF crystals are poorly faceted and partially intergrown.

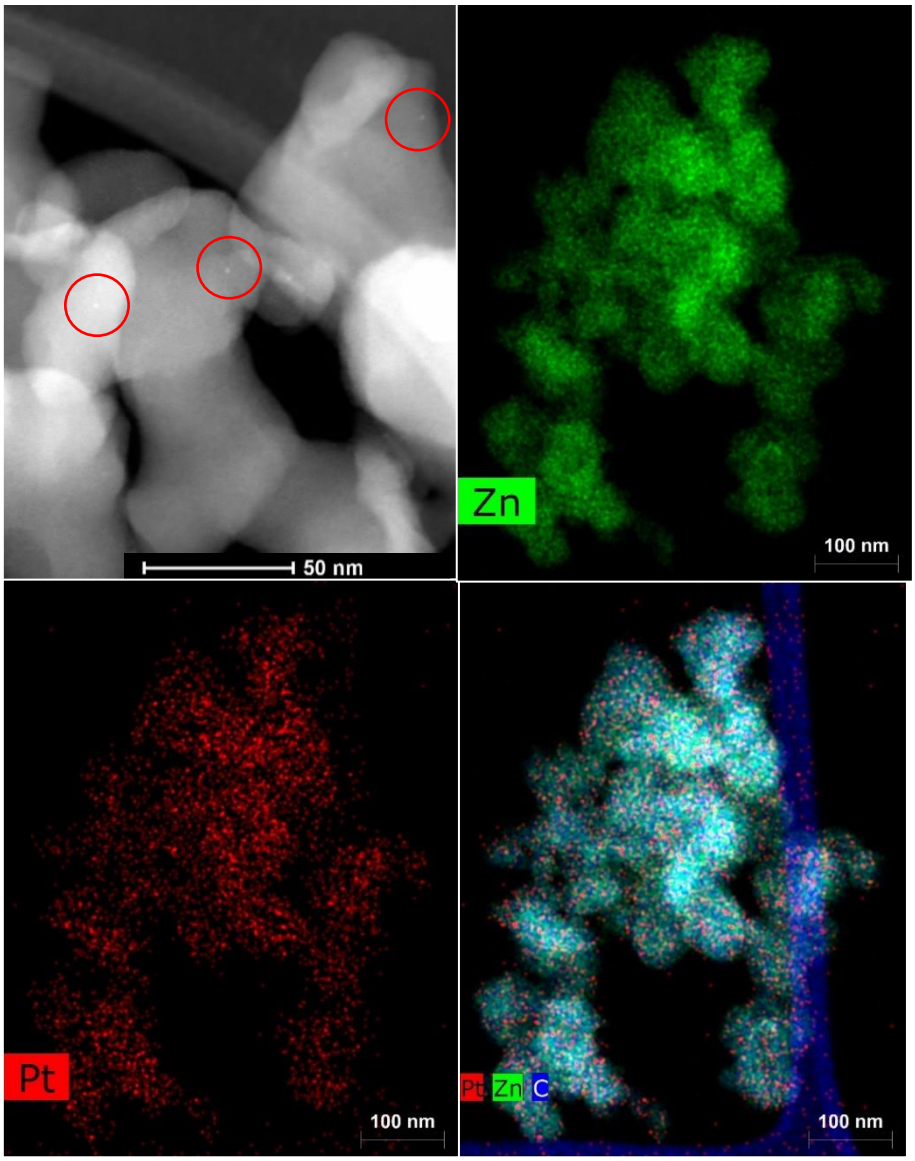

Figure 46: *Top left:* HAADF-STEM image of $Pt_{12\pm x}$@ZIF-90 with some Pt nanoclusters seen as bright spots highlighted by red circles. *Top right and bottom:* HAADF-STEM with elemental mapping of $Pt_{12\pm x}$@ZIF-90 with Zn, Pt and C in green, red and blue, respectively.

Although the Pt loading in ZIF-90 could not be increased to feasible amounts, basic catalytic studies to assess the accessibility of the Pt clusters in the framework were conducted. All hydrogenation reactions were carried out in *J. Young* NMR tubes under 1.5 bar of H_2 at room temperature for 24 h, after which conversions were checked *via* ^{1}H-NMR spectroscopy. The standard hydrogenation procedure of 1-hexene to hexane applied for $Pt_{12\pm x}$@ZIF-8 did not show any conversion with $Pt_{12\pm x}$@ZIF-90 as the catalyst, even when increasing the catalyst loading to 2 mol%. This result was attributed to the more hydrophilic, aldehyde functionalized ZIF-90 scaffold that does not allow the diffusion of 1-hexene to the catalytically active Pt centers. To overcome this problem, the more hydrophilic methyl vinyl ketone (MVK) was chosen as a substrate and indeed, with a catalyst loading of 1.3 mol% complete conversion was reached after 24 h. In contrast, the even more hydrophilic acrylic acid was converted much

more slowly, with a conversion of 24% under the same conditions. This indicates, that $Pt_{12\pm x}$@ZIF-90 will preferentially convert substrates in a certain range of hydrophilicity that optimally fits to the one of the ZIF-90 matrix due to enhanced diffusion. To corroborate these results, further catalytic studies with substrate mixtures could be carried out. Nonetheless, it was shown that the small amount of encapsulated Pt clusters is accessible for catalytic conversions.

Because the variation of the linker in the encapsulating matrix turned out to influence the system significantly and prevent efficient encapsulation, a second approach targeted the metal node. In ORR, many highly active catalyst systems contain a combination of Pt and Co.[71] With the Pt cluster encapsulated in a Co-containing matrix, the material could possibly be pyrolyzed to create Pt/Co sites to obtain potent catalysts. Following this idea, ZIF-67 with a structure analogous to ZIF-8 is assembled from 2-mIm and $Co(NO_3)_2 \cdot 6H_2O$ to yield $Co(2\text{-mIm})_2$. The first synthesis approach without additional base at room temperature in methanol yielded a bright purple precipitate, but PXRD revealed only amorphous material. Therefore, a literature-known synthesis under mild conditions with additional base NEt_3 was carried out. When combining the imidazole linker solution with the external base and the cobalt nitrate solution, immediately a bright purple suspension forms, whose PXRD pattern after washing and drying matches to calculated diffractogram of ZIF-67 (Figure 47). The encapsulation of $[Pt_9(CO)_{18}](NBu_4)_2$ in ZIF-67 was carried out analogously to the established ZIF-8 encapsulation. The first centrifugation of the purple, opaque suspension showed an almost colorless supernatant, indicating a successful encapsulation. However, the integrity of the incorporated cluster was not verifiable with DR-UV/Vis spectroscopy because the bands of the bright purple cobalt ZIF overlap with the characteristic cluster bands. Under air, no band shifts are observed due to possible cluster oxidation (Supplementary Figure 13, see experimental part).

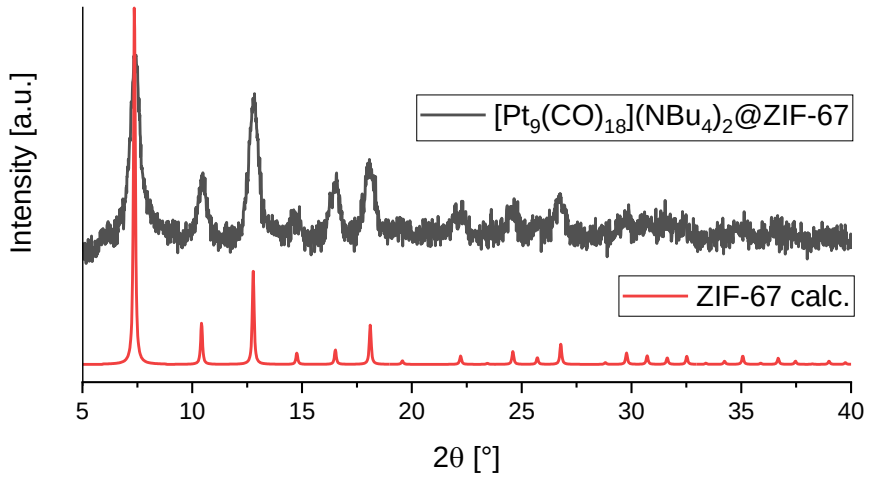

Figure 47: PXRD pattern of $[Pt_9(CO)_{18}](NBu_4)_2$@ZIF-67 compared to the calculated pattern of ZIF-67 showing the crystallinity of the framework.

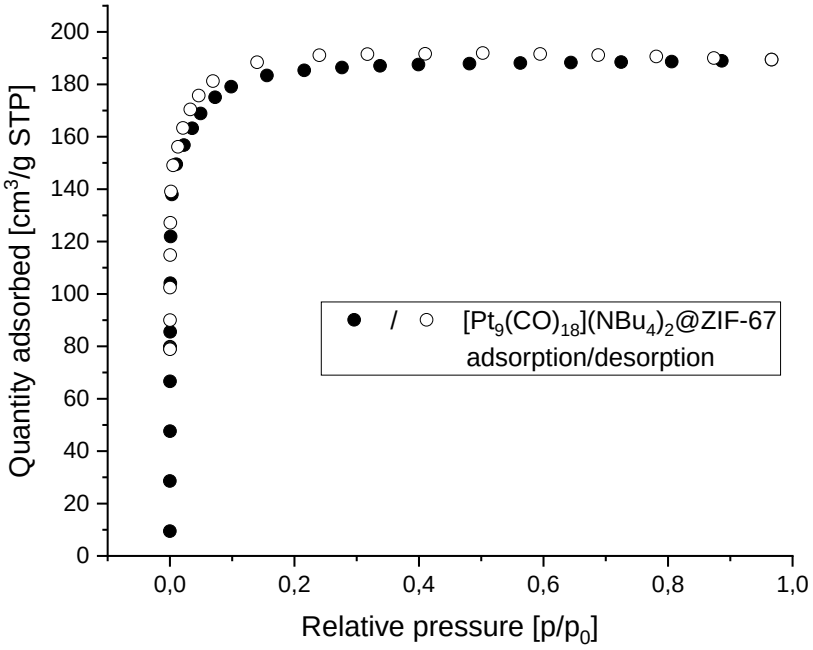

Figure 48: Nitrogen adsorption isotherm of $[Pt_9(CO)_{18}](NBu_4)_2$@ZIF-67 showing the porosity of the material with a BET surface area of 719 m^2/g.

In IR spectroscopy, both carbonyl bands of bridging and terminal ligands are clearly visible at 1862 cm^{-1} and 2043 cm^{-1}. A BET surface area of 719 m^2/g corresponded to the literature-reported data that range from about 600-900 m^2/g depending on the stoichiometry of the components (Figure 48). The cluster was decarbonylated under vacuum and elevated temperatures like the ZIF-8 material and IR confirmed the absence of carbonyl ligands as the respective bands vanished. The integrity and remaining high porosity of ZIF-67 was determined with PXRD and BET, where the surface area showed an increased value of 952 m^2/g. Further characterization with HR-TEM and HAADF-STEM is necessary in future studies to refute cluster agglomeration and assess the cluster diameter as a hint towards cluster nuclearity because it cannot be determined by DR-UV/Vis spectroscopy. The presumed material Pt_9@ZIF-67 constitutes an important indication towards the broad applicability of the encapsulation method previously established for ZIF-8, although further experiments to assess the exact nature of the Pt clusters are required. Furthermore, it could be a promising starting material for potential Pt/Co containing ORR catalysts that are obtainable *via* pyrolysis and could harbor particularly high activities.

Variation of Pt Cluster

After establishing the encapsulation of Pt_{12} in ZIF-8, the question arises if other Pt carbonyl clusters can be applied in a similar manner. By transferring the encapsulation to other cluster nuclearities, the investigation of size effects especially on catalytic properties would be interesting. For the ORR, computational screening predicted further NP diameters in the range of 2 nm with exceptional electrocatalytic activity. Thus, it should be explored what effect the cluster atomicity has on the diameter and size distribution of the NPs that can be obtained in the MOF-templated approach. Larger clusters could lead to larger NPs after the acidic digestion of ZIF-8, but it is also conceivable that their lower surface energy results in a lower degree of agglomeration. Therefore, the transfer of encapsulation, decarbonylation, and later also application in catalysis, to systems containing Pt clusters of various atomicities was an integral part of this work.

Encapsulation of other *Chini* clusters. Next to a Pt_{12} cluster, the encapsulation of other *Chini* clusters in ZIF-8 is self-evident due to their similar properties. The smaller cluster with a nuclearity of nine is an obvious choice as the encapsulation was already successful, although the cluster in ZIF-8 showed sensitivity towards oxidation and transformed to the larger Pt_{12}. Nonetheless, a decarbonylation of $[Pt_9(CO)_{18}](NBu_4)_2$@ZIF-8 without previous oxidation was tried to yield the smaller Pt_9 cluster that would be unable to exchange Pt_3 units for oxidative growth. The decarbonylation was similarly successful as the $Pt_{12\pm x}$@ZIF-8 material and IR and UV/Vis spectroscopy demonstrated the absence of CO and cluster bands, respectively. As expected, PXRD and BET showed the high crystallinity and porosity of Pt_9@ZIF-8 even after the decarbonylation. The distinction of Pt_9 and Pt_{12} in the ZIF-8 pores is not possible with HAADF-STEM, as no sufficient resolution can be achieved. This problem was previously discussed and results from the instability of the MOF under the high-intensity electron beam. Nonetheless, a significant agglomeration of the presumed, naked Pt_9 cluster can be excluded from the microscopy images and it is assumed that despite its smaller diameter, also the Pt_9 cluster is immobilized in the pore of ZIF-8 (Figure 49). In future experiments, this material should be investigated towards its activity in hydrogenation catalysis and electrocatalysis. It would be interesting if the small difference of only three atoms compared to $Pt_{12\pm x}$@ZIF-8 distinctly influences the NPs resulting from acidic MOF digestion and leads to a different catalytic activity in the ORR.

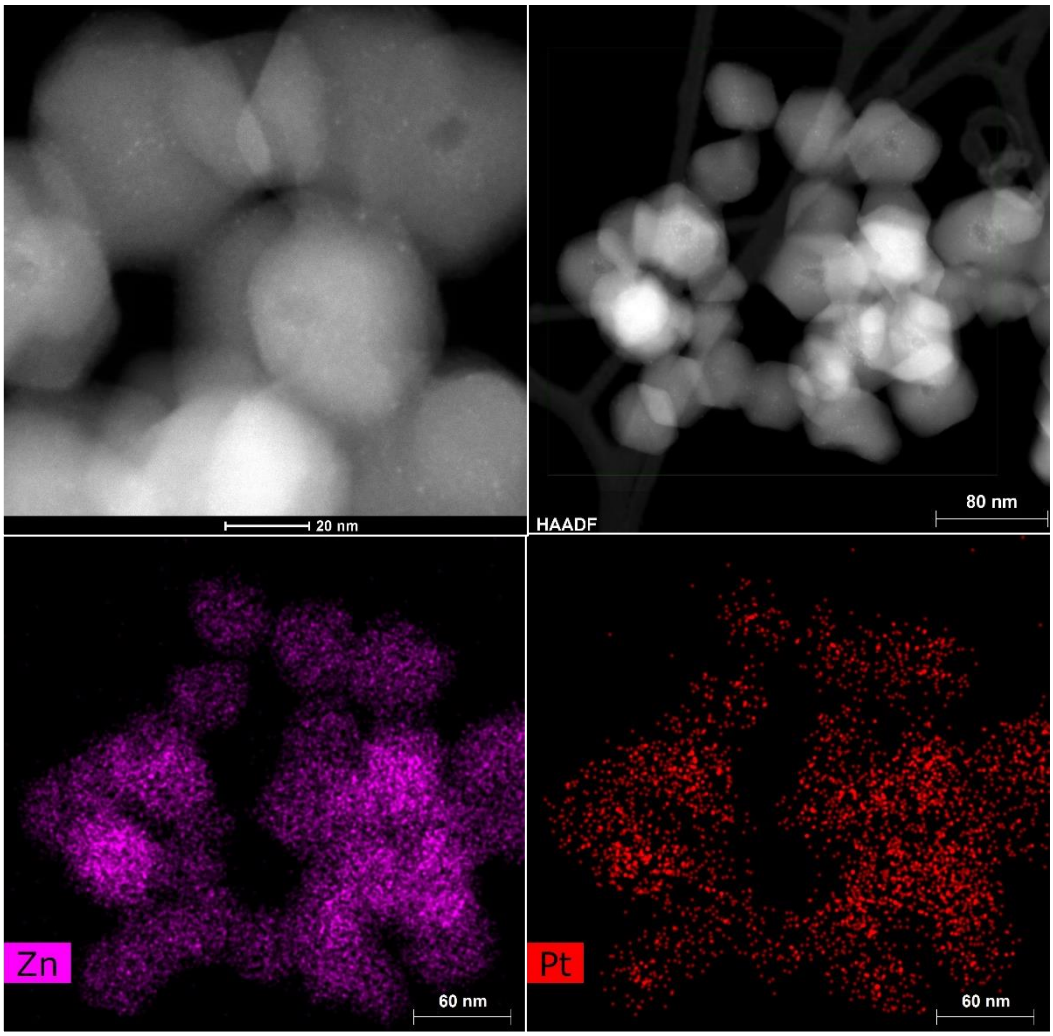

Figure 49: HAADF-STEM images with elemental mapping of Pt_9@ZIF-8. Small Pt clusters are visible as bright spots and are distributed homogeneously throughout the MOF as visible from elemental mapping. Pt and Zn are depicted in red and purple, respectively.

A consequence of the synthesis of $Pt_{9\pm x}$@ZIF-8 is the encapsulation of the larger *Chini* cluster $[Pt_{15}(CO)_{30}](NBu_4)_2$ in ZIF-8. In several experiments with the Pt_{15} cluster, no selective integration of the cluster in the framework without significant cluster transformation was achieved. Due to the presence of water of crystallization in $Zn(NO_3)_2 \cdot 6H_2O$ and the high concentration of basic 2-mIm, Pt_{15} is partially reduced to Pt_{12} during the encapsulation process as is evident from the two overlapping cluster DR-UV/Vis bands (Supplementary Figure 14, see experimental part). As the clusters' diameters do not allow for further rearrangement because of the pore confinement, a post-synthetic transformation to only one cluster species as with Pt_9/Pt_{12} mixtures is not possible. Although in principle, the encapsulation of Pt_{15} in ZIF-8 is feasible, this approach was discarded not only because of the unselective encapsulation, but also due to the complicated and hardly reproducible synthesis of Pt_{15} on silica (see chapter 3.1.1).

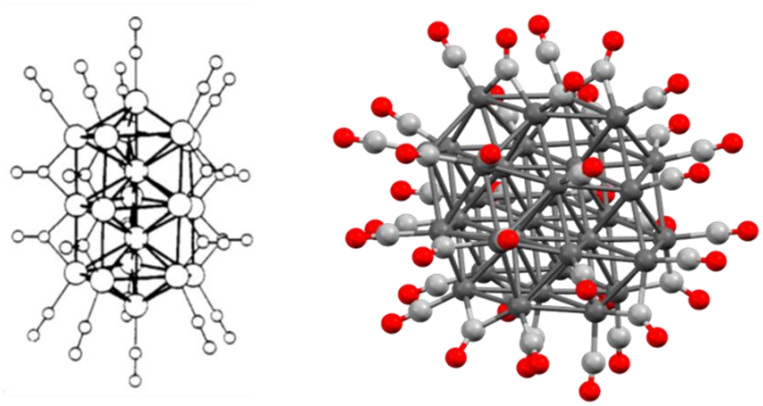

Figure 50: Crystal structures of the anionic clusters $[Pt_{19}(CO)_{22}](NBu_4)_4$ and $[Pt_{38}(CO)_{44}](NBu_4)_2$.[57,58]

Synthesis of larger Pt carbonyl clusters. Larger, spherical carbonyl clusters can be obtained from the established syntheses of *Chini* clusters mostly by carbonyl cleavage and cluster rearrangement at elevated temperatures in solution. Thus, the tetraanionic cluster $[Pt_{19}(CO)_{22}](NBu_4)_4$ could be obtained in high yields by simply heating $[Pt_9(CO)_{18}](NBu_4)_2$ in acetonitrile (Figure 50). An unambiguous identification of the cluster atomicity is more challenging than for the *Chini* clusters, as their distinctive UV/Vis bands are absent in larger Pt carbonyl clusters. Single-crystal XRD was discarded due to the tedious crystallization process and the fact that no information over the microcrystalline bulk solid, but only of one single crystal is obtained. Therefore, IR spectroscopy and the shift of the CO bands are compared to literature values to confirm the successful synthesis. Accordingly, with CO bands at 1765 cm^{-1} and 1950 cm^{-1} in the solid as well as 1799 cm^{-1} and 1993 cm^{-1} in acetonitrile solution, the integrity of the Pt_{19} cluster could be confirmed.

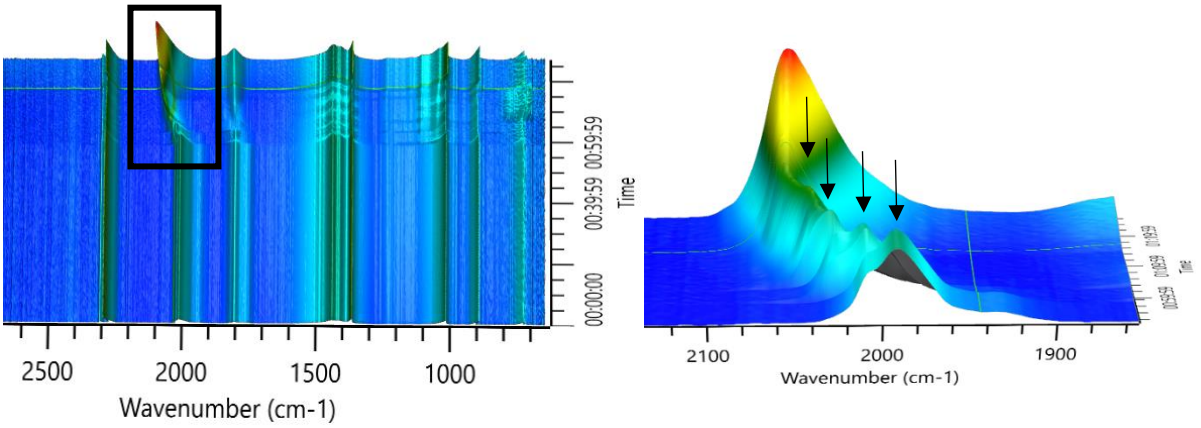

Figure 51: Time-resolved, *in situ* IR spectrum of $[Pt_{19}(CO)_{22}](NBu_4)_4$ in MeCN upon addition of HBF_4. Both CO bands shift distinctly and especially the shift of the band at 1993 cm^{-1} to 2054 cm^{-1} is characteristic for the formation of $[Pt_{38}(CO)_{44}](NBu_4)_2$ (region in the black frame of the overview spectrum (*left*) is shown enlarged (*right*)). Every addition of a drop of HBF_4, corresponding to roughly 10 µL, is marked by a black arrow.

Further analysis with ^{195}Pt-NMR spectroscopy did not yield any usable signals and also ESI-MS spectra did not show the mass of the intact cluster. The latter is not uncommon as also the less heavy *Chini* clusters could not be measured in ESI-MS without severe fragmentation.

From $[Pt_{19}(CO)_{22}](NBu_4)_4$, the synthesis of $[Pt_{38}(CO)_{44}](NBu_4)_2$ was envisaged. Upon addition of HBF_4, the carbonyl bands of the Pt_{19} cluster in acetonitrile gradually shifted as the cluster is oxidized to $[Pt_{19}(CO)_{22}]^-$, and the transformation to the Pt_{38} cluster could be observed in *in situ* FT-IR (Figure 51). With two defined CO bands, the transformation seems to be selective and IR spectroscopy is a good indication of the cluster integrity, although other analytical method like ESI-MS and SC-XRD would be desirable to further confirm the cluster nuclearity.

Because the so far largest and only recently discovered Pt carbonyl cluster $[Pt_{40}(CO)_{40}](NMe_3Bn)_6$ is desirable for the encapsulation to assess the upper limit of the cluster-based approach in ZIF-8, its synthesis was targeted starting from $[Pt_9(CO)_{18}](NMe_3Bn)_2$. The larger counter cation is chosen due to the later crystallization process of the Pt_{40} cluster, where only with this counterion, suitable crystals for X-ray diffraction could be obtained in the literature procedure.[64] The precipitation of Pt_9 was carried out analogous to the established procedure, although a decrease in yield was observed. After heating in acetonitrile, $[Pt_{19}(CO)_{22}](NMe_3Bn)_4$ is identified in FT-IR spectroscopy by its CO bands in the solid state at 1917 cm^{-1} and 1722 cm^{-1}. As already observed in the *in situ* IR experiment for the synthesis of Pt_{40}, several intermediate species are formed upon addition of HBF_4, among those the trianionic species $[Pt_{19}(CO)_{22}]^{3-}$ after the addition of 30 µL $HBF_4 \cdot Et_2O$, indicated by a shift of one CO band from 1993 cm^{-1} to 2024 cm^{-1}. This compound is reported to rearrange to the Pt_{40} cluster over time. Thus, the solution obtained after $HBF_4 \cdot Et_2O$ addition was layered with hexane, but no suitable crystals for IR or SC-XRD measurements could be obtained. Therefore, the encapsulation is conducted with the Pt_{38} cluster that exhibits a very similar nuclearity and a more reliable synthesis.

Encapsulation of $[Pt_{19}(CO)_{22}]^{4-}$. The encapsulation of the two larger clusters Pt_{19} and Pt_{38} is carried out analogously to the synthesis of $Pt_{12\pm x}$@ZIF-8. By dissolving $[Pt_{19}(CO)_{22}](NBu_4)_4$ in methanol and adding the precursor materials of ZIF-8, a brown solid is obtained after washing and drying. The supernatant shows only minimal coloration after centrifugation, indicating an almost complete encapsulation. To confirm the integrity of the ZIF-8 matrix, PXRD and BET measurements were carried out to show a high crystallinity and surface area of 1792 m^2/g (Supplementary Figure 15, see experimental part). Elemental analysis revealed a Pt content of 5.3 wt%, indicating the successful integration of the cluster in the framework. In IR, the characteristic CO bands of the carbonyl-stabilized cluster in ZIF-8 were clearly visible. In contrast to analysis in solution, a definite identification of the cluster species by means of IR spectroscopy is not possible because the characteristic CO bands of the cluster shift upon confinement in the MOF pore. The CO bands of $[Pt_{19}(CO)_{22}](NBu_4)_4$@ZIF-8 gradually vanish upon exposing the material to air (Figure 53). This is attributed to an insufficient stabilization of the carbonyl-ligated cluster that is apparently oxidized and decarbonylated under

atmospheric conditions. HR-TEM and HAADF-STEM images revealed that especially for samples with high loading, the clusters are preferentially deposited on the surface of ZIF-8. This is obvious from an increased concentration of particles on the edge of the MOF crystals, visible as bright lines in HAADF-STEM or in increased Pt concentrations in elemental mapping (Figure 45). This imperfect encapsulation is assumed to be the reason for the material's sensitivity to decarbonylation as the clusters experience a lower stabilizing effect on the surface in contrast to inside the pores of ZIF-8. Because the synthesis procedure is still in need of optimization, no cluster size distribution was determined from the microscopic images.

The cluster encapsulation seems to be based on a delicate template effect that is influenced by the cluster charge/hydrophilicity as well as the cavity size-matching of clusters and stabilizing matrix. In the case of Pt_{19}, the incomplete encapsulation cannot be explained by a lower negative charge per Pt atom compared to Pt_{12}, due to the fourfold negative charge of the Pt_{19} cluster. One reason for the lower affinity of the Pt_{19} clusters compared to $[Pt_{12}(CO)_{24}]^{2-}$ to go inside the pores is suspected to be the lower relative content of carbonyl ligands in larger Pt carbonyl clusters. Because the lower ratio of CO ligands influences the hydrophilic cluster properties, the interaction with Zn^{2+} ions and 2-mIm linkers during the encapsulation process could be decreased. Thus, the MOF does not form in close proximity to all of the Pt clusters and a fraction of the latter is deposited on the MOF crystal surface only after precipitation. In addition, the larger cluster diameter could be responsible for the difficult encapsulation, although ZIF-8 is known to assemble easily even around species as large as enzymes.[152] For a lower loading of only 0.55 wt%, no significant amount of cluster was found on the outer surface of ZIF-8 in HR-TEM and HAADF-STEM, but the low cluster amount makes the evaluation not reliable. Additionally, the evaluation of the stabilizing effect in ZIF-8 *via* the CO bands in IR spectroscopy was hindered by the low intensity due to the low loading.

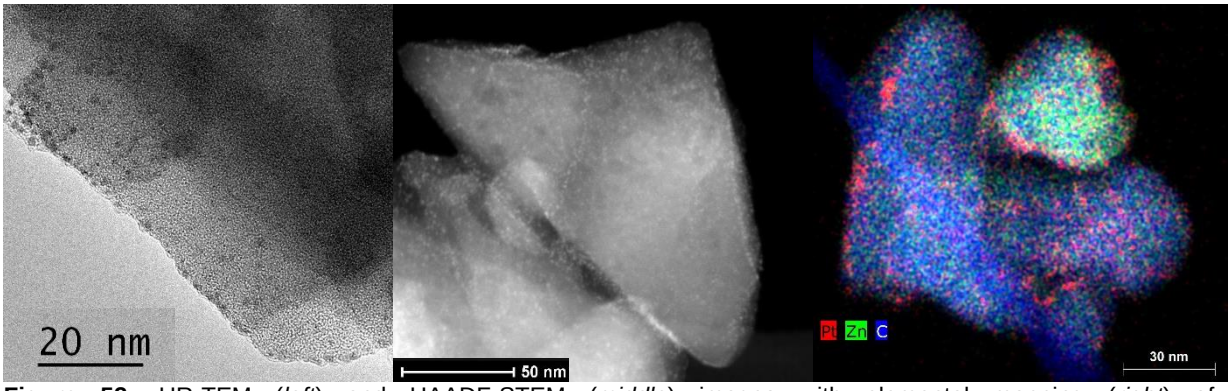

Figure 52: HR-TEM (*left*) and HAADF-STEM (*middle*) images with elemental mapping (*right*) of $[Pt_{19}(CO)_{22}](NBu_4)_4$@ZIF-8 showing a concentration on the surface of the ZIF crystals. Pt, Zn and C are marked in red, green and blue, respectively.

Due to the previous observations, $[Pt_{19}(CO)_{22}](NBu_4)_4$@ZIF-8 is kept under an inert atmosphere until the thermal decarbonylation that is carried out similar to the Pt_{12} material. The absence of carbonyl ligands is confirmed in IR spectroscopy and despite the presence of clusters on the ZIF-8 surface, HR-TEM and HAADF-STEM showed no pronounced agglomeration even after ligand removal. This fact points to a stabilization of the larger Pt_{19} clusters even when deposited on the ZIF-8 surface. Nonetheless, it must be investigated if this stabilizing effect is sufficient to prevent agglomeration even under catalytic conditions. Because a confinement of all clusters in the MOF pores would be desirable, one approach is the assembly of a second ZIF-8 shell around the formed $[Pt_{19}(CO)_{22}](NBu_4)_4$@ZIF-8 core. ZIF core-shell particles are well known and easy to synthesize by simple addition of further starting materials to a suspension of the ZIF crystals.[174] Thus, solutions of $Zn(NO_3)_2 \cdot 6H_2O$ and 2-mIm are combined with a suspension of $[Pt_{19}(CO)_{22}](NBu_4)_4$@ZIF-8 in MeOH to obtain $[Pt_{19}(CO)_{22}](NBu_4)_4$@ZIF-8@ZIF-8. After centrifugation and washing, PXRD showed no change in crystallinity and a slower decrease of the CO band intensity in FT-IR spectroscopy was observed, indicating an enhanced, but not perfect stabilization by a second ZIF-8 layer (Figure 53). To confirm the success of the core-shell approach, further synthetic optimization as well as microscopic studies are necessary to determine the location of the clusters in or on top of the ZIF-8 crystals.

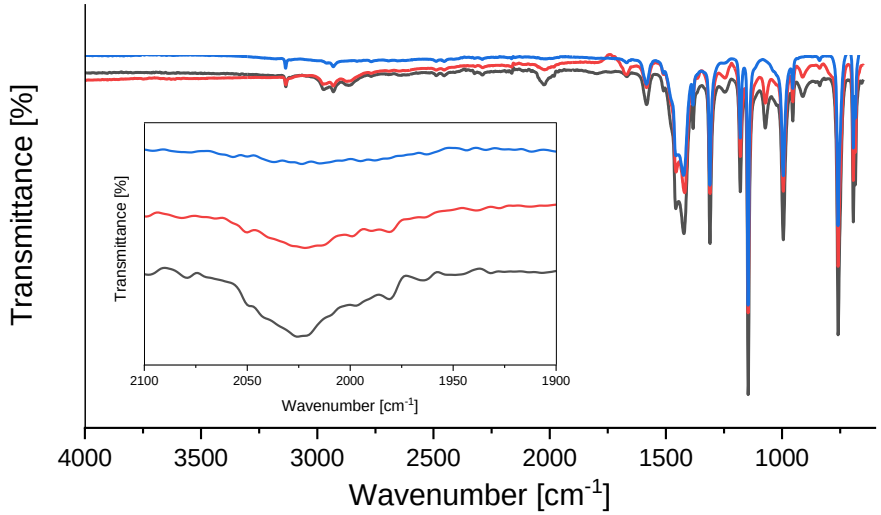

Figure 53: IR spectra of $[Pt_{19}(CO)_{22}](NBu_4)_4$@ZIF-8 under inert conditions (black) as well as after one (red) and two days (blue) under air. The inset shows the enlarged carbonyl band that decreases upon exposure to air.

Encapsulation of $[Pt_{38}(CO)_{44}]^{2-}$. $[Pt_{38}(CO)_{44}](NBu_4)_2$ was encapsulated in ZIF-8 according to the established procedure and the integrity of the framework was confirmed with PXRD and a high BET surface area of 1545 m^2/g (Supplementary Figure 15, see experimental part). The clearly visible CO bands of the ligands in FT-IR confirmed the cluster integrity (Figure 54) and elemental analysis revealed a platinum content of 5.6 wt%. As $[Pt_{19}(CO)_{22}](NBu_4)_4$@ZIF-8, also $[Pt_{38}(CO)_{44}](NBu_4)_2$@ZIF-8 was not stable against decarbonylation when exposed to air. Successful thermal decarbonylation was again confirmed *via* FT-IR spectroscopy and HR-TEM and HAADF-STEM measurements showed similar results as for Pt_{19}@ZIF-8: Also for Pt_{38}@ZIF-8, a pronounced concentration of clusters on the crystal edges was observed, although no large agglomerates were found (Figure 48). Because the core-shell approach for increased stabilization is not yet evaluated properly, it was not transferred to the Pt_{38} system.

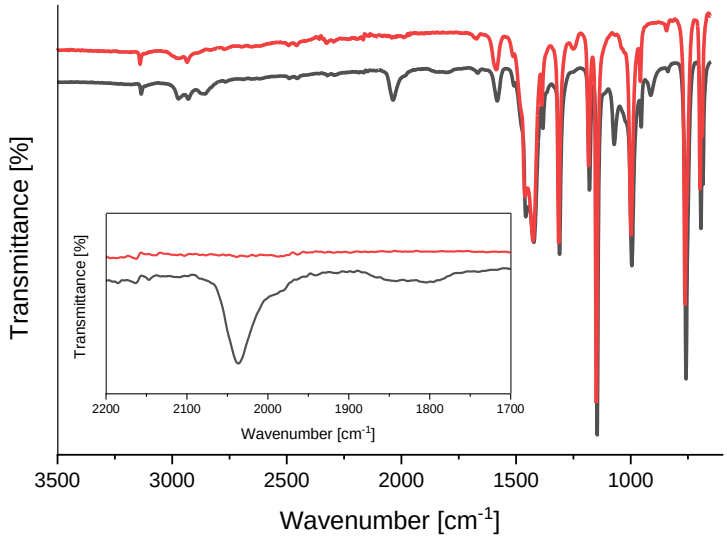

Figure 54: IR spectra of $[Pt_{38}(CO)_{44}](NBu_4)_2$@ZIF-8 under inert conditions (black) as well as after several hours under air (red). The inset shows the enlarged carbonyl bands that decrease upon exposure to air.

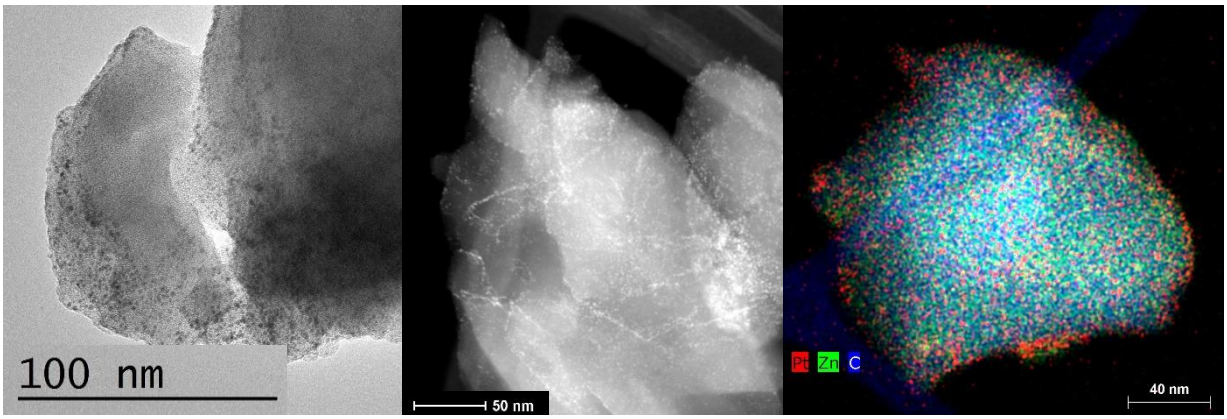

Figure 55: HR-TEM (*left*) and HAADF-STEM (*middle*) images with elemental mapping (*right*) of showing a concentration of $[Pt_{38}(CO)_{44}](NBu_4)_2$@ZIF-8 on the surface of the ZIF crystals. Pt, Zn and C are marked in red, green and blue, respectively.

Both materials Pt_{19}@ZIF-8 and Pt_{38}@ZIF-8 are applied in the hydrogenation of 1-hexene to evaluate their activity and stability under catalysis conditions as well as the accessibility of the clusters for substrates. Compared to the inclusion compound $Pt_{12\pm x}$@ZIF-8, a distinct activity enhancement is expected for the materials containing larger clusters due to their deposition on the ZIF-8 outer crystallite surface and the resulting decreased diffusion limitation. For Pt_{19}@ZIF-8, a catalyst loading of only 0.38 mol% (based on a cluster loading of 5.3 wt% Pt) lead to a complete conversion of 1-hexene to hexane after three hours. The increased activity compared to $Pt_{12\pm x}$@ZIF-8, where the same turnover was only achieved with 1 mol% catalyst, is attributed to the decreased diffusion limitation of the ZIF-8-supported Pt clusters. Analogously, Pt_{38}@ZIF-8 converted 1-hexene also in three hours with a catalyst loading of 4.7 mol%. For both catalysts, the integrity of ZIF-8 after the reaction was confirmed in PXRD. To refute agglomeration processes, further microscopic studies of the catalysts are necessary.

In summary, it is possible to encapsulate also larger clusters like $[Pt_{38}(CO)_{44}](NBu_4)_2$ and $[Pt_{19}(CO)_{22}](NBu_4)_4$ in ZIF-8, although problems with preferential deposition on the crystal surface occur and further optimization of the encapsulation procedure is necessary. With the help of microscopy combined with elemental mapping as well as size exclusion catalysis, e.g. with cyclooctene as a substrate, the position of the clusters with respect to the ZIF-8 matrix could be further evaluated in future experiments. Both materials Pt_{19}@ZIF-8 and Pt_{38}@ZIF-8 show high activities in catalytic hydrogenation, although up to now, distinctly different diffusion limitations hinder the direct comparison of the cluster sizes for the better understanding of cluster size effects.

3.2 Encapsulation of Gold Clusters in Metal-Organic Frameworks[4]

After establishing an encapsulation procedure for Pt clusters, we were interested if this approach could be transferred to the well-studied family of Au clusters. In contrast to Pt, for Au a more consecutive row of ligand-stabilized clusters with an atomicity below 20 atoms is accessible *via* literature-known procedures. Thus, not only clusters with an atom difference of three like for *Chini* clusters can be investigated, but the direct comparison of naked clusters with only one atom difference can be targeted. Nonetheless, the synthetic transfer from Pt carbonyl to ligated Au clusters is not trivial as no carbonyl-stabilized clusters are known, but mainly thiol and phosphine ligands are used in Au chemistry, that both bind more strongly to the gold core and will complicate ligand removal. Additionally, the complete change of the ligand shell to the herein chosen phosphine-stabilized clusters will demand an adaptation of the encapsulation procedure.

3.2.1 Synthesis and Characterization of Phosphine-Stabilized Gold Clusters

Firstly, the reproduction of literature-known Au clusters was targeted (overview over synthetic procedures, cluster core geometries and colors see Scheme 7, UV/Vis spectra see Figure 56). Starting from $HAuCl_4 \cdot 3H_2O$, the monophosphine gold(I) clusters $Au(PPh_3)Cl$ and subsequently $Au(PPh_3)NO_3$ by simple anion exchange with $AgNO_3$ were obtained without complications and in high yields. In a bottom-up synthesis, this mononuclear Au precursor was reduced with $NaBH_4$ to synthesize $[Au_9(PPh_3)_8](NO_3)_3$ after several washing procedures in literature yield.[175] The weakly coordinating anion thereby favors the selective formation of the Au_9 core with a toroidal crown structure and D_{2h} symmetry, and the product is obtained as a dark green powder with a brown color in solution. Because of the distinctive signals in ^{31}P-NMR and UV/Vis spectroscopy, the purity and integrity of the cluster could be unambiguously asserted. Based on the Au_9 cluster, several further core nuclearities are accessible. By a LEIST process induced by dppp, $[Au_9(PPh_3)_8](NO_3)_3$ is etched and the dark blue, core+*exo*-type $[Au_6(dppp)_4](NO_3)_2$ is formed.[176] The product is prone to contain small amounts of $[Au_8(dppp)_4Cl_2](NO_3)_2$ that is an intermediate of the reaction and can be identified by an additional signal at 515 nm in the UV/Vis spectrum. In contrast to Au_9, where only fragments could be identified, the Au_6 cluster shows a clear signal in ESI-MS spectra that together with ^{31}P-NMR and UV/Vis spectroscopy confirms the successful synthesis in literature yields. The mentioned $[Au_8(dppp)_4Cl_2](NO_3)_2$ cluster can also be selectively obtained from the Au_6 cluster *via* a growth reaction initiated by the addition of $Au(PPh_3)Cl$.[106]

[4] Large parts of this chapter are based on the master thesis of Kathrin Kollmannsberger.

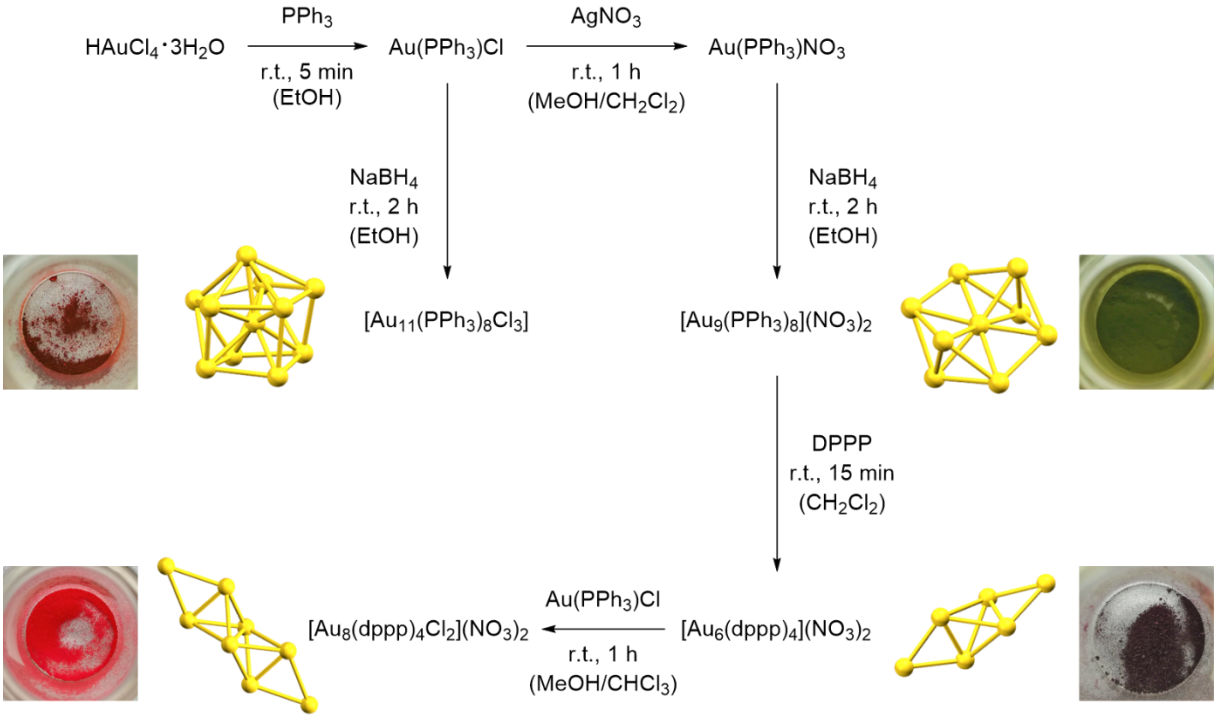

Scheme 7: Synthetic procedures towards different phosphine-stabilized gold clusters. Next to the molecular formula of each gold cluster, the cluster core structure as well as a picture of the cluster's colour in the solid state is given.

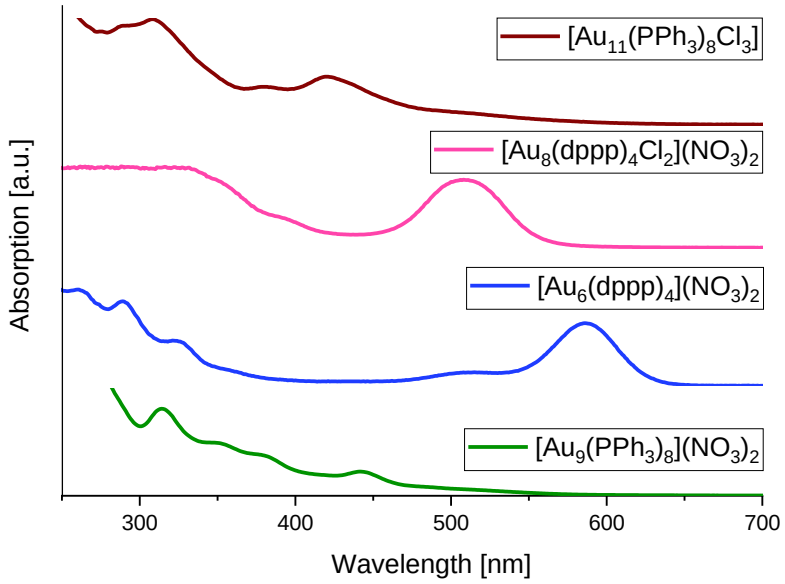

Figure 56: UV/Vis spectra of the clusters $[Au_9(PPh_3)_8](NO_3)_3$, $[Au_6(dppp)_4](NO_3)_2$, $[Au_8(dppp)_4Cl_2](NO_3)_2$ and $[Au_{11}(PPh_3)_8Cl_3]$. The color coding corresponds to the color of the clusters in the solid state and in solution except for Au_9, that appears brown when dissolved.

This pink, core+*exo* cluster is isolated as the hexafluorophosphate salt $[Au_8(dppp)_4Cl_2](PF_6)_2$ because of its slightly better solubility, although a sufficient concentration for analyzable NMR spectra was not possible in a variety of solvents (CH_2Cl_2, MeOH, THF, toluene). Nonetheless, UV/Vis spectroscopy and ESI-MS enabled an unambiguous identification of the cluster and literature yields could be matched. The fourth successfully synthesized cluster was obtained

from the reduction of $Au(PPh_3)Cl$, where because of the strongly coordinating counter ion, $[Au_{11}(PPh_3)_7Cl_3]$ instead of $[Au_9(PPh_3)_8](NO_3)_3$ was obtained despite similar reduction conditions with $NaBH_4$.[177] In contrast to Au_9, the Au_{11} cluster required several washing and precipitation steps to remove other cluster species, which resulted in low yields of only 2%. The heavy Au_{11} cluster was not detectable in ESI-MS due to pronounced fragmentation, but ^{31}P-NMR and UV/Vis spectroscopy again were in agreement with literature data.

All four clusters Au_6, Au_8, Au_9 and Au_{11} were applied in an encapsulation procedure analogous to the one established with the Pt carbonyl clusters. Solutions of the cluster, 2-mIm and $Zn(NO_3)_2 \cdot 6H_2O$ were combined under stirring and the turbid suspension was centrifuged. In all experiments, the cluster remained in solution as immediately visible by the colored supernatant and the white, precipitated ZIF-8. The absence of encapsulated cluster was confirmed in DR-UV/Vis spectroscopy after washing and drying of the powder. This phenomenon was explained by the insufficient interaction between the cluster and the MOF starting materials due to the non-polar and non-charged ligand shell of the PPh_3-stabilized Au clusters. In consequence, UiO-66 was chosen as an alternative MOF scaffold, where the BDC linkers should form π-π-interactions with the phenyl groups of the phosphine ligands and thus incorporate the cluster in its pores during MOF precipitation. However, a synthesis of crystalline UiO-66 requires solvothermal conditions in contrast to ZIF-8 which might conflict with cluster stability. Therefore, we applied a synthetic method developed at our chair where the SBU of UiO-66, the hexazirconium cluster $Zr_6O_4(OH)_2(OMc)_{12}$, is presynthesized and reacted with BDC and methacrylic acid as a modulator ("controlled SBU approach").[178] This enables milder conditions during the solvothermal synthesis. All four clusters with core sizes Au_9, Au_6, Au_8 and Au_{11} were applied in the synthesis at 70 °C for 24 h in the drying oven with a targeted loading of 2.15 wt% gold in the final metal@MOF compound. While Au_6 and Au_{11} decomposed to plasmonic Au NPs as indicated by the purple color, both Au_8 and Au_9 remained in solution while UiO-66 precipitated as a colorless solid. Thus, an even milder synthetic pathway was targeted and a slow encapsulation of Au_9 was carried out at room temperature over the course of four days. After washing and drying, the pale brown solid was analyzed, and revealed DR-UV/Vis bands in the $[Au_9(PPh_3)_8](NO_3)_3$@UiO-66 compound that matched those of the cluster in solution (Supplementary Figure 16, see experimental part). The low band intensity indicated an incomplete encapsulation of only low amounts of cluster which was corroborated by the dark brown color of the supernatant after the synthesis. In addition to reproducibility problems, the poor results made us discard this approach and abstain from further analytical efforts.

Based on this result, we intended to increase the hydrophilicity of the gold clusters and to introduce negative charges, aiming to enhance the attractive interactions with the MOF growth species (template effect). Thus, gold clusters bear more similarity to the twofold negatively

charged Pt clusters that could be encapsulated without complications. Additionally, thiol-stabilized gold clusters bearing polar groups could be scaffolded in ZIF-8 according to various literature reports.[163] Therefore, monosulfonated PPh_3 ligands should be combined with the atom-precise gold clusters *via* ligand exchange. The sulfonate group contributes the desired increase in hydrophilicity and the negative charge, while the sulfonation at only one ligand position is expected to result in minimal changes to the established synthetic procedures. The synthesis of the monosulfonated triphenylphosphine-3-sulfonic acid sodium salt (TPPMS) was complicated by problems with selectivity and purification. Nonetheless, TPPMS could be obtained from a sulfonation with oleum and purification in several pH-dependent extraction steps, although some batches contained small amounts of the disulfonated compound as an impurity. Several experiments to obtain the monosulfonated dppp linker for ligand exchange with $[Au_6(dppp)_4](NO_3)_2$ and $[Au_8(dppp)_4Cl_2](NO_3)_2$ were not successful due to failed purification.

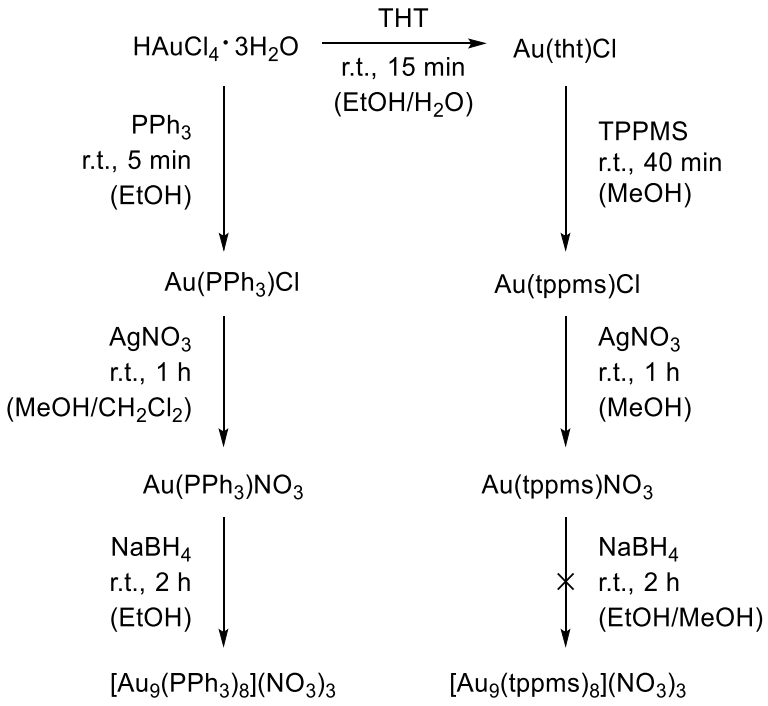

Scheme 8: Synthetic procedure to the hydrophilic $[Au_9(tppms)_8](NO_3)_3$ cluster in an analogous process to its non-polar analogue $[Au_9(PPh_3)_8](NO_3)_3$.

Initially, the established synthesis of $[Au_9(PPh_3)_8](NO_3)_3$ should be transferred to the TPPMS analogues (Scheme 8). The monometallic gold precursor Au(tppms)Cl was obtained in two steps from $HAuCl_4 \cdot 3H_2O$ and Au(tht)Cl, as a direct synthesis from the chloroauric acid was not possible.[179] Subsequently, the chloride salt was transferred to the nitrate compound $Au(tppms)NO_3$ and the purity of all TPPMS-containing precursor compounds was ensured with ^{31}P-NMR spectroscopy and ESI-MS. Similar to the selective reduction of $Au(PPh_3)NO_3$ to $[Au_9(PPh_3)_8](NO_3)_3$, $NaBH_4$ was added to a solution of $Au(tppms)NO_3$ which turned dark brown

instantly. The raw product was analyzed with ^{31}P-NMR spectroscopy and indeed only showed one signal at 45.1 ppm, indicating the selective formation of a single cluster species. The obtained UV/Vis bands could not be unambiguously assigned to the pattern of a certain cluster core and shows both characteristics of Au_8 and Au_9 cluster spectra. In addition, the large cluster fragmented too heavily in ESI-MS to obtain a cluster mass and the growth of a single crystal suitable for SC-XRD was unsuccessful. The known challenging single crystal analysis of gold clusters made us refrain from further efforts on this unknown compound and an alternative ligand exchange procedure was targeted.

The ligand exchange of $[Au_9(PPh_3)_8](NO_3)_3$ with TPPMS is reported in literature, although the obtained product was never thoroughly characterized, and no crystal structure is known due to the difficult crystallization.[180] The assumption that the obtained cluster is $[Au_8(tppms)_8](NO_3)_2$ is based on similarities with the non-polar $[Au_8(PPh_3)_8](NO_3)_2$ in ^{31}P-NMR and UV/Vis spectra. In a two-phase reaction with the organic phase containing the non-polar Au_9 cluster and TPPMS dissolved the aqueous phase, the red color of the initial Au_9 cluster is transferred to the aqueous phase, so that a complete discoloration of the organic phase indicates the completion of the reaction (Scheme 9). The reaction presumably includes a dissociation not only of PPh_3, but also of $Au(PPh_3)^+$ units in a LEIST process as it has been previously reported for ligand exchange reactions of Au clusters.[175] Further investigations of residual gold species in the organic phase could be undertaken to confirm this theory.

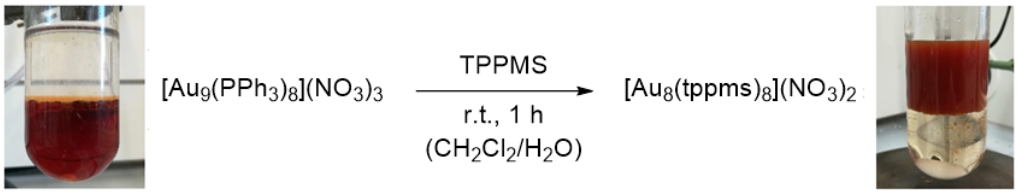

Scheme 9: Two-phase reaction to yield $[Au_8(tppms)_8](NO_3)_2$ with complete conversion indicated by a transfer of the brown color from the organic to the aqueous phase.

The hydrophilic Au_8 cluster is obtained selectively and in high yields when conducting the reaction under the exclusion of oxygen and in degassed solvents due to a sensitivity towards ligand oxidation of the solubilized cluster. Exposure to air results in a so far not elucidated cluster rearrangement back to a Au_9 core, as confirmed in NMR and UV/Vis experiments. Cluster signals in ^{31}P-NMR and UV/Vis spectroscopy matched the literature values, while elemental analysis showed deviations up to 5 wt% which was attributed on the one hand to problems with the reliable determination of Au, on the other hand impurities of salts that are not visible neither in NMR nor UV/Vis spectra cannot be excluded. Nonetheless, latter impurities should not influence the planned encapsulation procedure or influence the cluster nuclearity. In solid-state ^{31}P-MAS-NMR (magic-angle spinning NMR) spectroscopy, the main

broad signal at 53.9 ppm coincides with the signal of the spectrum of the Au_8 cluster in solution. In addition, signals with a chemical shift of 70 ppm and one with almost negligible intensity at 32 ppm can be observed as the chemical environment is presumably not identical for all phosphorus atoms due to their fixed positions in the solid state. Line broadening results from strains exerted in the material that is partially crystalline as confirmed by PXRD. The small peak at 32 ppm could be assigned to an oxidized TPPMS ligand after intentional oxidation of the free ligand for reference. The latter gave an NMR signal between 36.2 and 25.7 ppm in solution, depending on the solvent. The cluster contains water of crystallization as revealed by a weight loss of 10% from 25-125 °C in TGA measurements and bands at 3436 cm^{-1} and 1630 cm^{-1} in IR spectroscopy. The TGA curve also indicated the onset of cluster decomposition at 250 °C.

3.2.2 Encapsulation of Gold Clusters in ZIF-8

The encapsulation procedure for the hydrophilic Au_8 cluster was adopted from *Lai et al.* and is similar to the Pt cluster encapsulation procedure.[149] The Au cluster, 2-mIm and $Zn(NO_3)_2 \cdot 6H_2O$ are each dissolved in water and quickly combined under stirring. After centrifugation, the success of the encapsulation was indicated by the colorless supernatant and the brown precipitate of $[Au_8(tppms)_8](NO_3)_2$@ZIF-8. The raw material was washed twice with water and dried. An additional thermal treatment at 200 °C under vacuum removed an excess of 2-mIm *via* sublimation. The additional reflections in the PXRD pattern caused by the excess linker could thus be eliminated and the high crystallinity of ZIF-8 remained unaffected by the thermal treatment (Figure 58). The initially low BET surface area of 576 m^2/g significantly increased to 1530 m^2/g after the heat treatment (Supplementary Figure 17, see experimental part). This indicates that after the synthesis, most of the framework pores are blocked by excess 2-mIm linker that cannot be completely removed by washing. Thus, the literature surface area for the aqueous synthesis of ZIF-8 without the heat treatment procedure falls short of our value with only 1173 m^2/g.[149]

The theoretical overall cluster charge during the encapsulation in the presence of 2-mIm is a combination of the twofold positively charged cluster core and the eight TPPMS ligands. The latter are applied as the sodium salt and should therefore be present as anions. The resulting, assumed sixfold negative cluster charge could be one of the decisive factors for the successful encapsulation of the bulky gold cluster by increasing the interactions with the Zn^{2+} framework nodes during the MOF formation. The framework is expected to form some defects around the encapsulated Au clusters that exceed the pore diameter with ca. 18 Å vs. 11.6 Å. DR-UV/Vis spectroscopy verified the integrity of the encapsulated cluster as the bands in solid state

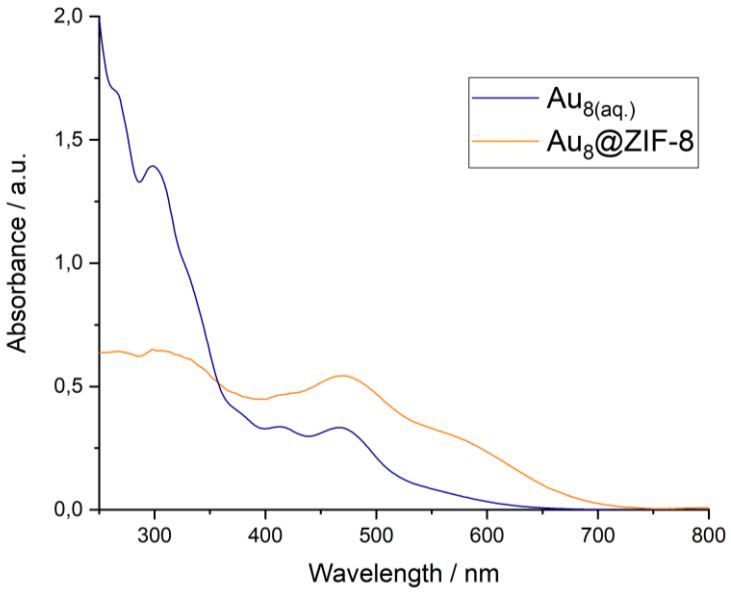

Figure 57: UV/Vis spectrum of solubilized and DR-UV/Vis spectrum of ZIF-encapsulated Au_8 cluster. The matching bands confirm a successful encapsulation.

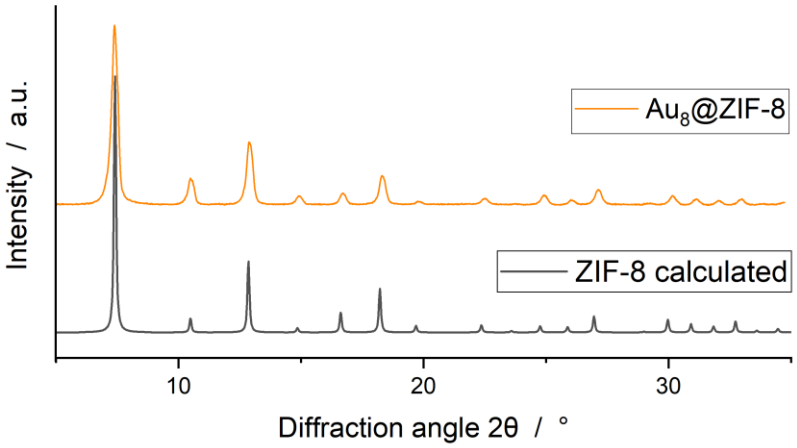

Figure 58: PXRD of Au_8@ZIF-8 compared to calculated pattern of ZIF-8 shows the high crystallinity and integrity of the framework.

matched those of $[Au_8(tppms)_8](NO_3)_2$ in solution (Figure 57). Elemental analysis revealed a gold content of 3.3 wt% for the standard loading experiment. The PXRD of $[Au_8(tppms)_8](NO_3)_2$@ZIF-8 showed the high crystallinity of the material (Figure 58).

To further investigate the integrity of the Au cluster inside the ZIF-8 pores, ^{31}P-MAS-NMR spectroscopy was carried out which revealed three main signals (see Figure 71 in chapter 3.2.1). The broad resonance at 52.9 ppm can be assigned to the TPPMS ligands bound to the Au_8 cluster as the chemical shift coincides with the one of the free cluster in solution (54 ppm). The signal at −3.90 ppm is assigned to free TPPMS ligand that is transferred from the metal core to the support as it has been previously reported for cluster deposition. The third signal corroborates this theory because the shift of 31.7 ppm matches to a free, oxidized TPPMS

ligand. After detachment from the gold core, the free phosphine would be prone to oxidation as the $[Au_8(tppms)_8](NO_3)_2$@ZIF-8 material is not handled under inert atmosphere after the encapsulation process.

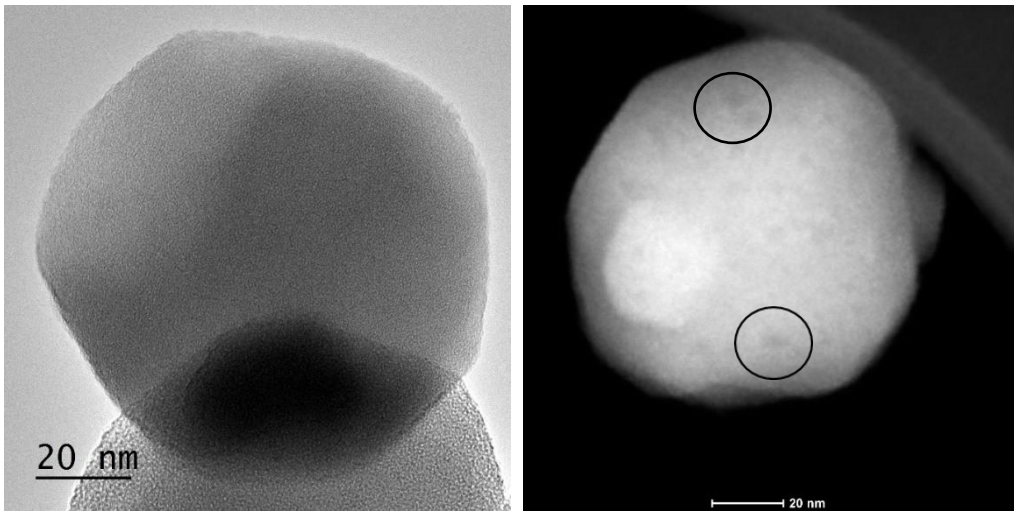

Figure 59: HR-TEM (*left*) and HAADF-STEM (*right*) image of $[Au_8(tppms)_8](NO_3)_2$@ZIF-8 after heat treatment at 200 °C under vacuum. No clusters or agglomerates are visible, indicating an insufficient resolution for the Au clusters with diameters <1 nm. Darker spots in the HAADF-STEM image are marked with black circles and are attributed to mesopores or surface defects.

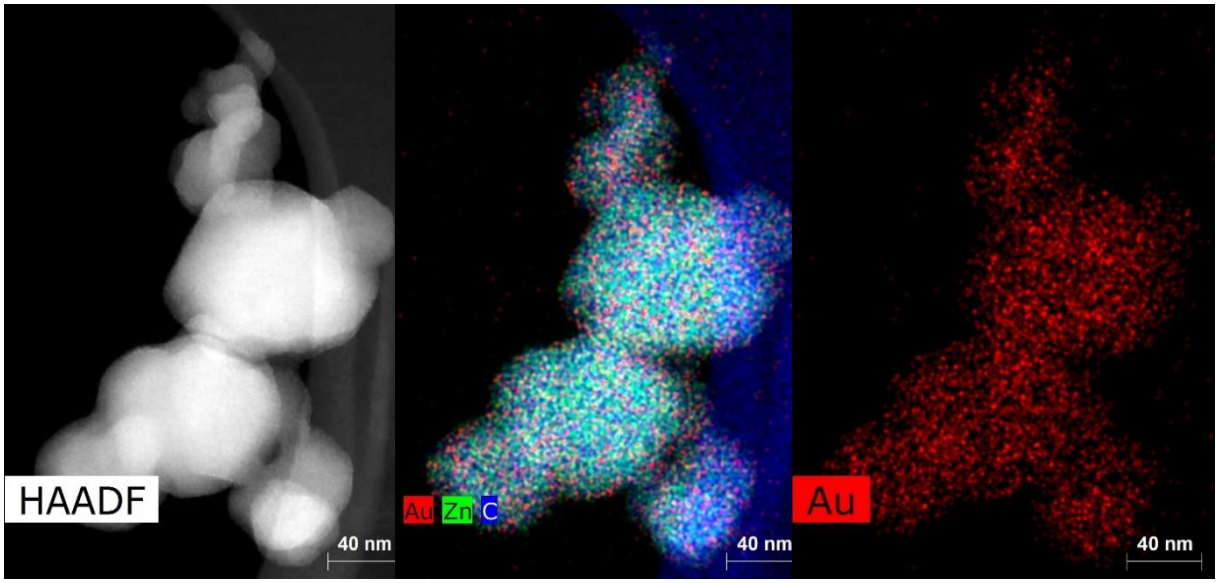

Figure 60: HAADF-STEM image of $[Au_8(tppms)_8](NO_3)_2$@ZIF-8 (*left*) with elemental mapping images of Au (*right*) and the overlay of Au, Zn and C (*middle*), demonstrating the homogeneous distribution of Au throughout the ZIF-8 crystals.

In HR-TEM and HAADF-STEM images, no Au NCs or agglomerated NPs could be detected, indicating that the Au_8 core was preserved in the encapsulation and the low cluster diameter prevented detection (Figure 59 and Figure 60). As mentioned for the case of $Pt_{12\pm x}$@ZIF-8, higher beam intensities with the goal of atomic resolution are not possible with MOFs due to severe beam damage. The darker grey spots visible in HAADF-STEM are attributed to mesopores or surface defects that could be formed during the extraction of excess 2-mIm. This effect is even more pronounced after the ligand stripping procedure and will be discussed in the respective section. When combining HAADF-STEM images with elemental mapping, a homogeneous distribution of Au throughout the ZIF-8 crystals was determined. The ZIF-8 crystals are heterogeneously distributed and poorly faceted due to the rapid, room-temperature synthesis.

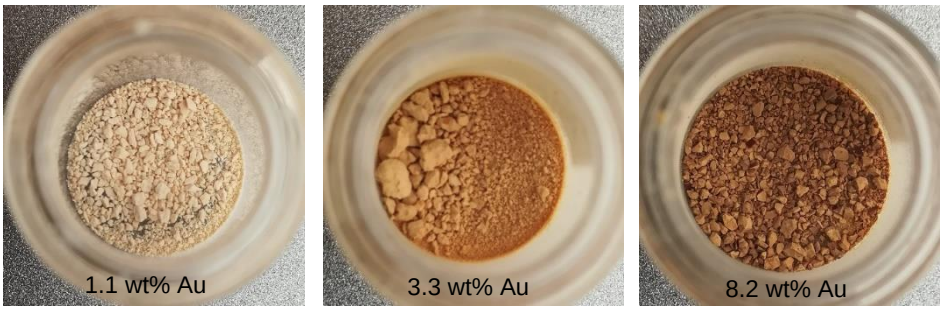

Figure 61: Photographs of $[Au_8(tppms)_8](NO_3)_2$@ZIF-8 with increasing gold loading (1.1 vs. 3.3 vs. 8.2 wt%) indicated by the more pronounced brown color.

The Au loading in the framework can be easily tuned by the concentration of cluster applied in the synthesis (see Figure 61). When applying an excess of cluster, the maximum loading obtained was 8.2 wt% Au which is significantly lower than the maximum loading of Pt in ZIF-8 obtained in the $Pt_{12\pm x}$@ZIF-8 material (21 wt%). Analogously, a Au loading of 8.2 wt% corresponds to 9.34% of all framework pores being filled with cluster, in contrast to the maximum pore filling of 44% for the Pt_{12} material. Due to the significantly larger diameter of the $[Au_8(tppms)_8](NO_3)_2$ with the bulky phosphine ligands (ca. 18 Å) compared to $[Pt_{12}(CO)_{24}](NBu_4)_2$ (ca. 8 Å), it is reasonable that the framework tolerates a lower amount of cluster in the case of Au without losing its crystallinity. In all cases of the loading variation study, the cluster integrity was confirmed in DR-UV/Vis spectroscopy and PXRD proved the high crystallinity of ZIF-8, although in the low loading case, the divergent intensity of one reflection could not be explained (Supplementary Figure 18, see experimental part).

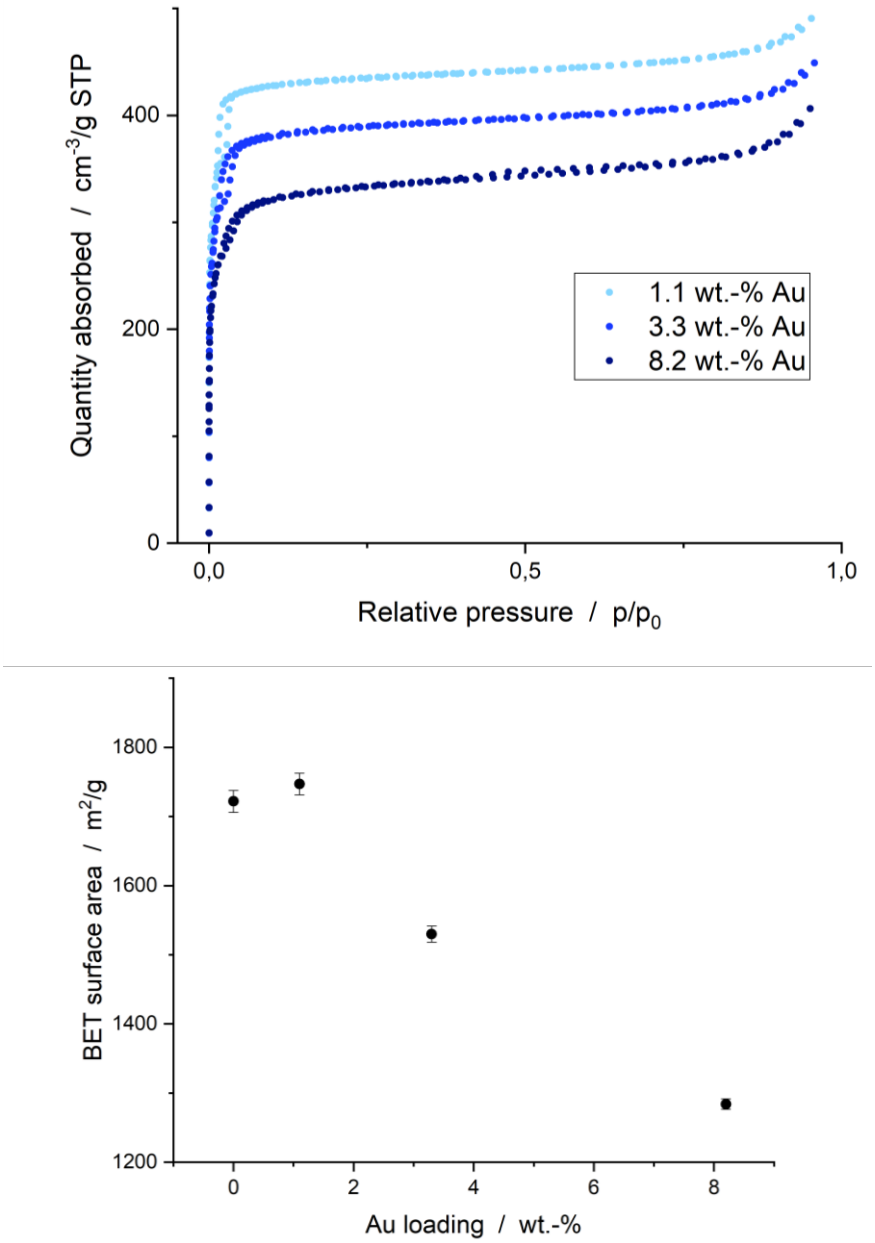

Figure 62: Nitrogen sorption isotherms for different Au loadings of $[Au_8(tppms)_8](NO_3)_2$@ZIF-8 (*top*) and linear decrease of the BET surface area with increasing loading (*bottom*).

The BET surface area decreases roughly linearly with the loading as expected due to the higher ratio of non-porous mass and the blocking of framework pores by the integrated clusters (1.1 wt%: 1747 m^2/g; 3.3 wt%: 1530 m^2/g; 8.2 wt%: 1284 m^2/g) (Figure 62). In XPS measurements, the Au 4f and Zn 3p signals overlapped and by deconvolution, the expected 2.5-fold increase in loading (3.3 wt% vs. 8.2 wt%) also resulted in 2.5 times higher intensity of the Au 4f signal (Figure 63). The binding energy remains constant.

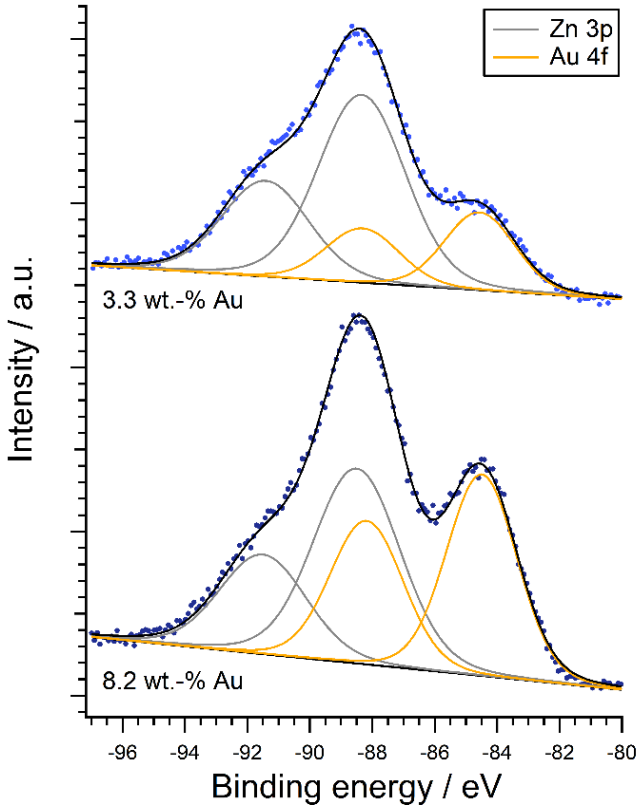

Figure 63: XP spectra of the Au 4f and Zn 3p region of $[Au_8(tppms)_8](NO_3)_2$@ZIF-8 with standard (3.3 wt%) and high (8.2 wt%) loading that is reflected in an increased signal intensity.

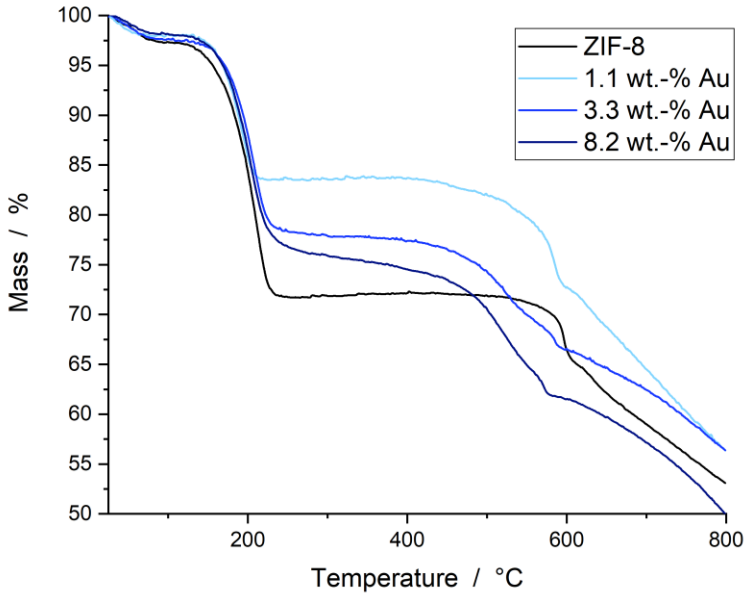

Figure 64: TGA curves of pristine ZIF-8 synthesized in water and of $[Au_8(tppms)_8](NO_3)_2$@ZIF-8 with different Au loadings, indicating a decreased stability for higher Au loadings.

TGA analysis of the empty ZIF-8 material as well as the $[Au_8(tppms)_8](NO_3)_2$@ZIF-8 with different loadings was carried out (Figure 64). In the TGA curve of pristine ZIF-8 synthesized in water, after an initial weight loss due to residual solvent, a large weight loss step of over 25 wt% was observed that is attributed to the sublimation of excess 2-mIm linker still present in the MOF. This phenomenon was discussed previously and resulted in the vacuum treatment of the raw material at 200 °C. Further decomposition of the framework occurs only above 550 °C, emphasizing the high thermal stability of ZIF-8. In the gold-loaded samples, similar general curve shapes are observed with initial weight loss due to solvent and linker removal with subsequent decomposition. Nonetheless, an unusual trend for the second weight loss step due to sublimation of excess linker is observed, with the lowest weight loss of only 14 wt% for the material with the lowest Au content (1.1 wt%). With this material being the most similar to pristine ZIF-8, an inverse trend is expected. A possible explanation could be slight differences in the washing procedure resulting in different amounts of 2-mIm in the pores for each material. As a second observation from the TGA data, the onset of framework decomposition shifts to lower temperatures when the Au cluster loading is increased. This is indeed expected and indicates a destabilization of the framework when more clusters are introduced due to an increased number of defects. These defective sites result from the cluster diameter exceeding the pore diameter and the framework having to assemble around the clusters. In summary, the synthesis of $[Au_8(tppms)_8](NO_3)_2$@ZIF-8 could be confirmed with an intact gold core and partial transfer of the ligands to the MOF support *via* DR-UV/Vis, microscopic, XPS and TGA measurements. The formed ZIF-8 exhibits high porosity and crystallinity as evidenced in PXRD and BET measurements and the gold loading could be easily tuned as high as 8.2 wt%.

Tempering Studies

To investigate the stability of $[Au_8(tppms)_8](NO_3)_2$@ZIF-8 (3.3 wt% Au) under elevated temperatures and the possibility of thermal ligand removal analogously to the carbonyl ligands in chapter 3.1.1, a series of tempering experiments was conducted. In first experiments under vacuum, where the $[Au_8(tppms)_8](NO_3)_2$@ZIF-8 material was heated gradually to 250, 300 and 350 °C for one hour each, no cluster agglomeration or degradation of the ZIF-8 matrix was observed. The DR-UV/Vis bands of the cluster remained unchanged and the PXRD confirmed the continuous high crystallinity of ZIF-8 (Supplementary Figure 19, see experimental part). In a similar study in a muffle furnace under air, significant changes to the material after heating to 250, 300, 350 and 400 °C for one hour each could be observed. When comparing the PXRD patterns after each heating step, the crystalline structure remains intact up to 300 °C but collapses completely at 350 °C. The decomposition of the stabilizing matrix apparently leads to agglomeration and formation of Au NPs that show broadened Au(111) and Au(222)

reflections. Upon heating to 400 °C, these reflections become less defined and broad diffraction peaks emerge that resemble the characteristic signals of ZnO between 30° and 40° reported in a literature study for thermal ZIF-8 decomposition (Figure 65).[149]

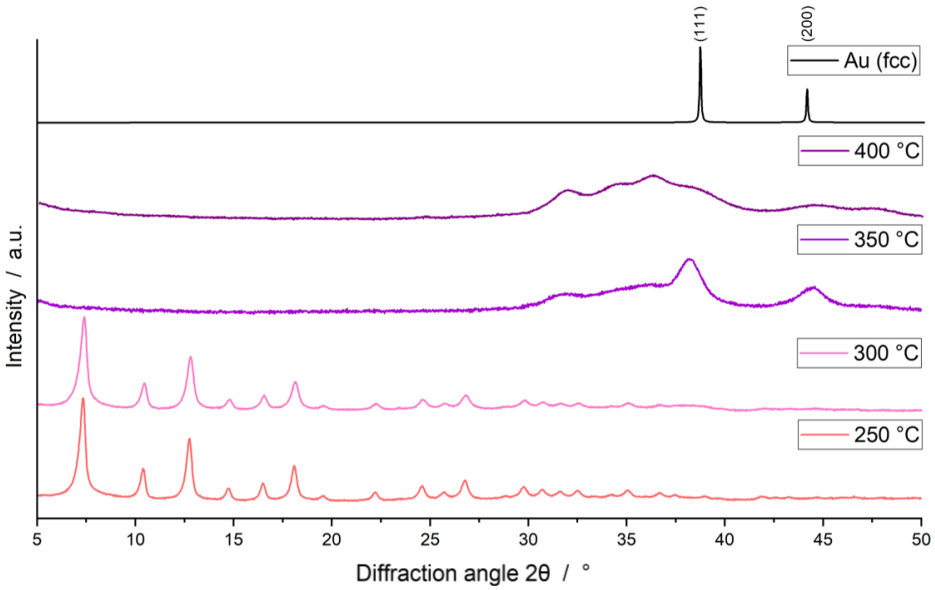

Figure 65: PXRD patterns of $[Au_8(tppms)_8](NO_3)_2$@ZIF-8 (3.3 wt% Au) after each heat treatment step. The ZIF-8 structure collapses at 350 °C and reflections of Au NPs emerge (see Au(fcc) pattern for comparison, top).[149]

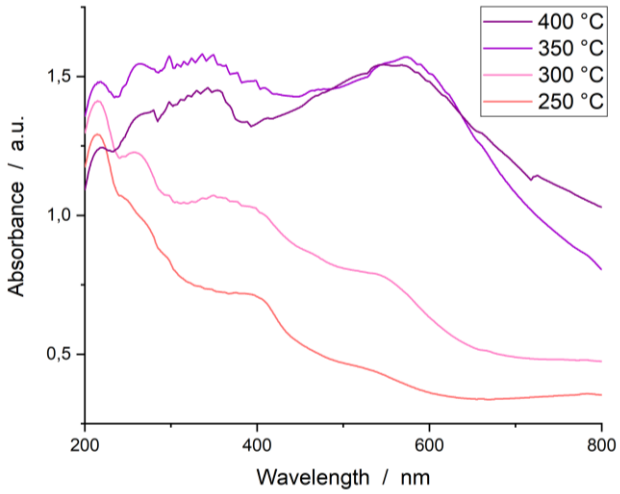

Figure 66: DR-UV/Vis spectra of $[Au_8(tppms)_8](NO_3)_2$@ZIF-8 (3.3 wt% Au) after each heat treatment step. While up to 300 °C discrete cluster bands are visible, plasmonic resonance bands stemming from agglomerated Au NPs are evident at 350 and 400 °C.

Analogously, the heat-treated samples were examined *via* DR-UV/Vis spectroscopy and compared to the pristine Au_8 cluster (Figure 66). Already after heating to 250 °C under air, the characteristic features of the Au_8 cluster are replaced by a band at 400 nm that hints to the formation of an intermediate, unidentified cluster species. An additional band at 550 nm increases in intensity upon further heating and is assigned to the plasmonic resonance of agglomerated gold NPs with a diameter >2 nm. At 400 °C, a red shift to 570 nm indicates further agglomeration to even larger NPs. With the naked eye, a color change from brown to the characteristic pink and purple of plasmonic Au NPs can be observed.

After selected heating steps, an additional microscopic study *via* HR-TEM and HAADF-STEM was conducted. Upon heating at 300 °C under O_2 for one hour, HAADF-STEM revealed limited agglomeration to NPs with diameters between 1.5 and 2.5 nm with few larger agglomerates around 5 nm (Figure 67, left). When the heating time is prolonged to one hour at 250 °C and one hour at 300 °C, the agglomeration is more pronounced with several agglomerates above 5 nm as seen in HR-TEM (Figure 67, right). For the prolonged heating time, combining HAADF-STEM with elemental mapping allows conclusions about the fate of the TPPMS ligands after heat-induced cluster agglomeration. Large Au NPs do not only appear as bright spots in Au mapping, but in the same spots also distinct P and S signals are observed, indicating the presence of TPPMS ligands adsorbed in the matrix and on the surface of agglomerated Au NPs (Figure 68).

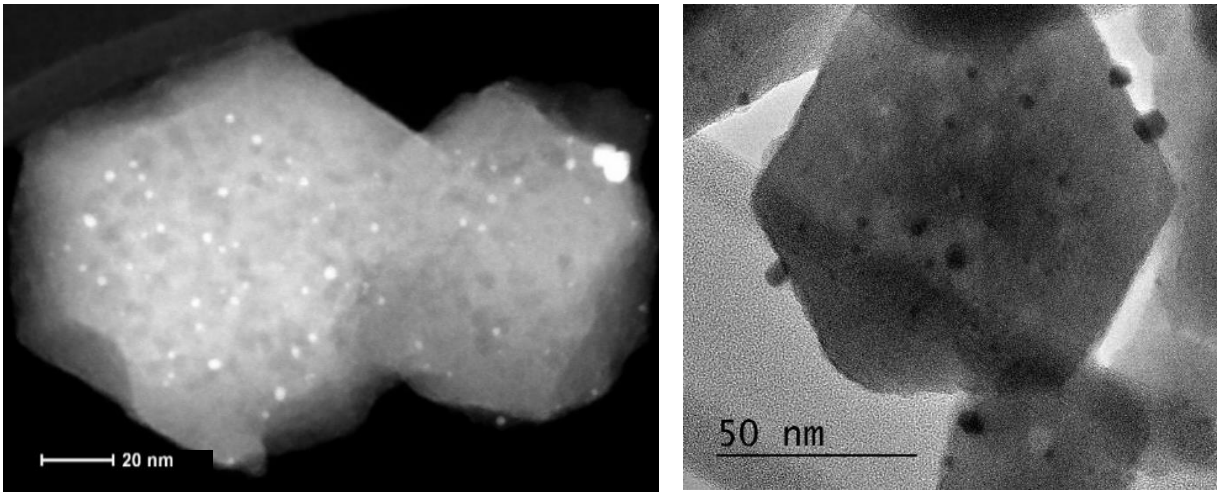

Figure 67: *Left:* HAADF-STEM image of $[Au_8(tppms)_8](NO_3)_2$@ZIF-8 (3.3 wt% Au) after heating to 300 °C for 1 h. *Right:* HR-TEM image of the same material after heating to 250 °C and 300 °C for one hour each, showing more pronounced agglomeration.

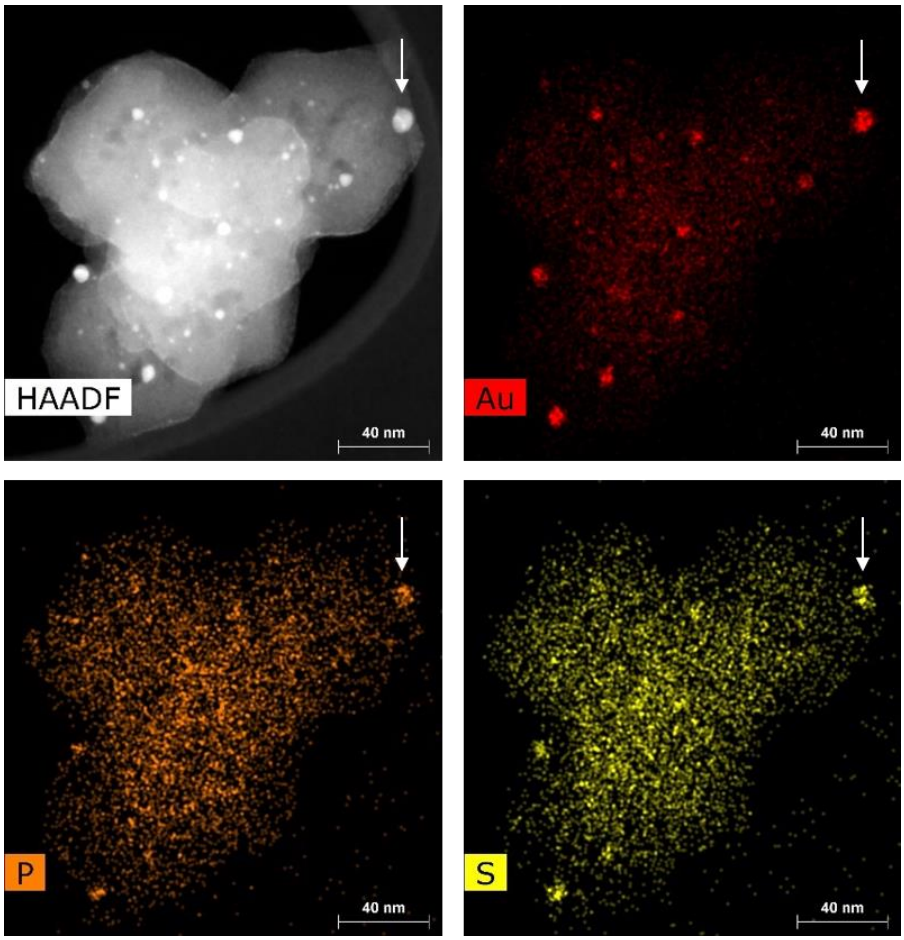

Figure 68: HAADF-STEM with elemental mapping for $[Au_8(tppms)_8](NO_3)_2$@ZIF-8 (3.3 wt% Au) after heating to 250 °C and 300 °C for 1 h each. Energy-dispersive X-ray spectroscopy (EDX) maps for Au (red, *top right*), P (orange, *bottom left*) and S (yellow, *bottom right*) indicate the presence of TPPMS ligands in the matrix and on agglomerated Au species, one NP exemplarily marked with a white arrow.

In summary, a gradual agglomeration of the former subnanometer Au_8 clusters can be observed upon increasing the temperature and heating time of the sample. Above 350 °C, the ZIF-8 lattice completely decomposes, and large, TPPMS-capped agglomerates can be observed. Thus, a different approach to detach the stabilizing ligands from the cluster core must be targeted as the tempering studies did not yield naked nanoclusters.

3.2.3 Ligand Removal and Preliminary Catalytic Investigations with Au_8@ZIF-8

According to literature, a complete detachment of phosphine ligands from a gold cluster core could be achieved *via* thermal treatment under oxygen and subsequent treatment under hydrogen pressure for supported gold clusters on titania or silica.[112,181] For the ligand removal procedure, the $[Au_8(tppms)_8](NO_3)_2$@ZIF-8 (3.3 wt% Au) powder was pressurized in a *Fisher-Porter* tube and heated in a sand bath. Initially, the literature procedure was adapted to a first heating step under 1 bar O_2, followed by an increase in O_2 pressure to 3 bar and subsequent H_2 treatment at 3 bar, each step at 200 °C for two hours. The obtained material was characterized after every step and PXRD confirmed the integrity of ZIF-8 and the absence of characteristic Au NP reflections (Figure 69).

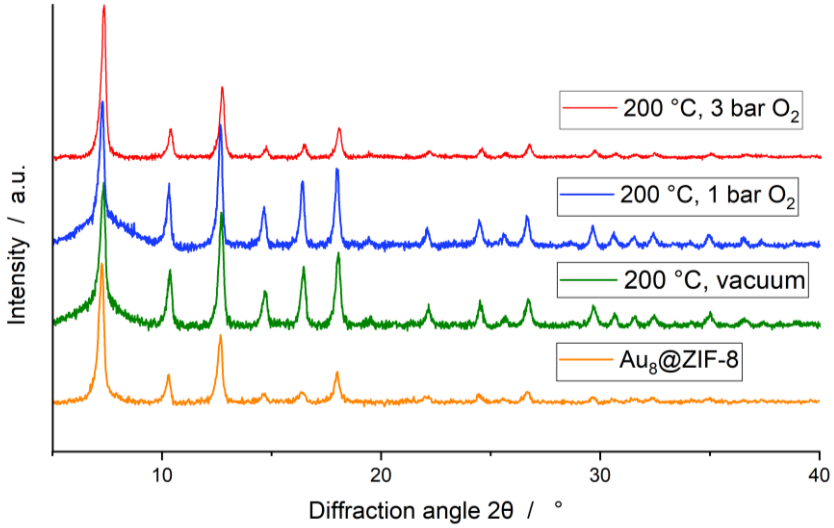

Figure 69: PXRD patterns for the ligand removal procedure of $[Au_8(tppms)_8](NO_3)_2$@ZIF-8, showing the integrity of ZIF-8 even after the thermal, oxidative treatment.

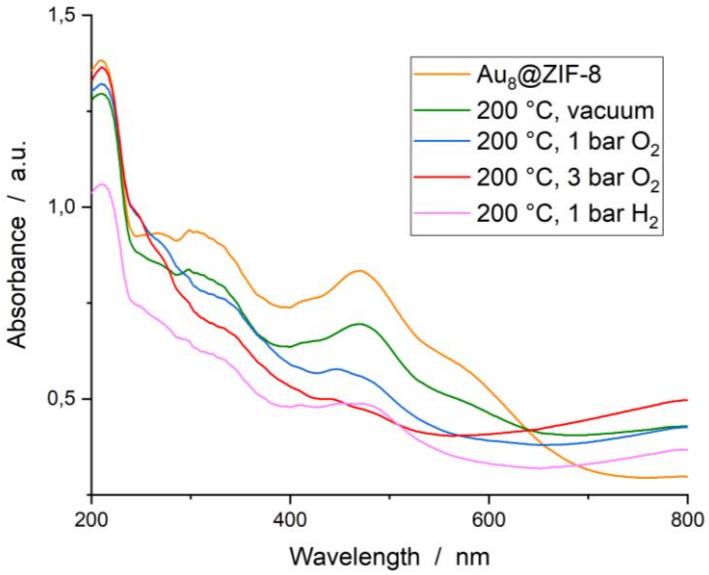

Figure 70: DR-UV/Vis spectra for the ligand removal procedure of $[Au_8(tppms)_8](NO_3)_2$@ZIF-8, showing a decrease in intensity of the characteristic cluster bands.

The typical DR-UV/Vis bands of the Au_8 cluster gradually decrease in intensity which could be an indication of ligand removal as the electronic influence of the TPPMS ligands on the UV/Vis signals stemming from the cluster core decreases (Figure 69). As in PXRD, the presence of Au NPs exhibiting plasmonic resonance can be excluded as no bands around 600 nm are observed. The strongest source of information about the state of the TPPMS ligands after oxidative treatment is ^{31}P-MAS-NMR spectroscopy as the phosphorus species present in the material can be directly observed. The three recorded signals can be assigned to the same signals that were also present in the spectrum of the free Au_8 cluster and ligand: TPPMS ligands bound to the cluster at 57.4 ppm, the oxidized TPPMS species at 32.0 ppm and the free TPPMS ligand at −4.08 ppm. While the highly symmetric TPPMS and TPPMS oxide result in sharp NMR signals, the peak of cluster-bound ligands is broadened by the asymmetric environment in the ligand shell that cannot be compensated in the solid state by free movement as in solution NMR. In contrast to the previously recorded spectrum, the intensities of these signals after the 1 bar oxygen treatment differ significantly (Figure 71, left). While the signal for free TPPMS is almost vanished due to linker oxidation, also the cluster-bound TPPMS signal intensity decreases, indicating a ligand dissociation from the cluster core and an immediate oxidation of the free phosphine. Indeed, the TPPMS oxide signal shows significantly increased intensity. When applying a higher oxygen pressure of 3 bar, the effect is even more pronounced, to the extent that almost no ligated TPPMS is discernible anymore (Figure 71, right). This qualitative analysis corroborates the successful removal of most TPPMS ligands from the cluster core, although the phosphine species are still present as TPPMS oxide in the framework pores.

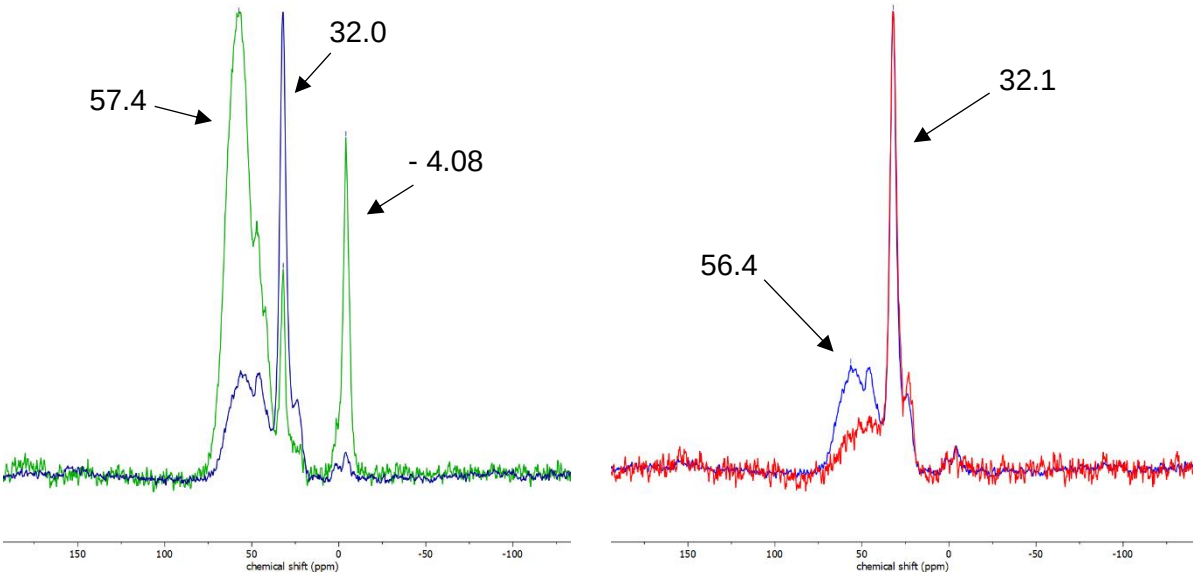

Figure 71: ^{31}P-MAS-NMR spectra of $[Au_8(tppms)_8](NO_3)_2$@ZIF-8 before (green) and after (blue) 1 bar oxygen treatment (*left*) as well as comparison of the latter with the 3 bar oxygen treatment (red, *right*). The signal at -4.08 ppm assigned to the free phosphine disappears due to oxidation and the signal for the oxidized ligand at 32 ppm increases significantly, while also the peak for cluster-bound phosphine ligands (ca. 57 ppm) decreases.

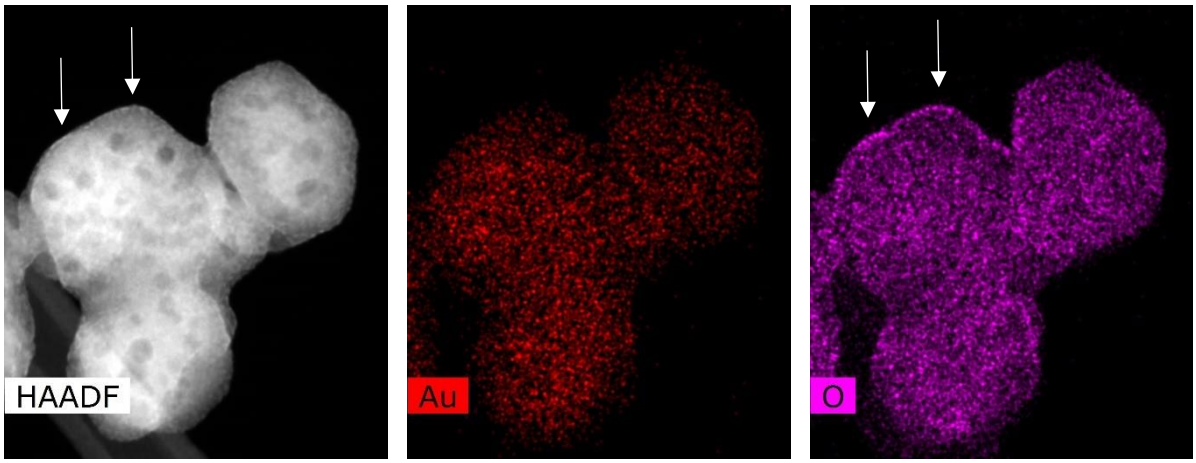

Figure 72: HAADF-STEM images with elemental mapping of $[Au_8(tppms)_8](NO_3)_2$@ZIF-8 (3.3 wt% Au) after heating to 200 °C under 3 bar O_2. Partial degradation of the ZIF-8 matrix is observed, although Au clusters remain homogeneously distributed and no agglomeration occurs. Spots assigned to ZnO formation are marked with white arrows.

Although PXRD patterns revealed a high crystallinity of the ZIF-8 matrix, in HR-TEM and HAADF-STEM images, a partial degradation of the framework is observed with dark spots resembling holes in the crystal surface. The decreased stabilization of ZIF-8 under a pure-oxygen atmosphere is literature-known,[182] and elemental mapping reveals an increase concentration of oxygen on the crystal surface, indicating the presence of ZnO. Nonetheless, the remaining crystallinity evidenced in PXRD provides enough stabilization to prevent the agglomeration of the encapsulated Au clusters, as elemental mapping of Au confirms the still homogeneous distribution in ZIF-8. Accordingly, the BET isotherm shows a distinct hysteresis that can be attributed to the formed mesopores, and also the surface area is decreased (Supplementary Figure 20, see experimental part).

Further treatment with 1 bar hydrogen at 200 °C for two hours did not lead to any changes in the ^{31}P-MAS-NMR or DR-UV/Vis spectra, and the last step of the literature procedure was therefore discarded. Due to reproducibility problems in further experiments with 3 bar oxygen at 200 °C, where an unknown cluster transformation could be observed in DR-UV/Vis spectroscopy (Supplementary Figure 20, see experimental part), the standard ligand removal procedure was established after optimization as a heating process under 1 bar oxygen at 150 °C for two hours. This reproducible approach resulted in similar efficiency in ligand removal as proven *via* ^{31}P-MAS-NMR spectroscopy (Supplementary Figure 21, see experimental part), but no cluster disintegration. PXRD revealed a high crystallinity and the values for the BET surface area did not decrease and no hysteresis was observed in contrast to the previous oxygen treatment. XP spectra before and after the oxidation process clearly showed the spin-orbit split peaks of Au after deconvolution ($4f_{7/2}$ and $4f_{5/2}$ with the doublet ratio of 8:6). The $4f_{7/2}$ signal of 84.5 eV fits to the reported binding energy found for gold nanoclusters and is slightly shifted compared to the one of metallic Au(0) with 83.0 eV (Figure 73, left).[183]

The sample after 1 bar oxygen treatment at 150 °C shows an increased intensity of the Au signals by 20%, which might result from decreased shielding of the Au core due to dislodged ligands. The XP spectra in the Au $4d_{5/2}$ region confirm the results (Supplementary Figure 22, see experimental part). In addition, after the oxygen treatment the peak corresponding to N 1s is shifted compared to the other samples (Figure 73, right). This indicates that a structural and/or chemical change is induced by the oxygen treatment and confirms the observations in microscopy.

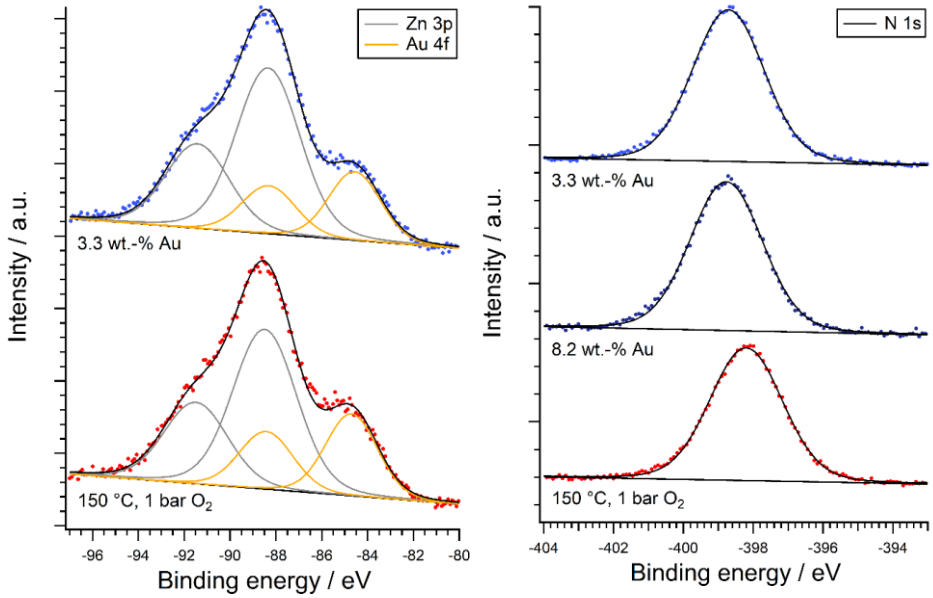

Figure 73: XP spectra of the Au 4f and Zn 3p region (*left*) and the N 1s region (*right*) before and after treatment under 1 bar O_2 at 150 °C. While an increase in loading does not change the N 1s signal, a distinct shift after treatment of the standard loading sample is observed, indicating a chemical and/or structural change in the ZIF-8 matrix.

In summary, by treating $[Au_8(tppms)_8](NO_3)_2$@ZIF-8 with 1 bar oxygen at 150 °C for two hours, a reproducible cleavage of the majority of TPPMS ligands could be achieved and the new material with mostly naked Au clusters is denoted as "Au_8@ZIF-8", although further investigations need to be conducted to identify the exact atomicity and ligand-free state of the encapsulated Au clusters. Nonetheless, the absence of Au NP diffractions in PXRD and no plasmonic resonance bands can refute significant agglomeration after ligand removal and also microscopic studies show no Au species over 1 nm, indicating the integrity of small Au clusters with an atomicity close to eight. Although ^{31}P-MAS-NMR studies hint towards a successful ligand removal from the cluster surface, the removal of the free, oxidized ligands from the framework pores was so far not successful. An oxidative change in the ZIF-8 matrix could be evidenced with HR-TEM, HAADF-STEM and XPS, although the exact nature of this change remains the subject of further studies.

With Au_8@ZIF-8, first catalytic studies are performed to assess the size-dependent activity of the naked gold cluster. The oxidation of benzyl alcohol and the reduction of nitrophenol are chosen as test reactions, because confined Au NCs/NPs have previously been applied as catalysts.

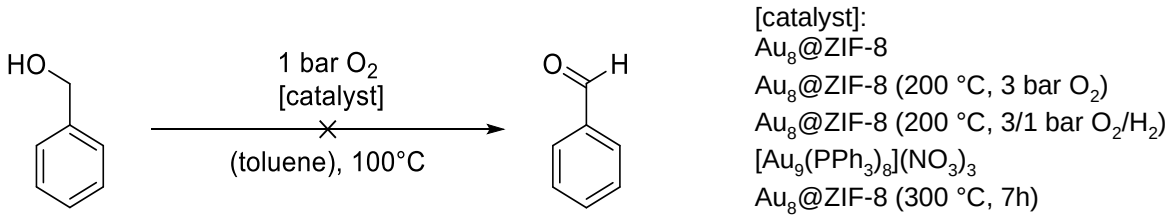

Scheme 10: Oxidation of benzyl alcohol with molecular oxygen as a catalytic test reaction for various supported Au catalysts.

Au_8@ZIF-8 was first applied in the oxidation of benzyl alcohol to benzaldehyde in toluene (Scheme 10). Unfortunately, independent of the material treatment, no conversion was observed *via* gas chromatography, and also the free cluster $[Au_9(PPh_3)_8](NO_3)_3$ did not show any activity. This could be attributed to blocking effects either by oxidized ligands still present in ZIF-8 pores or by ligands attached to the Au cluster core as in the case of the free Au_9 cluster. Another explanation for the inactivity of the materials is the presumably small size of the Au cluster core that could lie below the threshold for catalytic activity for certain reactions.[109]

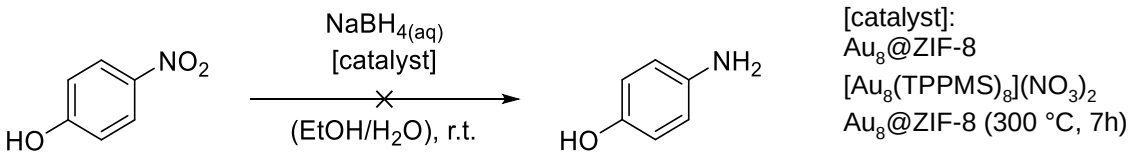

Scheme 11: Reduction of nitrophenol to aminophenol as a catalytic test reaction for various supported Au catalysts.

Analogously, a variety of supported Au catalysts was tested for their activity in the reduction of nitrophenol with $NaBH_4$ (Scheme 11). The conversion is easily monitored *via* the blue-shift of the distinctive absorption band in UV/Vis spectra. Similar to the previous oxidation, no activity for any of the gold catalysts was observed independent of the treatment of Au_8@ZIF-8. As a thiol-stabilized Au_{25} cluster was active in this reaction as the ligand-stabilized and also as the ZIF-8-supported cluster, it is assumed the main reason for the inactivity is the small and thus inactive Au core size.[163]

4 CONCLUSION AND OUTLOOK

In this work, a proof-of-concept system for the wet-chemical encapsulation of molecular, ligand-stabilized Pt clusters in ZIFs was established. Procedures for carbonyl ligand removal were introduced and the acidic digestion of the stabilizing MOF matrix was shown to produce high-precision Pt NPs in the range of 1 nm with narrow size distributions and high activity in electrocatalysis. The principle was initially demonstrated for small Pt clusters in ZIF-8 and subsequently, preliminary investigations towards the generalization of the concept were undertaken, including a transfer to larger Pt clusters, different ZIFs and ultimately to an example of a Au cluster in ZIF-8.

The *Chini* cluster $[Pt_9(CO)_{18}](NBu_4)_2$ could be successfully encapsulated in ZIF-8 under mild conditions and the carbonyl ligands were removed thermally without compromising the cluster atomicity or the integrity of the framework. The resulting material $Pt_{12\pm x}$@ZIF-8 comprised naked, highly precise platinum clusters and was extensively investigated with DR-UV/Vis and IR spectroscopy, TGA, PXRD, nitrogen sorption, XPS, HR-TEM and HAADF-STEM with elemental mapping, among others. Pt loadings could easily be varied by adjusting the cluster concentration during the synthesis and a maximum loading of 21 wt% Pt was achieved. The confined clusters were accessible for substrates and showed high activity and recyclability in catalytic hydrogenations, where no agglomeration was observed. In addition, $Pt_{12\pm x}$@ZIF-8 represents a container for readily available Pt nanospecies which was demonstrated by the generation of ultrasmall and precise Pt NPs on a glassy carbon electrode. By acidic digestion of ZIF-8, Pt NPs with a diameter of 1.1±0.17 nm could be obtained that were highly active in the electrocatalytic ORR. With a specific activity of 1.49 mA/cm^2 and a mass activity of 0.87±0.14 A/mg_{Pt}, the narrowly distributed NPs more than doubled the activity of commercially applied pure Pt catalysts (0.61 mA/cm^2 and 0.42 A/mg_{Pt}, respectively). The obtained results were corroborated by a computational study that had previously predicted NP diameters where exceptional ORR activities were expected. The theoretical activity of 0.99 A/mg_{Pt} for NPs of the obtained diameter and size distribution coincided with our experimental study. The MOF template concept therefore represents a novel approach for the challenging synthesis of precise NPs in the range of 1 nm, where narrow size distributions are crucial for high catalytic activity.[171]

The concept was explored for larger clusters like $[Pt_{19}(CO)_{22}](NBu_4)_2$ and $[Pt_{38}(CO)_{44}](NBu_4)_2$ which could be successfully synthesized and encapsulated in ZIF-8, although an increased cluster concentration was found at the MOF crystal surface. Due to incomplete confinement and stabilization, the synthesis procedure needs to be improved in future experiments, potentially further exploring a core-shell approach towards Pt_x@ZIF-8@ZIF-8. Instead of in ZIF-8, the *Chini* cluster $[Pt_9(CO)_{18}](NBu_4)_2$ was also tried to be integrated into other ZIFs with

varying functionalities. The only moderately successful experiment was its inclusion in ZIF-90, however only low Pt contents were achieved. The reason for the latter could so far not be elucidated, although several explanations were refuted *via* control experiments. The aldehyde functionalities in ZIF-90 provided an additional stabilization to the cluster and significantly slowed down its oxidation under atmospheric conditions. These variations of the initial $Pt_{12\pm x}$@ZIF-8 systems constitute the starting point for several further investigations where after the optimization of the syntheses, studies towards cluster size effects in catalysis are conceivable. Additionally, the influence of cluster size and MOF functionality on the size of NPs resulting from acidic MOF digestion are of high interest. This way, important tuning parameters towards the synthesis of high-precision NPs with potential extraordinary electrocatalytic activities would be available.

In the second part of this project, the MOF template approach was transferred from Pt to Au clusters, where a great variety of cluster compounds with precise atomicities is known to literature. Due to the tendency of gold to agglomeration and the need for more strongly binding ligands like thiols and phosphines, the realization of Au@ZIF-8 compounds was not trivial. Several phosphine-stabilized Au clusters were reproduced from literature but could not be encapsulated in ZIF-8 due to insufficient interactions. Therefore, the hydrophilic cluster $[Au_8(tppms)_8](NO_3)_2$ was synthesized *via* a biphasic ligand exchange reaction and subsequently introduced into ZIF-8 to yield $[Au_8(tppms)_8](NO_3)_2$@ZIF-8 in different loadings. After adaptation of ligand removal procedures for supported Au phosphine clusters from literature, a thermal and oxidative treatment was established for the novel material. Primarily with ^{31}P-NMR studies, it could be demonstrated that the majority of phosphine ligands was detached from the Au core and was present as phosphine oxide in the MOF pores. All materials were extensively characterized with DR-UV/Vis and IR spectroscopy, PXRD, nitrogen sorption, XPS, HR-TEM and HAADF-STEM, among others. First trials with the catalyst Au_8@ZIF-8 failed, presumably due to the small Au core size of the embedded clusters that is catalytically inactive.

Future studies should aim at a better understanding of the governing factors for the encapsulation of cluster species in the MOF pores, as well as the transfer of the concept to other mono- and bimetallic metal clusters for encapsulation in different MOFs. Further methods to determine the exact cluster size could be envisaged, such as X-ray absorption near edge structure (XANES), small-angle X-ray scattering (SAXS) or small-angle neutron scattering (SANS). Nonetheless, if with SAXS and SANS sufficient resolution for the subnanometer Pt clusters can be achieved, these methods only give an average particle diameter and cannot give information about the atomic precision of every cluster. Additionally, in XANES and SAXS

beam damage to the stabilizing framework as in the failed EXAFS experiments cannot be excluded.

The manifold of parameters to influence the controlled agglomeration of the clusters upon ZIF digestion has not been explored yet. One of the most crucial, potential variations is the choice of support to deposit the metal@MOF material on before the acidic digestion. Apart from the applied glassy carbon, studies with tungsten carbide are currently underway in collaboration with *Patrick Bretzler* from the chair of *Prof. Köhler* at the TU Munich,[184] but also titania or silica supports are feasible for catalytic applications. In addition, many highly active catalysts could be derived from MOFs *via* pyrolysis.[162] Due to the insulating nature of ZIF-8, it is necessary to remove the framework before electrocatalysis, but pyrolysis to doped carbon would render the material conductive. It is questionable, to what degree the clusters e.g. in $Pt_{12\pm x}$@ZIF-8 would agglomerate, and if bimetallic NPs could be incorporated and stabilized in such an approach. Thus, the synthesized $Pt_{12\pm x}$@ZIF-67 could yield Pt/Co sites, for which exceptional electrocatalytic activity has been reported in other materials.[71]

For the "Au_8@ZIF-8" system, further experiments towards a better understanding of the exact nature of the cluster species in the MOF are still pending, including the exact cluster charge, the number of ligands still attached to the Au core, as well as the location and removal of the free, oxidized phosphine ligands in the pores. Additionally, it would be highly interesting to use the gold inclusion compound as a source for small NPs *via* the digestion of "Au_8@ZIF-8" on a glassy carbon electrode analogously to the Pt NP procedure. An initial trial for the application in the HER showed a promising result for the specific activity, although the latter must be appropriately normalized to the Au loading and compared to the mass activity of a Au(111) surface. Studies in the *Bandarenka* group are underway to establish an electrochemical setup for the Au-catalyzed methanol oxidation to further evaluate the potential of "Au_8@ZIF-8"-derived nanocatalysts.

With alloy catalysts as a promising method to reduce electrocatalyst costs, further bimetallic NPs could be obtained with the introduced template approach. Several carbonyl-stabilized Pt/Ni or Pt/Co clusters are literature-known and could be encapsulated similarly to the *Chini* clusters. A cooperation with *Prof. Stefano Zacchini*, University of Bologna, Italy, is currently being established to obtain atom-precise, mixed-metal clusters directly from the carbonyl cluster experts. Subsequent encapsulation and decarbonylation should lead to novel alloy@MOF materials, from which precise NPs with potentially high activities could be generated. Unpublished computational studies of our cooperation partners also predict high ORR activities for core-shell structures with small Au NPs coated with few monolayers of Pt.[185] For such materials, the utilization of the Au_8@ZIF-8 material could be further investigated as a possibility to synthesize small and precise Au NPs.

5 EXPERIMENTAL PART

5.1 General Methods

Preparation Techniques

All commercially available chemicals (mainly *Sigma-Aldrich*, *abcr* and *Acros*) were used without further purification, unless stated otherwise. Methanol was dried over magnesium and iodine and stored over molecular sieves. All solvents were thoroughly degassed before usage. Reactions with air or moisture sensitive compounds were handled under *Schlenk* conditions in preheated glassware under argon atmosphere, while an overpressure of argon was maintained during the whole reaction. Herein, argon was purified by successively passing it over a heated copper(I) catalyst and activated molecular sieves (4 Å) to remove residual oxygen and water contents. All glassware was flame dried in vacuum and silylated prior to usage. To this end, small amounts of 1,1,1,3,3,3-hexamethyldisilazane were heated to reflux inside the closed apparatus using a hot air gun and subsequently removed under reduced pressure. Centrifugations under *Schlenk* conditions are carried out in specially designed *Schlenk* centrifugation tubes in a Rotanta 460 by *Hettich* with 2000 rpm for 10 min each.

Electrochemical measurements

For the rotating disk electrode (RDE) measurements the glassy carbon RDE with 5 mm diameter purchased from *Pine instruments*, USA was used. BioLogic VSP-300 potentiostat (*BioLogic*, France) was used for all of the electrochemical techniques. All of the reported potentials in this work are referred *vs.* RHE. The solid powder of commercial Pt/C catalyst (19.6 wt% TEC10V20E) produced by *Tanaka Kikinzoku* was used as received, and the ORR activity tests we done under similar conditions as for Pt NPs. Initially the Pt@ZIF-8 was dispersed in pure methanol, then an aliquot from the solution was dried on a glassy carbon electrode while rotating at 300 rpm in order to produce a homogeneous catalyst layer. Stability test were done by making 1500 cycles between 0.6–1.0 V vs RHE in 0.1M $HClO_4$ at 50 mV/s. Prior to each measurement the glassy carbon electrode is polished with 1, 0.3, 0.05 µm alumina paste, respectively and rinsed with ultra-pure water. Cyclic voltammograms were recorded in Ar-saturated 0.1M $HClO_4$ solution. For ORR activity measurements, O_2 saturated 0.1M $HClO_4$ was used as an electrolyte. In all of the measurements, Pt wire and mercury-mercury sulfate were used as a counter and reference electrodes, respectively. For the HER experiments with Au_8@ZIF-8, 10 mg of the material were dispersed in 10 ml of pure MeOH and sonicated for 30 min. 10 µL of this suspension were deposited on a glassy carbon electrode and dried while rotating at 400 rpm. Afterwards, the cyclic voltammograms were

recorded in Ar saturated 0.1M $HClO_4$ at 1600 rpm with a scan speed of 50 mV/s. Other specifications are identical to the ORR experiment.

Olefin hydrogenation catalysis

For hydrogenation reactions, 10 mg of $[Pt_{12\pm x}]$@ZIF-8 (1 mol%; 1 wt.% Pt) are suspended with the respective amount of alkene in toluene-d_8 (0.5 mL) in a *J Young* NMR tube. The tube is frozen, evacuated, and pressurized with 1.5 bar H_2 at room temperature. Conversions are determined *via* ^{1}H-NMR in regular time intervals. Reactions with $[Pt_{12}(CO)_{24}](NBu_4)_2$@ZIF-8 as a catalyst are carried out analogously. For recycling reactions, the reaction was scaled up to 100 mg of catalyst and carried out in a *Fisher-Porter* bottle with pressure gauge. After 3 h, the reaction suspension was centrifuged and complete conversion was confirmed via NMR. The catalyst was dried and activated at 150 °C under vacuum for 2 h and then reapplied in the catalysis.

5.2 Analytical Methods

UV/Vis spectroscopy

UV/Vis spectra in solution were measured on a Cary 60 UV/Vis spectrometer from *Agilent Technologies*. All spectra were measured at room temperature in dry methanol in a SUPRASIL® quartz cuvette with a layer thickness of 10 mm and an attached *Schlenk* valve. Solid state UV/Vis spectra were collected in diffuse reflectance mode with a UV-3600 Plus with integrating sphere unit by *Shimadzu*. Air-sensitive samples were put between two glass slides in the glovebox and sealed with silicon grease.

FT-IR spectroscopy

FT-IR spectroscopy was performed on a *PerkinElmer* Frontier FT-IR spectrometer with an ATR sampling unit or in a glovebox LABstar ECO by *MBRAUN* on a *Bruker* ALPHA with PLATINUM-ATR unit. Spectra were collected from 4000−650 cm^{-1} with 16 scans and a resolution of 4 cm^{-1}.

In-situ IR measurements (see chapter 3.1.1) were performed by Miguel Rivera Torrente in the group of Prof. Bert Weckhuysen, Utrecht, Netherlands. Spectra were recorded on a *PerkinElmer* System 2000 instrument (32 scans, 4 cm^{-1} resolution, DTGS detector, cell with KBr windows). To avoid any effects of palletization, the materials were prepared by suspending a few milligrams in MeOH (HPLC Spectrograde, 99.999%, *Sigma-Aldrich*) and then casted over 1x1 cm^2 pure Si wafers (non-doped, 250 µm thick, *Sil'Tronix*, Archamps, France), which resulted in a fine material layer. Thereafter, the wafers were introduced in the cell and

evacuated under vacuum ($p < 1 \cdot 10^{-5}$ mbar) at 298 K for 30 min. After this time, the cell was heated (2 $K \cdot min^{-1}$) to 473 K and spectra recorded at the described temperatures.

Kinetic measurements in solution using *in situ* IR spectroscopy were performed under an argon atmosphere using a ReactIR 45m from *Mettler Toledo* equipped with a DST series AgX fiber conduit (1.5 m, 9.5 mm) with a SiComp sensor. Spectra were processed with iC IR 7.0 software from *Mettler Toledo*.

Powder X-Ray Diffraction (PXRD)

PXRD measurements were performed on a *PANalytical* Empyrean diffractometer equipped with a *PANalytical* PIXcel 1D detector. X-ray Cu K_α radiation (λ_1=1.5406 Å, λ_2=1.5444 Å, λ_1/λ_2=0.5) was used for the measurements, while K_β radiation was removed with a nickel filter. The voltage was 45 kV and the intensity 40 mA. The measurement range was from 5.08 to 50.08 (2θ) with a step size of 0.0408 (2θ) and an acquisition time of 35 seconds per step. Simple control measurements of standard samples were in part carried out on the *PANalytical* Aeris Benchtop PXRD at the chair of Prof. Fässler, Technical University of Munich.

Nitrogen Adsorption (BET)

Adsorption measurements with N_2 at 77 K were carried out on a 3Flex Physisorption from *Micromeritics Instrument Corp.*, which uses a volumetric method to determine the amount adsorbed under an equilibrated gas pressure. Adsorption data was processed using the 3Flex Software Version 5.01 by *Micromeritics*. Samples were weighed into sample tubes and capped with *Micromeritics* CheckSeals. Samples were subsequently activated again for twelve hours at room temperature using a SmartVac Prep by *Micromeritics* to ensure absence of unwanted adsorbates and identical pre-measurement states of all samples. The mass of the adsorbens was then recorded, generally in the range of 25-100 mg. Free-space of the sample tube is determined prior to measuring each adsorption isotherm using Helium**.** A liquid nitrogen bath is used for measurements at 77 K. Calculations for the fraction of pores occupied by Pt clusters are based on the molar amount of zinc with the condition that there are six times more zinc atoms than pores in ZIF-8. This results in 0.59% of pores being occupied with the usual Pt loading of 1 wt% and a theoretical Pt loading of 47.5 wt% if all pores held a *Chini* cluster.

Thermogravimetric Analysis (with Mass Spectrometry, TGA-MS)

Thermogravimetric studies (TGA and TGA-MS) were conducted on a *Mettler Toledo* TGA/STA 409 PC device and a *Netzsch* QMS 403 Aeolos device for additional mass spectrometry analysis. Measurements were carried out in aluminum oxide pans (70 µL with lid) with sample amounts of 1 to 5 mg.

X-Ray Photoelectron Spectroscopy (XPS)

XPS measurements were performed by Tim Kratky in the group of Prof. Dr. Sebastian Günther, Technical University of Munich, Germany. XP spectra were recorded on a *Leybold-Heraeus* LHS 10 spectrometer using a non-monochromatized Mg K_α source (1253.6 eV). The powder samples were pressed into cavities and measured as pellets. Preparation of $[Pt_9(CO)_{18}](NBu_4)_2$@ZIF-8 and the transfer into the XPS spectrometer were carried out under argon atmosphere. $[Pt_9(CO)_{18}](NBu_4)_2$@ZIF-8 was oxidized in 200 mbar O_2 at room temperature overnight and subsequently heated to 200 °C under vacuum (≤10^{-6} mbar) for 3 hours leading to $[Pt_{12\pm x}]$@ZIF-8. All spectra were acquired in an ultra-high vacuum chamber at a pressure below 5×10^{-8} mbar. The analyzer was operated at a constant pass energy of 100 eV leading to an energy resolution with a full width at half-maximum (FWHM) of ~1.1 eV. The energy scale of the spectra was corrected for sample charging by using the C 1s main signal (284.8 eV, adapted from literature for ZIF-8). The intensity of all spectra was scaled to the total peak S4 area of Zn $2p_{3/2}$. Core level spectra were deconvoluted by using *Doniach-Sunjic* functions, *Voigt* functions, and linear background subtraction.

Elemental Analysis

All measurements were carried out in the microanalytics laboratory of the catalysis research center. C, H, N, S analysis was performed with an elemental analyzer Euro EA by *HEKAtech via* flash combustion and subsequent chromatographic separation. Zn and Au were analyzed by AAS (Atomic Absorption Spectroscopy) utilizing an *Agilent Technologies 200* (280FS AA). Pt, Ti and P loadings were determined by acidic digestion of the material. For Pt, $SnCl_2$ solution was added and the amount of Pt was determined photometrically *via* UV/Vis spectroscopy on an *Agilent Technologies* Cary 100-UV/Vis. The phosphorus content was quantified photometrically as phosphate vanadate complex.

Microscopic Methods (HR-TEM and HAADF-STEM)

HR-TEM and HAADF-STEM measurements were performed by Ing. Ondřej Tomanec, RCPTM (www.rcptm.com), Olomouc, Czech Republic. For high-resolution transmission electron microscopy (HR-TEM), samples were prepared by drying a methanol dispersion of the powder sample on a holey carbon film on a copper grid. Samples were measured with a High-Resolution Transmission Electron Microscope Titan G2 (*FEI*) with Image corrector on accelerating voltage 80 kV. Images were taken with a BM UltraScan CCD camera (*Gatan*). STEM images were taken with HAADF detector 3000 (*Fishione*). Energy Dispersive Spectrometry (EDS) was performed in Scanning TEM (STEM) mode by Super-X system with four silicon drift detectors (*Bruker*).

HR-TEM measurements of digested [$Pt_{12\pm x}$]@ZIF-8 samples were performed by Jan Michalička, CEITEC (www.ceitec.eu), Brno, Czech Republic. To investigate NPs after ZIF dissolution, HR-TEM samples were prepared by dropping a suspension of [$Pt_{12\pm x}$]@ZIF-8 (100 mg dispersed in 10 mL MeOH) on carbon-coated Cu400 TEM grids. After drying the grid was immersed in 1M $HClO_4$ for 2 h. Samples were imaged by HR-TEM FEI TITAN Themis 60-300 equipped with X-FEG type emission gun operated at 300 kV and spherical aberration C*s* image corrector improving resolution limit in TEM mode below 0.7 nm.

Electrospray Ionization with Mass Spectrometry (ESI-MS)

ESI-MS spectra were recorded on a *Thermo Scientific LCQ Fleet Spectrometer* of *Thermo Fisher Scientific*. A time-of-flight analyzer was used for mass detection.

Nuclear Magnetic Resonance Spectroscopy (NMR)

Liquid phase, high resolution ^{1}H-NMR (400 MHz) and ^{31}P-NMR (162 MHz) were measured on a *Bruker* Advance III AV400 US or a *Bruker* DRX-400 spectrometer at 298 K. Spectra are referenced relative to the residual solvent signals ($CDCl_3$ 7.26 ppm, CD_2Cl_2 5.32 ppm, toluene-d_8 7.09 ppm, D_2O 4.79 ppm). Chemical shifts (δ) are given in ppm (parts per million) downfield shifted from TMS. Multiplicities are abbreviated as s = singlet, d = doublet, t = triplet, m = multiplet, brs = broad singlet. Spectral data was processed using TopSpin 2.1 software packages and manipulated using the software MestReNova (*Mestrelab Research S.L.*).

Solid state MAS-NMR measurements were performed by Dr. Gabriele Raudaschl-Sieber at 298 K on a *Bruker* Avance 300 (^{1}H-NMR: 300 MHz, ^{13}C-NMR: 75 MHz, ^{31}P-NMR: 121 MHz) in a 4 mm ZrO_2 rotor fixed to a 4 mm MAS probe head (rotation frequency 15 kHz or 8 kHz). The ^{1}H-spectra were recorded with single pulse technique, the ^{13}C-spectra with cross polarisation (CPMAS) and the ^{31}P-spectra with high power decoupling (HPDEC). The external standard for ^{1}H- and ^{13}C-measurements was adamantane with a chemical shift of 2.00 ppm and 29.47 ppm (both vs. TMS), respectively. $NH_4H_2PO_4$ with a chemical shift of 1.11 ppm was used as the external standard for the ^{31}P-NMR measurements (versus $H_3PO_{4,konz.}$with 0.00 ppm).

Hydrogen Absorption Measurements

Hydrogen absorption measurements (see chapter 3.1.1) were performed by Sebastian Ehrling at the chair of Prof. Kaskel, Technical University Dresden. Hydrogen adsorption isotherms were measured at 77 K using a *Quantachrome* Autosorb-1C apparatus. Prior to the measurement, the samples were evacuated at 423 K for 10 h.

Methanol Adsorption

Methanol adsorption measurements (see chapter 3.1.1) were performed by Rifan Hardian at the chair of Prof. Llewellyn, Université Aix-Marseille, France. MeOH was distilled and stored over molecular sieves prior to use. The laboratory-made adsorption apparatus includes a symmetrical balance and allows a continuous introduction of vapor to the sample in a slow enough manner to ensure quasi-equilibrium between the vapor and solid and a high-resolution isotherm plot.

5.3 Synthetic Procedures

Most of the following procedures were taken or adapted from the literature. References are given in each case.

5.3.1 Platinum clusters

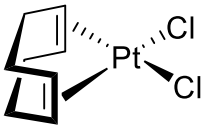

[Pt(COD)Cl$_2$]

M = 374.16 g/mol

In a 500 mL round bottom flask, 2.00 g K_2PtCl_4 (4.82 mmol, 1.00 eq.) are dissolved in a mixture of water (54 mL) and acetic acid (64 mL). 1.60 mL 1,5-cyclooctadiene (1.41 g, 13.0 mmol, 2.70 eq.) is added and the reaction mixture is heated to 110 °C for two hours. The pale-yellow solution with few white needles is reduced to ca. 40 mL under reduced pressure and stored at 0 °C overnight. The cold suspension is filtered and the white solid is washed with water, EtOH and Et_2O (20 mL each). The product is dissolved from the filter with CH_2Cl_2 (80 mL) and the solvent is removed to obtain 1.70 g of $Pt(COD)Cl_2$ (4.54 mmol, 94%) as a white powder.[186]

^{1}H-NMR (400 MHz, CD_2Cl_2, 298 K): δ = 5.57 (t, 4H, C*H*), 2.84 – 2.60 (m, 4H, CH*H*), 2.43 – 2.14 (m, 4H, C*H*H).

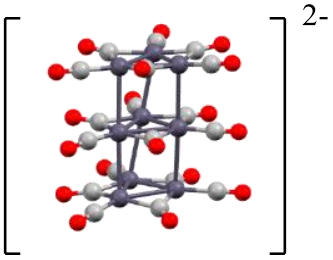

[Pt$_9$(CO)$_{18}$](NBu$_4$)$_2$

M = 2744.93 g/mol

A solution of 1.85 g K_2CO_3 (13.4 mmol, 20.0 eq.) in degassed MeOH (60 mL) is added *via* a Teflon cannula to a suspension of 250 mg $Pt(COD)Cl_2$ (668 μmol, 1.00 eq., 3 wt% Pt/SiO_2) and fumed SiO_2 (4.35 g) in degassed acetone (100 mL). The slurry is stirred overnight, and the solvent is removed *in vacuo*. The resulting yellow powder is transferred to a *Fisher-Porter* tube in the glovebox and exposed to CO (1 bar) for 72 h at room temperature. The purple powder is extracted with MeOH (4 × 20 mL) on a glass frit and the dark red solution is concentrated to 30 mL under vacuum. By adding 300 mg NBu_4Cl (1.08 mmol, 14.6 eq.) in degassed water (10 mL), the cluster is precipitated. With a Whatman filter, the supernatant is removed and the solid is washed with degassed water (2 × 10 mL). After drying under vacuum, 124 mg of $[Pt_9(CO)_{18}](NBu_4)_2$ (45.2 μmol, 59%) are obtained as a dark red powder.[62]

UV/Vis (MeOH): λ_{max} (nm) = 364, 423, 503, 557.

IR: ν_{CO} (cm^{-1}) = 1794, 1827, 1996.

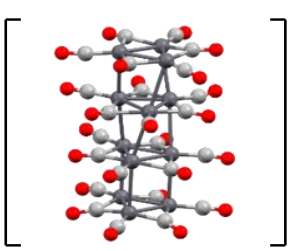

$2\ NBu_4^+$

$[Pt_{12}(CO)_{24}](NBu_4)_2$

M = 3498.27 g/mol

500 mg Na_2PtCl_6 (1.10 mmol, 1.00 eq.) are added to a solution of 200 mg NaOH (5.00 mmol, 4.55 eq.) in MeOH (10 mL) and a slow stream of CO was bubbled through the reaction mixture for twelve hours. The orange solution turns blue-green and a white precipitate forms that is removed by Whatman filtration. The solution is concentrated *in vacuo* and precipitated *via* addition of 200 mg NBu_4Br (620 µmol, 6.76 eq.) in MeOH (3 mL). After storing at −80 °C overnight, the solid is separated by filtration, washed with THF (2 × 5 mL) and dried under vacuum. 30.0 mg $[Pt_{12}(CO)_{24}](NBu_4)_2$ (8.58 µmol, 9%) are obtained as a black-blue powder.[54]

UV/Vis (MeOH): λ_{max} (nm) = 390, 508, 616.

IR: ν_{CO} [cm^{-1}] = 1813, 1848, 2025.

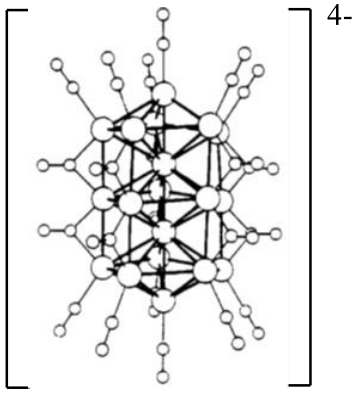

$4\ NBu_4^+$

$[Pt_{19}(CO)_{22}](NBu_4)_4$

M = 5292.81 g/mol

A solution of 100 mg $[Pt_9(CO)_{18}](NBu_4)_2$ (36.4 µmol, 1.00 eq.) in acetonitrile (20 mL) was stirred at 80 °C for 90 minutes. Subsequently, the solvent was removed and the resulting solid was dried under vacuum. 64.9 mg of $[Pt_{19}(CO)_{22}](NBu_4)_4$ (12.3 µmol, 72%) are obtained as a black solid.[58]

IR: ν_{CO} [cm^{-1}] = 1765, 1950.

IR: ν_{CO} [cm^{-1}] (MeCN) = 1799, 1993.

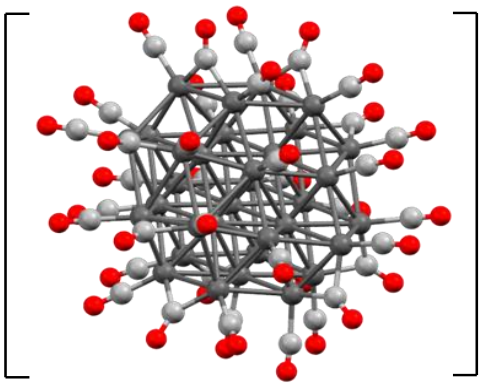

2 NBu_4^+

$[Pt_{38}(CO)_{44}](NBu_4)_2$

M = 5292.81 g/mol

40 mg $[Pt_{19}(CO)_{22}](NBu_4)_4$ (7.56 µmol, 1.00 eq.) are dissolved in acetonitrile (5 mL) and under stirring, 600 µL $HBF_4 \cdot Et_2O$ (4.37 mmol, 578 eq.) is added dropwise. After 15 min, the supernatant is removed via Whatman filtration and the solid is washed with acetonitrile (3 × 2 mL) and dried under vacuum. 2.30 mg $[Pt_{38}(CO)_{44}](NBu_4)_2$ (0.435 µmol, 6%) are obtained as a dark grey powder.[57]

IR: ν_{CO} [cm^{-1}] = 1796, 1992.

IR: ν_{CO} [cm^{-1}] (MeCN) = 1804, 2054.

5.3.2 Gold clusters

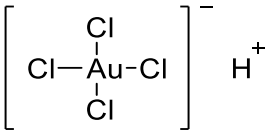

$HAuCl_4 \cdot 3H_2O$

M = 393.83 g/mol

Under stirring, 10.0 g of Au (50.8 mmol, 1.00 eq.) are dissolved in a wide crystallization dish in aqua regia (75% conc. HCl, 25% conc. HNO_3, 300 mL) over 24 h at 50 °C. The orange solution is reduced to 50 mL at 140 °C and concentrated HCl (50 mL) is added. The procedure of concentration and HCl addition is repeated until no more evolution of nitric vapors is observed (ca. five times). After subsequent reduction of the solution to 30 mL, H_2O (100 mL) is added and once more, reduction of the solution to 50 mL at 80 °C and further addition of H_2O is repeated, until a litmus paper held into the vapors indicates a pH of 7 (ca. 1.5 L of H_2O). The solution is concentrated to 150 mL, filtered, and the crystallization dish is put into a desiccator with conc. H_2SO_4. Under a vacuum of 300 mbar, $HAuCl_4$ crystallizes over the course of several weeks. 19.8 g (50.3 mmol, 99%) of the product are obtained as orange needles.

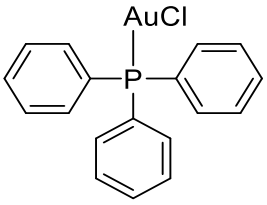

Au(PPh$_3$)Cl

M = 494.71 g/mol

A solution of 2.73 g PPh_3 (10.4 mmol, 1.80 eq.) in degassed ethanol (54 mL) is added at once to a solution of 2.00 g $HAuCl_4$ (5.87 mmol, 1.00 eq.) in degassed ethanol (27 mL). A white precipitate forms immediately and the mixture is stirred for 5 min at room temperature. The suspension is filtered under air and the white solid is washed with diethyl ether (3 × 20 mL) and dried under vacuum. 2.11 g (4.27 mmol, 73%) of the product was obtained as a white powder.[187]

^{1}H-NMR (400 MHz, CD_2Cl_2, 298 K): δ (ppm) = 7.65 – 7.41 (m, 15H, H-Ar).

^{31}P-NMR (162 MHz, CD_2Cl_2, 298 K): δ (ppm) = 33.1.

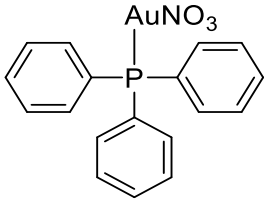

Au(PPh$_3$)NO$_3$

M = 521.26 g/mol

To a solution of 2.50 g Au(PPh_3)Cl (5.05 mmol, 1.00 eq.) in CH_2Cl_2 (50 mL) is added dropwise a solution of 1.80 g $AgNO_3$ (10.6 mmol, 2.10 eq.) in MeOH (100 mL). The suspension is stirred for one hour under the exclusion of light and filtered over a glass frit with 2 cm of Celite to remove pale pink AgCl. After washing with CH_2Cl_2 (50 mL), the solvent is removed under vacuum and the white precipitate is again dissolved in CH_2Cl_2 (50 mL). A second filtration of a 2 cm layer of Celite with subsequent washing with CH_2Cl_2 (50 mL) yielded the product after solvent removal and drying under vacuum. 2.48 g Au(PPh_3)NO_3 (4.76 mmol, 94%) are obtained as a white powder.[188]

^{1}H-NMR (400 MHz, CD_2Cl_2, 298 K): δ (ppm) = 7.65 – 7.44 (m, 15H, H-Ar).

^{31}P-NMR (162 MHz, CD_2Cl_2, 298 K): δ (ppm) = 27.2.

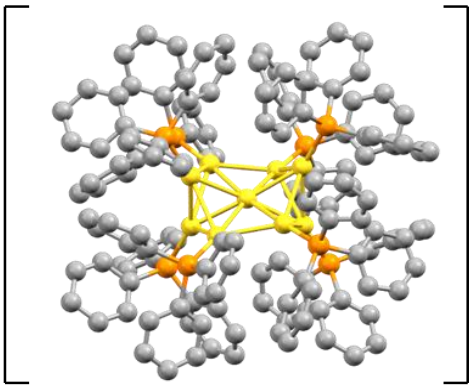

$[Au_9(PPh_3)_8](NO_3)_3$

M = 4057.04 g/mol

1.00 g $Au(PPh_3)NO_3$ (1.92 mmol, 1.00 eq.) is suspended in EtOH (40 mL) and a solution of 18.0 mg $NaBH_4$ (476 µmol, 0.25 eq.) in EtOH (23 mL) is added dropwise. The brown reaction mixture is stirred for two hours under exclusion of light, filtered, and the solvent is removed in vacuo. The residue is dissolved in CH_2Cl_2 (10 mL), filtered a second time and upon solvent removal at reduced pressure, a brown, foamy solid is obtained. After careful washing with MeOH (5 mL) and THF (2 × 8 mL), and drying under vacuum, 276 mg of $[Au_9(PPh_3)_8](NO_3)_3$ (68.0 µmol, 32%) are obtained as a dark green powder.[175]

^{31}P-NMR (162 MHz, CD_2Cl_2, 298 K): δ (ppm) = 56.9.

UV/Vis (MeOH): λ_{max} (nm) = 314, 349, 379, 442.

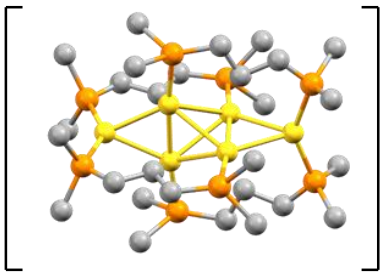

$[Au_6(dppp)_4](NO_3)_2$

M = 2955.61 g/mol

Under exclusion of light, 509 mg dppp (1.23 mmol, 20.0 eq.) are added to a solution of 250 mg $[Au_9(PPh_3)_8](NO_3)_3$ (61.6 µmol, 1.00 eq.) in CH_2Cl_2 (16 mL) and stirred for 15 min. The product was precipitated by addition of toluene (80 mL), filtered and washed with toluene (20 mL) and Et_2O (20 mL). After drying *in vacuo*, 55.0 mg $[Au_6(dppp)_4](NO_3)_2$ (18.6 µmol, 45%) are obtained as a blue powder.[176]

^{1}H-NMR (400 MHz, CD_2Cl_2, 298 K): δ (ppm) = 7.27 (d, ^3J = 6.5 Hz, 16H, H-Ar), 7.12 (t, ^3J = 7.4 Hz, 8H, H-Ar), 6.93 (m, 40H, H-Ar), 6.49 (t, ^3J = 7.5 Hz, 16H, H-Ar), 2.81 (br s, 8H, CH_2), 1.98 (br s, 8H, CH_2), 1.85 (br s, 8H, CH_2).

^{31}P-NMR (162 MHz, CD_2Cl_2, 298 K): δ (ppm) = 62.5, 53.3.

UV/Vis (MeOH): λ_{max} (nm) = 261, 289, 324, (515), 587.

ESI-MS (m/z): 609.78 ($[Au_2(dppp)_2]^{2+}$), 1012.60 ($[Au_4(dppp)_3]^{2+}$), 1209.60 ($[Au_6(dppp)_3]^{2+}$), 1414.81 ($[Au_6(dppp)_4]^{2+}$).

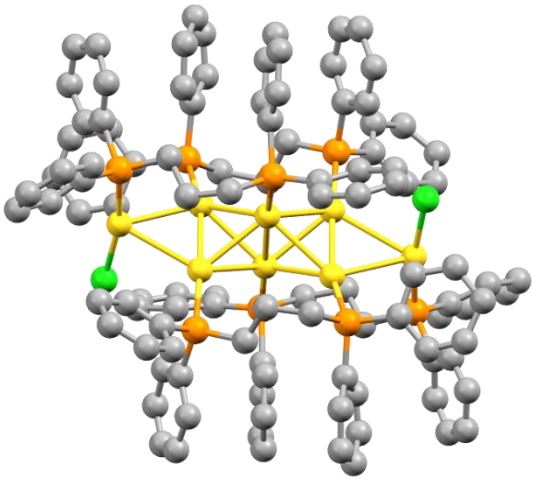

$[Au_8(dppp)_4Cl_2](PF_6)_2$

M = 3586.87 g/mol

A solution of 60.3 mg $Au(PPh_3)Cl$ (122 µmol, 9.04 eq.) in $CHCl_3$ (2 mL) is added dropwise to a solution of 40.0 mg $[Au_6(dppp)_4](NO_3)_2$ (13.5 µmol, 1.00 eq.) in MeOH (5 mL). Upon stirring for 60 min, the dark blue solution turns bright pink. By addition of Et_2O (60 mL) and stirring for 30 min, the cluster is precipitated as the nitrate salt, filtered and washed with ^{i}PrOH (20 mL). The pink solid is dissolved in EtOH/MeOH (1/1, 160 mL), 40.0 mg NaPF6 () are added and the mixture is stirred for 30 min. The pink solid is removed via filtration, washed with EtOH (40 mL) and dried under vacuum. 11.5 mg $[Au_8(dppp)_4Cl_2](PF_6)_2$ (3.21 µmol, 24%) are obtained as a bright pink powder.[106]

UV/Vis (MeOH): λ_{max} (nm) = 389, 508.

PL (λ_{ex} = 510 nm, MeOH): λ_{max} (nm) = 591.

ESI-MS (m/z): 1209.46 ($[Au_6(dppp)_3]^{2+}$), 1647.22 ($[Au_8(dppp)_4Cl_2]^{2+}$).

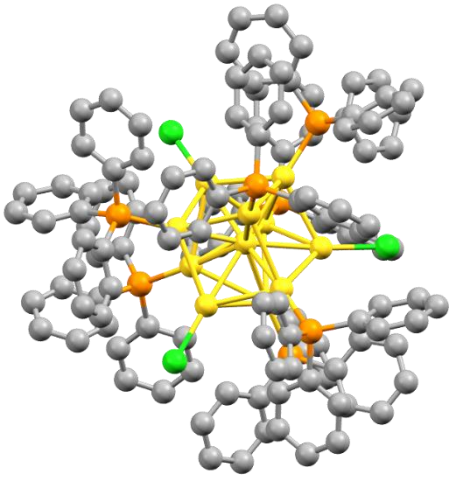

$[Au_{11}(PPh_3)_8Cl_2]$

M = 4371.32 g/mol

500 mg $Au(PPh_3)Cl$ (1.01 mmol, 1.00 eq.) are suspended in EtOH (28 mL) and 38.0 mg $NaBH_4$ (1.00 mmol, 1.00 eq.) is added in several portions over 15 min. The reaction mixture is stirred for two hours at room temperature and then poured into hexane (500 mL). The cluster is left to precipitate for 20 h, filtered and washed with hexane (40 mL). The brown solid is dissolved in CH_2Cl_2 (150 mL), again precipitated with hexane (150 mL), filtered and washed with hexane (40 mL). This procedure is repeated three times until after drying, 8.70 mg $[Au_{11}(PPh_3)_8Cl_2]$ (1.99 μmol, 0.2%) are obtained as an orange solid.[177]

^{31}P-NMR (162 MHz, CD_2Cl_2, 298 K): δ (ppm) = 53.0.

UV/Vis (MeOH): λ_{max} (nm) = 308, 379, 421.

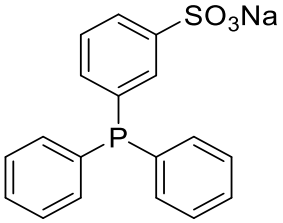

Triphenylphosphine-3-sulfonic acid sodium salt (TPPMS)

M = 364.33 g/mol

In an argon atmosphere and at 0 °C, 4.08 g PPh_3 (15.6 mmol, 1.00 eq.) are added in several portions to oleum (25% SO_3, 20 mL, 95.0 mmol SO_3, 6.08 eq.) and after complete dissolution, the reaction mixture is stirred for two hours at room temperature. The viscous liquid is carefully poured into H_2O (60 mL) in an ice bath. After the addition of 13.5 mL tri*iso*ctylamine (10.8 g, 31.1 mmol, 2.00 eq.) and toluene (5 mL), the solution is stirred for 30 min. After phase separation, the aqueous phase is extracted with 8 wt% $NaOH_{(aq)}$ (ca. 15 mL), until a pH value of 3 is reached. A second extraction with 3 wt% $NaOH_{(aq)}$ (ca. 15 mL) to pH 7-8 and drying of the aqueous phase in vacuo yielded 1.42 g TPPMS (3.90 mmol, 25%) as a white powder. In

some experiments, the product contained up to 15% of the disulfonated compound as an impurity.[189]

^{1}H-NMR (400 MHz, D_2O, 298 K): δ (ppm) = 7.57 (m, 2H), 7.41 (m, 6H), 7.36 (m, 1H), 7.24 (m, 4H), 7.83 (m, 1H), 7.76 (m, 1H), 7.39 (m, 12H).

^{31}P-NMR (162 MHz, D_2O, 298 K): δ (ppm) = -6.64 .

ESI-MS (m/z): 341.30 ($P(C_6H_5)_2(C_6H_4SO_3^-)$).

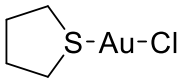

Au(tht)Cl

M = 320.58 g/mol

500 mg THT (5.67 µmol, 2.22 eq.) are added to a solution of 1.01 g $HAuCl_4$ (2.56 µmol, 1.00 eq.) in EtOH (8.5 mL) and H_2O (0.5 mL). The white suspension is stirred for 15 min at room temperature before filtering and washing with ethanol. After the removal of the solvent under vacuum, 712 mg Au(tht)Cl (2.22 µmol, 87%) of a white solid are obtained.[190]

^{1}H-NMR (400 MHz, $CDCl_3$, 298 K): δ (ppm) = 3.40 (brs, 4H, CH_2-C*H*$_2$-S), 2.18 (brs, 4H, C*H*$_2$-CH_2-S).

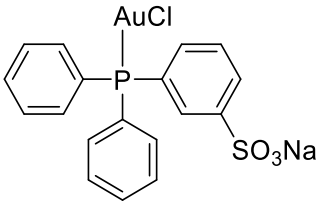

Au(tppms)Cl

M = 596.75 g/mol

805 mg TPPMS (2.22 µmol, 1.00 eq.) are added to a suspension of 712 mg Au(tht)Cl (2.22 µmol, 1.00 eq.) in MeOH (150 mL). The reaction mixture is stirred for 40 min, filtered over *Celite*®, washed with Et_2O (20 mL) and dried under vacuum. 899 mg Au(tppms)Cl (1.51 µmol, *68%*) are obtained as a white powder.[179]

^{1}H-NMR (400 MHz, D_2O, 298 K): δ (ppm) = 8.04 (m, 2H, H-Ar), 7.60 (m, 12H, H-Ar).

^{31}P-NMR (162 MHz, D_2O, 298 K): δ (ppm) = 33.3.

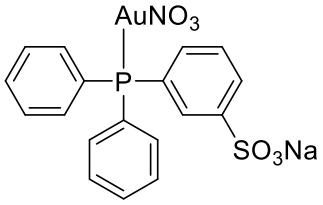

Au(tppms)NO_3

M = 623.30 g/mol

A solution of 1.15 g Au(TPPMS)Cl (1.93 mmol, 1.00 eq.) in MeOH (65 mL) is added dropwise to a solution of 654 mg $AgNO_3$ (3.85 mmol, 2.00 eq.) in MeOH (100 mL). The suspension was stirred for one hour, filtered over *Celite*® and the residue is washed with MeOH. The solvent is removed *in vacuo* at room temperature and 868 mg Au(tppms)NO_3 (1.39 mmol, *72%*) are obtained as a white, temperature-sensitive powder.[188]

^{1}H-NMR (400 MHz, D_2O, 298 K): δ (ppm) = 8.07 (m, 2H, H-Ar), 7.63 (m, 12H, H-Ar).

^{31}P-NMR (162 MHz, D_2O, 298 K): δ (ppm) = 27.7 .

ESI-MS (m/z): 564.28 ($[AuTPPMS]^-$), 878.92 ($[Au(TPPMS)_2]^-$).

$[Au_8(tppms)_8](NO_3)_2$

M = 4614.44 g/mol

A solution of 40.8 mg TPPMS (112 µmol, 9.11 eq.) in degassed H_2O (30 mL) is combined with a solution of 49.7 mg $[Au_9(PPh_3)_8](NO_3)_3$ (12.3 µmol, 1.00 eq.) in degassed CH_2Cl_2 (30 mL) under argon atmosphere. The biphasic reaction mixture is vigorously stirred for one hour and the aqueous phase is separated and centrifuged. The supernatant is dried *in vacuo* and 28.0 mg $[Au_8(tppms)_8](NO_3)_2$ (6.59 µmol, *55%*) are obtained as an orange-brown powder.[180]

^{1}H-NMR (400 MHz, D_2O, 298 K): δ (ppm) = 7.51 (m, 1H), 7.20 (m, 4H), 7.09 (m, 4H), 6.76 (m, 4H), 6.39 (m, 1H).

^{31}P-NMR (162 MHz, D_2O, 298 K): δ (ppm) = 54.4.

UV/Vis (MeOH): λ_{max} (nm) = 470, 415, 300.

5.3.3 ZIF procedures

If not stated otherwise, all procedures are carried out under argon in dried and degassed solvents. All ZIF samples were characterized by FTIR, nitrogen adsorption and PXRD as discussed in the main text with more details in the supplementary figures (see experimental part). Literature values for the surface area of each ZIF are given in parentheses together with the solvent used in the respective literature procedure.

ZIF-8 in H_2O under air ($Zn(mIm)_2$)

A solution of 5.78 g 2-mIm (70.4 mmol, 70.4 eq.) in H_2O (20 mL) is rapidly added to 298 mg $Zn(NO_3)\cdot 6H_2O$ (1.00 mmol, 1.00 eq.) in H_2O (2 mL) and stirred for 5 min. The white precipitate is separated by centrifugation, washed with H_2O (2 × 15 mL) and dried under vacuum. The raw material is heated to 200 °C in vacuo to remove excess 2-mIm and 45.0 mg ZIF-8 (198 µmol, *20%*) are obtained as a white powder.[149]

BET surface area (N_2, 77 K) (m^2/g): 1722. (Lit. (H_2O): 1079)[149]

ZIF-8 in MeOH

Two solutions of 700 mg $Zn(NO_3)_2\cdot 6H_2O$ (2.35 mmol, 1.00 eq.) and 1.55 g 2-mIm (18.9 mmol, 8.04 eq.) in MeOH (20 mL each) are quickly combined under vigorous stirring. After stirring for 5 min, the solution is left to stand for 10 min and the white precipitate is separated by centrifugation. After washing with THF (3 × 20 mL) and drying overnight at 70 °C, 104 mg of ZIF-8 (457 µmol, 19%) are obtained as a white powder. To compare pristine ZIF-8 with $Pt_{12\pm x}$@ZIF-8, an analogous procedure is carried out under inert atmosphere and in dry and degassed MeOH at 50 °C to obtain ZIF-8(50 °C).[148]

BET surface area (N_2, 77 K) (m^2/g): 1533. (Lit. (MeOH): 962, Lit. (DMF): 1630)[145,148]

ZIF-67 ($Co(mIm)_2$)

A solution of 717 mg $Co(NO_3)_2$ (3.92 mmol, 1.00 eq.) in MeOH (40 mL) is quickly poured into a solution of 1.62 g 2-mIm (19.7 mmol, 5.03 mmol) and 2.75 mL NEt_3 (2.00 g, 19.8 mmol, 5.05 eq.) in MeOH (50 mL). The mixture immediately turns bright purple and the purple precipitate is separated by centrifugation and washed with H_2O (2 × 50 mL). After drying overnight at 120 °C, 674 mg ZIF-67 (3.02 mmol, 77%) are obtained as a bright purple powder.[191]

BET surface area (N_2, 77 K) (m^2/g): 398. (Lit. (H_2O): 868)[191]

ZIF-90 ($Zn(ImCOH)_2$)

700 mg $Zn(NO_3)_2 \cdot 6H_2O$ (2.35 mmol, 1.00 eq.) are dissolved in MeOH (20 mL) and 1.81 g ImCOH (18.8 mmol, 8.00 eq.) are dissolved in MeOH (60 mL) together with 2.50 mL NEt_3 (1.82 g, 18.0 mmol, 7.66 eq.). Both solutions are quickly combined under vigorous stirring. After stirring for 5 min, the solution is left to stand for 10 min and the white precipitate is separated by centrifugation. After washing with THF (3 × 40 mL) and drying overnight at 100 °C, 548 mg of ZIF-90 (2.13 mmol, 91%) are obtained as a beige powder.[192]

BET surface area (N_2, 77 K) (m^2/g): 949. (Lit. (DMF): 1250)[192]

ZIF-71 ($Zn(dcIm)_2$)

200 mg $Zn(NO_3)_2 \cdot 6H_2O$ (672 μmol, 1.00 eq.) are dissolved in MeOH (5 mL) and 730 mg dcIm (5.33 mmol, 7.97 eq.) are dissolved in MeOH (20 mL) together with 300 μL NEt_3 (218 mg, 2.15 mmol, 3.20 eq.). Both solutions are quickly combined under vigorous stirring. After stirring for 5 min, the solution is left to stand for 10 min and the white precipitate is separated by centrifugation. After washing with THF (3 × 20 mL) and drying under vacuum, 91.5 mg of ZIF-71 (270 μmol, 40%) are obtained as a beige powder.

BET surface area (N_2, 77 K) (m^2/g): 763. (Lit. (MeOH): 782)[193]

ZIF-65 ($Zn(nIm)_2$)

100 mg $Zn(NO_3)_2 \cdot 6H_2O$ (336 μmol, 1.00 eq.) are dissolved in MeOH (5 mL) and 306 mg nIm (2.71 mmol, 8.06 eq.) are dissolved in MeOH (5 mL) together with 300 μL NEt_3 (218 mg, 2.15 mmol, 6.40 eq.). Both solutions are quickly combined under vigorous stirring. After stirring for 5 min, the solution is left to stand for 10 min and the white precipitate is separated by centrifugation. After washing with THF (3 × 20 mL) and drying under vacuum, 87.2 mg of ZIF-65 (299 μmol, 89%) are obtained as a white powder.

BET surface area (N_2, 77 K) (m^2/g): 333.

ZIF-7 under air ($Zn(bIm)_2$)

700 mg $Zn(NO_3)_2 \cdot 6H_2O$ (2.35 mmol, 1.00 eq.) are dissolved in MeOH (20 mL) and 2.20 g bIm (18.6 mmol, 7.92 eq.) are dissolved in MeOH (20 mL) together with 2.00 mL NEt_3 (1.45 g, 14.3 mmol, 6.09 eq.). Both solutions are quickly combined under vigorous stirring. After stirring for 5 min, the solution is left to stand for 10 min and the white precipitate is separated by centrifugation. After washing with THF (3 × 20 mL) and drying overnight at 80 °C, 603 mg of ZIF-7 (2.00 mmol, 85%) are obtained as a white powder.

ZIF-4 under air ($Zn(Im)_2$)

700 mg $Zn(NO_3)_2 \cdot 6H_2O$ (2.35 mmol, 1.00 eq.) are dissolved in MeOH (20 mL) and 1.25 g Im (18.4 mmol, 7.83 eq.) are dissolved in MeOH (20 mL) together with 2.00 mL NEt_3 (1.45 g, 14.3 mmol, 6.09 eq.). Both solutions are quickly combined under vigorous stirring. After stirring for 5 min, the solution is left to stand for 10 min and the white precipitate is separated by centrifugation. After washing with THF (3 × 20 mL) and drying overnight at 80 °C, 466 mg of ZIF-7 (2.31 mmol, 98%) are obtained as a beige powder.

BET surface area (N_2, 77 K) (m^2/g): 0.

5.3.4 Encapsulation and ligand removal

General procedure for Pt clusters: Encapsulation

700 mg $Zn(NO_3)_2 \cdot 6H_2O$ (2.35 mmol, 1.00 eq.) and 1.55 g 2-methylimidazole (18.9 mmol, 8.02 eq.) are dissolved in methanol (20 mL each) in a Schlenk centrifugation flask. The amount of $[Pt_9(CO)_{18}](NBu_4)_2$ needed for the desired loading is dissolved in methanol (5−10 mL). The cluster and the imidazole solution are added at once under vigorous stirring to the zinc nitrate solution at 50 °C. After one minute of stirring, the turbid suspension is cooled to room temperature and centrifuged (2000 rpm, 10 min). The clear supernatant is removed with a syringe and the red-purple solid is washed with dry THF (3×20 mL) and dried under vacuum. In one experiment, ca. 250 mg $[Pt_9(CO)_{18}](NBu_4)_2$@ZIF-8 (1.09 mmol, 46%) are obtained as a red-purple powder, the amount varying with the cluster loading. For other ZIFs or clusters, the respective ZIF synthesis is combined with the desired amount of dissolved cluster in an analogous procedure.

DR-UV/Vis: λ_{max} (nm) = 374, 508, 56.

General procedure for Pt_9 clusters: Oxidation to Pt_{12} cluster

To oxidize $[Pt_9(CO)_{18}](NBu_4)_2$@ZIF-8 to $[Pt_{12}(CO)_{24}](NBu_4)_2$@ZIF-8, the desired amount is exposed to air overnight. $[Pt_{12}(CO)_{24}](NBu_4)_2$@ZIF-8 is obtained in quantitative yield as a blue powder without any need for purification.

DR-UV/Vis: λ_{max} (nm) = 374, 491, 612.

IR: ν_{CO} [cm^{-1}] = 1868, 2051.

General procedure for Pt clusters: Ligand removal/Decarbonylation

For the decarbonylation, the respective amount of $[Pt_{12}(CO)_{24}](NBu_4)_2$@ZIF-8 (50-500 mg depending on the experiment) is heated to 200 °C in a Schlenk flask under vacuum in a sand bath for four hours. $[Pt_{12\pm x}]$@ZIF-8 is obtained as a grey powder with quantitative yield.

$[Pt_{12\pm x}]$@ZIF-8 digestion for ORR and HR-TEM imaging

$[Pt_{12\pm x}]$@ZIF-8 is dispersed in methanol and an aliquot of the solution is dried on a glassy carbon electrode while rotating at 300 rpm in order to produce a homogeneous catalyst layer. Highly active Pt NPs with a diameter of 1.1±0.17 nm formed upon immersion of the electrode in the acidic electrolyte (0.1M $HClO_4$). The HR-TEM grids for imaging of the Pt NPs after digestion were prepared analogously, for details see chapter 6.2.

General procedure for Au clusters: Encapsulation

A solution of 27.0 mg $Au_8(TPPMS)_8(NO_3)_2$ (5.85 µmol, 0.006 eq.) in H_2O (2.5 mL) and 5.78 g 2-mIm (70.4 mmol, 70.4 eq.) in H_2O (20 mL) are added at once to a solution of 298 mg $Zn(NO_3)\cdot 6H_2O$ (1.00 mmol, 1.00 eq.) in H_2O (2 mL). This resulting white suspension is stirred for 5 min, centrifuged and washed with H_2O (2 × 7.5 mL). After drying *in vacuo*, the raw material is heated to 200 °C under vacuum for 2 h to remove excess 2-mIm. 175 mg $[Au_8(tppms)_8](NO_3)_2$@ZIF-8 (0.77 mmol, *77%*) are obtained as a brown powder. For different Au loadings, the amount of cluster is adjusted respectively.

^{31}P-MAS-NMR (121 MHz, 297 K): δ (ppm) = 57.8, 32.0, -4.3.

DR-UV/Vis: λ_{max} (nm) = 415, 470.

BET surface area (N_2, 77 K) (m^2/g): 1530.

General procedure for Au clusters: Oxidative ligand removal

The desired amount of $[Au_8(tppms)_8](NO_3)_2$@ZIF-8 is heated to 150 °C under 1 bar O_2 in a sand bath in a Fisher-Porter bottle equipped with a pressure gauge for the desired amount of time. $[Au_8]$@ZIF-8 is obtained in quantitative yield as a beige to yellow powder.

^{31}P-MAS-NMR (121 MHz, 297 K): δ (ppm) = 56.4, 32,1.

5.4 Supplementary Data

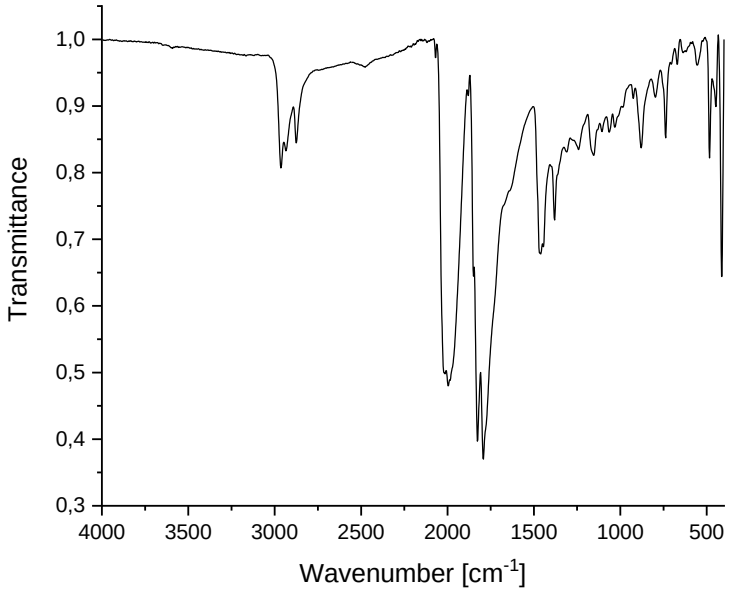

Supplementary Figure 1: FT-IR spectrum of $[Pt_9(CO)_{18}](NBu_4)_2$ with the intense bands for bridging (1790 cm^{-1}) and terminal (1992 cm^{-1}) CO ligands.

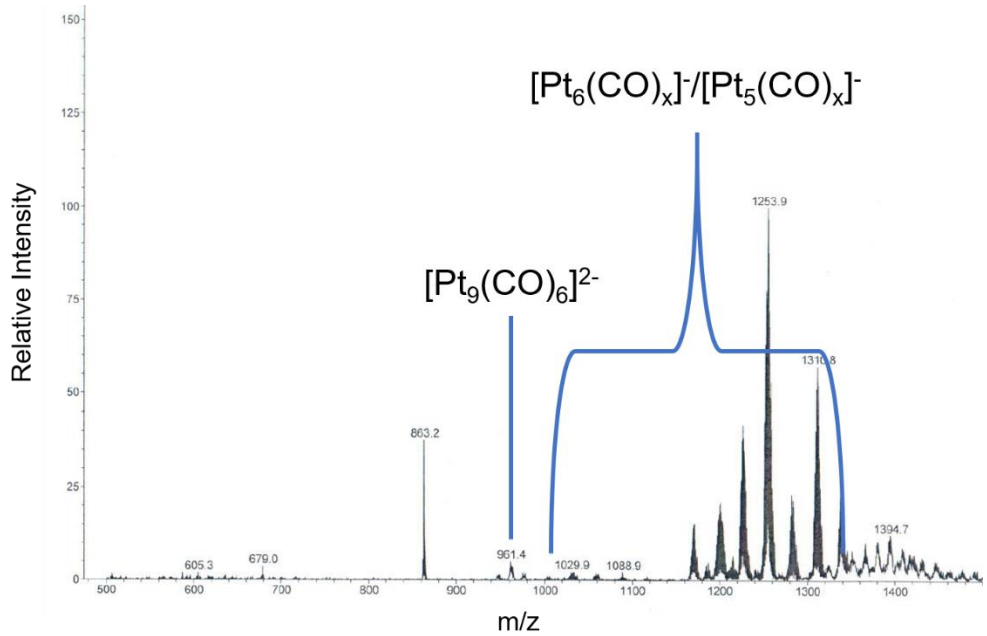

Supplementary Figure 2: ESI-MS spectrum of $[Pt_9(CO)_{18}]^{2-}$ in methanol. Strong fragmentation prevents the detection of the intact cluster.

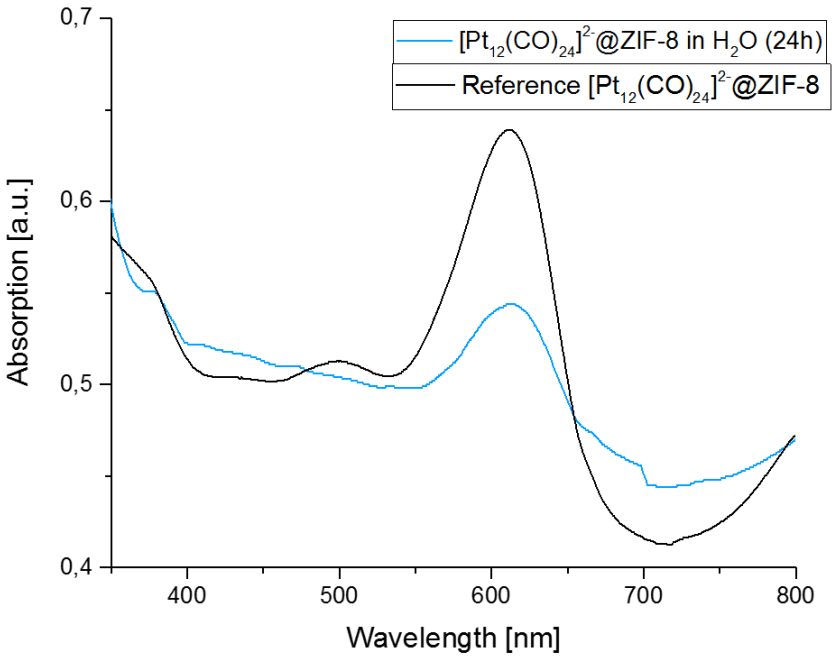

Supplementary Figure 3: DR-UV/Vis spectrum of $[Pt_{12}(CO)_{24}](NBu_4)_2$@ZIF-8 after stirring for 24 h in boiling water. The unchanged position of the distinctive band at 620 nm proves the integrity of the cluster and confirms the stabilizing effect of the framework.

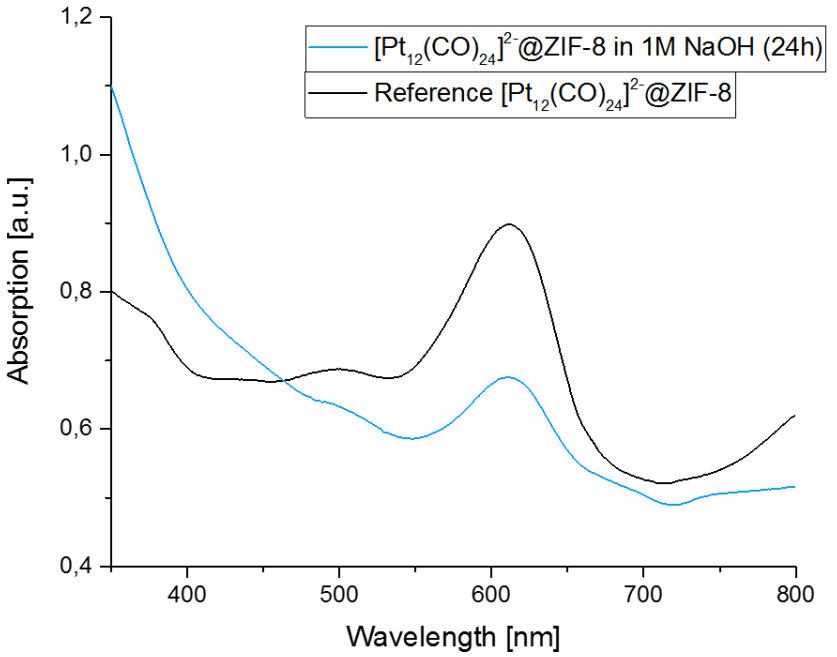

Supplementary Figure 4: DR-UV/Vis spectrum of $[Pt_{12}(CO)_{24}](NBu_4)_2$@ZIF-8 after stirring for 24 h in 1M NaOH solution. The unchanged position of the distinctive band at 620 nm proves the integrity of the cluster and confirms the stabilizing effect of the framework.

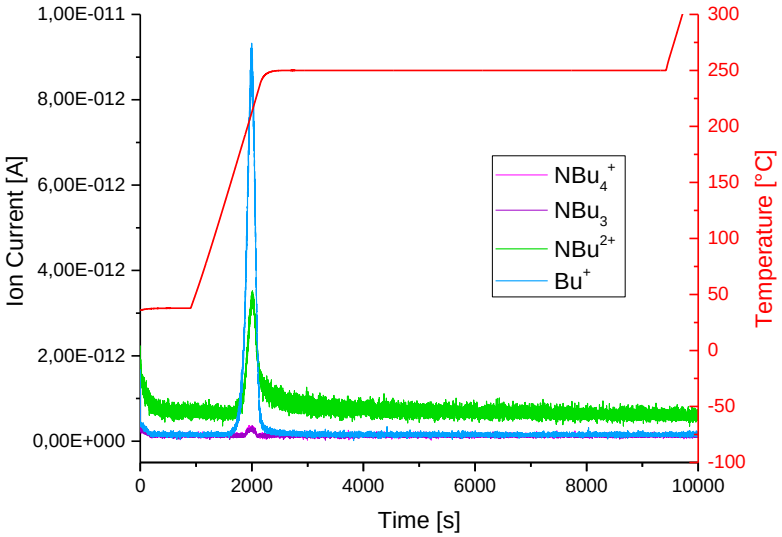

Supplementary Figure 5: TGA-MS of NBu_4Cl. Mass traces of the fragments NBu_4^+, NBu_3, NBu_2^+ and Bu^+ are detected around 200 °C.

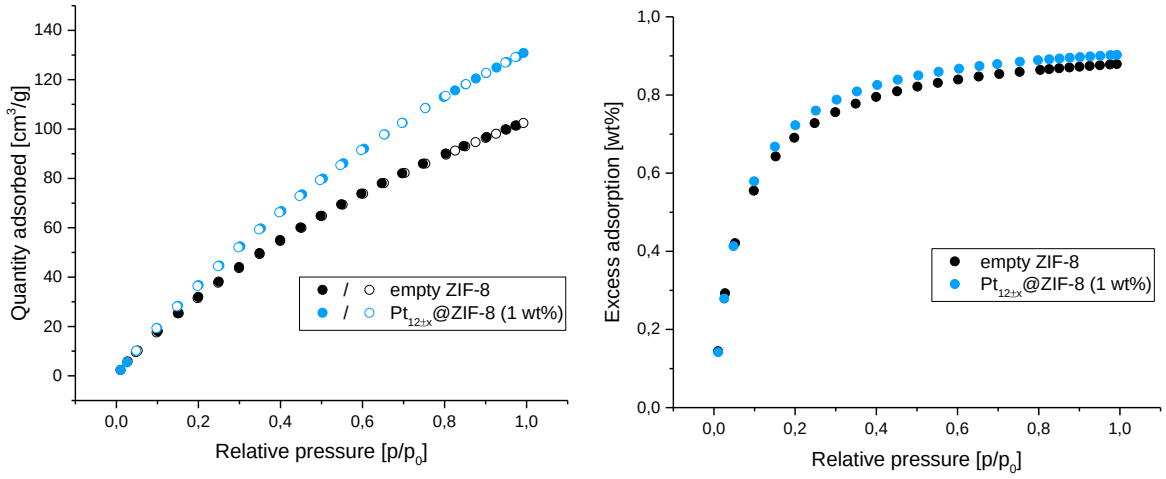

Supplementary Figure 6: Hydrogen adsorption of $Pt_{12\pm x}$@ZIF-8. *Left:* Adsorption and desorption curves of $Pt_{12\pm x}$@ZIF-8 compared to pristine ZIF-8. *Right:* Excess adsorption of $Pt_{12\pm x}$@ZIF-8 in comparison to empty ZIF-8.

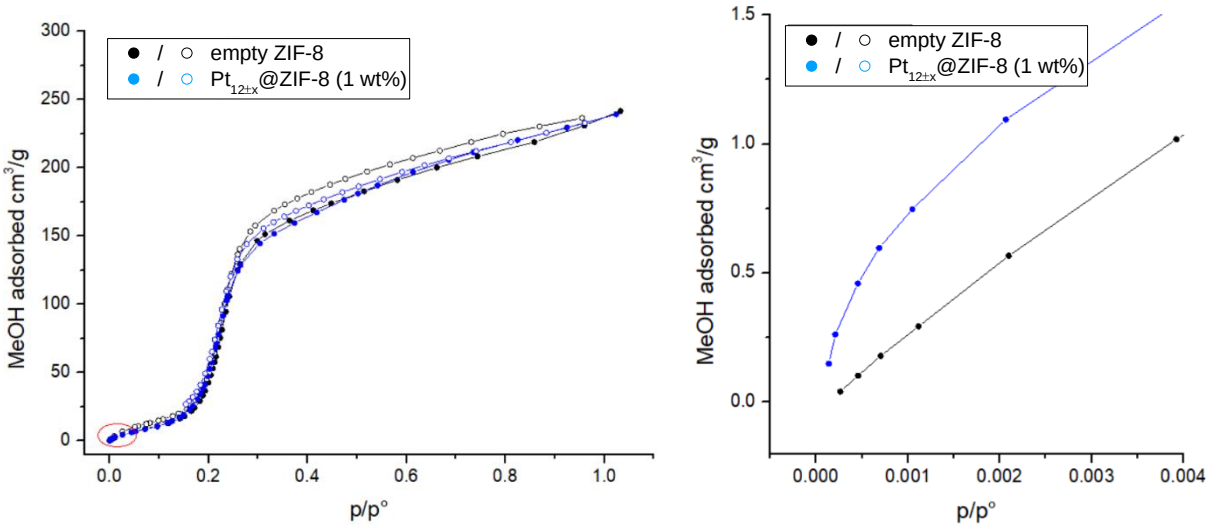

Supplementary Figure 7: Methanol adsorption measurements on $Pt_{12\pm x}$@ZIF-8 (1 wt% Pt). *Left:* Methanol adsorption and desorption for $Pt_{12\pm x}$@ZIF-8 compared to empty ZIF-8. *Right:* Enlarged low-pressure region of the methanol adsorption experiment, marked in red in the left graph.

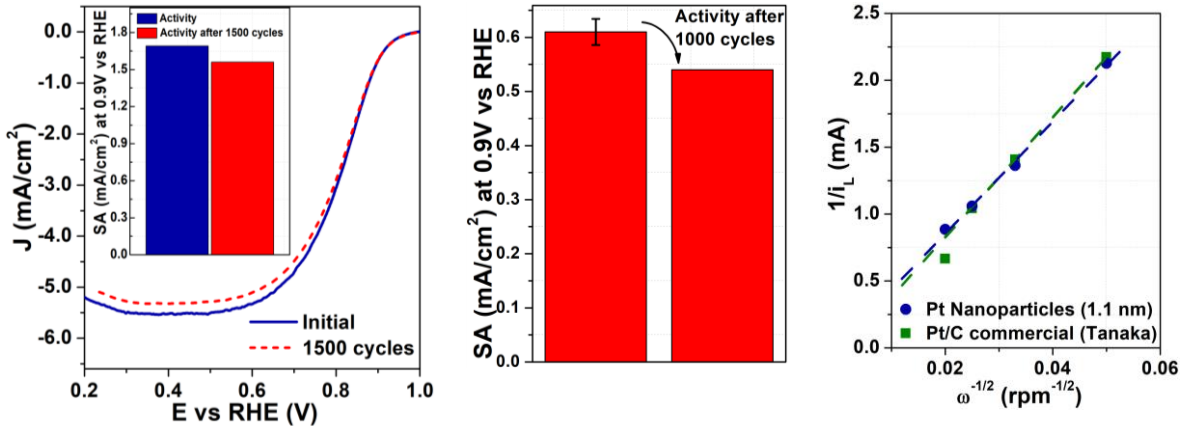

Supplementary Figure 8: *Left:* Polarization curve of Pt NPs before and after 1500 cycles in O_2-saturated 0.1M $HClO_4$ at a scan speed of 50 mV/s and a rotation speed of 1600 rpm. The inset shows the specific activity of Pt NPs at 0.9 V vs. RHE before and after 1500 durability cycles (between 0.6-1.0 V vs RHE in 0.1M $HClO_4$ at 50 mV/s), demonstrating the stability of the Pt catalyst. *Middle:* Specific activity of the commercial Pt/C at 0.9 V vs RHE initially and after 1000 cycles under the same conditions to show the comparable stability of both catalysts. *Right: Levich* plot of Pt NPs and Pt/C. Similar slopes indicate the ORR proceeds through same $4e^-$ mechanism on both catalysts.

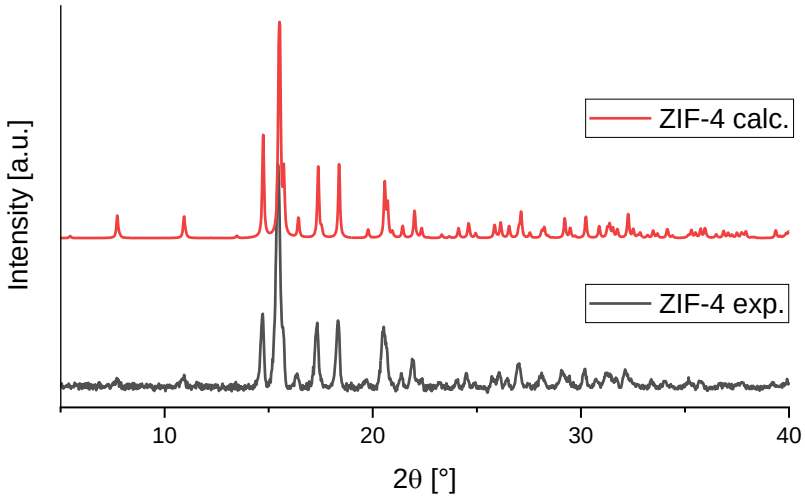

Supplementary Figure 9: Experimental and calculated PXRD pattern of a $Zn(Im)_2$ structure denoted as ZIF-4 in this work showing the crystallinity of the material.

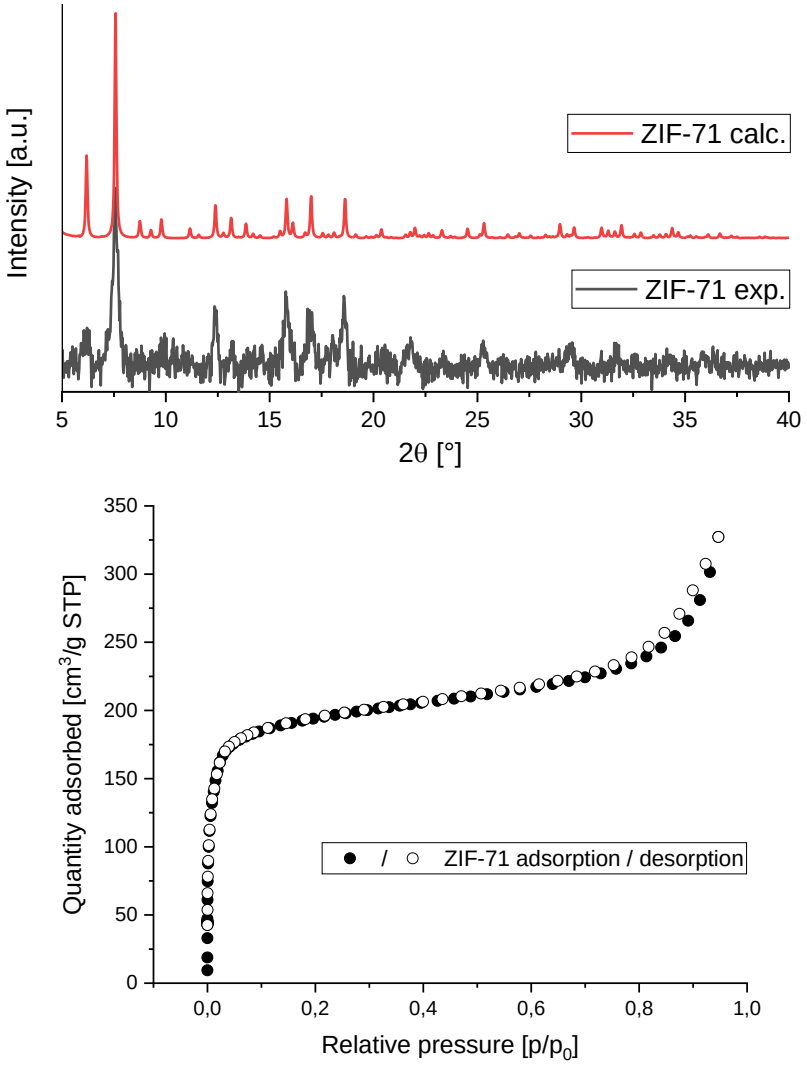

Supplementary Figure 10: Experimental and calculated PXRD pattern (*top*) as well as nitrogen adsorption isotherm (bottom) of ZIF-71 showing the moderate crystallinity and porosity of the material.

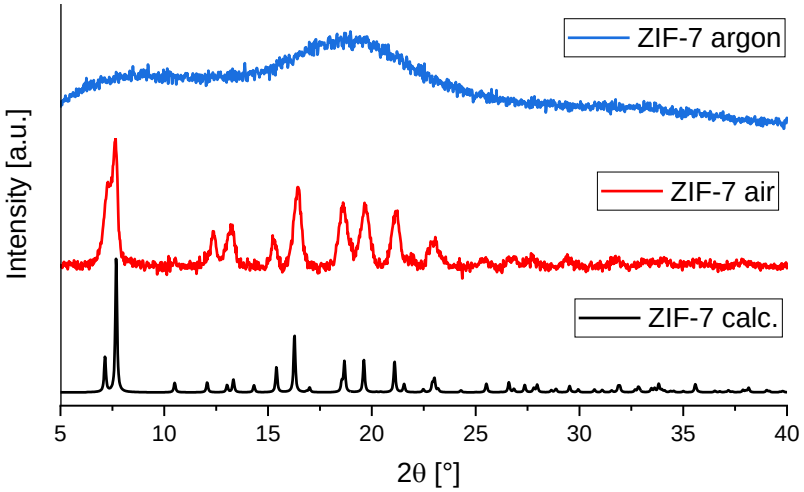

Supplementary Figure 11: Experimental and calculated PXRD pattern of ZIF-7 synthesized under air and under argon with only the former material showing distinct reflections and thus crystallinity.

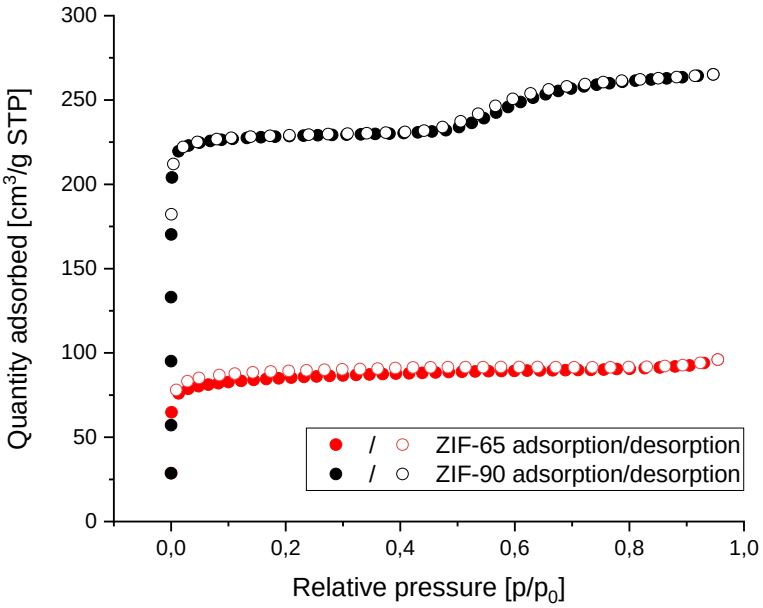

Supplementary Figure 12: Nitrogen adsorption isotherms of ZIF-90 and ZIF-65 showing the moderate porosity of both materials.

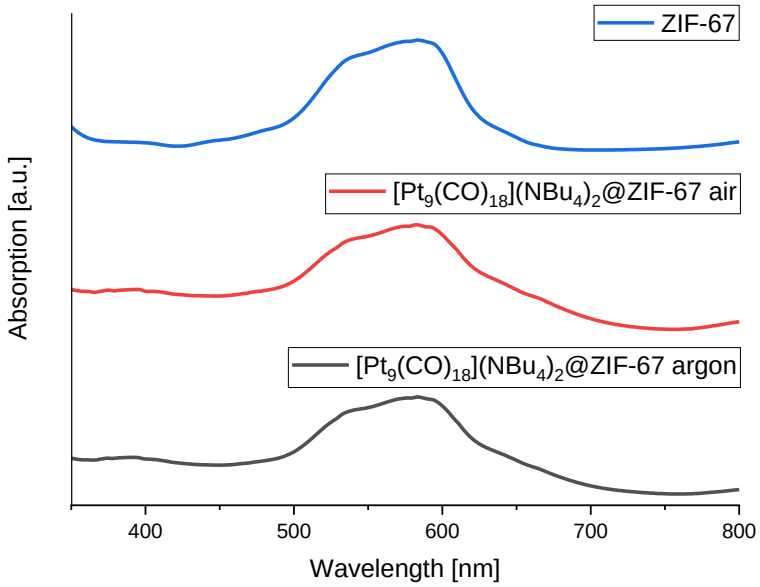

Supplementary Figure 13: DR-UV/Vis spectra of the Pt_9 *Chini* cluster encapsulated in ZIF-67 with the cluster bands overlapping with the one of the bright purple cobalt ZIF.

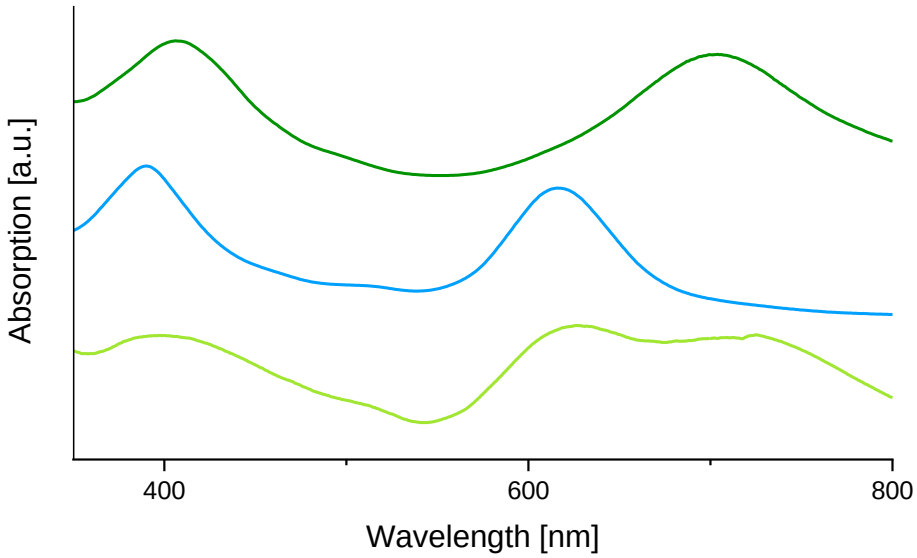

Supplementary Figure 14: DR-UV/Vis spectrum of the material resulting from the encapsulation of $[Pt_{15}(CO)_{30}](NBu_4)_2$ in ZIF-8 (light green) compared to the UV/Vis spectra of the pure Pt_{12} (blue) and Pt_{15} (green) clusters in solution. No selective encapsulation could be achieved, but the Pt_{15} cluster (706 nm) is partially reduced to the smaller Pt_{12} cluster (620 nm) to give about a 1:1 mixture.

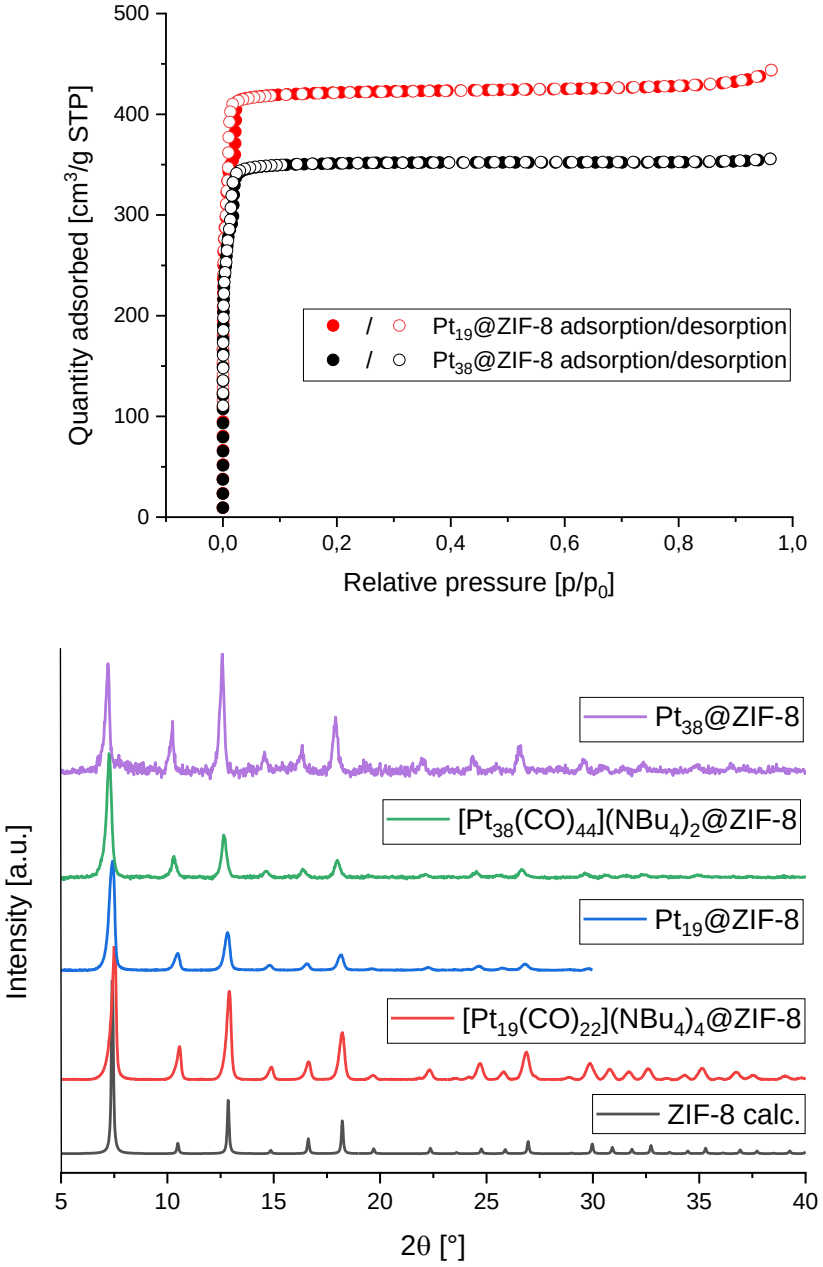

Supplementary Figure 15: Nitrogen adsorption isotherms of Pt_{19}@ZIF-8 and Pt_{38}@ZIF-8 (*top*) and PXRD patterns (*bottom*) of $[Pt_{19}(CO)_{22}](NBu_4)_4$@ZIF-8, Pt_{19}@ZIF-8, $[Pt_{38}(CO)_{44}](NBu_4)_2$@ZIF-8 and Pt_{38}@ZIF-8 compared to the calculated pattern of ZIF-8, showing the high crystallinity and porosity of all materials.

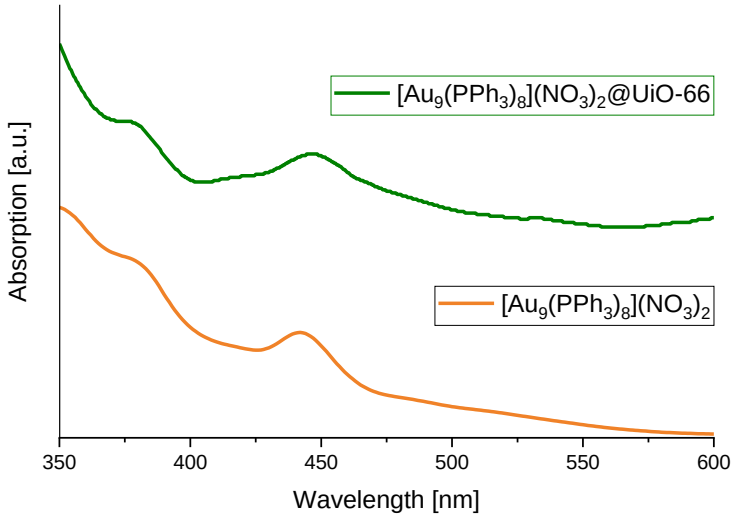

Supplementary Figure 16: Comparison of UV/Vis spectrum of $[Au_9(PPh_3)_8](NO_3)_2$ and DR-UV/Vis spectrum of $[Au_9(PPh_3)_8](NO_3)_2$@UiO-66 showing the successful encapsulation of the cluster. The bad quality of the latter spectrum stems from the low band intensity.

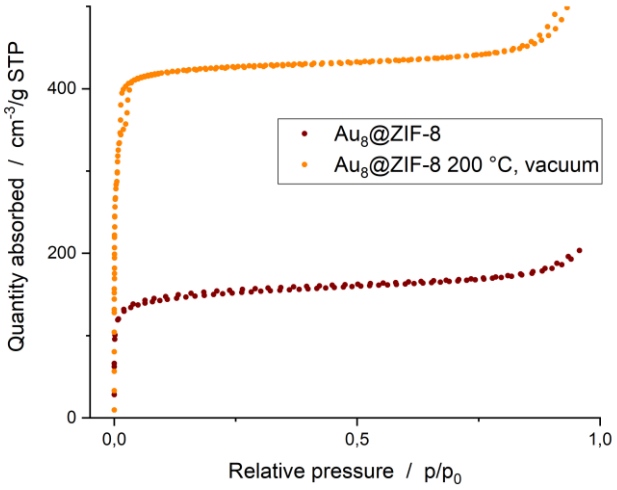

Supplementary Figure 17: BET isotherms of ZIF-8 before and after heating under dynamic vacuum at 200 °C. The internal surface area increases due to the removal of residual 2-mIm from the pores.

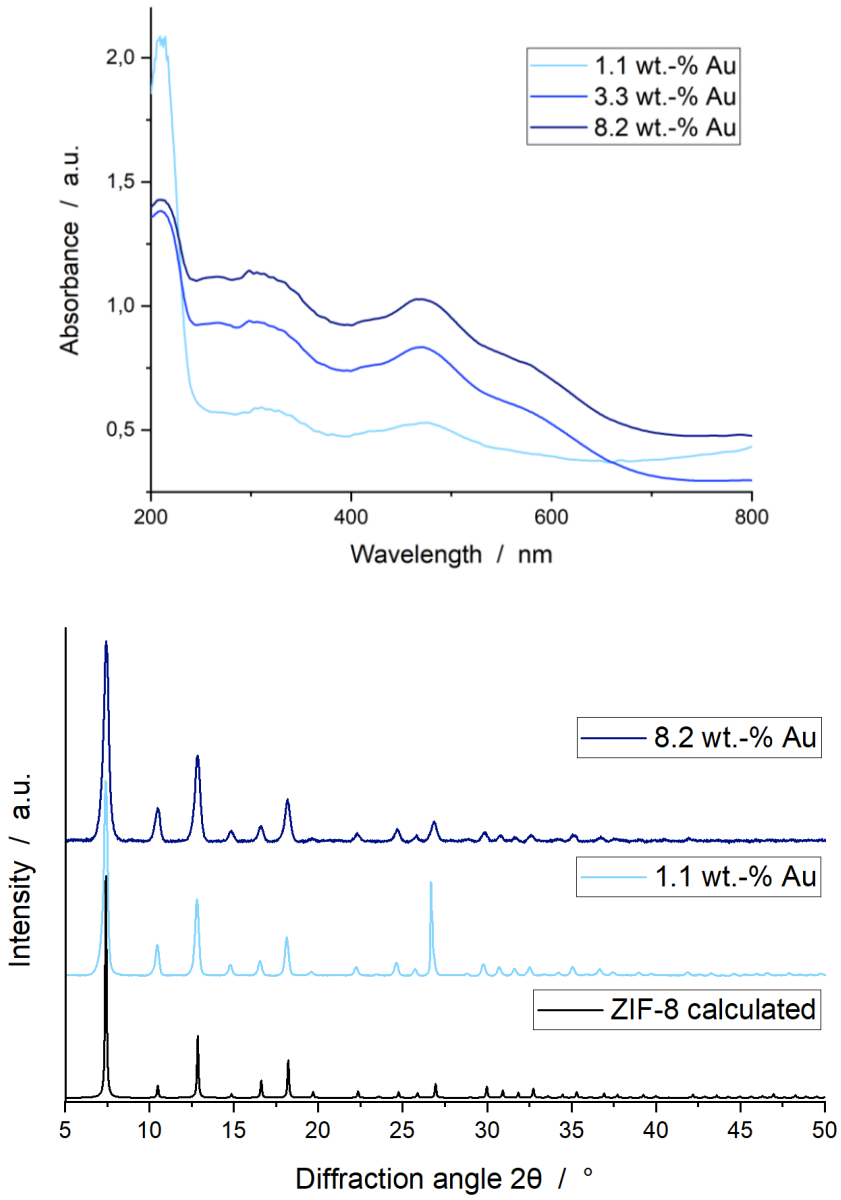

Supplementary Figure 18: DR-UV/Vis spectroscopy (*top*) and PXRD (*bottom*) of $[Au_8(tppms)_8](NO_3)_2$@ZIF-8 with different Au cluster loadings showing the integrity of the clusters after encapsulation as well as the high crystallinity of the stabilizing ZIF matrix.

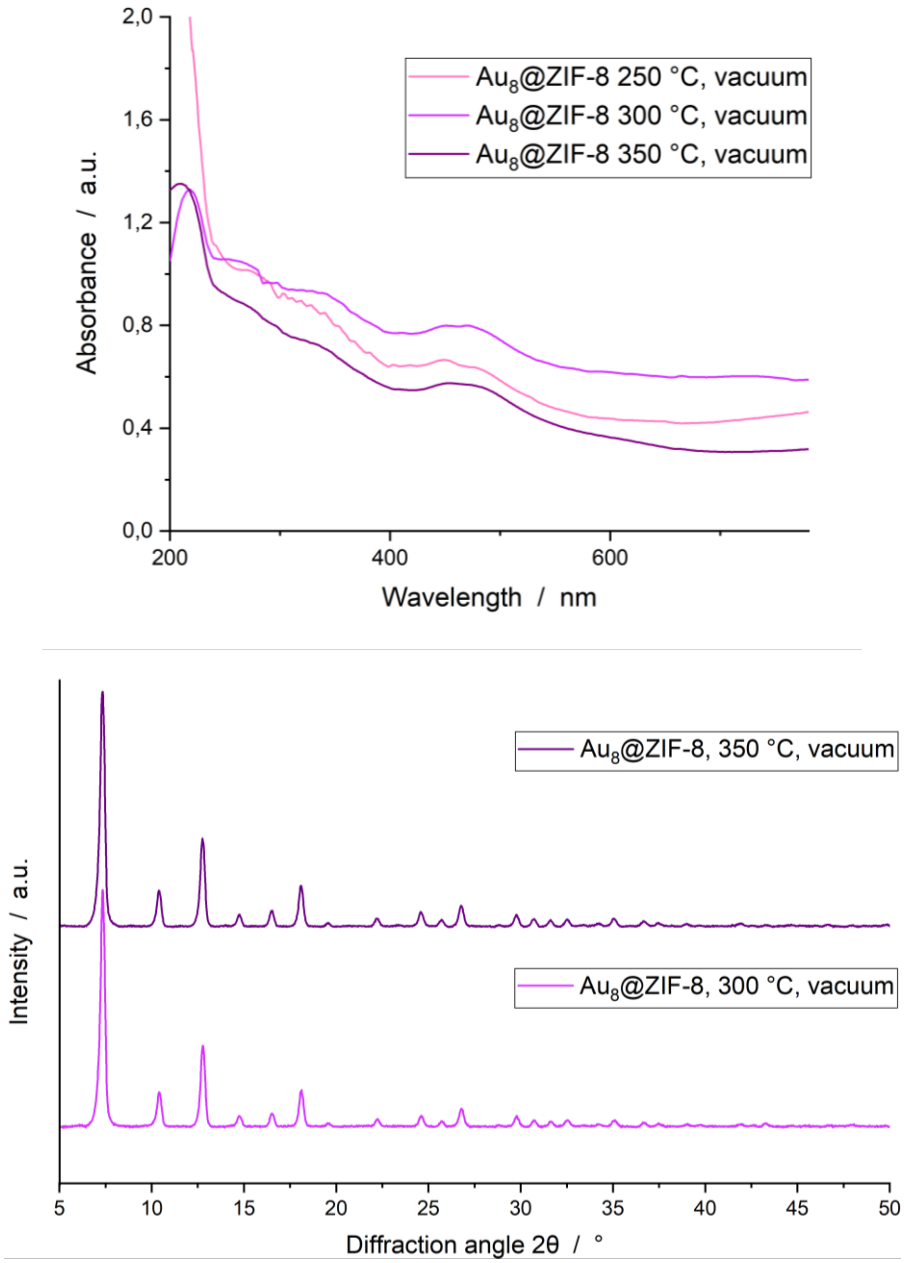

Supplementary Figure 19: DR-UV/Vis spectra (*top*) and PXRD patterns (*bottom*) of $[Au_8(tppms)_8](NO_3)_2$ @ZIF-8 after heat treatment under vacuum at 250, 300 and 350 °C showing the integrity of the cluster and the framework even at elevated temperatures.

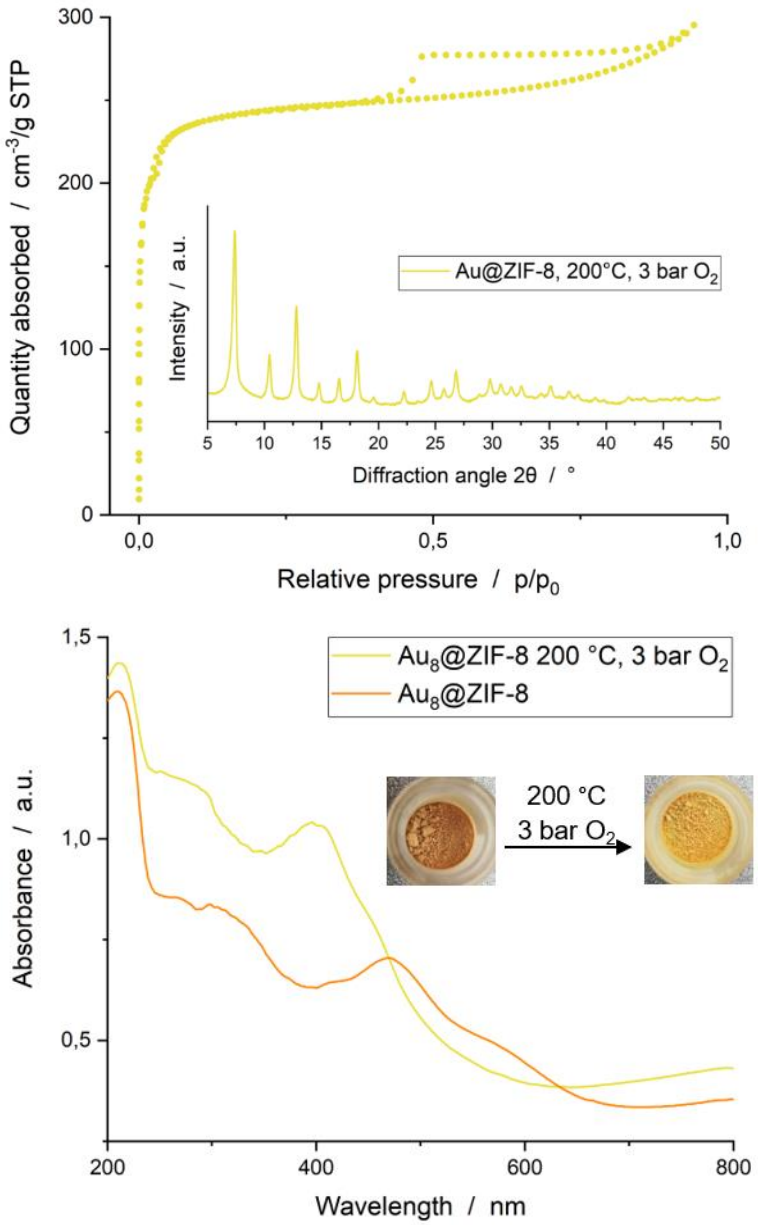

Supplementary Figure 20: BET isotherm (*top*), PXRD pattern (*inset top*) and DR-UV/Vis spectra (*bottom*) of $[Au_8(tppms)_8](NO_3)_2$@ZIF-8 after treatment at 200 °C under 3 bar O_2, inducing partial framework degradation and cluster transformation.

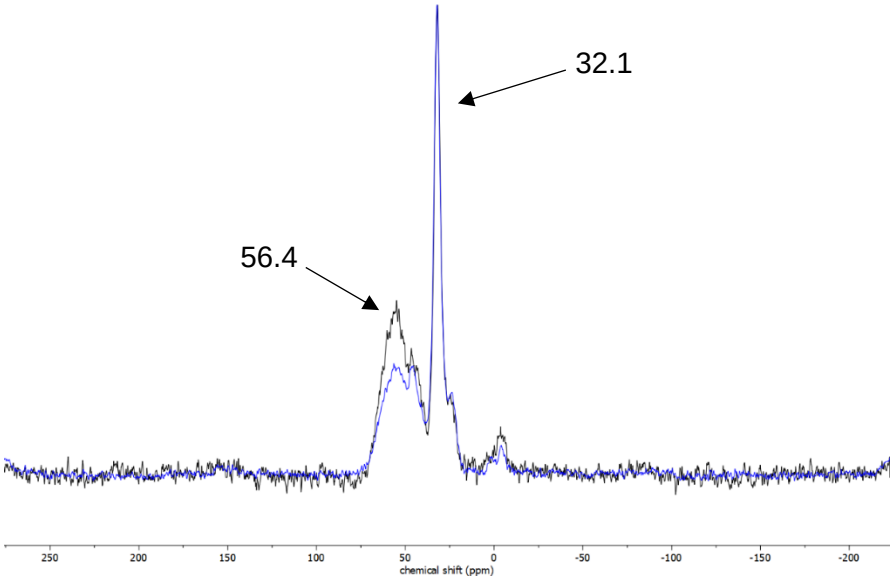

Supplementary Figure 21: ^{31}P-MAS-NMR spectra of $[Au_8(tppms)_8](NO_3)_2$@ZIF-8 after 1 bar oxygen at 150 °C (black) and under 3 bar oxygen at 200 °C (blue). The change in oxygen pressure does not significantly influence the ratio of free, oxidized phosphine (32.1 ppm) and cluster-bound phosphine (56.4 ppm).

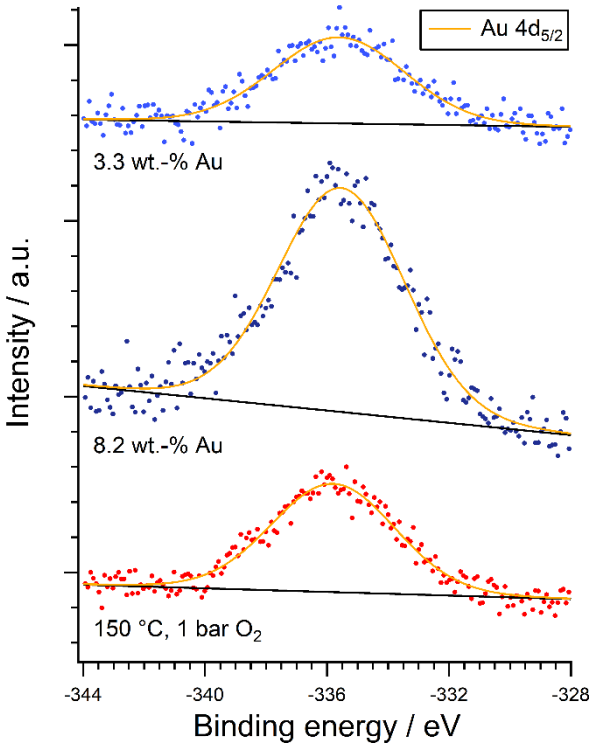

Supplementary Figure 22: XP spectra of the Au $4d_{5/2}$ region of Au_8@ZIF-8 with standard, high loading and after heating to 150 ° under 1 bar oxygen. The Au signal changes in intensity when the loading is varied, but heating does not introduce a significant signal shift.

6 REFERENCES

[1] T. Turner, *Proc. Natl. Acad. Sci. USA* **1908**, *81*, 301.
[2] M. Faraday, *Phil. Trans. R. Soc. Lon* **1857**, *147*, 145.
[3] G. Mie, *Ann. Phys.* **1908**, *330*, 377.
[4] Z. Luo, A. W. Castleman, *Acc. Chem. Res.* **2014**, *47*, 2931.
[5] E. C. Tyo, S. Vajda, *Nat. Nanotechnol.* **2015**, *10*, 577.
[6] J. Juan-Alcañiz, J. Gascon, F. Kapteijn, *J. Mater. Chem.* **2012**, *22*, 10102.
[7] P. Falcaro, R. Ricco, A. Yazdi, I. Imaz, S. Furukawa, D. Maspoch, R. Ameloot, J. D. Evans, C. J. Doonan, *Coord. Chem. Rev.* **2016**, *307*, 237.
[8] Z. Guo, C. Xiao, R. V. Maligal-Ganesh, L. Zhou, T. W. Goh, X. Li, D. Tesfagaber, A. Thiel, W. Huang, *ACS Catal.* **2014**, *4*, 1340.
[9] D. Esken, S. Turner, O. I. Lebedev, G. van Tendeloo, R. A. Fischer, *Chem. Mater.* **2010**, *22*, 6393.
[10] F. R. Fortea-Pérez, M. Mon, J. Ferrando-Soria, M. Boronat, A. Leyva-Pérez, A. Corma, J. M. Herrera, D. Osadchii, J. Gascon, D. Armentano et al., *Nat. Mater.* **2017**, *16*, 760.
[11] M. Mon, M. A. Rivero-Crespo, J. Ferrando-Soria, A. Vidal-Moya, M. Boronat, A. Leyva-Pérez, A. Corma, J. C. Hernández-Garrido, M. López-Haro, J. J. Calvino et al., *Angew. Chem. Int. Ed.* **2018**, *57*, 6186.
[12] K. Kratzl, T. Kratky, S. Günther, O. Tomanec, R. Zbořil, J. Michalička, J. M. Macak, M. Cokoja, R. A. Fischer, *J. Am. Chem. Soc.* **2019**, *141*, 13962.
[13] A. Phan, C. J. Doonan, F. J. Uribe-Romo, C. B. Knobler, M. O'Keeffe, O. M. Yaghi, *Acc. Chem. Res.* **2010**, *43*, 58.
[14] J. C. Calabrese, L. F. Dahl, P. Chini, G. Longoni, S. Martinengo, *J. Am. Chem. Soc.* **1974**, *96*, 2614.
[15] G.-J. Li, T. Fujimoto, A. Fukuoka, M. Ichikawa, *Catal. Lett.* **1992**, *12*, 171.
[16] T. Fehlner, J.-F. Halet, J.-Y. Saillard, *Molecular Clusters*, Cambridge University Press, Cambridge, **2007**.
[17] F. A. Cotton, *Q. Rev., Chem. Soc.* **1966**, *20*, 389.
[18] a) *Scientific basis for the definition of the term "nanomaterial."*, European Commission, Brussels, **2010**; b) S. H. Yau, O. Varnavski, T. Goodson, *Acc. Chem. Res.* **2013**, *46*, 1506.
[19] O. Varnavski, G. Ramakrishna, J. Kim, D. Lee, T. Goodson, *J. Am. Chem. Soc.* **2010**, *132*, 16.
[20] P. K. Jain, X. Huang, I. H. El-Sayed, M. A. El-Sayed, *Acc. Chem. Res.* **2008**, *41*, 1578.
[21] F. T. Rabouw, C. de Mello Donega in *Topics in Current Chemistry Collections* (Ed.: A. Credi), Springer, Cham, **2017**, pp. 1–30.
[22] K. Konishi in *Structure and Bonding*, *Vol. 161* (Eds.: D. M. P. Mingos, J. Broda), Springer, Cham, **2014**, pp. 49–86.
[23] M. Brack, *Rev. Mod. Phys.* **1993**, *65*, 677.
[24] a) O. Echt, K. Sattler, E. Recknagel, *Phys. Rev. Lett.* **1981**, *47*, 1121; b) D. A. Pichugina, N. E. Kuz'menko, A. F. Shestakov, *Russ. Chem. Rev.* **2015**, *84*, 1114.
[25] A. L. Mackay, *Acta Cryst.* **1962**, *15*, 916.
[26] D. E. Bergeron, A. W. Castleman, T. Morisato, S. N. Khanna, *Science* **2004**, *304*, 84.
[27] L. J. de Jongh, *Appl. Organometal. Chem.* **1998**, *12*, 393.
[28] J. D. Aiken, R. G. Finke, *J. Mol. Catal. A-Chem.* **1999**, *145*, 1.
[29] Y. Du, H. Sheng, D. Astruc, M. Zhu, *Chem. Rev.* **2019**.
[30] Y. Lei, F. Mehmood, S. Lee, J. Greeley, B. Lee, S. Seifert, R. E. Winans, J. W. Elam, R. J. Meyer, P. C. Redfern et al., *Science* **2010**, *328*, 224.
[31] F. Tao, S. Dag, L.-W. Wang, Z. Liu, D. R. Butcher, H. Bluhm, M. Salmeron, G. A. Somorjai, *Science* **2010**, *327*, 850.

[32] S. M. Lang, T. M. Bernhardt, R. N. Barnett, B. Yoon, U. Landman, *J. Am. Chem. Soc.* **2009**, *131*, 8939.
[33] D. K. Böhme, H. Schwarz, *Angew. Chem. Int. Ed.* **2005**, *44*, 2336.
[34] a) S. Abbet, A. Sanchez, U. Heiz, W.-D. Schneider, *J. Catal.* **2001**, *198*, 122; b) S. Vajda, M. J. Pellin, J. P. Greeley, C. L. Marshall, L. A. Curtiss, G. A. Ballentine, J. W. Elam, S. Catillon-Mucherie, P. C. Redfern, F. Mehmood et al., *Nat. Mater.* **2009**, *8*, 213.
[35] S. Lee, M. Di Vece, B. Lee, S. Seifert, R. E. Winans, S. Vajda, *ChemCatChem* **2012**, *4*, 1632.
[36] R. D. Adams, B. Captain, *Angew. Chem. Int. Ed.* **2008**, *47*, 252.
[37] S. Feyel, D. Schröder, X. Rozanska, J. Sauer, H. Schwarz, *Angew. Chem. Int. Ed.* **2006**, *45*, 4677.
[38] a) F. Dong, S. Heinbuch, Y. Xie, J. J. Rocca, E. R. Bernstein, Z.-C. Wang, K. Deng, S.-G. He, *J. Am. Chem. Soc.* **2008**, *130*, 1932; b) H. Schwarz, *Angew. Chem. Int. Ed.* **2011**, *50*, 10096.
[39] J. F. Goellner, J. Guzman, B. C. Gates, *J. Phys. Chem. B* **2002**, *106*, 1229.
[40] C. P. Pradeep, D.-L. Long, C. Streb, L. Cronin, *J. Am. Chem. Soc.* **2008**, *130*, 14946.
[41] F. F. Schweinberger, M. J. Berr, M. Döblinger, C. Wolff, K. E. Sanwald, A. S. Crampton, C. J. Ridge, F. Jäckel, J. Feldmann, M. Tschurl et al., *J. Am. Chem. Soc.* **2013**, *135*, 13262.
[42] G. Lu, S. Li, Z. Guo, O. K. Farha, B. G. Hauser, X. Qi, Y. Wang, X. Wang, S. Han, X. Liu et al., *Nat. Chem.* **2012**, *4*, 310.
[43] D.-E. Jiang, *Nanoscale* **2013**, *5*, 7149.
[44] P. Chini, *J. Organomet. Chem.* **1980**, *200*, 37.
[45] K. Mayer, J. Weßing, T. F. Fässler, R. A. Fischer, *Angew. Chem. Int. Ed.* **2018**, *57*, 14372.
[46] a) Y. Lin, R. G. Finke, *J. Am. Chem. Soc.* **1994**, *116*, 8335; b) M. Pohl, D. K. Lyon, N. Mizuno, K. Nomiya, R. G. Finke, *Inorg. Chem.* **1995**, *34*, 1413.
[47] T. Imaoka, H. Kitazawa, W.-J. Chun, S. Omura, K. Albrecht, K. Yamamoto, *J. Am. Chem. Soc.* **2013**, *135*, 13089.
[48] T. Imaoka, H. Kitazawa, W.-J. Chun, K. Yamamoto, *Angew. Chem. Int. Ed.* **2015**, *54*, 9810.
[49] K. Yamamoto, T. Imaoka, W.-J. Chun, O. Enoki, H. Katoh, M. Takenaga, A. Sonoi, *Nat. Chem.* **2009**, *1*, 397.
[50] J. Kašpar, P. Fornasiero, N. Hickey, *Catal. Today* **2003**, *77*, 419.
[51] M. Shao, Q. Chang, J.-P. Dodelet, R. Chenitz, *Chem. Rev.* **2016**, *116*, 3594.
[52] V. I. Chernyshov, I. M. Kisil, *Platin. Met. Rev.* **1993**, *37*, 136.
[53] I. Ciabatti, C. Femoni, M. C. Iapalucci, G. Longoni, S. Zacchini, *J. Clust. Sci.* **2014**, *25*, 115.
[54] G. Longoni, P. Chini, *J. Am. Chem. Soc.* **1976**, *98*, 7225.
[55] a) C. Femoni, F. Kaswalder, M. C. Iapalucci, G. Longoni, S. Zacchini, *Chem. Comm.* **2006**, 2135; b) M. J. D'Aniello, C. J. Carr, M. G. Zammit, *Inorg. Synth.* **1989**, 319.
[56] C. Femoni, F. Kaswalder, M. C. Iapalucci, G. Longoni, M. Mehlstäubl, S. Zacchini, A. Ceriotti, *Angew. Chem. Int. Ed.* **2006**, *45*, 2060.
[57] A. Ceriotti, N. Masciocchi, P. Macchi, G. Longoni, *Angew. Chem. Int. Ed.* **1999**, *38*, 3724.
[58] D. M. Washecheck, E. J. Wucherer, L. F. Dahl, A. Ceriotti, G. Longoni, M. Manassero, M. Sansoni, P. Chini, *J. Am. Chem. Soc.* **1979**, *101*, 6110.
[59] a) D. J. Underwood, R. Hoffmann, K. Tatsumi, A. Nakamura, Y. Yamamoto, *J. Am. Chem. Soc.* **1985**, *107*, 5968; b) C. Mealli, *J. Am. Chem. Soc.* **1985**, *107*, 2245.
[60] C. Brown, B. T. Heaton, A. D.C. Towl, P. Chini, A. Fumagalli, G. Longoni, *J. Organomet. Chem.* **1979**, *181*, 233.
[61] a) J. R. Chang, D. C. Koningsberger, B. C. Gates, *J. Am. Chem. Soc.* **1992**, *114*, 6460; b) J. Puga, R. Patrini, K. M. Sanchez, B. C. Gates, *Inorg. Chem.* **1991**, *30*, 2479.

[62] C. Dragonetti, A. Ceriotti, D. Roberto, R. Ugo, *Organometallics* **2007**, *26*, 310.
[63] F. Rabilloud, M. Harb, H. Ndome, P. Archirel, *J. Phys. Chem. A* **2010**, *114*, 6451.
[64] E. Cattabriga, I. Ciabatti, C. Femoni, T. Funaioli, M. C. Iapalucci, S. Zacchini, *Inorg. Chem.* **2016**, *55*, 6068.
[65] I. Ciabatti, C. Femoni, M. C. Iapalucci, G. Longoni, T. Lovato, S. Zacchini, *Inorg. Chem.* **2013**, *52*, 4384.
[66] F. Jaouen, E. Proietti, M. Lefèvre, R. Chenitz, J.-P. Dodelet, G. Wu, H. T. Chung, C. M. Johnston, P. Zelenay, *Energy Environ. Sci.* **2011**, *4*, 114.
[67] L. Dai, Y. Xue, L. Qu, H.-J. Choi, J.-B. Baek, *Chem. Rev.* **2015**, *115*, 4823.
[68] E. Onstad, "Exclusive: Bosch goes for platinum-light fuel cells", **2019**.
[69] M. Shao, A. Peles, K. Shoemaker, *Nano Lett.* **2011**, *11*, 3714.
[70] J. Larminie, A. L. Dicks, *Fuel Cell Systems Explained*, John Wiley and Sons Inc., Hoboken, NJ, **2003**.
[71] L. Chong, J. Wen, J. Kubal, F. G. Sen, J. Zou, J. Greeley, M. Chan, H. Barkholtz, W. Ding, D.-J. Liu, *Science* **2018**, *362*, 1276.
[72] Y. Bing, H. Liu, L. Zhang, D. Ghosh, J. Zhang, *Chem. Soc. Rev.* **2010**, *39*, 2184.
[73] J. Wu, H. Yang, *Acc. Chem. Res.* **2013**, *46*, 1848.
[74] S. Treimer, A. Tang, D. C. Johnson, *Electroanalysis* **2002**, *14*, 165.
[75] J. K. Nørskov, J. Rossmeisl, A. Logadottir, L. Lindqvist, J. R. Kitchin, T. Bligaard, H. Jónsson, *J. Phys. Chem. B* **2004**, *108*, 17886.
[76] P. L. Rodríguez-Kessler, A. R. Rodríguez-Domínguez, *J. Chem. Phys.* **2015**, *143*, 184312.
[77] F. Calle-Vallejo, J. Tymoczko, V. Colic, Q. H. Vu, M. D. Pohl, K. Morgenstern, D. Loffreda, P. Sautet, W. Schuhmann, A. S. Bandarenka, *Science* **2015**, *350*, 185.
[78] J. Stacy, Y. N. Regma, B. Leonard, M. Fan, *Renew. Sust. Energ. Rev.* **2017**, *69*, 401.
[79] I. E. L. Stephens, A. S. Bondarenko, U. Grønbjerg, J. Rossmeisl, I. Chorkendorff, *Energy Environ. Sci.* **2012**, *5*, 6744.
[80] H. Li, Y. Li, M. T. M. Koper, F. Calle-Vallejo, *J. Am. Chem. Soc.* **2014**, *136*, 15694.
[81] M. Rück, A. Bandarenka, F. Calle-Vallejo, A. Gagliardi, *J. Phys. Chem. Lett.* **2018**, *9*, 4463.
[82] F. J. Perez-Alonso, D. N. McCarthy, A. Nierhoff, P. Hernandez-Fernandez, C. Strebel, I. E. L. Stephens, J. H. Nielsen, I. Chorkendorff, *Angew. Chem. Int. Ed.* **2012**, *51*, 4641.
[83] Y. Liu, L. Zhang, B. G. Willis, W. E. Mustain, *ACS Catal.* **2015**, *5*, 1560.
[84] C. Wang, H. Daimon, T. Onodera, T. Koda, S. Sun, *Angew. Chem. Int. Ed.* **2008**, *47*, 3588.
[85] M. Rück, A. Bandarenka, F. Calle-Vallejo, A. Gagliardi, *Nanoscale Adv.* **2019**, *1*, 2901.
[86] a) S. Kunz, K. Hartl, M. Nesselberger, F. F. Schweinberger, G. Kwon, M. Hanzlik, K. J. J. Mayrhofer, U. Heiz, M. Arenz, *Phys. Chem. Chem. Phys.* **2010**, *12*, 10288; b) U. Heiz, A. Sanchez, S. Abbet, W.-D. Schneider, *J. Am. Chem. Soc.* **1999**, *121*, 3214.
[87] A. von Weber, S. L. Anderson, *Acc. Chem. Res.* **2016**, *49*, 2632.
[88] E. Toyoda, R. Jinnouchi, T. Hatanaka, Y. Morimoto, K. Mitsuhara, A. Visikovskiy, Y. Kido, *J. Phys. Chem. C* **2011**, *115*, 21236.
[89] G. Schmid, R. Pfeil, R. Boese, F. Bandermann, S. Meyer, G. H. M. Calis, J. W. A. van der Velden, *Chem. Ber.* **1981**, *114*, 3634.
[90] M. Walter, M. Moseler, R. L. Whetten, H. Häkkinen, *Chem. Sci.* **2011**, *2*, 1583.
[91] a) Q. Tang, G. Hu, V. Fung, D.-E. Jiang, *Acc. Chem. Res.* **2018**, *51*, 2793; b) R. Jin, C. Zeng, M. Zhou, Y. Chen, *Chem. Rev.* **2016**, *116*, 10346.
[92] D.-E. Jiang, M. L. Tiago, W. Luo, S. Dai, *J. Am. Chem. Soc.* **2008**, *130*, 2777.
[93] Y. Negishi, K. Nobusada, T. Tsukuda, *J. Am. Chem. Soc.* **2005**, *127*, 5261.
[94] R. L. Donkers, D. Lee, R. W. Murray, *Langmuir* **2004**, *20*, 1945.
[95] R. Jin, H. Qian, Z. Wu, Y. Zhu, M. Zhu, A. Mohanty, N. Garg, *J. Phys. Chem. Lett.* **2010**, *1*, 2903.

[96] C. Zeng, Y. Chen, A. Das, R. Jin, *J. Phys. Chem. Lett.* **2015**, *6*, 2976.
[97] N. A. Sakthivel, S. Theivendran, V. Ganeshraj, A. G. Oliver, A. Dass, *J. Am. Chem. Soc.* **2017**, *139*, 15450.
[98] M. Zhu, C. M. Aikens, F. J. Hollander, G. C. Schatz, R. Jin, *J. Am. Chem. Soc.* **2008**, *130*, 5883.
[99] N. K. Chaki, Y. Negishi, H. Tsunoyama, Y. Shichibu, T. Tsukuda, *J. Am. Chem. Soc.* **2008**, *130*, 8608.
[100] H. Qian, R. Jin, *Nano Lett.* **2009**, *9*, 4083.
[101] L. Malatesta, *Gold Bull.* **1975**, *8*, 48.
[102] G. Lugo, V. Schwanen, B. Fresch, F. Remacle, *J. Phys. Chem. C* **2015**, *119*, 10969.
[103] H. Yao, S. Tsubota, *Chem. Phys.* **2017**, *493*, 149.
[104] E. C. Dreaden, A. M. Alkilany, X. Huang, C. J. Murphy, M. A. El-Sayed, *Chem. Soc. Rev.* **2012**, *41*, 2740.
[105] M. Walter, J. Akola, O. Lopez-Acevedo, P. D. Jadzinsky, G. Calero, C. J. Ackerson, R. L. Whetten, H. Grönbeck, H. Häkkinen, *Proc. Natl. Acad. Sci. USA* **2008**, *105*, 9157.
[106] Y. Kamei, Y. Shichibu, K. Konishi, *Angew. Chem. Int. Ed.* **2011**, *50*, 7442.
[107] S. M. Lang, T. M. Bernhardt, R. N. Barnett, U. Landman, *Chemphyschem* **2010**, *11*, 1570.
[108] S. M. Lang, T. M. Bernhardt, R. N. Barnett, U. Landman, *Angew. Chem. Int. Ed.* **2010**, *49*, 980.
[109] A. Sanchez, S. Abbet, U. Heiz, W.-D. Schneider, H. Häkkinen, R. N. Barnett, U. Landman, *J. Phys. Chem. A* **1999**, *103*, 9573.
[110] a) A. Shivhare, S. J. Ambrose, H. Zhang, R. W. Purves, R. W. J. Scott, *Chem. Comm.* **2013**, *49*, 276; b) Y. Zhu, H. Qian, B. A. Drake, R. Jin, *Angew. Chem. Int. Ed.* **2010**, *49*, 1295.
[111] Y. Liu, H. Tsunoyama, T. Akita, T. Tsukuda, *Chem. Comm.* **2010**, *46*, 550.
[112] D. P. Anderson, R. H. Adnan, J. F. Alvino, O. Shipper, B. Donoeva, J.-Y. Ruzicka, H. Al Qahtani, H. H. Harris, B. Cowie, J. B. Aitken et al., *Phys. Chem. Chem. Phys.* **2013**, *15*, 14806.
[113] B. Liu, H. Yao, W. Song, L. Jin, I. M. Mosa, J. F. Rusling, S. L. Suib, J. He, *J. Am. Chem. Soc.* **2016**, *138*, 4718.
[114] W. Chen, S. Chen, *Angew. Chem. Int. Ed.* **2009**, *48*, 4386.
[115] K. Kwak, W. Choi, Q. Tang, M. Kim, Y. Lee, D.-E. Jiang, D. Lee, *Nat. Commun.*, *8*, 1.
[116] a) H.-C. Zhou, J. R. Long, O. M. Yaghi, *Chem. Rev.* **2012**, *112*, 673; b) H. Li, M. Eddaoudi, M. O'Keeffe, O. M. Yaghi, *Nature* **1999**, *402*, 276.
[117] D. J. Tranchemontagne, J. L. Mendoza-Cortés, M. O'Keeffe, O. M. Yaghi, *Chem. Soc. Rev.* **2009**, *38*, 1257.
[118] C. Dong, Z. Jiahua, Z. Pengfei, D. Sheng, *Polyhedron* **2019**, *162*, 59.
[119] J. Lee, O. K. Farha, J. Roberts, K. A. Scheidt, S. T. Nguyen, J. T. Hupp, *Chem. Soc. Rev.* **2009**, *38*, 1450.
[120] "Tony Boehle (https://commons.wikimedia.org/wiki/File:MOF-5.png), „MOF-5“, https://creativecommons.org/licenses/by-sa/3.0/legalcode".
[121] P. García-Holley, B. Schweitzer, T. Islamoglu, Y. Liu, L. Lin, S. Rodriguez, M. H. Weston, J. T. Hupp, D. A. Gómez-Gualdrón, T. Yildirim et al., *ACS Energy Lett.* **2018**, *3*, 748.
[122] L. J. Murray, M. Dincă, J. R. Long, *Chem. Soc. Rev.* **2009**, *38*, 1294.
[123] R. C. Lochan, R. Z. Khaliullin, M. Head-Gordon, *Inorg. Chem.* **2008**, *47*, 4032.
[124] M. P. Suh, H. J. Park, T. K. Prasad, D.-W. Lim, *Chem. Rev.* **2012**, *112*, 782.
[125] J.-R. Li, R. J. Kuppler, H.-C. Zhou, *Chem. Soc. Rev.* **2009**, *38*, 1477.
[126] R. Matsuda, R. Kitaura, S. Kitagawa, Y. Kubota, R. V. Belosludov, T. C. Kobayashi, H. Sakamoto, T. Chiba, M. Takata, Y. Kawazoe et al., *Nature* **2005**, *436*, 238.

[127] J. A. R. Navarro, E. Barea, A. Rodríguez-Diéguez, J. M. Salas, C. O. Ania, J. B. Parra, N. Masciocchi, S. Galli, A. Sironi, *J. Am. Chem. Soc.* **2008**, *130*, 3978.
[128] A. Schneemann, V. Bon, I. Schwedler, I. Senkovska, S. Kaskel, R. A. Fischer, *Chem. Soc. Rev.* **2014**, *43*, 6062.
[129] M. D. Allendorf, C. A. Bauer, R. K. Bhakta, R. J. T. Houk, *Chem. Soc. Rev.* **2009**, *38*, 1330.
[130] M. Kurmoo, *Chem. Soc. Rev.* **2009**, *38*, 1353.
[131] M. J. Ingleson, J. P. Barrio, J. Bacsa, C. Dickinson, H. Park, M. J. Rosseinsky, *Chem. Comm.* **2008**, 1287.
[132] D. Zacher, O. Shekhah, C. Wöll, R. A. Fischer, *Chem. Soc. Rev.* **2009**, *38*, 1418.
[133] K. Schlichte, T. Kratzke, S. Kaskel, *Micropor. Mesopor. Mat.* **2004**, *73*, 81.
[134] F. Vermoortele, R. Ameloot, L. Alaerts, R. Matthessen, B. Carlier, E. V. R. Fernandez, J. Gascon, F. Kapteijn, D. E. de Vos, *J. Mater. Chem.* **2012**, *22*, 10313.
[135] K. Epp, A. L. Semrau, M. Cokoja, R. A. Fischer, *ChemCatChem* **2018**, *10*, 3506.
[136] S. Dissegna, K. Epp, W. R. Heinz, G. Kieslich, R. A. Fischer, *Adv. Mater.* **2018**, *30*, e1704501.
[137] Y. Liu, S.-Y. Moon, J. T. Hupp, O. K. Farha, *ACS nano* **2015**, *9*, 12358.
[138] A. M. Shultz, O. K. Farha, J. T. Hupp, S. T. Nguyen, *J. Am. Chem. Soc.* **2009**, *131*, 4204.
[139] D. Feng, Z.-Y. Gu, Y.-P. Chen, J. Park, Z. Wei, Y. Sun, M. Bosch, S. Yuan, H.-C. Zhou, *J. Am. Chem. Soc.* **2014**, *136*, 17714.
[140] L. Ma, C. Abney, W. Lin, *Chem. Soc. Rev.* **2009**, *38*, 1248.
[141] S.-H. Cho, B. Ma, S. T. Nguyen, J. T. Hupp, T. E. Albrecht-Schmitt, *Chem. Comm.* **2006**, 2563.
[142] K. Tanaka, S. Oda, M. Shiro, *Chem. Comm.* **2008**, 820.
[143] A. Hu, H. L. Ngo, W. Lin, *J. Am. Chem. Soc.* **2003**, *125*, 11490.
[144] G. Férey, C. Mellot-Draznieks, C. Serre, F. Millange, J. Dutour, S. Surblé, I. Margiolaki, *Science* **2005**, *309*, 2040.
[145] K. S. Park, Z. Ni, A. P. Côté, J. Y. Choi, R. Huang, F. J. Uribe-Romo, H. K. Chae, M. O'Keeffe, O. M. Yaghi, *Proc. Natl. Acad. Sci. USA* **2006**, *103*, 10186.
[146] R. Banerjee, A. Phan, B. Wang, C. Knobler, H. Furukawa, M. O'Keeffe, O. M. Yaghi, *Science* **2008**, *319*, 939.
[147] B. Wang, A. P. Côté, H. Furukawa, M. O'Keeffe, O. M. Yaghi, *Nature* **2008**, *453*, 207.
[148] J. Cravillon, S. Münzer, S.-J. Lohmeier, A. Feldhoff, K. Huber, M. Wiebcke, *Chem. Mater.* **2009**, *21*, 1410.
[149] Y. Pan, Y. Liu, G. Zeng, L. Zhao, Z. Lai, *Chem. Commun.* **2011**, *47*, 2071.
[150] U. P. N. Tran, K. K. A. Le, N. T. S. Phan, *ACS Catal.* **2011**, *1*, 120.
[151] H. He, H. Han, H. Shi, Y. Tian, F. Sun, Y. Song, Q. Li, G. Zhu, *ACS Appl. Mater. Inter.* **2016**, *8*, 24517.
[152] F.-K. Shieh, S.-C. Wang, C.-I. Yen, C.-C. Wu, S. Dutta, L.-Y. Chou, J. V. Morabito, P. Hu, M.-H. Hsu, K. C.-W. Wu et al., *J. Am. Chem. Soc.* **2015**, *137*, 4276.
[153] H. R. Moon, D.-W. Lim, M. P. Suh, *Chem. Soc. Rev.* **2013**, *42*, 1807.
[154] A. Aijaz, A. Karkamkar, Y. J. Choi, N. Tsumori, E. Rönnebro, T. Autrey, H. Shioyama, Q. Xu, *J. Am. Chem. Soc.* **2012**, *134*, 13926.
[155] M. S. El-Shall, V. Abdelsayed, A. E. R. S. Khder, H. M. A. Hassan, H. M. El-Kaderi, T. E. Reich, *J. Mater. Chem.* **2009**, *19*, 7625.
[156] H.-L. Jiang, B. Liu, T. Akita, M. Haruta, H. Sakurai, Q. Xu, *J. Am. Chem. Soc.* **2009**, *131*, 11302.
[157] D. Esken, X. Zhang, O. I. Lebedev, F. Schröder, R. A. Fischer, *J. Mater. Chem.* **2009**, *19*, 1314.
[158] J. Reboul, S. Furukawa, N. Horike, M. Tsotsalas, K. Hirai, H. Uehara, M. Kondo, N. Louvain, O. Sakata, S. Kitagawa, *Nat. Mater.* **2012**, *11*, 717.

[159] K. Khaletskaya, J. Reboul, M. Meilikhov, M. Nakahama, S. Diring, M. Tsujimoto, S. Isoda, F. Kim, K.-i. Kamei, R. A. Fischer et al., *J. Am. Chem. Soc.* **2013**, *135*, 10998.
[160] S.-T. Zheng, X. Zhao, S. Lau, A. Fuhr, P. Feng, X. Bu, *J. Am. Chem. Soc.* **2013**, *135*, 10270.
[161] a) S. Proch, J. Herrmannsdörfer, R. Kempe, C. Kern, A. Jess, L. Seyfarth, J. Senker, *Chemistry* **2008**, *14*, 8204; b) M. Müller, S. Hermes, K. Kähler, M. W. E. van den Berg, M. Muhler, R. A. Fischer, *Chem. Mater.* **2008**, *20*, 4576.
[162] S. Ji, Y. Chen, Q. Fu, Y. Chen, J. Dong, W. Chen, Z. Li, Y. Wang, L. Gu, W. He et al., *J. Am. Chem. Soc.* **2017**, *139*, 9795.
[163] Y. Luo, S. Fan, W. Yu, Z. Wu, D. A. Cullen, C. Liang, J. Shi, C. Su, *Adv. Mater.* **2018**, *30*.
[164] L. Liu, Y. Song, H. Chong, S. Yang, J. Xiang, S. Jin, X. Kang, J. Zhang, H. Yu, M. Zhu, *Nanoscale* **2016**, *8*, 1407.
[165] A. Schejn, L. Balan, V. Falk, L. Aranda, G. Medjahdi, R. Schneider, *CrystEngComm* **2014**, *16*, 4493.
[166] J. Nováková, *Phys. Chem. Chem. Phys.* **2001**, *3*, 2704.
[167] a) S. Liua, F. Chen, S. Lia, X. Peng, Y. Xiong, *Appl. Catal. B* **2017**, *211*, 1; b) R. L. Papporello, E. E. Miró, J. M. Zamaro, *Micropor. Mesopor. Mat.* **2015**, *211*, 64.
[168] C. Wiktor, M. Meledina, S. Turner, O. I. Lebedev, R. A. Fischer, *J. Mater. Chem. A* **2017**, *5*, 14969.
[169] M. Sadakiyo, H. Kasai, K. Kato, M. Takata, M. Yamauchi, *J. Am. Chem. Soc.* **2014**, *136*, 1702.
[170] V. M. Frolov, *Platinum Metals Rev.* **1996**, *40*, 8.
[171] B. Garlyyev, K. Kratzl, M. Rück, J. Michalička, J. Fichtner, J. M. Macak, T. Kratky, S. Günther, M. Cokoja, A. S. Bandarenka et al., *Angew. Chem. Int. Ed.* **2019**, *58*, 9596.
[172] J. Koutecky, V. G. Levich, *Zh. Fiz. Khim.* **1958**, *32*, 1565.
[173] T. Yang, T.-S. Chung, *J. Mater. Chem. A* **2013**, *1*, 6081.
[174] J. Yang, F. Zhang, H. Lu, X. Hong, H. Jiang, Y. Wu, Y. Li, *Angew. Chem. Int. Ed.* **2015**, *54*, 10889.
[175] F. Wen, U. Englert, B. Gutrath, U. Simon, *Eur. J. Inorg. Chem.* **2008**, *2008*, 106.
[176] J. W. A. van der Velden, J. J. Bour, J. J. Steggerda, P. T. Beurskens, M. Roseboom, J. H. Noordik, *Inorg. Chem.* **1982**, *21*, 4321.
[177] B. S. Gutrath, U. Englert, Y. Wang, U. Simon, *Eur. J. Inorg. Chem.* **2013**, *2013*, 2002.
[178] A. L. Semrau, S. Wannapaiboon, S. P. Pujari, P. Vervoorts, B. Albada, H. Zuilhof, R. A. Fischer, *Cryst. Growth Des.* **2019**, *19*, 1738.
[179] S. Sanz, L. A. Jones, F. Mohr, M. Laguna, *Organometallics* **2007**, *26*, 952.
[180] Y. Pan, S. Neuss, A. Leifert, M. Fischler, F. Wen, U. Simon, G. Schmid, W. Brandau, W. Jahnen-Dechent, *Small* **2007**, *3*, 1941.
[181] R. H. Adnan, G. G. Andersson, M. I. J. Polson, G. F. Metha, V. B. Golovko, *Catal. Sci. Technol.* **2015**, *5*, 1323.
[182] H. Yin, H. Kim, J. Choi, A. C.K. Yip, *Chem. Eng. J.* **2015**, *278*, 293.
[183] C. Battistoni, G. Mattogno, F. Cariati, L. Naldini, A. Sgamellotti, *Inorganica Chim. Acta* **1977**, *24*, 207.
[184] D. V. Esposito, S. T. Hunt, Y. C. Kimmel, J. G. Chen, *J. Am. Chem. Soc.* **2012**, *134*, 3025.
[185] M. Rück, B. Garlyyev, A. Bandarenka, A. Gagliardi, *submitted*.
[186] A. Tronnier, A. Poethig, E. Herdtweck, T. Strassner, *Organometallics* **2014**, *33*, 898.
[187] P. Braunstein, H. Lehner, D. Matt, K. Burgess, M. J. Ohlmeyer in *Inorg. Synth.*, pp. 218–221.
[188] A. M. Mueting, B. D. Alexander, P. D. Boyle, A. L. Casalnuovo, L. N. Ito, B. J. Johnson, L. H. Pignolet, M. Leeaphon, K. E. Meyer, R. A. Walton et al. in *Inorg. Synth.*, pp. 279–298.

[189] G. Schmid, N. Klein, L. Korste, U. Kreibig, D. Schönauer, *Polyhedron* **1988**, *7*, 605.
[190] R. Uson, A. Laguna, M. Laguna, D. A. Briggs, H. H. Murray, J. P. Fackler in *Inorg. Synth.*, pp. 85–91.
[191] A. F. Gross, E. Sherman, J. J. Vajo, *Dalton Trans.* **2012**, *41*, 5458.
[192] F.-K. Shieh, S.-C. Wang, S.-Y. Leo, K. C.-W. Wu, *Chemistry* **2013**, *19*, 11139.
[193] Y. Li, L. H. Wee, J. A. Martens, I. F. J. Vankelecom, *J. Mater. Chem. A* **2014**, *2*, 10034.

7 APPENDIX

7.1 Active Participation in Scientific Conferences

2nd European Conference on MOFs and Porous Polymers	Encapsulation of Ligand-Stabilized Clusters in Metal-Organic Frameworks (**poster presentation**) **K. Kratzl**, W. Heinz, R. A. Fischer 29.10-01.11.2017, *Delft*, Netherlands
6th International Conference on Metal-Organic Frameworks	Catalytic Applications of Ultrasmall, Atom-precise Platinum Clusters in ZIF-8 (**poster presentation**) **K. Kratzl**, B. Garlyyev, A. Bandarenka, R. A. Fischer 09.-13.12.2018, *Auckland*, New Zealand
AC@TUM Get-Together 2019	Nanomaterials for Electrocatalysis (**oral presentation**) **K. Kratzl**, W.-J. Li, R. A. Fischer 25.-26.06.2019, *Raitenhaslach*, Germany
258th ACS National Meeting & Exposition	Encapsulation of Ligand- Stabilized Clusters in Metal-Organic Frameworks (**oral presentation**) **K. Kratzl**, R. A. Fischer 24.-29.08.2019, *San Diego*, USA
ECS Workshop 2019	Encapsulation of Ligand- Stabilized Clusters in Metal-Organic Frameworks (**oral presentation**) **K. Kratzl**, R. A. Fischer 10.-11.10.2019, *Raitenhaslach*, Germany

7.2 Publications in Scientific Journals

J. Am. Chem. Soc.
2019, *141*, 13962–13969

Generation and Stabilization of Small Platinum Clusters $Pt_{12\pm x}$ Inside a Metal-Organic Framework
K. Kratzl, T. Kratky, S. Günther, O. Tomanec, R. Zbořil, J. Michalička, J. M. Macak, M. Cokoja, R. A. Fischer*

Angew. Chem. Int. Ed.
2019, *58*, 9596–9600

Angew. Chem.
2019, *131*, 9697–9702

Optimizing the Size of Platinum Nanoparticles for Enhanced Mass Activity in the Electrochemical Oxygen Reduction Reaction
Optimierung der Größe von Platin-Nanopartikeln für eine erhöhte Massenaktivität der elektrochemischen Sauerstoffreduktion
B. Garlyyev,‡ **K. Kratzl**,‡ M. Rück,‡ J. Michalička, J. Fichtner, J. M. Macak, T. Kratky, S. Günther, M. Cokoja, A. S. Bandarenka, Alessio Gagliardi, R. A. Fischer*

Several press releases concerning the publication, e.g.: TUM press release „Activity of fuel cell catalysts doubled“, 03.07.2019

‡ Shared first authorship; * Corresponding author

7.3 Declaration of Project Contributions

This work was realized in close collaboration with several partners at the TUM as well as at national and international universities and institutes. Mirza Cokoja, Roland A. Fischer and I conceived and designed the project. I was responsible for sample syntheses, characterization and catalytic experiments on NMR scale. In addition, I coordinated the collaboration projects for electrochemical measurements and for additional analytic methods inhouse and at international institutes. Lorenzo Facco as a guest student from the University of Padua conducted his master's thesis under my close supervision and was responsible for the variation of the ZIF matrix in the Pt system, where ZIF-8 and in part also ZIF-90 had already been established. The concept of expanding the encapsulation concept to gold clusters was initiated by myself and I conducted preliminary syntheses of the proof-of-concept system "Au_8@ZIF-8". The optimization, variation and understanding of this material were significantly advanced in the master's thesis of Kathrin Kollmannsberger that was supervised by me.

Batyr Garlyyev (Chair of Physics of Energy Conversion and Storage, Prof. A. Bandarenka, TUM) conducted all electrochemical characterization experiments. Marlon Rück (Chair of Simulation of Nanosystems for Energy Conversion, Prof. A. Gagliardi, TUM) was responsible for computational activity screenings. Tim Kratky (Chair of Physical Chemistry with Focus on Catalysis, Prof. S. Günther, TUM) performed XPS measurements. Ondřej Tomanec (Regional Centre of Advanced Technologies and Materials (RCPTM), Prof. R. Zbořil, Czech Republic) conducted and analyzed HR-TEM and HAADF-STEM experiments. Jan Michalička and Jan Macák (Central European Institute of Technology (CEITEC), Czech Republic) measured HR-TEM of Pt samples digested on TEM grids. Rifan Hardian (Aix-Marseille Université, Prof. P. Llewellyn, France) performed methanol adsorption studies. Miguel Rivera-Torrente (Utrecht University, Prof. B. Weckhuysen, Netherlands) measured *in-situ* IR spectra for sample decarbonylation. Sebastian Ehrling (Technical University Dresden, Chair of Inorganic Chemistry I, Prof. S. Kaskel) conducted hydrogen adsorption studies.

I have been directly involved in the analysis and critical evaluation of all the experimental data obtained during this collaborative work. The thesis is a comprehensive scientific presentation of the results.